# Impact of Light-Matter Interactions in Mapping Ultrafast Excited-State Dynamics of GFP Chromophore Derivatives: A Theoretical Perspective

A Thesis Submitted
In Partial Fulfillment of the Requirements
for the Degree of
**DOCTOR OF PHILOSOPHY**

by

**Bittu Lama**
Roll No. 186122008

*Under the Supervision of*
**Prof. Manabendra Sarma**


**Department of Chemistry**
**Indian Institute of Technology Guwahati**
**Guwahati-781039, Assam, India**
August 2025

*Dedicated to my Maa and Baba*

**INDIAN INSTITUTE OF TECHNOLOGY GUWAHATI**
**Department of Chemistry**

# Declaration

I hereby declare that the work incorporated in the thesis entitled **"Impact of Light-Matter Interactions in Mapping Ultrafast Excited-State Dynamics of GFP Chromophore Derivatives: A Theoretical Perspective"** is the result of research work carried out by me in the Department of Chemistry, under the supervision of Prof. Manabendra Sarma, Professor, Department of Chemistry, Indian Institute of Technology Guwahati, Assam, India.

In keeping with the general practice of reporting scientific observation, due acknowledgment has been accorded wherever the research presented is based on the outcomes of other investigations.

**Date**: November 2, 2025 **Bittu Lama**
**Place**: IIT Guwahati

**INDIAN INSTITUTE OF TECHNOLOGY GUWAHATI**
**Department of Chemistry**

# Certificate

This is to certify that the work contained in the thesis entitled **"Impact of Light-Matter Interactions in Mapping Ultrafast Excited-State Dynamics of GFP Chromophore Derivatives: A Theoretical Perspective"** has been carried out by Miss Bittu Lama (Roll No. 186122008) for the Degree of Doctor of Philosophy at the Department of Chemistry, Indian Institute of Technology Guwahati, under my supervision. This work has not been submitted in part or in full to any other university or Institute for the award of any degree.

**Date**: November 2, 2025

**Prof. Manabendra Sarma**
Thesis Supervisor
Department of Chemistry
IIT Guwahati

# *Acknowledgements*

With an extreme sense of gratitude, I take this opportunity to thank all the individuals who have guided, supported, and encouraged me in this long and crucial journey of my Ph.D.

First and foremost, I would like to extend my whole-hearted acknowledgment to my supervisor, Prof. Manabendra Sarma, for his excellent guidance, constant encouragement, and unwavering support throughout these years of my Ph.D tenure. Thank you sir, for consistently pushing and assisting me in achieving this goal. I will forever cherish the opportunities you have provided and the doors you have opened for insightful discussions that taught me to deal with science and challenges with curiosity and purpose, and can be made interesting to ease out a solution. I will forever be grateful for the opportunity to have him as my mentor.

I would also like to extend my sincere thanks and gratitude to my doctoral committee members, Prof. Kalyanasis Sahu, Prof. Aditya Narayan Panda, and Dr. Priyadarshi Satpati, for periodically evaluating my work and providing valuable suggestions and comments for its improvement. My sincere thanks also go to all the faculty and staff members of the Department of Chemistry, IIT Guwahati, for their kind help and cooperation whenever required.

I would like to acknowledge the Ministry of Human Resource and Development (MHRD), India, for providing me the financial assistance during my Ph.D tenure, and IIT Guwahati for providing me with all the facilities to carry out my research work. My deepest thanks also go to the IIT Guwahati supercomputing facilities Param-Ishan and Param-Kamrupa, without which the completion of my dissertation would not have been possible.

My special thanks and appreciation to all the past and present lab members of CHEL-104, Dr. Kisan Haobam Singh, Dr. Himangshu Pratim Bhattacharyya, Dr. Juhi Dutta, Niharika Keot, Upasana Nath, Monalisha Sarma, Biman Medhi, Rabu Ranjan Changmai, Shubham, Manash Pratim Sarmah, Samsung Daimari, Anand Kumar Yadav, Rimi Chyrmang, Yugant P. M. Guddha, and Madhab Morang, for their kind help, suggestions, and cooperation during this journey. I would also like to thank my junior labmates Harsh Baliyan and Papu Kalita for the cheerful moments and discussions we shared during their period in the lab.

I will forever be grateful for having a few amazing friends and batchmates, Rinki Brahma, Sabina Yasmin, Sandeep Kumar, Pran Govinda Nandi, Manideepa Paul, Sagnik De, Debjyoti Pal, Tanumoy Sarkar, Aritra Mitra, Vinay Arora, Bikoshita Porashar, Samir Roy, Monuranjan Konwar, and others, for all the joyous moments, trips, and celebrations we shared during this journey. I owe special thanks to my closest friends Rinki Brahma and Sabina Yasmin for being by my side during my highs

and lows in this journey. I would also like to express my gratitude to a few friends outside the campus, Junali Kasyap and Lupamudra Rajkhowa, whose presence has shaped my personality and made me who I am today. Also, I would like to extend my heartfelt appreciation to Rupam Saikia for his steadfast presence through the highs and lows as a true friend.

Teachers play a profound role in shaping the life of a student in countless ways, and I consider myself fortunate to have been mentored by some truly wonderful individuals throughout different stages of my life, especially Dr. Palashmoni Saikia, Diganta Baruah, Kalu Lama, and Karuna Nath. I would like to express my deepest gratitude to all the teachers who have been a part of my academic journey.

Since family is among life's greatest gifts, I feel truly fortunate to have a big family. My heartfelt thanks to all my aunts and uncles, especially Ganga Lama, Padum Bahadur Lama, Monmaya Tamang, Kaleb Bahadur Tamang, Manmaya Tamang, Amar Lama, and all others, and to my grandfather Dhan Bahadur Tamang, whose love, wisdom, and guidance have played a significant role in my life. I am also blessed to have cousins, especially Namrata Lama, Purnima Tamang, Lajyolmo Tamang, Sarsija Tamang, Ratna Kumari Tamang, Gautam Lama, Wangchuk Tamang, Tulku Tamang, Kumari Lama, Bikash Lama, and others, whose companionship and support have been a cherished part of my life.

Most importantly, no words would be enough to thank all the selfless sacrifices, boundless love, support, and encouragement of my Maa and my Late Baba, the very reason I stand where I am today. Throughout my life, my mother has been a steadfast pillar, shielding me from all the troubles and allowing me to concentrate on my goal. Thank you, Baba, for always ensuring I had everything I needed for my studies and beyond, even during the most challenging times. I am deeply grateful to them for their faith in me, giving me the wings to fly and the opportunity to chase my dreams. Without their prayers and support, finishing my Ph.D thesis work would have been nearly impossible. I am also blessed to have two little sisters, Komal Lama and Tanushree Lama, to have by my side through all the thick and thin.

In the end, words fall short in expressing my gratitude to the Almighty, whose grace, hope, and strength have carried me to this point in my journey.

"*To be human was to continually dumb the world down into an understandable story that keeps things simple.*"

—Matt Haig, The Midnight Library

# *Abstract*

The interaction of light with living and non-living systems is a complex phenomenon that converges the branches of chemistry, physics, and biology. Over the past few decades, quantum mechanics has helped in understanding the photochemical panorama that goes beyond the Born-Oppenheimer approximation to account for the strong nonadiabatic couplings between the electronic states. These optically active entities undergo photoreactions via either adiabatic or nonadiabatic pathways. Based on the quantum-mechanical and quantum-classical methods, we have investigated the photophysical and photochemical behaviour of the Green Fluorescent Protein (GFP) chromophore and its derivatives upon absorption of a photon. The combined approach of quantum mechanical and quantum-classical dynamics enabled a detailed understanding of the structure and dynamics of GFP chromophore derivatives, as well as the factors affecting their photochemical mechanisms. Our studies demonstrate how the steric and electronic environments significantly influence the photophysics of GFP chromophore derivatives, resulting in different phenomena such as excited-state inter and intramolecular proton transfer (ESIPT), *cis-trans* isomerization, etc., thereby modulating their fluorescent behaviours. Thus, the thesis aims to provide a comprehensive perspective on leveraging light-matter interactions to biological and organic chromophores and control molecular events.

# Contents

# List of Figures

# List of Tables

# List of Abbreviations

| | |
|---|---|
| **GFP** | Green Fluorescent Protein |
| ***p*-HBDI** | *p*-hydroxybenzylideneimidazolinone |
| ***o*-HBDI** | 4-(2-hydroxybenzylidene)-1H-imidazol-5(4H)-one |
| **PES** | Potential Energy Surface |
| **CT** | Charge Transfer |
| **MO** | Molecular Orbital |
| **HOMO** | Highest Occupied Molecular Orbital |
| **LUMO** | Lowest Unoccupied Molecular Orbital |
| **IC** | Internal Conversion |
| **ISC** | Intersystem Crossing |
| **MECI** | Minimum Energy Conical Intersection |
| **BHA** | Born-Huang Approximation |
| **BOA** | Born-Oppenheimer Approximation |
| **HF** | Hartree-Fock |
| **DFT** | Density Functional Theory |
| **TDDFT** | Time-Dependent Density Functional Theory |
| **TSH** | Trajectory Surface Hopping |
| **AIMS** | ab initio Multiple Spawning |
| **QM/MM** | Quantum Mechanics/Molecular Mechanics |
| **CASSCF** | Complete Active Space Self Consistent Field |
| **CASPT2** | Complete Active State Second Order Perturbation |
| **MS-CASPT2** | Multi-State Complete Active State Second-Order Perturbation |
| **XMS-CASPT2** | Extended Multi-State Complete Active Space Second-Order Perturbation |
| **ADC** | Algebraic Diagrammatic Construction |
| **FSSH** | Fewest-Switches Surface Hopping |
| **ESPT** | Excited State Proton Transfer |
| **LIIC** | Linear Interpolation in Internal Coordinate |
| **VEEs** | Vertical Excitation Energies |

# Chapter 1

# Introduction

Photochemistry is an intriguing branch of chemistry that deals with the interactions between light and molecules. It focuses on the chemical reactions and various physicochemical phenomena induced by the absorption of light, resulting in notable chemical transformations. Upon photon absorption, a molecule undergoes an electronic state transition, exciting it to a higher energy state, without necessarily resulting in its chemical transformation. The concept of photochemistry was formulated by Grotthuss in 1917, followed by Draper in 1842, forming the Grotthuss-Draper law, which states that a molecule must absorb light for a photochemical reaction to occur. Later, with the advancement of quantum theory, Stark and Einstein reformulated the concept, leading to the Stark-Einstein law, which states that the photochemical or photophysical reaction in a molecule is triggered by the absorption of one photon of light. The simulation of a light-induced phenomenon holds a significant importance, as evidenced by its diverse applications in fields such as molecular biology,[1–3] medicine, and material science.[4–6]

When a photon of energy $\boldsymbol{hv}$ interacts with a molecule, its electrons are excited from the electronic ground state to higher energy electronic states, generating a wave packet that evolves in time. The electronic ground state of a molecule usually exists as a singlet state; however, its multiplicity can vary to doublet, triplet, or even higher, depending on the number of electrons and their pairing configurations. On considering that the absorption of light occurs in the singlet ground state, the molecule will be excited to a higher energy singlet electronic state, with the excitation energy governed by the energy of the absorbed photon. This led the molecule towards a different geometry in the excited state, which eventually relaxes to a new minimum, depending on the topography of its potential energy surface, thereby generating a long-lived excited state. The molecule in the excited state then decays back to the ground state through various radiative and nonradiative processes.[7, 8] The energetic

relationships between the electronic states, summarizing the various photophysical and photochemical phenomena that occur after photoexcitation of a molecule, can be represented by the Jablonski diagrams, as illustrated in Figure 1.1. In the photochemical mechanism, the nomenclature used to designate the electronic states is based on their spin multiplicity, with $S_n$ representing singlets and $T_n$ for triplets, the two key spin manifolds for most photoactive molecules. The suffix 'n' denotes the number of electronic states, such as 0 for the electronic ground state, 1 for the first excited state, and so on, according to the ordering of their energy.

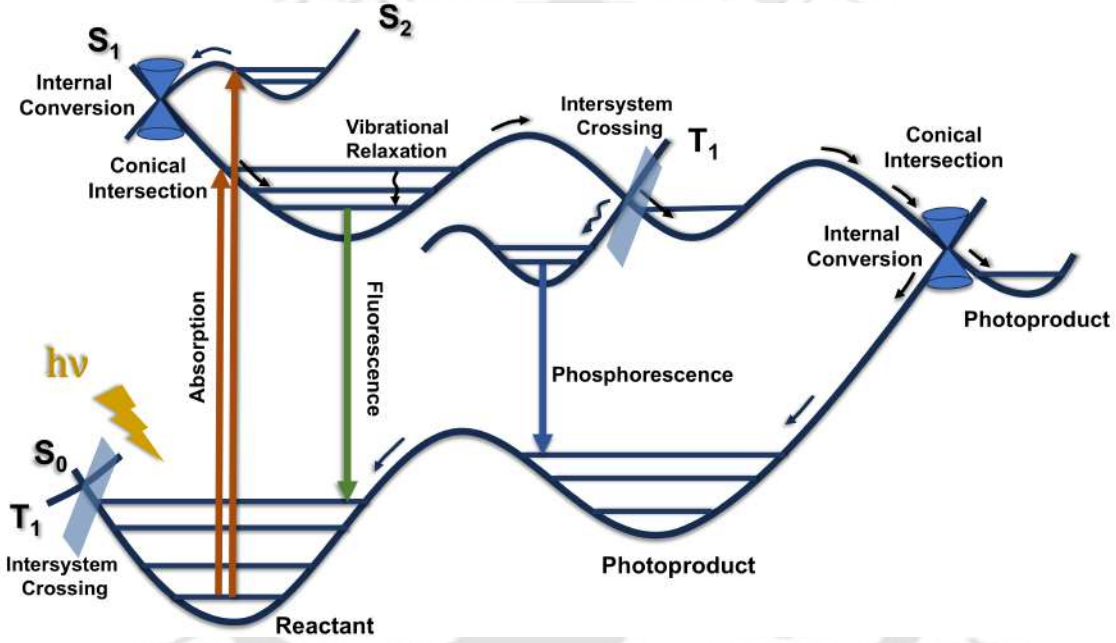


**Figure 1.1:** Jabłonski diagram with potential energy surfaces illustrating various photophysical and photochemical processes that occur after the absorption of light ***hν***.

Photochemical mechanisms are typically described in terms of several potential energy surfaces (PESs) that a molecule can access following light-induced excitation, with each PES corresponding to a distinct electronic state which often undergoes changes in its electronic character and may cross in various ways. Depending on whether light emission involves a transition between the electronic states of the same multiplicity, such as from the singlet $S_1$ to $S_0$ state, or involves a spin change, from the triplet $T_1$ to the singlet $S_0$ state, as illustrated in Figure 1, the radiative processes are categorized as fluorescence (F) and phosphorescence (P). In fluorescence, the molecule relaxes from its excited state to the ground state of the same multiplicity by emitting energy in the form of light. The emitted photon typically has lower energy than

the absorbed photon, and the difference in energy between them is referred to as the Stokes shift. However, if the radiative emission occurs during the relaxation of the molecule from its excited state to its ground state with different multiplicity, the phenomenon is termed as phosphorescence.

The nonradiative transition includes both the bright states, defined by excitation wavelength, and the dark states, which do not have a significant oscillator strength but are populated through the bright states. The nonradiative transition occurring between the electronic states of the same multiplicity is referred to as internal conversion (IC), such as from singlet $S_2$ to $S_1$ or from triplet $T_2$ to $T_1$. The IC processes are mediated via crossing points termed as conical intersections,[9, 10] because of their characteristic double-cone topography at the degeneracy point. In contrast, the crossing points responsible for the transitions between the electronic states of different multiplicity, for example, from singlet $S_1$ to triplet $T_1$, are termed as intersystem crossing (ISC), provided that spin-orbit coupling (SOC) is not negligible. Thus, the ISC mediated by the spin-orbit coupling is another form of vibronic or non-adiabatic coupling between the electronic states.

The probability of population transfer is greater when the energy gap between the electronic states is smaller. As a result, the surface crossing like, conical intersection (CI) or hyperfine line, is the most favorable topology for population transfer since both electronic states have the same spatial and spin symmetry. While for ISC, the probability of population transfer is largest in the widest region of the PES, as the factors, the smallest energy gap and the largest spin-orbit couplings, have to be balanced. These crossing points, where the commonly referred to "nonadiabatic coupling" between the PESs occurs, inducing the population transfer from one electronic level to another, mark the breakdown of the Born-Oppenheimer approximation (BOA). At this point, electronic and nuclear motion becomes coupled. This leads to a radiationless return to the ground state, resulting in the formation of either the reactant or new photoproducts. These non-adiabatic couplings between the PES serve a crucial role in photochemistry in determining which states and geometrical conformations are populated following the excitation. If the molecule, after going through different PESs, adopts a new geometrical configuration distinct from its initial configuration, the process is referred to as photochemical reaction. However, if it restores the original electronic ground state of the reactant, it is termed as photophysics.

Thus, a thorough knowledge of PES is essential to understand the underlying

processes following excitation. The PESs representing the electronic energy levels of a molecule are extended across 3N-6 dimensions, where N is the number of atoms. As a result, characterizing the PES becomes increasingly complicated for polyatomic molecules because of higher dimensionality and electronic complexity.[8, 11] Also, it is important to comprehend how the characteristics of a molecule evolve along the PESs corresponding to these electronic states after excitation. To address these challenges and provide a clearer insight into the excited state phenomena, two approaches in theoretical and computational chemistry, i.e., static approach and dynamics approach, have been developed based on the key electronic time-independent Schrödinger equation and the time-dependent Schrödinger equation. The static approach identifies the key geometries, such as minima, transition states, or crossing points, to get the photochemical pathway. However, it does not provide information about the time scales required during the processes and the quantum yield. In contrast, the dynamics approach directly captures the critical geometries formed after photoexcitation, revealing the decay channels through simulations of the evolution of electrons and nuclei. Also, it offers insights into the timescales of the excited state phenomena as well as the quantum yields. Both approaches have evolved significantly over the past few decades, giving rise to numerous methods that have common objectives. In the dynamics approach, a large number of consecutive quantum calculations for the propagation of electrons are required to study under the influence of the surrounding classical nuclear motions, allowing the nonadiabatic transitions between different PESs.[8, 11–13] Thus, this approach deals with the coupled electron-nuclear dynamics of a system considering a manifold of the electronic states and full configurational space, beyond the BO approximation. Over the years, numerous dynamics simulation methods have been developed to simulated the excited state dynamics, some of the most well-known are Multiconfigurational Time-Dependent Hartree (MCTDH) and its variants,[14–17] Trajectory Surface Hopping (TSH),[18–22] multiconfigurational Ehrenfest (MCE),[23] mean-field Ehrenfest (MFE),[24] ab initio multiple spawning (AIMS),[25, 26] mixed quantum-classical Liouville equation (QCLE),[27, 28] and exact factorization of the electron-nuclear wave function methods.[29, 30] Thus, the nonadiabatic dynamics simulations have emerged as a key area for modelling the ultrafast photochemical and photophysical phenomena in a system.[8, 11, 31–36]

Experimental techniques such as pump-probe experiments, transient absorption spectroscopy, time-resolved fluorescence spectroscopy, time-resolved photoelectron

spectroscopy, etc, have been used to study the photoinduced chemical reactions and measure the excited state dynamics in photochemical processes.[37–43] Such techniques are highly advanced and tailored to capture the ultrafast processes, transient species, and relaxation pathways; however, the mechanistic details underlying many of these experimental observations has not been clearly provided. Theoretical studies have the potential to provide valuable insights into the unresolved aspects of light-induced reactions.[11] Theoretical simulations aid in identifying the relevant states responsible for the photoinduced molecular reactions [44–49]; enable the exploration of high-dimensional PESs accessible upon light absorption and locate the structures associated with the relaxation pathways.[13, 50–54] It also provides insight into the probabilities of various reaction channels for a photochemical reaction.[13] Thus, experimental observations in combination with the theoretical studies provide a comprehensive framework for better understanding photoinduced molecular reactions and their photostability.[8, 11, 12, 55, 56]

Whether in photochemistry or photophysics, light-induced reactions prevail everywhere around us. The most well-known example of a light-induced reaction is the photosynthesis process, one of the fundamental natural processes that converts carbon dioxide into glucose and oxygen.[57–59] The ability to synthesize Vitamin D in human skin on adequate exposure to sunlight is another example of photochemical process. Few other examples includes the bioluminescence phenomena observed in organisms ranging from marine vertebrates and invertebrates to terrestrial arthropods; photodynamic therapy in which tumor cells are being destroyed on the application of light in the presence of photosensitized and reactive oxygen; photoisomerization reaction of the chromophore retinal of rhodopsin in eye that enable us to see;[60–64] the photochemical reaction that causes the photostability of amino acids contributing to the diverse photochemistry of proteins and peptides;[65–67] photocatalysis[68] and photovoltaic devices.[69, 70] Despite their diversity, all the above-mentioned photochemical reactions have a common characteristic, i.e., they are governed by a manifold of excited states, which are accessible after providing a certain amount of energy. Thus, the key requirement of any photo-induced reactions is the ability of a molecule to absorb light and excited to higher energy electronic states. Also, to understand the fundamental concept of nature and life, it is very crucial to have knowledge about the photochemical and photophysical processes occurring within the biological systems and the close environment.

Light-induced processes in the field of bioluminescence and bioimaging have gathered significant attention in recent years.[71–75] A wide range of fluorescent proteins (FPs), responsible for these phenomena, have been discovered and revolutionized with color spanning nearly the entire visible spectrum. The first and most widely used FP is the Green Fluorescent Protein (GFP), extracted from the body of a jellyfish called Aequorea Victoria in 1962. Green Fluorescent Protein and its structural analogues, such as red fluorescent protein (RFP), blue fluorescent protein (BFP), yellow fluorescent protein (YFP), etc., have emerged as a unique fluorescent biological marker. Their amazing ability to generate a highly visible and efficiently emitting fluorophore has led to their evolution into an important platform in cell biology and biotechnology.[76–78] In 1955, Davenport and Nicol first reported the fluorescent nature of Aequorea Victoria jellyfish when irradiated with ultraviolet light.[79] However, it was Osamu Shimomura who was the first to identify that a protein was responsible for its green fluorescence.[80] Two proteins, aequorin (a calcium-binding protein) and green fluorescent protein, were found to be involved in the bioluminescence phenomenon in Aequorea. The protein aequorin, which contains coelenterazine, interacts with three calcium ions, resulting in the oxidation of coelenterazine with a protein-bound oxygen. This process forms a $Ca_3$-apo-aequorin-coelenteramide complex that gives off blue light in vitro.[77, 81, 82] However, in jellyfish, radiationless (Förster-type) energy transfer occurs from aequorin to green fluorescent protein, which subsequently emits green fluorescence,[83–85] see Figure 1.2. In 1971, Shimomura uncovers the structure of the GFP chromophore as a 4-(p-hydroxybenzylidene)-5-imidazolidinone moiety,[86] as shown in Figure 1.2. The structure of the chromophore was later confirmed by many studies.[87, 88]

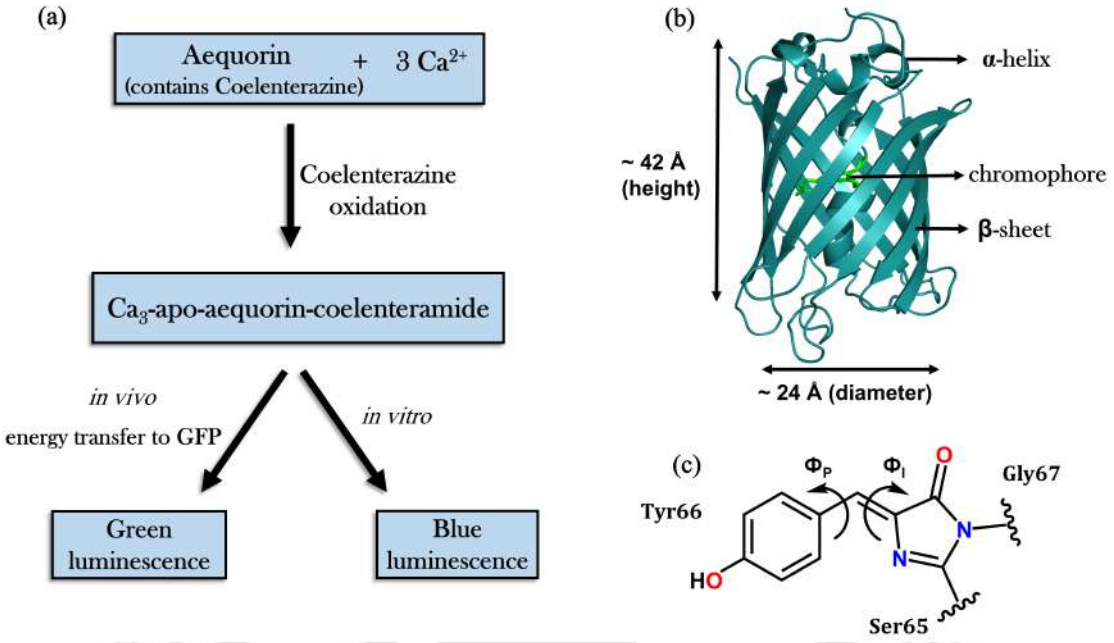


**Figure 1.2:** (a) Light-generating reactions in Aequorea victoria, (b) Structural representation of Green Fluorescent Protein (GFP), and (c) Structure of GFP chromophore, 4-(p-hydroxybenzylidene)-5-imidazolidinone or *p*-HBDI.[77]

Green Fluorescent Protein consists of 238 amino acids and has a unique 11-stranded $\beta$-barrel-like structure which forms nearly a perfect cylinder referred as "$\beta$-can" with a diameter of about 24 Å and height of 42 Å, with an $\alpha$-helix that runs diagonally through the cylinder.[76, 88, 89] The chromophore is located at the center of the $\beta$-can covalently bonded to the $\alpha$-helix, as shown in Figure 1.2. The GFP chromophore (*p*-hydroxybenzylideneimidazolinone) is formed by an intramolecular autocatalytic post-translational modification (see Scheme 1.1) of three amino acid sequence, Ser65-Tyr66-Gly67.[90, 91] This characteristic is responsible for restricting the motion of the chromophore and protects it from the surrounding water solvent, which would otherwise quench its fluorescence. Thus, the $\beta$-can structure shields the chromophore and is responsible for the stability of the GFP. Several polar groups and water molecules were observed to be located adjacent to the chromophore, forming hydrogen-bonding interactions and appear to play an important role in the photophysics of GFP.[77, 92]

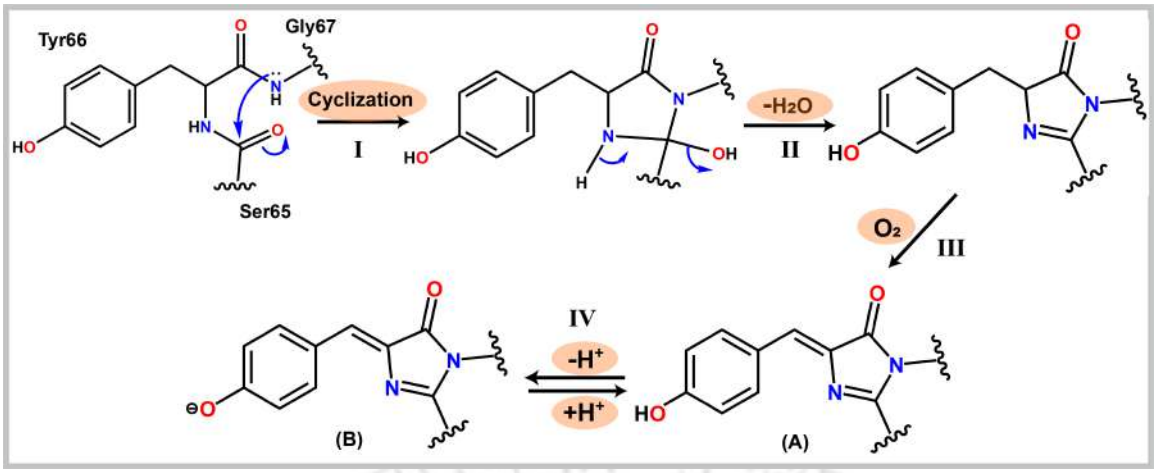


**Scheme 1.1:** Mechanistic overview of the proposed mechanism for chromophore formation in wild-type Green Fluorescent Protein (wt-GFP).[90, 91]

Substantial attention has been directed towards unraveling the photophysics of the embedded chromophore, driven by the importance of GFP as a bioimaging tool, with a particular focus on understanding the structural transformations and the dynamics triggered by photoexcitation. Under ambient conditions, the wild-type (wt) GFP has been widely recognized to exist in two forms—the neutral (A) and anionic (B) forms, as shown in Figure 1.3, related by the deprotonation of the chromophore via a proton shuttle mechanism that predominantly stabilizes the neutral form in vivo. Due to the existence of these two interconvertible forms of the chromophore, the wt-GFP exhibits a major absorption band at 398 nm and a minor absorption at 475 nm.[84, 90, 93] The absorption band at 398 nm is attributed to the neutral form, while the band at 475 nm is due to the anionic form of the chromophore.[93] Excitation at either band leads to the generation of highly efficient green fluorescence with a peak at around 508 nm.[90]

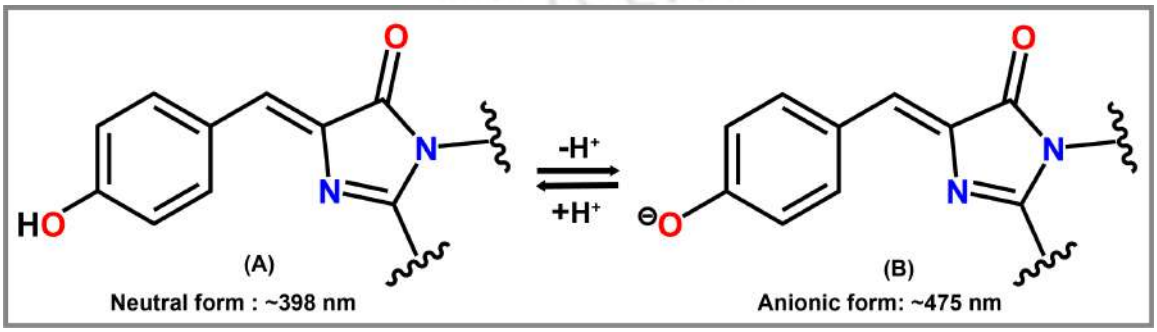


**Figure 1.3:** Neutral (A) and anionic (B) forms of the wt-GFP chromophore.

Various spectroscopic techniques and theoretical models have been implemented to study the excited-state dynamics of wt-GFP.[77, 78, 90, 91, 94–97] In 1996, Chattoraj et al. reported that the time-resolved fluorescence of wt-GFP and concluded that photoinduced conversion of the neutral form (A) of the chromophore to its anionic form (B) occurs via an excited-state proton transfer (ESPT) process, passing through intermediate form (I).[94] In proceeding from A to B-form in the excited state, initially a Tyr66 phenolic proton is transferred through a hydrogen bonding network to the carboxylate oxygen of Glu222, followed by a subsequent conformational change of Thr203 on going from I to A-form, as demonstrated in Figure 1.4. Creemer and his coworkers characterized A, I, and B photoinduced forms of the chromophore and revealed that they have distinct photophysical properties.[98] Several experimental techniques have demonstrated that the ground-state conversion from the A-form to I-form occurs very slowly, with the ground-state I-form higher in energy than the ground-state A- and B-forms.[94, 98] However, the barrier between A* and I* forms is significantly lower in the excited state, resulting in rapid excited-state proton transfer due to the increased in acidity of the Tyr66 phenol moiety. Hence, the conversion of A* to I* form is efficient, whereas the conversion of I* to B* form is comparatively slower as it requires the rotation of Thr203.

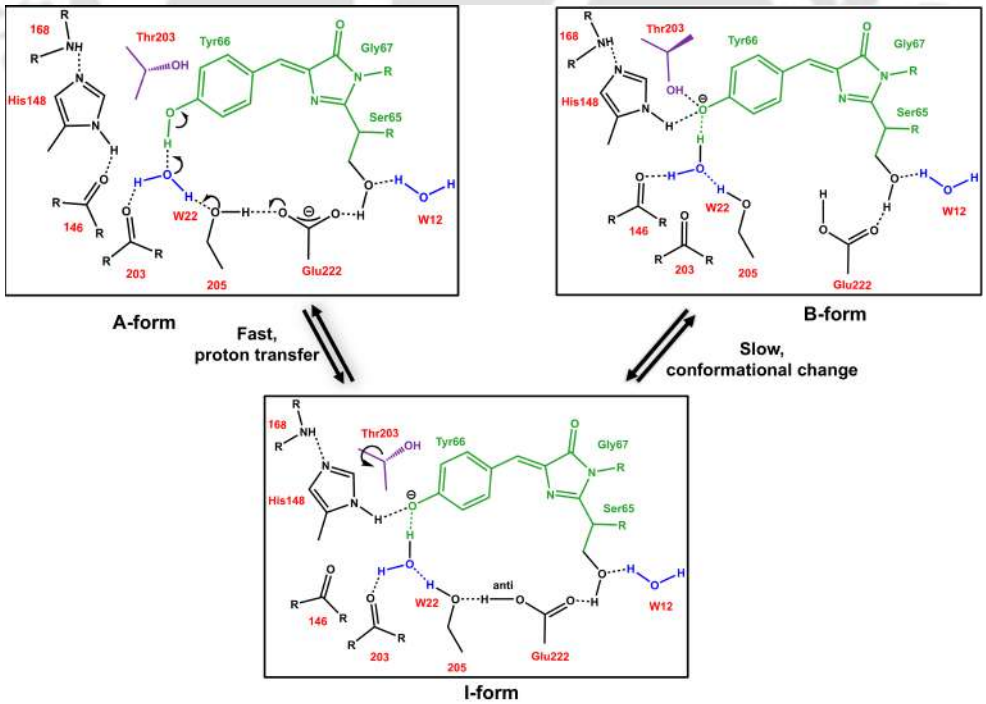


**Figure 1.4:** Mechanistic pathway proposed by Brejc et. al for the photoisomerization process in wt-GFP, based on structural and spectroscopic data.[89] The neutral species is depicted as A-form, intermediate as I-form, and anionic species as B-form.

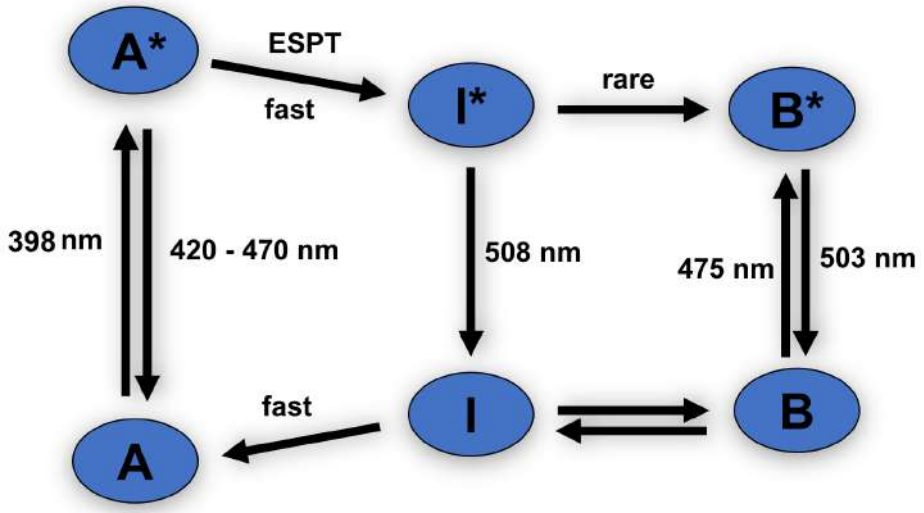


**Figure 1.5:** Schematic representation of the interconversion between A, I, and B states in its ground and excited state of wt-GFP, a three-state model.[94, 95]

The occurrence of the ESPT process can be explained by the increase in absorption at 475 nm following excitation at 398 nm. Also, fluorescence at 508 nm was observed to increase in a similar picosecond timescale as the non-single exponential decay of A* state.[94, 95, 98] Thus, GFP can be summarized as: irradiation of neutral chromophore (A-form) at 398 nm generates the excited state A* form, which subsequently undergoes proton transfer process to form an intermediate excited state I*. The I* form then returns to the ground state I-intermediate by emitting a photon at around 508 nm, or less frequently, undergoes the nonradiative conversion to the B* excited state, as depicted in Figure 1.5. The resemblance in the emission maxima for I* → I (508 nm) and B* → B (503 nm) transitions can be attributed to the fact that intermediate I* is electronically (chromophore in anionic state) similar to B* forms in the excited states.[94, 95, 98] However, I* is environmentally similar to the ground and excited state of A form. The population of the anionic B-form of the ground state increases very slowly, even though the decay of the A* form occurs very fast upon irradiation. This observation indicates that the primary pathway of the deprotonated excited state involves fluorescence through I*→I transition, followed by reprotonation to regenerate the ground state A-form. If the decay of A* had proceeded through the pathway leading to the B* state, then a rapid increase in the population of B-form would have been observed. Based on these findings, Chattoraj et al. have proposed a model as illustrated in Figure 1.5.[94] The ultrafast pump-dump-probe spectroscopy and spectral hole burning measurements further support

the proton transfer dynamics during I→A transition in the ground state, the energies of all the electronic states, and the interconversion between them.[89, 98–100]

The wt-GFP exhibits a fluorescence quantum yield ($\Phi_f$) of 0.8,[84] whereas the quantum yield of the isolated chromophore in solution was measured to be $10^{-3}$.[93] Time-resolved spectroscopy studies revealed that it has an excited state lifetime in the order of nanosecond timescale.[94, 101]

Quantum mechanical calculations have been performed for the ground ($S_0$) and excited ($S_1$) states of different protonated forms (neutral, cationic, anionic, and zwitterionic) of the chromophore.[102, 103] The electronic excitation from $S_0$ to $S_1$ was observed to alter the conformation of the chromophore. The studies revealed that for the neutral, anionic, and cationic forms of the chromophore, the perpendicular conformations formed by the rotation of exocyclic bonds result in maximum energy at the $S_0$ state and minimum energy at $S_1$ state, resulting in avoided crossing. Based on these findings, the author proposed that fluorescence quenching occurs due to internal conversion facilitated by the small energy gap between the $S_0$ and $S_1$ potential energy surfaces at the perpendicular orientation of the isolated chromophore. However, the cis-trans photoisomerization cannot occur in the protein environment by rotating the dihedral angles to 180°.[103]

Following these studies, Weber *et al.*[104] developed a model, an extension of the previous three-state model (see Figure 1.6), that explains the photophysical phenomena occurring in bare GFP chromophore based on the quantum mechanical calculations. It also explains the existence of short and long-lived dark states and the associated excited-state decay pathways in the GFP chromophore. In certain forms, the potential energy surface of the $S_0$ and $S_1$ states come very close to each other, enabling the nonadiabatic crossing (NAC) between them, which results in the radiationless decay through NAC. These NAC between $S_0$ and $S_1$ states result from *cis-trans* isomerization due to $\Phi_I$ and $\Phi_P$ dihedral angle rotations. These findings support the experimentally observed blinking and switching phenomena of single GFP mutants on different timescales. Molecular mechanics calculations support the photoisomerization mechanism in the GFP chromophore.[103]

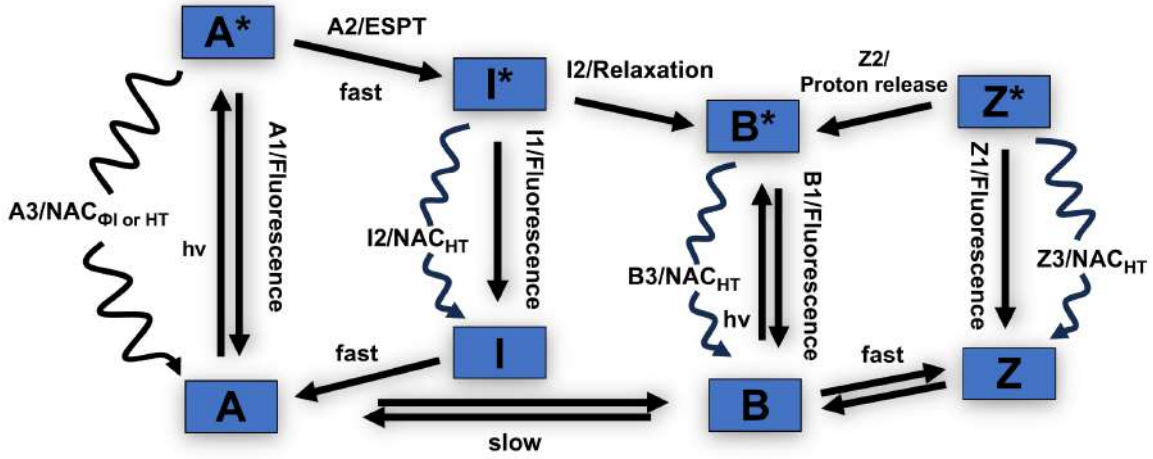


**Figure 1.6:** Proposed mechanism for photophysics of the wt-GFP chromophore referred to as the four-state model by Weber *et al.* [104]

Several studies have reported arguing about how the proton moves, the existence of intermediate (I), cationic, and zwitterionic forms and the validity of proposed models.[94, 105–111] For the past few years, significant theoretical studies including the electronic structure calculations, mixed quantum mechanics/molecular mechanics calculations, and molecular dynamics simulations, have also been performed on GFP to explain the photophysical and photochemical phenomena.[104, 111–117] The tunable chromophore located at the center of GFP governs the light emission, and its photophysical properties can be profoundly altered through mutations. Depending on the surrounding environment, the chromophore exhibits photoisomerization,[118–126] excited state proton transfer,[94, 127–129] photochromism,[130–132] intermolecular photochemical reactions,[133–135] and electron transfer.[136] This intriguing photophysics and diversity of GFP has thus inspired extensive experimental and theoretical investigations,[77, 95–97, 119, 124, 137–146] and has been established as one of the most important tools in a wide range of applications beyond bioimaging depending on the chromophore and its environment.

To get a detailed understanding of the steric and electronic environment of the chromophore, Kojima *et al.*[147] first synthesized para-hydroxybenzylidene-2,3-dimethylimidazolinone (*p*-HBDI), which serves as a model of GFP chromophore for further studies. The anionic form of *p*-HBDI (i.e., *p*-HBDI$^-$) effectively mimics the deprotonated form of the chromophore that is responsible for fluorescence.[94, 148] Though the GFP has a very high quantum yield (0.8), the *p*-HBDI$^-$ experiences internal conversion in vacuum and solution at ambient temperature. The synthesized

*p*-HBDI$^-$ chromophore has been used to predict the photophysics of GFP, causing the ultrafast radiationless decay due to photoisomerization and the net effect of various residues acting on the chromophore. Quantum chemical calculations indicate that the excited-state decay proceeds via two distinct pathways, involving the rotation of exocyclic methine bridge bonds, i.e., either the imidazolinone (I) or phenolate (P) bond.[124, 125, 146, 149–151] These I- and P- bonds exhibit the double and single bond characteristics, respectively. The I- or P- bond rotations are accompanied by the twisted intermolecular charge transfer (TICT) across the bridge in opposite directions.[124, 126] Twisting around these bridging bonds in an isolated chromophore leads to ultrafast deactivation through internal conversion via conical intersection (CI), thereby decreasing the fluorescence quantum yield.[93, 152] Previous studies have demonstrated that the direction of charge transfer (CT) in the excited state is influenced by the dihedral angle ($\Phi_I$ and $\Phi_P$) rotations occurring along the I- or P-bonds.[124, 126] The rotation of $\Phi_I$ facilitates the CT from the I- (or imidazolinone) ring to the P- (or phenolate) ring, whereas the rotation of $\Phi_P$ induces the CT in the reverse direction, from P- ring to I- ring. Internal conversion occurring through I-twisted CI results in the formation of the E-isomer, whereas P- bonds rotation restores the original ground state Z-isomer.

In line with this, Carrascosa *et al.*[153] provided experimental evidence that photoexcitation of the isolated *p*-HBDI$^-$ chromophore successfully induces isomerization, resulting in the formation of E-isomer photoproducts. On excitation of $S_0 \rightarrow S_1$ transition in the gas phase, the chromophore undergoes interconversion between Z and E isomers, provoking both Z $\rightarrow$ E and E $\rightarrow$ Z photoisomerization processes. However, the experiments could not ascertain whether the photoisomerization occurs through a direct pathway via internal conversion or indirectly involving torsional barrier crossing on the hot ground state. Also, in solution at ambient temperature, the isolated *p*-HBDI$^-$ chromophore exhibits weak fluorescence due to internal conversion via conical intersections, which involve twisted structures corresponding to either $\Phi_I$ or $\Phi_P$ dihedral rotations.[154] However, as the temperature is lowered,[148, 155] the fluorescence quantum yield increases, attributed to solvent-induced frictional inhibition of twisting on the first excited state. This restriction of molecular motions suggests a dependence on solvent viscosity, with the fluorescence traced back to an intrinsic property of the chromophore via excited-state trapping. Further, the volume-conserving "Hula-twist" deactivation mechanism has also been suggested to be responsible for the minimal

dependence of the excited-state lifetime of the chromophore on solvent viscosity.[104, 156, 157] However, several higher-level studies such as trajectory surface-hopping dynamics,[121, 123] ab initio multiple spawning (AIMS),[126, 158, 159] and quantum mechanics/molecular mechanics (QM/MM) simulations[122, 125, 160–163] method using complete active space self-consistent field (CASSCF), multi-state multiconfigurational second-order perturbation theory (CASPT2), the extended multireference second-order perturbation theory (XMS-CASPT2), spin-flip time-dependent density functional theory (SF-TDDFT), and floating occupation molecular orbital (FOMO), further confirmed that significant tortional motion around one the methine bridge bonds is responsible for the ultrafast deactivation in GFP chromophore. These studies examine the competition between the I- and P- deactivation pathways, and observed that the decay predominantly proceeds through the I-twisted channel.

GFP chromophore (*p*-HBDI) shows a Z/E photoisomerization quantum yield of ∼50% in aprotic solvent, which decreases to ∼10 - 20% in protic solvent.[118, 163] This significant reduction in Z/E photoisomerization in protic solvents is attributed to the competing excited-state proton transfer process. Torsion around the $\Phi_I$ coordinate leads to the formation of the E-isomer, whereas torsion around the $\Phi_P$ regenerates the Z-isomer, indistinguishable from the initial ground state reactant due to the symmetry of the phenolic ring. Therefore, to design a fluorophore based on the GFP chromophore with an enhanced fluorescence quantum yield, it is very crucial to minimize the photoisomerization process by restricting the tortional rotation as a result of the methine bridge I- and P- bonds.

These observations have prompted efforts to control the torsional motion along the I- and P- bridging bonds and improve the fluorescence quantum yield. Numerous efforts have been made over the past half-century in modeling and synthesizing the GFP chromophore, according to its various applications corresponding to its different photophysical and photochemical properties. The photophysics of the GFP chromophore is dominated by ultrafast radiationless deactivation and photoisomerization. Various approaches have been employed to enhance the fluorescence quantum yield, which includes, introduction of bulkier substituents to restrict the tortional motions, formation of the intramolecular hydrogen bonding cyclization between the imidazolinone and phenolic groups,[164, 165] incorporation of metals and other groups to form metal-complexes,[166, 167] formation of the intermolecular hydrogen binding interaction resulting in excited-state proton transfer (ESPT), and the incorporation

of solvent effects. Restricting the torsional rotation around the I- and P- bridging bonds resulted in rigid chromophore with significantly enhanced fluorescence quantum yield even at room temperature.

Figure 1.7 demonstrates the molecular structure of a set of GFP chromophore derivatives that have been designed and synthesized over the past few decades, each exhibiting distinct photophysical properties. While some derivatives in Figure 1.7 display nonfluorescent behaviour, others demonstrate significantly enhanced fluorescent properties.

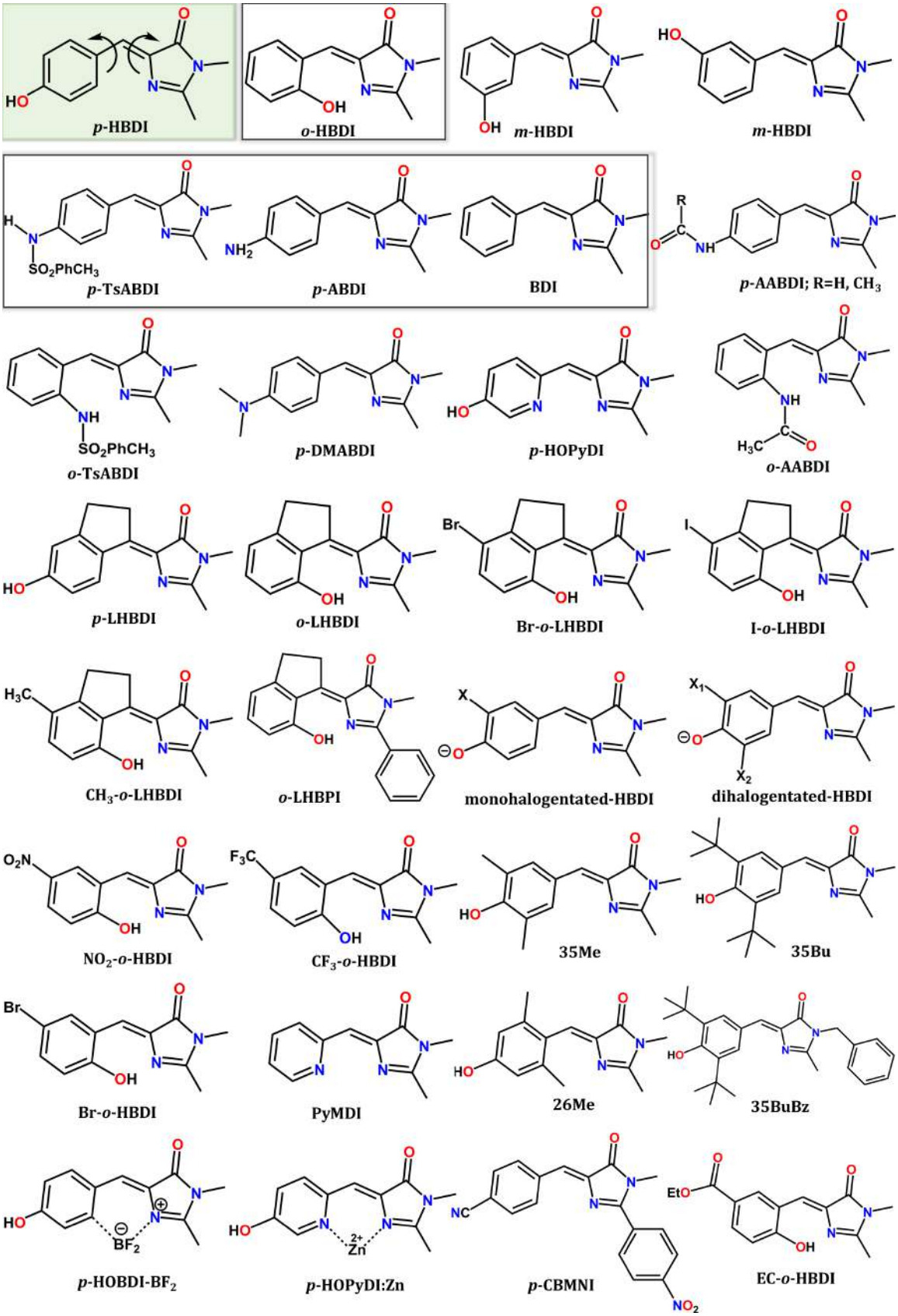


**Figure 1.7:** Molecular geometries of all GFP chromophore derivatives synthesized and reported previously. The chromophore highlighted within the boxes indicates the molecular systems considered for our investigation.

**Aim of the thesis**: In this thesis, we focused on various photophysical and photochemical processes occurring in Green Fluorescent Protein (GFP) chromophore derivatives, with the implementation of electronic structure methods coupled with mixed quantum-classical dynamics simulation for understanding the phenomena upon photoabsorption of light. These efforts aim to advance the theoretical and computational studies, and more generally, provide insights for designing and synthesizing GFP chromophore derivatives with enhanced photophysical properties based on their applications. The work on this thesis is structured as follows.

Chapter 1 of the thesis provides a brief discussion on the photochemistry, beyond the Born-Oppenheimer approximation, and the impact of light-induced processes in the field of biology, material science, and medicine. This chapter includes the mechanistic details of the photoinduced reaction, with the description of various radiative and nonradiative processes, and the electronic states involved. It further discusses examples of a few photochemical processes taking place in our environment and our body, followed by a detailed description of the renowned and widely used fluorescent protein called Green Fluorescent Protein (GFP), highlighting its significance and the motivation behind its application. Chapter 2 presents the theoretical background for various quantum mechanical calculations and mixed quantum-classical trajectory surface hopping dynamics simulation. The chapter begins with an overview of the approximations to solve the molecular Schrodinger equation, followed by a detailed explanation of the hierarchy of approximations that constitute the backbone of photochemistry. Additionally, this chapter emphasizes the key characteristics defining the trajectory surface hopping dynamics.

In Chapter 3, we have primarily focused on the unusual dual emissive behaviour of the GFP chromophore analogue, namely para-sulfonamide (*p*-TsABDI) analogue, and investigated how the structural and solvent factors affect the photophysical processes upon photoabsorption of light. To unravel the excited-state phenomena and the reason behind this peculiar behaviour in the GFP chromophore analogue, we implemented the electronic structure methods, followed by the on-the-fly molecular dynamics simulation studies.

Chapter 4 aims to investigate the reversible photoswitching property between the cis and trans form of a GFP chromophore derivative, and illustrates the photochemical pathways involved after being excited to the $S_1$ state, by means of nonadiabatic dynamics simulations based on Tully's fewest switches surface hopping method. The

theoretical investigation presented herein provides valuable insight into the ultrafast cis-trans photoisomerization mechanisms and reveals that the decay to the ground state is facilitated by $S_1/S_0$ conical intersection involving the tortional rotation of imidazolinone and phenolate methine bridge bonds. In chapter 5, we examine the photodynamical response of the GFP chromophore derivative upon dimerization, characterized by weak $\pi$-$\pi$ stacking interactions. The photophysics of high-energy (hot) excitons generated in the GFP chromophore derivative dimer upon photoexcitation to higher-energy excited states have been investigated, and the time-evolution and relaxation mechanism provide an insight into the nonadiabatic dynamics of the dimer. Chapter 6 explores the photoexcited dynamics of an ortho-substituted analogue of GFP chromophore, which undergoes an ultrafast excited-state intramolecular proton transfer (ESIPT) leading to the formation of a seven-membered ring intermediate. This excited state proton transfer behaviour shows a competitive pathway with the dominant *cis-trans* photoisomerization phenomena of bare GFP chromophore in gas and solvent phase. Further, this ESIPT also mimics the intrinsic proton transfer reaction of the native GFP chromophore, *p*-HBDI, within its protein environment.

Finally, we summarize the works presented in this thesis and draw conclusions about the photophysical and photochemical phenomena of the Green Fluorescent Protein (GFP) chromophore, its derivatives, and the impact of the interaction of light on its structure and dynamics.

# Chapter 2

# Methodology

This chapter discusses the theoretical background and mathematical formulation of all the methods employed in quantum chemical calculations and dynamics simulations to investigate the photoinduced mechanism. The explanation begins with the fundamental concept of the Schrödinger equation, followed by the introduction of the Born-Huang and Born-Oppenheimer approximation, which forms the basis of electronic structure theory. This is followed by a detailed discussion of methods such as Hartree-Fock (HF), Density Functional Theory (DFT), Time-dependent Density Functional Theory (TDDFT), Multi-Configurational Self-Consistent Field (MCSCF), and Post-Hartree-Fock Theories, i.e., Algebraic diagrammatic construction (ADC). Finally, to describe nonadiabatic dynamics simulation, we explain the most commonly used mixed quantum-classical approach, the Trajectory Surface Hopping (TSH) method, to capture the dynamics and time evolution of photophysical processes.

## 2.1 Time-dependent Schrödinger Equation

The primary objective of quantum chemistry is to provide an accurate description of the behaviour of a molecular system. This behaviour can be described by a multi-dimensional molecular wavefunction $\Psi(\mathbf{r}, \mathbf{R}, t)$, a mathematical function that completely describes the quantum state of all particles in a molecular system, i.e., electrons and nuclei. The wavefunction $\Psi(\mathbf{r}, \mathbf{R}, t)$ explicitly depends on time t, electronic coordinates $\mathbf{r}$, and nuclear coordinates $\mathbf{R}$ and encapsulates all information about the molecular system.

The complete time evolution of a wavefunction and its properties relative to its surroundings is described by a time-dependent Schrödinger equation (TDSE),[168,

169] which can be written as

$$i\hbar\frac{\partial\Psi(\mathbf{r},\mathbf{R},t)}{\partial t} = \hat{H}(\mathbf{r},\ \mathbf{R})\Psi(\mathbf{r},\mathbf{R},t) \tag{2.1}$$

Where $\hat{H}(\mathbf{r},\ \mathbf{R})$ is the molecular Hamiltonian that considers kinetic and potential energy terms to calculate the total energy of a system. For n electrons and m nuclei, $\hat{H}(\mathbf{r},\ \mathbf{R})$ can be defined as

$$\hat{H}(\mathbf{r},\mathbf{R}) = -\sum_{i=1}^{n}\frac{\hbar^2}{2M_i}{\nabla_i}^2 - \sum_{\alpha=1}^{m}\frac{\hbar^2}{2M_\alpha}{\nabla_\alpha}^2 - \frac{1}{4\pi\epsilon_0}\sum_{\alpha=1}^{n}\sum_{i=1}^{m}\frac{e^2 Z_\alpha}{|\mathbf{R}_\alpha - \mathbf{r}_i|} + \frac{1}{4\pi\epsilon_0}\sum_{i=1}^{n}\sum_{j>i}^{n}\frac{e^2}{|\mathbf{r}_i - \mathbf{r}_j|} + \frac{1}{4\pi\epsilon_0}\sum_{\alpha=1}^{m}\sum_{\beta>\alpha}^{m}\frac{e^2 Z_\alpha Z_\beta}{|\mathbf{R}_\alpha - \mathbf{R}_\beta|} \tag{2.2}$$

In atomic units, explicitly including $\hbar$, the molecular Hamiltonian becomes

$$\hat{H}(\mathbf{r},\mathbf{R}) = -\sum_{i=1}^{n}\frac{\hbar^2}{2}{\nabla_i}^2 - \sum_{\alpha=1}^{m}\frac{\hbar^2}{2M_\alpha}{\nabla_\alpha}^2 - \sum_{i=1}^{n}\sum_{\alpha=1}^{m}\frac{Z_\alpha}{|\mathbf{R}_\alpha - \mathbf{r}_i|} + \sum_{i=1}^{n}\sum_{j>i}^{n}\frac{1}{|\mathbf{r}_i - \mathbf{r}_j|} + \sum_{\alpha=1}^{m}\sum_{\beta>\alpha}^{m}\frac{Z_\alpha Z_\beta}{|\mathbf{R}_\alpha - \mathbf{R}_\beta|} \tag{2.3}$$

$$= \hat{T}_m(\mathbf{R}) + \hat{H}_n(\mathbf{r},\mathbf{R}) \tag{2.4}$$

Where $\hat{T}_m(\mathbf{R}) = -\sum_{\alpha}^{m}\frac{\hbar^2}{2M_\alpha}\nabla_\alpha^2$ represents the operator for the kinetic energy of nuclei and $\hat{H}_n(\mathbf{r},\mathbf{R})$ is defined as the electronic Hamiltonian which includes operator for the kinetic energy of electrons, the Coulomb attraction between electrons and nuclei, and the repulsion between electrons and between nuclei, respectively. The $i$ and $j$ are denoted as electrons, whereas $\alpha$ and $\beta$ are denoted as nuclei. $M_\alpha$ is the mass of nucleus and $Z_\alpha$ is the atomic number of $\alpha^{th}$ nucleus. The Laplacian operator $\nabla_i^2$ and $\nabla_\alpha^2$ signifies the differentiation with respect to the coordinates of $i^{th}$ electrons and $\alpha^{th}$ nucleus. By inserting equation 2.3 in equation 2.1 results in the detailed explanation for the time-dependent Schrödinger equation (TDSE).

When the nuclei are fixed i.e., $\hat{T}_m(\mathbf{R}) = 0$, and the electronic Hamiltonian $\hat{H}_n(\mathbf{r},\ \mathbf{R})$ can be evaluated at each fixed nuclear configuration $\mathbf{R}$. This yields the eigen function referred to as adiabatic states $\Phi_j(\mathbf{r};\ \mathbf{R})$ and their corresponding eigen values fulfill

the solution to the time-independent Schrödinger equation (TISE) at fixed nuclear position, also known as the *clamped nuclei approximation*.

$$\hat{H}_n(\mathbf{r},\mathbf{R})\Phi_j(\mathbf{r};\mathbf{R}) = E_j^n(R)\Phi_j(\mathbf{r};\mathbf{R}) \tag{2.5}$$

This concept of adiabatic states serves as a basis for expressing the total wavefunction $\Psi(\mathbf{r},\mathbf{R},t)$ in the Born-Huang expansion.

## 2.2 Born-Huang Approximation

The Born-Huang approximation (BHA)[170] explains the total molecular wavefunction $\Psi(\mathbf{r},\mathbf{R},t)$ as

$$\Psi(\mathbf{r},\mathbf{R},t) = \sum_j^{\infty} \Phi_j(\mathbf{r};\mathbf{R})\chi_j(\mathbf{R},t) \tag{2.6}$$

In this expansion, time and nuclear position dependent coefficients $\chi_j(\mathbf{R},t)$ encode the time-dependence and can be defined as the time-dependent nuclear wave function. On substituting $\Psi(\mathbf{r},\mathbf{R},t)$ of equation 2.1 by equation 2.6 we obtains,

$$\begin{aligned} i\hbar\sum_j^{\infty}\Phi_j(\mathbf{r};\mathbf{R})\frac{\partial\chi_j(\mathbf{R},t)}{\partial t} = \sum_j^{\infty}\{\chi_j(\mathbf{R},t)\Phi_j(\mathbf{r};\mathbf{R})E^n(\mathbf{R}) - \sum_\alpha^m \frac{\hbar^2}{2M_\alpha}\chi_j(\mathbf{R},t)\nabla_\alpha^2\Phi_j(\mathbf{r};\mathbf{R}) \\ - \sum_\alpha^m \frac{\hbar^2}{2M_\alpha}\Phi_j(\mathbf{r};\mathbf{R})\nabla_\alpha^2\chi_j(\mathbf{R},t) - \sum_\alpha^m \frac{\hbar^2}{2M_\alpha}2\nabla_\alpha\Phi_j(\mathbf{r};\mathbf{R})\nabla_\alpha\chi_j(\mathbf{R},t)\} \end{aligned} \tag{2.7}$$

The equation 2.7 is multiplied from the left by $\Phi_j^*(\mathbf{r};\mathbf{R})$ and integrated over the electronic coordinates, and the following equation is obtained.

$$i\hbar\frac{\partial\chi_i(\mathbf{R},t)}{\partial t} = \left[-\sum_\alpha^m \frac{\hbar^2}{2M_\alpha}\nabla_\alpha^2 + E_i^n(\mathbf{R})\right]\chi_i(\mathbf{R},t) - \sum_j^{\infty} C_{ij}(\mathbf{R})\chi_j(\mathbf{R},t) \tag{2.8}$$

The coefficients $C_{ij}$ represent the nonadiabatic coupling (NAC) matrix elements that cause coupling between adiabatic states, which read

$$C_{ij}(\mathbf{R}) = \sum_{\alpha}^{m} \frac{\hbar^2}{2M_\alpha} \int \Phi_i^*(\mathbf{r};\mathbf{R}) \nabla_\alpha^2 \Phi_j(\mathbf{r};\mathbf{R}) d\mathbf{r} + \sum_{\alpha}^{m} \frac{\hbar^2}{M_\alpha} \int \Phi_i^*(\mathbf{r};\mathbf{R}) \nabla_\alpha \Phi_j(\mathbf{r};\mathbf{R}) d\mathbf{r} \cdot \nabla_\alpha \tag{2.9}$$

$$C_{ij}(\mathbf{R}) = \sum_{\alpha}^{m} \frac{\hbar^2}{2M_\alpha} D_{ij}^{\alpha}(\mathbf{R}) + \sum_{\alpha}^{m} \frac{\hbar^2}{M_\alpha} d_{ij}^{\alpha}(\mathbf{R}) \cdot \nabla_\alpha \tag{2.10}$$

where $D_{ij}^{\alpha}(\mathbf{R}) = \int \Phi_i^*(\mathbf{r};\mathbf{R}) \nabla_\alpha^2 \Phi_j(\mathbf{r};\mathbf{R}) d\mathbf{r}$ are the second-order nonadiabatic coupling element and $d_{ij}^{\alpha}(\mathbf{R}) = \int \Phi_i^*(\mathbf{r};\mathbf{R}) \nabla_\alpha \Phi_j(\mathbf{r};\mathbf{R}) d\mathbf{r}$ are the first-order nonadiabatic coupling vector. The NACs provide details of how the electronic wavefunction varies in response to the nuclear coordinates. The interactions are categorized as inter-state coupling (i $\neq$ j) and intra-state coupling (i=j). For intra-state coupling, the first-order coupling term becomes zero.

## 2.3 Born-Oppenheimer Approximation

The Born-Oppenheimer approximation (BOA) introduced by Born and Oppenheimer in 1927 is one of the most important approximations in quantum chemistry.[171] The BOA is based on the fact that electrons in a molecule move much faster than the nuclei due to the heavier mass of the nuclei. Thus, the electrons can be considered to be moving in the field of fixed nuclei. In this framework, the large difference in mass between electrons and nuclei of a molecule enables the separation of the motions. Consequently, the Hamiltonian is partitioned into electronic and nuclear terms, allowing the molecular wavefunction $\Psi(\mathbf{r}, \mathbf{R}, t)$ to be expressed as a product of corresponding electronic and nuclear wavefunctions.

$$\Psi(\mathbf{r}, \mathbf{R}, t) = \chi_i(\mathbf{R}, t) \Phi_i(\mathbf{r};\mathbf{R}) \tag{2.11}$$

Where $\chi_i(\mathbf{R}, t)$ and $\Phi_i(\mathbf{r};\mathbf{R})$ denotes the nuclear and electronic wavefunctions. A key point to note is that the electronic wavefunction depends explicitly on the electronic coordinates but parametrically depends on the nuclear coordinates. Equation 2.8 illustrates that intra-state coupling enables the population transfer between two different adiabatic states. However, within the BOA approximation, such coupling terms are neglected, thereby preventing the nuclear population transfer between two different adiabatic states. So, equation 2.8 becomes

$$i\hbar\frac{\partial\chi_i(\mathbf{R},t)}{\partial t} = \left[-\sum_{\alpha}^{m}\frac{\hbar^2}{2M_\alpha}\nabla_\alpha^2 + E_i^n(\mathbf{R}) - \sum_{\alpha}^{m}\frac{\hbar^2}{2M_\alpha}\int\Phi_i^*(\mathbf{r};\mathbf{R})\nabla_\alpha^2\Phi_i(\mathbf{r};\mathbf{R})d\mathbf{r}\right]\chi_i(\mathbf{R},t) \tag{2.12}$$

This equation governing the nuclear motions assumes the form of the time-dependent Schrödiger equation, in which $\chi_i(\mathbf{R},t)$ serves as the nuclear motion. Again in BOA, second-order NAC terms of Equation 2.12 break down near the crossing of two or more adiabatic states. Hence, the NAC terms are typically excluded, leading to the Born-Oppenheimer approximation being regarded as the adiabatic approximation, which reads as

$$i\hbar\frac{\partial\chi_i(\mathbf{R},t)}{\partial t} = \left[-\sum_{\alpha}^{m}\frac{\hbar^2}{2M_\alpha}\nabla_\alpha^2 + E_i^n(\mathbf{R})\right]\chi_i(\mathbf{R},t) \tag{2.13}$$

The potential energy surface (PES) obtained from this approximation is referred to as adiabatic.

## 2.4 Hartree-Fock Theory

The description of the approximate solution of the Schrödinger equation for a many-body quantum system is impossible due to its complexity. In response, the Hartree-Fock (HF) approximation was introduced as a central method for simplifying such problems. Hartree-Fock theory forms the cornerstone of modern electronic structure methods and constitutes the first step towards the other, more accurate approximations. It solves the electronic Schrödinger equation that emerges from the time-independent Schrödinger equation, which reads as (in atomic units)

$$\left[-\frac{1}{2}\sum_{i=1}^{n}\nabla_i{}^2 - \sum_{i=1,\alpha=1}^{n,m}\frac{Z_\alpha}{r_{\alpha i}} + \sum_{i=1,j>i}^{n}\frac{1}{\mathbf{r}_{ij}} + \sum_{\alpha=1,\beta>\alpha}^{m}\frac{Z_\alpha Z_\beta}{\mathbf{R}_{\alpha\beta}}\right]\Phi_j(\mathbf{r};\mathbf{R}) = E_j^n(\mathbf{R})\Phi_j(\mathbf{r};\mathbf{R}) \tag{2.14}$$

or

$$\left[\hat{T}_e(\mathbf{r}) + \hat{V}_{eN}(\mathbf{r};\mathbf{R}) + \hat{V}_{NN}(\mathbf{R}) + \hat{V}_{ee}(\mathbf{r})\right]\Phi_j(\mathbf{r};\mathbf{R}) = E_j^n(\mathbf{R})\Phi_j(\mathbf{r};\mathbf{R}) \tag{2.15}$$

which describes the electronic motion in the field of nuclei.

The electronic problem can be solved exactly for the simplest atom, hydrogen. However, when an additional electron is introduced to obtain $H^-$, it seems reasonable, as a starting point, to assume that the electrons do not react with each other, i.e., $\hat{V}_{ee}$=0. Under this assumption, the Hamiltonian becomes separable, and the total electronic wavefunction $\Phi_{el}(\mathbf{r_1}, \mathbf{r_2})$ describing the motion of the two electrons would be a product of two hydrogen orbitals $\phi_H(\mathbf{r_1})\phi_H(\mathbf{r_2})$.

Thus, in order to solve the many-body problem, the n-electron wavefunction can be written as a product of one-electron orbitals as

$$\Phi^{el}(\mathbf{r_1}, \mathbf{r_2}..., \mathbf{r_n}) = \phi_1(\mathbf{r_1})\phi_2(\mathbf{r_2})...\phi_n(\mathbf{r_n}) \tag{2.16}$$

This is known as Hartree products.

However, it only depends on the spatial coordinates and fails to fulfill the antisymmetry principle, which asserts that the total electronic wavefunction must be antisymmetric under the exchange of the spatial and spin coordinates. So to completely describe an electron, two spin functions $\alpha(\omega)$ and $\beta(\omega)$ were introduced, corresponding to the spin-up and spin-down, respectively. Thus, in this formalism, an electron is described by a set of spatial $\mathbf{r}$ and spin coordinates $\omega$, denoted as $\mathbf{x} = \{\mathbf{r}, \omega\}$. The orbital is expressed as $\chi(\mathbf{x})$, representing a spin orbital instead of a spatial orbital $\phi(\mathbf{r})$. The Hartree product becomes,

$$\Phi^{el}(\mathbf{x_1}, \mathbf{x_2}, ..., \mathbf{x_n}) = \chi_1(\mathbf{x_1})\chi_2(\mathbf{x_2})...\chi_1(\mathbf{x_n}) \tag{2.17}$$

where,

$$\chi(\mathbf{x}) = \begin{cases} \phi(r)\alpha(\omega) \\ \phi(r)\beta(\omega) \end{cases} \tag{2.18}$$

This wavefunction, equation 2.17, doesn't satisfy the antisymmetric principle, but can be obtained an antisymmetric wavefunction by considering the linear combination of Hartree products. Thus, for an n-electron system, the generalized wavefunction satisfying the antisymmetric principle can be written as

$$\Phi^{el}(\mathbf{x_1}, \mathbf{x_2}..., \mathbf{x_n}) = \frac{1}{\sqrt{n}} \begin{vmatrix} \chi_1(\mathbf{x_1}) & \chi_2(\mathbf{x_1}) & \cdots & \chi_n(\mathbf{x_1}) \\ \chi_1(\mathbf{x_2}) & \chi_2(\mathbf{x_2}) & \cdots & \chi_n(\mathbf{x_2}) \\ \vdots & \vdots & \ddots & \vdots \\ \chi_1(\mathbf{x_n}) & \chi_2(\mathbf{x_n}) & \cdots & \chi_n(\mathbf{x_n}) \end{vmatrix} \tag{2.19}$$

The determinant of spin orbitals is called the Slater determinant. Here, $\frac{1}{\sqrt{2}}$ is a normalization factor. The approximation that the wavefunction can be described by a Slater determinant is equivalent to the assumption that each electron moves independently, experiencing the Coulomb repulsion due to the average positions of all electrons. Hence, the Hartree-Fock theory is also referred to as mean-field theory.[172] Now, in an n-electron system Slater determinant can be expressed as

$$\Phi^{el}(\mathbf{x_1}, \mathbf{x_2}..., \mathbf{x_n}) = \Big|\chi_i(x_1)\chi_j(x_2)...\chi_k(x_n)\Big\rangle \tag{2.20}$$

or

$$\Phi^{el}(\mathbf{x_1}, \mathbf{x_2}..., \mathbf{x_n}) = \Big|\chi_i\chi_j...\chi_k\Big\rangle \tag{2.21}$$

Thus, the simplest antisymmetric wavefunction representing the ground state of an n-electron system is given by a single Slater determinant.

$$\Big|\Phi_0\Big\rangle = \Big|\chi_1\chi_2...\chi_n\Big\rangle \tag{2.22}$$

According to the variation principle, the optimal wavefunction of this functional form is the one that minimizes the total energy of the system.

$$E_0 = \langle\Phi_0\Big|\hat{H}_{el}\Big|\Phi_0\rangle \tag{2.23}$$

Where $\hat{H}_{el}$ is denoted as the full electronic Hamiltonian. An equation derived by minimizing the total energy $E_0$ with respect to the spin orbitals is referred to as the Hartree-Fock equation. The Hartree-Fock equation is an eigenvalue equation and determines the optimal spin orbitals, which reads as

$$f(i)\chi(\mathbf{x_i}) = \varepsilon\chi(\mathbf{x_i}) \tag{2.24}$$

Where $f(i)$ is an effective one-electron operator, known as the Fock operator, which can be expressed as

$$f(i) = -\frac{1}{2}\nabla_i^2 - \sum_{\alpha=1}^{m}\frac{Z_\alpha}{\mathbf{r_{i\alpha}}} + \nu^{HF}(i) \tag{2.25}$$

Here i=1,2,..,n and $\nu^{HF}(i)$ is the average potential experienced by the $i^{th}$ electron due to the presence of other electrons. Thus, the Hartree-Fock approximation solves the many-body problem by an effective one-electron problem, where the electron-electron repulsion is treated in a mean-field manner, and the procedure to solve the Hartree-Fock equation is known as the self-consistent field (SCF) method.

## 2.5 Density Functional Theory

As the wavefunction of an n-electron system depends on 4n variables, the three spatial and one spin coordinates for each electron, resulting in the wavefunction being significantly complex for many-body systems. Thus, an alternative approach has been introduced to reduce the complexity of many-body problems by substituting the full interactive wavefunction with electron density as the primary variable. Thus, the objective of DFT is to reformulate the quantum properties of many-body electron systems based on the electronic density function $\rho(\mathbf{r})$, which depends only on the three spatial coordinates $\mathbf{r} = (r_x, r_y, r_z)$. This stands in contrast to the many-electron wavefunction $\Phi_{el}(\mathbf{r_1}, \mathbf{r_2}, .., \mathbf{r_n})$ that depends on the position $(\mathbf{r_1}, \mathbf{r_2}, .., \mathbf{r_n})$ of each electron. Hence, the degree of freedom for spatial coordinates in DFT has been reduced from 3N to 3. The electron density for an n-electron system is defined as the square of the wavefunction, integrated over n-1 electron coordinates, with each spin depending only on three spatial coordinates.

DFT was formulated by Hohenberg and Kohn in 1964 with their two Hohenberg-Kohn theorems,[173] which were further advanced through the Kohn-Sham theorem in 1965[174] by Kohn and Sham.

The Hamiltonian for n-electrons in the presence of clamped nuclei, which causes an external potential due to coulombic interaction ($V_{eN}$=$V_x$), can be written as

$$\hat{H} = \hat{T}_e + \hat{V}_x + \hat{V}_{ee} \tag{2.26}$$

Where

$$\hat{T}_e = -\frac{1}{2}\sum_{i}^{n}\nabla_i^2 \tag{2.27}$$

$$\hat{V}_x = \sum_{i}^{n}\sum_{\alpha}^{m}\frac{-Z_\alpha}{|\mathbf{r_i} - \mathbf{R_i}|} \tag{2.28}$$

$$\hat{V}_{ee} = \frac{1}{2}\sum_{i}^{n}\sum_{j>i}^{n}\frac{1}{|r_i - r_j|} \tag{2.29}$$

The wavefunction $\Phi_k$ is the eigenstate of the Hamiltonian, with energy eigenvalue of $E_k$, which can be expressed as

$$\hat{H}\Phi_k(\mathbf{r_1}\sigma_1, \mathbf{r_2}\sigma_2, ..., \mathbf{r_n}\sigma_n) = E_k\Phi_k(\mathbf{r_1}\sigma_1, \mathbf{r_2}\sigma_2, ..., \mathbf{r_n}\sigma_n) \tag{2.30}$$

Where $k$ labels a set of many-electron quantum numbers and $\sigma_i$ denotes the spin of electron $i$. Since the solution of the wavefunction can be antisymmetric when expressed in terms of a Slater determinant from sets of one-electron orbitals $\phi_1, ..., \phi_n$

$$\Phi_k(\mathbf{r_1}\sigma_1, \mathbf{r_2}\sigma_2, ..., \mathbf{r_n}\sigma_n) = \frac{1}{\sqrt{n}} \begin{vmatrix} \phi_1(\mathbf{r_1}\sigma_1) & \phi_2(\mathbf{r_1}\sigma_1) & \cdots & \phi_n(\mathbf{r_1}\sigma_1) \\ \phi_1(\mathbf{r_2}\sigma_2) & \phi_2(\mathbf{r_2}\sigma_2) & \cdots & \phi_n(\mathbf{r_2}\sigma_2) \\ \vdots & \vdots & \ddots & \vdots \\ \phi_1(\mathbf{r_n}\sigma_n) & \phi_2(\mathbf{r_n}\sigma_n) & \cdots & \phi_n(\mathbf{r_n}\sigma_n) \end{vmatrix} \tag{2.31}$$

The electron density for $n$ electron system can be defined as,

$$\rho(\mathbf{r}) = n \int \left|\Phi(\mathbf{r_1}, \mathbf{r_2}, ..., \mathbf{r_n})\right|^2 d^3\mathbf{r}_2, ..., d^3\mathbf{r}_n \tag{2.32}$$

Since the main goal of DFT is to replace the many-body problem by electron density, $\rho(\mathbf{r})$=$\rho_\uparrow(\mathbf{r})$ + $\rho_\downarrow(\mathbf{r})$. Now it is possible to determine the ground-state wavefunction $\Phi_0(\mathbf{r_1}, \mathbf{r_2}, .., \mathbf{r_n})$ from the ground state density $\rho_0(\mathbf{r})$, or in other words, $\Phi$ is a unique functional of $\rho_0(\mathbf{r})$, so

$$\Phi_0 = \Phi[\rho_0(\mathbf{r})] \tag{2.33}$$

As a result, the ground-state expectation value of any operator, for example, ground-state energy ($E_0$), is also a functional of $\rho_0(\mathbf{r})$, so

$$E_0 = E[\rho_0(\mathbf{r})] = \langle\Phi[\rho_0(\mathbf{r})]|\hat{T}_e + \hat{V}_x + \hat{V}_{ee}|\Phi[\rho_0(\mathbf{r})]\rangle \tag{2.34}$$

Thereafter, to determine the correct ground-state energy and electron density, the energy functional should be minimized by the variational method. The limitation of this approach is that the exact form of this energy functional is not known. So, Kohn and Sham proposed a solution using an auxiliary ideal system of non-interacting electrons. Since the system consists of non-interacting electrons, its wavefunction can be represented by a Slater determinant, and with orbitals must satisfy a Schrödinger equation form as,

$$\Big[-\frac{1}{2}\nabla^2 + V_f(\mathbf{r})\Big]\varphi_i(\mathbf{r}) = \hat{H}_i[\rho(\mathbf{r}), \mathbf{r}]\varphi_i = \varepsilon_i\varphi_i(\mathbf{r}) \tag{2.35}$$

Where $\varphi_i(\mathbf{r})$ are the Kohn-Sham eigenfunctions for non-interacting electron systems, and are referred to as Kohn-Sham orbitals. $\varepsilon_i$ are the Kohn-Sham energy levels. The orbital $\varphi_i(\mathbf{r})$ reproduces the electron density $\rho(\mathbf{r})$ of the real many-body system as

$$\rho(\mathbf{r}) = \sum_{i}^{n} \left|\varphi_i(\mathbf{r})\right|^2 \tag{2.36}$$

The effective potential or Kohn-Sham potential, $V_f(\mathbf{r})$, can be represented in the form as,

$$V_f(\mathbf{r}) = V_x(\mathbf{r}) + \int \frac{n(\mathbf{r}')}{|\mathbf{r} - \mathbf{r}'|} d^3r' + V_{xc}[n(\mathbf{r})] \tag{2.37}$$

As the Hartree and exchange-correlation terms depend on $\rho(\mathbf{r})$, which is determined from $\phi_i$, and these further are solutions to $V_f$, hence the Kohn-Sham equation has to be solved in a self-consistent approach (i.e., iterative method), until convergence is reached.

Where $V_x(\mathbf{r})$ is the *external potential*, the second term is the potential due to Coulomb repulsion, also known as the *Hartree potential*, and the third term, $V_{xc}$, is the *exchange-correlation potential*, which takes into account all the many-particle interactions omitted in other terms. The exchange correlation potential $V_{xc}$ can be deduced by considering a functional derivative of the exchange and correlation energy functional $E_{xc}$ with respect to the density, which reads as below,

$$V_{xc} = \frac{\delta E_{xc}[\rho(\mathbf{r})]}{\delta \rho(\mathbf{r})} \tag{2.38}$$

DFT can provide the molecular energies while accounting for electron correlation effects at a computational cost similar to the HF method. However, a key issue associated with this method lies in the exchange-correlation functional approximation, which lacks an exact form, leading to the development of a large number of functionals, and consequently a wide range of DFT methods.

## 2.6 Time-dependent Density Functional Theory

Time-dependent Density Functional Theory (TDDFT) extends the framework of the ground-state DFT to describe the electronic excited states and capture time-dependent phenomena. To solve the time-dependent n-electron systems, one must

solve the time-dependent Schödinger equation, which can be expressed as,

$$i\hbar\frac{\partial}{\partial t}\Phi(\mathbf{r}_1\sigma_1,..,\mathbf{r}_n\sigma_n,t) = \hat{H}\Phi(\mathbf{r}_1\sigma_1,..,\mathbf{r}_n\sigma_n,t) \tag{2.39}$$

The TDDFT is fundamentally based on the Runge–Gross (RG) theorem,[175] which is an analogue of the Hohenberg–Kohn theorem. This RG theorem states that there is an occurrence of a unique mapping (i.e, one-to-one correspondence) between the time-dependent external potential and the one-electron density for a many-body system from an initial wavefunction. This one-to-one correspondence in TDDFT allows us to work with a fictitious non-interacting system of electrons, whose density is equivalent to the time-dependent density of the real one. Then the corresponding time-dependent Kohn-Sham equation becomes

$$i\frac{\partial}{\partial t}\Phi_i(\mathbf{r},t) = \Big[-\frac{\nabla^2}{2} + \int\frac{n(\mathbf{r}',t)}{|\mathbf{r}-\mathbf{r}'|}d^3r' + V_x(\mathbf{r},t) + V_{xc}(\mathbf{r},t)\Big]\Phi_i(\mathbf{r},t) \tag{2.40}$$

or

$$i\frac{\partial}{\partial t}\Phi_i(\mathbf{r},t) = \Big[-\frac{\nabla^2}{2} + V_{KS}[\rho](\mathbf{r},t)\Big]\Phi_i(\mathbf{r},t) \tag{2.41}$$

$$= \hat{H}_{KS}(\mathbf{r},t)\Phi_i(\mathbf{r},t) \tag{2.42}$$

in which the density $\rho(\mathbf{r},t)$ is defined to be identical to that of the real system, which reads as

$$\rho(\mathbf{r},t) = \sum_{i=1}^{n}\Big|\Phi_i(\mathbf{r},t)\Big|^2 \tag{2.43}$$

Owing to the one-to-one correspondence as mentioned previously, the potential generating this density is unique and thus, the exchange-correlation potential can be defined via,

$$V_{KS}(\mathbf{r},t) = V_x(\mathbf{r},t) + V_H(\mathbf{r},t) + V_{xc}(\mathbf{r},t) \tag{2.44}$$

where the first term $V_x(\mathbf{r},t)$ is the external potential, the second term is denoted as the Hartree potential and has the form, in terms of time-dependent density, as

$$V_H(\mathbf{r},t) = \int\frac{n(\mathbf{r}',t)}{|\mathbf{r}-\mathbf{r}'|}d^3r' \tag{2.45}$$

And the last term includes all the non-trivial many-body effects, which must be approximate. In a particular approach, the $V_{xc}$ is approximated in TDDFT using the local spin density approximation (LSDA) approach for the adiabatic version, which presumes that the change of exchange-correlation potential in time is adiabatic, and the approach is referred to as adiabatic local density approximation (ALDA), which takes into account one density function per time step.

$$V_{xc}[\rho(\mathbf{r},t)] \approx V_{xc}^{GS}[\rho_t(\mathbf{r})] \tag{2.46}$$

Where $V_{xc}^{GS}[\rho_t(\mathbf{r})]$ is the ground-state DFT exchange-correlation potential.

Among several variants of the TDDFT formalism, the Casida approach is one of the most widely used.

## 2.7 Multiconfigurational Methods

The electron configuration interaction based on the HF reference serves as an approach to generate an excited-state electronic wavefunction and is categorized as a single-reference (SR) method, as it constructs the correlated wavefunctions from the orbitals of a single Slater determinant. Thus, the method fails to describe the systems exhibiting multi-reference character, such as metal complexes, organic radicals, bond-breaking or forming processes, dihedral rotation processes, etc. To address the multiconfigurational problem, an approach was introduced where the configuration interaction calculations are performed with simultaneous variational optimization of orbitals and the coefficients of electronic configurations. The approach is known as the multiconfigurational self-consistent field (MCSCF) method.[176–179]

The MCSCF wavefunctions $\left|\Psi_{MCSCF}\right\rangle$ can be expressed as a linear expansion of a set of many-electron configurations $|\Phi_j\rangle$, j=1....$N_{CI}$ as[179]

$$\left|\Psi_{MCSCF}\right\rangle = \sum_{j=1}^{N_{CI}} c_j \left|\Phi_j\right\rangle \tag{2.47}$$

Here, $c_j$ are the coefficients, and many electron configurations can be constructed from molecular orbitals, either as individual determinants or as configuration state functions (CSFs). Among all multiconfigurational methods, complete active space self-consistent field (CASSCF)[180–182] is the most widely used MCSCF approach, in which the orbitals are classified into a set of active, inactive, and secondary orbitals

to construct CSFs. Within the CASSCF wavefunctions, the configuration included in CI expansions is generated by all doubly occupied inactive orbitals, electrons in active orbitals with any occupancy, and unoccupied secondary orbitals. A CASSCF calculation involving an active space of **N** electrons distributed over **M** orbitals is denoted as CAS(**N**,**M**) methods, signifying that all the possible configurations of the electrons within the specified orbitals are considered in constructing the wavefunctions. Selecting a suitable active space requires prior knowledge of the excited states properties and chemical intuition, which is not a trivial task. However, the CASSCF method cannot capture the dynamic correlation arising from a large number of configurations.

This limitation of CASSCF methods has been addressed by treating the CASSCF wavefunction as a zero-order reference, upon which the dynamic correlation can be incorporated via configuration interaction theory, like multiconfiguration configuration interaction (MRCI), or perturbation approaches like complete active state second-order perturbation (CASPT2), multi-state complete active state second-order perturbation (MS-CASPT2), and extended multi-state complete active space second-order perturbation theory (XMS-CASPT2). In the CASPT2 approach,[183, 184] since the CASSCF wavefunction serves as the reference wavefunction, so

$$|\Psi^{(0)}\rangle = |\Phi^{CAS}\rangle \tag{2.48}$$

Subsequently, the first-order interacting wavefunction can be obtained by applying the excitation operator to $|\Phi^{CAS}\rangle$. The configuration space within this framework is categorized into four subspaces[179, 183, 184] : (i) $V_0$, the subspace defined by $|\Phi^{CAS}\rangle$, (ii)$V_K$, the subspace consisting of configurations that are orthogonal to $|\Phi^{CAS}\rangle$ within the restricted full CI space, (iii) $V_{SD}$, the subspace due to all the single and double excitations from $|\Phi^{CAS}\rangle$, and (iv) $V_{TQ..}$, the subspace as a result of all other higher excitations. As the functions in the subspaces $V_K$ and $V_{TQ}$ do not interact with the zeroth-order wavefunction, the first-order perturbed wavefunction $|\Psi^{(1)}\rangle$ can be expressed as

$$|\Psi^{(1)}\rangle = \sum_j C_j |\Phi^{(SD)}\rangle \tag{2.49}$$

The set of linear equations then represents the expansion coefficients as,

$$\sum_j C_j \left\langle \Phi_i^{SD} | \hat{H}_0 - E^{(0)} | \Phi_j^{SD} \right\rangle = - \left\langle \Phi_i^{SD} | \hat{H} | \Phi^{CAS} \right\rangle \tag{2.50}$$

Here $\hat{H}_0$ is denoted as zeroth-order Hamiltonian, $E_0$ is zeroth-order energy, where $E^{(0)} = \langle \Phi^{CAS} | \hat{H}_0 | \Phi_i^{CAS} \rangle$.

Then the second-order energy can be expressed as

$$E^{(2)} = \langle \Phi^{CAS} | \hat{H} | \Psi^{(1)} \rangle \tag{2.51}$$

By introducing a generalized Fock operator $\hat{F}$, equation 2.50 can re reformulated as,

$$(\mathbf{F} - E_0 \mathbf{S})\mathbf{C} = -\mathbf{V} \tag{2.52}$$

In equation 2.52, $\mathbf{F}_{ij} = \langle \Phi_i^{SD} | \hat{F} | \Phi_j^{SD} \rangle$, $S_{ij} = \langle \Phi_i^{SD} | \Phi_j^{SD} \rangle$, and $V_i = \langle \Phi_i^{SD} | \hat{H} | \Phi_j^{CAS} \rangle$.

The perturbation theory originally formulated was defined as single-state CASPT2 (SS-CASPT2) and follows a "diagonalize the perturb" approach. In this approach, diagonalization of the Hamiltonian over the reference space results in the zeroth-order wavefunction, which is subsequently followed by perturbation expansion over this zeroth-order wavefunction. This procedure results in a serious issue when the perturbation (considering the full two-electron interactions) induces mixing of two states, such as valence and Rydberg or covalent or ionic states. Further, the contribution of each state depends on the corresponding molecular geometry, e.g., at the crossing region, leading to a difference in wavefunction character in multireference treatment. This issue has been addressed by introducing the multistate formalism in CASPT2 method, referred as MS-CASPT2 method,[185] in which the energies of the perturbed states and the coupling between them are first obtained, followed by the diagonalization of the resulting Hamiltonian. A notable advantage of this approach is that it results in conical shape topology when an interaction occurs between the states of the same multiplicity, unlike in SS-CASPT2 method. The MS-CASPT2 approach has been further reformulated to its extended variants, referred to as extended multi-state complete active space second- order perturbation theory (XMS-CASPT2),[186, 187] which results in an improved potential near the conical intersections and avoided crossing regions.

## 2.8 Post-Hatree-Fock Theory

Although Hartree-Fock approximation offers a solution to the many-body electron problems, it fails to account for the electron correlation effect, which results in the deviation of energy. To overcome the limitations of the Hartree-Fock method, a large set of approximations has been introduced by incorporating the electron correlation effects more accurately, which are commonly referred to as Post-Hartree-Fock methods. Notable methods under this framework include Møller–Plesset perturbation (MP2) theory, Coupled Cluster (CC) theory, Multi-configuration time-dependent Hartree (MCTDH), Algebraic Diagrammatic Construction (ADC), etc. The Post-Hartree-Fock methods utilized in this thesis are described in greater detail in the following sections.

### 2.8.1 Algebraic diagrammatic construction

The algebraic diagrammatic construction (ADC) is a formalism of the polarization propagator for the electronically excited state based on the many-body Green Function theory.[188–190] In the ADC procedure, a Hermitian secular matrix is diagonalized, which combines with the Rayleigh-Schrodinger perturbation theory to evaluate the matrix elements. The ADC approximation was originally developed based on the diagrammatic perturbation theory applied to the polarized propagator, which has confusing properties like excitation energies and spectral ground-to-excited state transitions. This has further been reformulated in terms of intermediate state representation (ISR),[190–193] where the Hamiltonian is expressed with respect to the basis set of explicitly correlated states, referred to as intermediate states (IS). The intermediate state enables the explicit representation of the excited state wavefunctions, thereby providing a direct approach to compute the excited state properties along with the transition moment between different excited states. Now, let us consider an n-electron system with Hamiltonian $\hat{H}$, and a non-degenerate ground-state $|\Psi_0\rangle$ and the energy $E_0$. The polarized propagator can be defined in general algebraic form as

$$\mathbf{\Pi}^{+}(\omega) = \mathbf{f}^{\dagger}(\omega - \mathbf{M})^{-1}\mathbf{f} \tag{2.53}$$

Where $\omega$ is the excitation energy and can be expressed as $\omega = E_n - E_0$. $\mathbf{M}$ is the ADC secular matrix, which can be defined as the representation of the shifted

Hamiltonian $(\hat{H} - E_0)$, w.r.t. the intermediate state $\langle\widetilde{\Psi}_I|$, as

$$\mathbf{M}_{IJ} = \langle\widetilde{\Psi}_I|\hat{H} - E_0|\widetilde{\Psi}_J\rangle \tag{2.54}$$

and $\mathbf{f}$ is defined as the matrix of effective transition amplitudes, which reads as

$$f_{J,rs} = \langle\widetilde{\Psi}_J|c_r^\dagger c_s|\widetilde{\Psi}_0\rangle \tag{2.55}$$

The intermediate state mentioned here is expressed in detail below. Again, the vertical excitation energies, which are denoted as

$$\Omega_n = E_n - E_0 \tag{2.56}$$

are obtained from the eigenvalues of $\mathbf{M}$, which can be expressed as

$$\mathbf{MX} = \mathbf{X\Omega}, \quad \mathbf{X}^\dagger\mathbf{X} = 1 \tag{2.57}$$

In equation 2.57, $\Omega$ and $\mathbf{X}$ represent the diagonal eigenvalue matrix and the matrix of eigen vector $\underline{X}^{(n)}$. The excited state can be represented in terms of eigenvector components and intermediate states as

$$\big|\Psi_n\rangle = \sum_J \mathbf{X_{Jn}}\big|\widetilde{\Psi}_J\rangle \tag{2.58}$$

so the transition moment is given by

$$T_n = \langle\Psi_n|\hat{D}|\Psi_0\rangle \tag{2.59}$$

Also, it can be expressed in terms of the scalar product of $\underline{X}_n^\dagger$ and a vector $\mathbf{F}$ as

$$T_N = \underline{X}_n^\dagger\mathbf{F} \tag{2.60}$$

Here, $\mathbf{F}$ is called the effective transition moment and has the form

$$F_J = \langle\widetilde{\Psi}_J|\hat{D}|\Psi_0\rangle = \sum_{rs} d_{rs}f_{J,rs} \tag{2.61}$$

Where $\hat{D}{=}\sum d_{rs}c_r^\dagger c_s$ and is referred to as dipole moment operator, $d_{rs} = \langle\varphi_r|\hat{d}|\varphi_s\rangle$ are denoted as one-particle matrix elements, and $f_{J,rs}$ given by equation 2.54 are called

effective transition amplitudes.

In the original ADC formalism, the matrix **M** and **f** can be expressed in the form of a perturbation expansion without the use of intermediate states as below,

$$\mathbf{M} = \mathbf{M}^{(0)} + \mathbf{M}^{(1)} + .... \tag{2.62}$$

$$\mathbf{f} = \mathbf{f}^{(0)} + \mathbf{f}^{(1)} + .... \tag{2.63}$$

This procedure enables the determination of successively higher-order contributions to **M** and **f**, thereby generating a hierarchy of consistent nth-order approximations known as ADC(n) approximations. As the ADC formalism is based on the MP reference via intermediate state representation, its accuracy is highly sensitive to the quality of the MP reference and fails to describe the character near the degenerated region. Hence, ADC formalism is a single-reference approximation and is not suitable for exhibiting multi-reference character.

## 2.9 Nonadiabatic Molecular Dynamics

The nonadiabatic dynamics offers mechanistic insights into the photochemical phenomena that take place after the photoabsorption of light, and thus plays a pivotal role in understanding the processes of our environment. During a photochemical reaction, the motion of the electrons is instantaneous to the nuclear motion, and thus the details of the electronic dynamics can often be neglected. In such cases, the Born-Oppenheimer approximation enables decoupling of the electronic and motions, resulting in the on-the-fly evaluation of the potential energy surface at the molecular geometries encountered during the dynamics. However, there occurs the breakdown of the Born-Oppenheimer approximation when the dynamics is initiated from the excited electronic states due to nonadiabatic transitions, and thus requires a quantum mechanical treatment of both the nuclei and the electrons. Numerous theoretical and computational approaches have been proposed over the past few decades to address the challenge of simulating the dynamics beyond the Born-Oppenheimer approximation. Among the most commonly used are multiconfiguration time-dependent Hartree (MCTDH),[14, 15] ab initio multiple spawning (AIMS),[25, 26] trajectory surface hopping (TSH),[18–20] mean-field Ehrenfest (MFE),[24] multiconfigurational Ehrenfest (MCE),[23] etc. In this thesis, TSH dynamics have been implemented over

the other alternative approaches primarily due to the significantly higher computational cost for our systems. Further, TSH has been observed to provide accurate results for the photochemical processes in similar chromophores.

### 2.9.1 Trajectory Surface Hopping

In the trajectory surface hopping (TSH) approach, by Tully,[18, 19, 194] the nuclei were assumed to propagate along a trajectory, $\mathbf{R}^I(t)$, which is treated classically. The electronic wavefunction can then be expressed in terms of the electronic basis as,

$$\Phi(\mathbf{r}, \mathbf{R}^c, t) = \sum_j c_j(t)\phi_j(\mathbf{r}; \mathbf{R}^c(t)) \tag{2.64}$$

Where $\mathbf{r}$ is the electronic coordinate and the superscript $c$ denotes that the observables are treated at fixed nuclei $\mathbf{R}^c(t)$. Now, substituting this in the time-dependent electronic Schrödinger equation shown below

$$(i\hbar\frac{\partial}{\partial t} - H_e)\Phi(\mathbf{r}, \mathbf{R}, t) = 0 \tag{2.65}$$

generates a set of differential equations for coefficient $c_k(t)$ as shown below

$$i\hbar\frac{\partial c_l}{\partial t} + \sum_j (-H^c_{kj} + i\hbar\mathbf{F}^c_{kj}.\mathbf{v}^c)c_j = 0 \tag{2.66}$$

Here, $H_{kj}$ corresponds to the matrix element of the electronic Hamiltonian $\langle\phi_k|H_e|\phi_j\rangle$, and $\mathbf{F}^c_{kj}$ denotes the nonadiabatic coupling vector between states k and j, and $\mathbf{v}^c$ is the nuclear velocity vector. And,

$$\mathbf{F}^c_{kj} \cdot \mathbf{v}^c = \langle\Phi_k \left|\frac{\partial}{\partial t}\right| \Phi_j\rangle_r \tag{2.67}$$

Equation 2.66 is referred to as the semiclassical time-dependent Schrödinger equation (SC-TDSE). Within the TSH approach, the nuclear motion evolves according to Newton's equation, which propagates in a trajectory of a single electronic state. Thus, for a nucleus of coordinate m having mass M, it can be expressed as

$$\frac{d^2\mathbf{R}^c_m}{dt^2} - \frac{\mathbf{f}^c_m}{M_m} = 0 \tag{2.68}$$

Where the force $\mathbf{f}^c_m$ is proportional to the gradient of potential energy

$$\mathbf{f}_m^c = -\nabla_{R_m} H_{ll}^c \tag{2.69}$$

Further, during the propagation of the dynamics, there is a probability of a trajectory for hopping between the different electronic states. And, among the several methods TSH approaches to compute the transition probabilities, the most commonly used is the fewest-switch approach by Tully.[19] According to this approach, the number of hopping events is minimized within a time-step $\Delta$t and the transition probabilities of a trajectory from one electronic state m to another state l are computed as

$$\mathbf{P}_{m\to l} = \frac{\text{population increment in } l \text{ due to flux from } m \text{ during } \Delta t}{\text{population of } m} \tag{2.70}$$

The population of each electronic state l can be represented by the diagonal terms of the density matrix, which depend on the coefficients $c_l(t)$ and are defined as

$$\rho_{ml}(t) = c_m c_l^* \tag{2.71}$$

Hence, equation 2.66 can be expressed as

$$P_{m\to l} = \max\left[0, \frac{2\Delta t}{\rho_{mm}}\left(\hbar^{-1} Ix(\rho_{lm}) H_{ml}^c - \mathrm{Re}(\rho_{lm})\,\mathbf{F}_{lm}^c \cdot \mathbf{v}^c\right)\right] \tag{2.72}$$

According to the fewest-switch method, there is an instantaneous probability of a nonadiabatic event at each time step along the trajectory propagation. However, a hopping from surface m to l at time t was considered to be successful only under the following two conditions; Firstly, a random number $r_t$ in the [0,1] must satisfy,

$$\sum_{n=1}^{l-1} P_{m\to n}(t) < r_t \leq \sum_{n=1}^{l} P_{m\to n}(t) \tag{2.73}$$

And secondly, the energy gap between the final and initial state must satisfy

$$V_l(\mathbf{R}^c(t)) - V_m(\mathbf{R}^c(t)) \leq \frac{\left(\sum_x^{N_{at}} \mathbf{v}_x^c \cdot \mathbf{F}_{lm}^{c,x}\right)^2}{2\sum_x^{N_{at}} \mathbf{M}^{-1}\left(\mathbf{F}_{lm}^{c,x}\right)^2} \tag{2.74}$$

The situation when only the first condition is satisfied is referred to as a frustrated hop. And according to the second condition, the total energy after hopping should

not increase, and there should be conservation of energy.

Since the SC-TDSE in TSH propagates along a single trajectory $\mathbf{R}^c$ governed by the gradients of a particular electronic state, the decoherence issue arises. However, during this propagation, the amplitudes $c_j$ of all other electronic states are artificially constrained to evolve along $\mathbf{R}^c$ of the same trajectory, despite the fact that the gradients of these states would lead them to evolve along different paths. To provide a solution to the decoherence issue, Granucci *et al.* [195] modified the time-dependent coefficient in the electronic state $l$ and $m$ at every time step as below

$$c_l' = c_l exp\left(\frac{-\Delta t}{\tau_{lm}}\right) \forall l \neq 1 \tag{2.75}$$

$$c_m' = c_m \left[\frac{1 - \sum_{l\neq 1} |c_l'|}{|c_m|^2}\right]^{\frac{1}{2}} \tag{2.76}$$

$$\tau_{lm} = \frac{\hbar}{|V_{ll} - V_{mm}|}\left[1 + \frac{\alpha}{E_{kin}}\right] \tag{2.77}$$

Here, $E_{kin}$ is defined as nuclear kinetic energy, $\Delta$t is the integration time set, and $\alpha$ is the empirical parameter whose value is recommended to be 0.1 hartree. The discussion on TSH is drawn from a review by Babartti.[20, 196]

# Chapter 3

# Mechanistic Insight into the Dual Fluorescence Behaviour in GFP Chromophore Analogue

(The work of this Chapter is published in *J. Phys. Chem. B* **2022**, *126*, 9930–9944.)
*This article has appeared as a Cover Feature of the Journal.*

## 3.1 Introduction

Dual fluorescence has gathered significant interest in research over the past few decades. It is one of the most intriguing and rare photophysical phenomena observed in a certain group of fluorophores that exhibits two fluorescence bands as a consequence of the involvement of two pronounced electronic excited-state minima.[197] The phenomenon of dual fluorescence was initially reported in azulene derivatives,[198] and later it was observed in many chemical systems.[199, 200] For the most part, the origin of dual fluorescence was ascribed to an electronic and/or conformational rearrangement of the fluorophore in the excited state, resulting in two electronic excited states.[201, 202] This anomalous photophysical phenomenon appears in compounds that have an electron-donating and accepting moiety, which participates in an excited-state intramolecular charge transfer (ICT) process,[203, 204] twisted intramolecular charge transfer (TICT) process,[201, 205] or in the fluorophores having both a hydrogen donor-acceptor pair in close proximity, where excited-state intramolecular/intermolecular proton transfer (ESIPT) can occur.[206–208] Compounds that exhibit dual fluorescence could have a variety of uses in chemistry and biology such as a ratiometric DNA detector,[209] white organic-light emitting devices (OLEDs),[209] ratiometric fluorescence probes for chemo/biosensing and bioimaging,[210] fluorescence ion and pH indicators,[211, 212] multicolor cell-imaging,[213]

etc.

In recent years, a number of chromophores based on the Green Fluorescent Protein (GFP) chromophore, i.e., *p*-hydroxybenzylideneimidazolidinone (*p*-HBDI), has been modeled, synthesized, and reported by various researchers.[214–219] Under certain conditions, some exhibit dual fluorescence,[214, 215] and some emit simply a single emission[216–218] while some have a nonfluorescent property.[219]

Green fluorescent protein (GFP) and its structural analogues have been exploited ubiquitously in cellular biology, biotechnology, and medical research as a unique genetically encoded fluorescent marker.[76, 77, 220, 221] GFP is a bioluminescent polypeptide isolated from the body of a jellyfish called Aequorea Victoria and displays a green color when exposed to light.[76, 220] It is made up of an 11-stranded-$\beta$-barrel-like structure with $\alpha$-helices at either end to form a cylinder threaded with a diameter of 24 Å and height of about 42 Å generating a "$\beta$-can" structure with the chromophore encapsulated within it.[88, 89] GFP is composed of 238 amino acids, from which autocatalytic cyclization of Ser65, Tyr66, and Gly67 amino acid residues generates a visible green fluorescent light-emitting structure. The GFP chromophore is structurally locked by some covalent and hydrogen bonds, preventing it from rotating around the exocyclic $\Phi_P$- and $\Phi_I$-bond and shielding it from other amino acid residues and water molecules that would quench its fluorescence.[222]

Wild-type Green Fluorescent Protein (wt-GFP) displays two electronic excitation bands at 398 nm (major) and 475 nm (minor), which correspond to the neutral and anionic chromophores.[88, 89, 222] Upon photoexcitation, the neutral protonated form of the chromophore (*p*-HBDI) significantly exhibits a fast excited-state proton transfer (ESPT) process, emitting green light at 508 nm with 80% fluorescence quantum yield.[94] This ESPT phenomenon is caused by proton relay between the active sites of the chromophore through the neighboring residues and internal water molecules via a multiple proton transfer mechanism, which is not present in the solvents for the bare chromophore.[223–225] Moreover, the existence of the ESPT phenomenon in GFP is validated by GFP double mutant T203V/S205V, which emits blue lights as a result of non-ESPT-related photophysics.[226, 227] However, the ESPT-related photophysical phenomenon of the GFP chromophore is still arguable and has yet to be resolved. Consequently, various experimental as well as theoretical strategies have been implemented to elucidate the ESPT-related photophysical properties of the GFP chromophore in greater detail, but failed to reproduce to a

greater extent since the excited state of the GFP chromophore exhibits ultrafast radiationless transitions.[154] Furthermore, rotation about a single and/or double exocyclic bridging bond (i.e., $\Phi_P$ and $\Phi_I$ twist, Chart 3.1) has been demonstrated to have a tremendous impact on the photophysical properties of the analogues of GFP chromophore, leading the isolated GFP chromophore to be nonfluorescent due to the occurrence of easy isomerization.[228–230] Thus, while designing the fluorophore based on *p*-HBDI, the photoisomerization process should be minimized; i.e., rotation of the $\Phi_P/\Phi_I$ bond should be hindered.[229, 230]

**Chart 3.1**. Molecular structures of the GFP chromophore, *p*-TsABDI chromophore analogue, and model clusters.

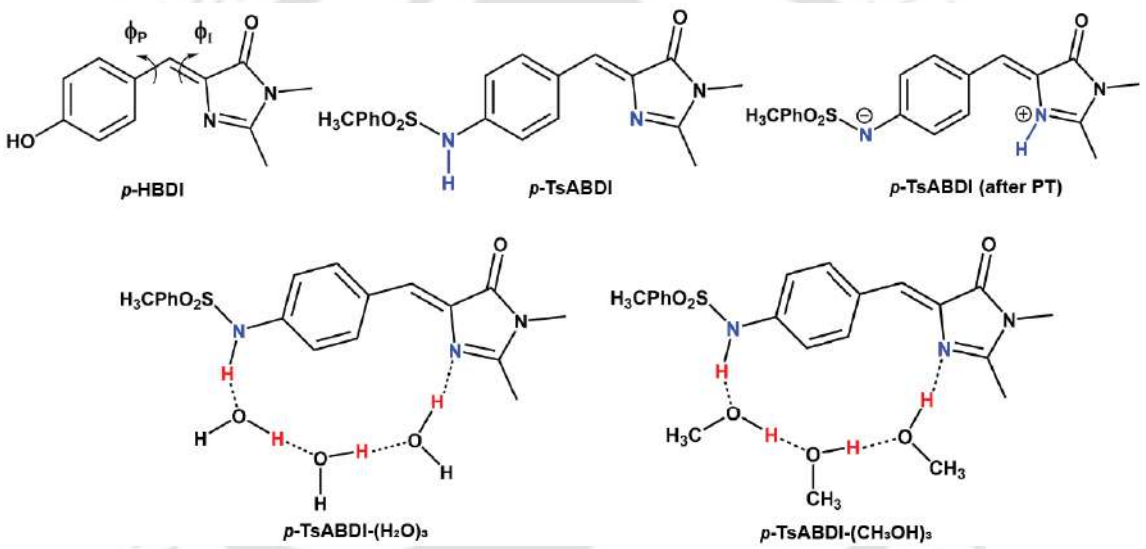


Sung and co-workers have synthesized a para-sulfonamide (*p*-TsABDI) analogue of the GFP chromophore to mimic its structure and properties for the further study of the ESPT related photophysical phenomenon of GFP.[231] The synthesized para-sulfonamide (*p*-TsABDI) analogue of the GFP chromophore was found to display the ESPT phenomenon, qualifying as a model compound for further research into the ESPT related photophysical phenomenon of GFP. These authors have also illustrated the effects of solvent on the photophysical phenomena of the *p*-TsABDI analogue; however, they did not show the mechanistic pathways underlying its dual fluorescence nature.[231]

Thus, there is a strong quest to unveil the origin of dual fluorescence and its mechanistic pathway, along with its effect in various types of solvents for the *p*-TsABDI analogue of GFP. So, to have a better insight into the ESPT-related photophysics of

the GFP chromophore, the experimentally synthesized parasulfonamide (*p*-TsABDI) compound has been considered for further investigation since it comprises both the acidic and basic moieties; i.e., both the proton donating and accepting groups are present.

## 3.2 Computational Details

### 3.2.1 Static Calculations

All the calculations have been performed in the Gaussian 16 program.[232] The structure of the compound was first constructed using the X-ray crystallographic structure of the green fluorescent protein (GFP) (PDB code: 1GFL, resolutions 1.90 Å)[233] extracted from the Protein Data Bank (PDB). All the amino acid residues and the water molecules were omitted, and models were generated based on the synthesized para-sulfonamide analogue (*p*-TsABDI) of GFP. The ground ($S_0$) and excited ($S_1$) state geometries were optimized employing density functional theory (DFT)[234] and time-dependent DFT (TDDFT)[235] combined with Becke's three-parameter with Lee-Yang-Parr hybrid exchange correlation functional (B3LYP)[236] and a range-separated Coulomb-attenuated hybrid exchange corrected correlation functional (CAM-B3LYP)[237]. The hybrid meta-functional M06[238] was also implemented during the computations to ensure the accuracy of the results. The 6-31G(d,p)[239, 240] and TZVP[241] basis sets were employed throughout. Harmonic frequency calculations were carried out for all the stationary points at the same level of computational method to confirm that the optimized $S_0$- and $S_1$-states geometries were real minima. Moreover, vertical electronic transition energies at the Franck-Condon points were also computed for $S_0$ and $S_1$ optimized geometries to compute the electronic excitation and emission spectra. Solvent effects were considered by implementing the integral equation formalism variant of the polarizable continuum model (IEFPCM)[242, 243] in various solvents with a wide range of polarity. Both the linear response (LR)[244] and state-specific (SS)[245, 246] solvation models have been implemented to calculate electronic absorption and emission energies for *p*-TsABDI analogue.

Furthermore, to investigate the ESPT process in the compound, the $S_0$ and $S_1$ potential energy curves (PECs) for compound *p*-TsABDI (with protic solvents) involving

the PT coordinates were constructed by fixing the N1-H1 bond distance (Figure3.1) at different values with a step of 0.05 Å.

The RDG function[247, 248] has been used to predict various types of noncovalent interactions and their strengths. The concerned equation can be defined as

$$\mathrm{RDG(r)} = \frac{1}{2(3\pi^2)^{\frac{1}{3}}} \frac{|\nabla\rho(r)|}{\rho(r)^{\frac{4}{3}}} \tag{3.1}$$

where RDG(r) is the reduced density gradient of the exchange contribution and $\rho$(r) is the total electron density. The nature of noncovalent interactions can be determined by plotting the reduced density gradient with respect to electron density. The spikes appearing in the RDG scattered maps are correlated with the interaction of critical points (ICP), which can be visualized in a 3D isosurface with the location of noncovalent interactions. Moreover, the Laplacian of electron density, $\nabla^2\rho = \lambda 1 + \lambda 2 + \lambda 3$, in which the second eigenvalue of the electron density Hessian matrix $\lambda 2$ represents whether the interactions are attractive ($\lambda 2 < 0$) or repulsive ($\lambda 2 > 0$) in nature. The results are calculated and plotted using the Multiwfn[249] program and VMD[250] software.

### 3.2.2 Dynamics Simulation

To explain the excited-state intermolecular proton transfer (ESIPT) phenomenon in the *p*-TsABDI analogue in solvent clusters, on-the-fly dynamics simulations were performed on the first excited-state ($S_1$) surface. For each complex, a set of 100 trajectories has been generated for the initial condition for each trajectory employing a Wigner distribution of the ground-state vibrational quantum harmonic oscillator[251] of the ground-state minimum, as implemented in the NEWTON-X program[252] interfaced with the Gaussian 16 program package.[232] Thereafter, $S_1$ dynamics simulations were carried out in the NEWTON-X program in the solvent phase with a microcanonical ensemble using Born-Oppenheimer energies and gradients provided by the TDDFT/CAM-B3LYP/6-31G(d,p) theoretical level with 0.5 fs integration time step and a maximum time of 300 fs. This approach has previously been employed and was found to be suitable in dynamics simulation studies.[253–256] The nuclear motions of all the atoms at each step of the dynamics simulations were computed using numerical integration of Newton's equation by the Velocity-Verlet algorithm.[257] The trajectories for each complex were analyzed and classified into two categories

based on the results obtained from the on-the-fly dynamics simulations: (a) ESIPT, where the intermolecular proton transfer occurs in the excited-state during the given simulation time via solvent molecules, and (b) NO PT, where there occurs no PT within the simulation time. The PT time is defined as the time at which the breaking bonds and forming bonds intersect, implemented in previous investigations.[253, 255, 256] Moreover, the details of the PT time, PT probability, and PT mechanism along the H-bonded chain and relative energy difference were obtained by the statistical analysis of all the active PT trajectories.

## 3.3 Results & Discussion

### 3.3.1 Calculated Electronic Properties and their Structural Parameters

The ground ($S_0$)- and excited ($S_1$)-state optimized geometries of the GFP chromophore analogue para-sulfonamide (*p*-TsABDI) with the polar solvents (i.e., water and methanol) are depicted in Figure 3.1.

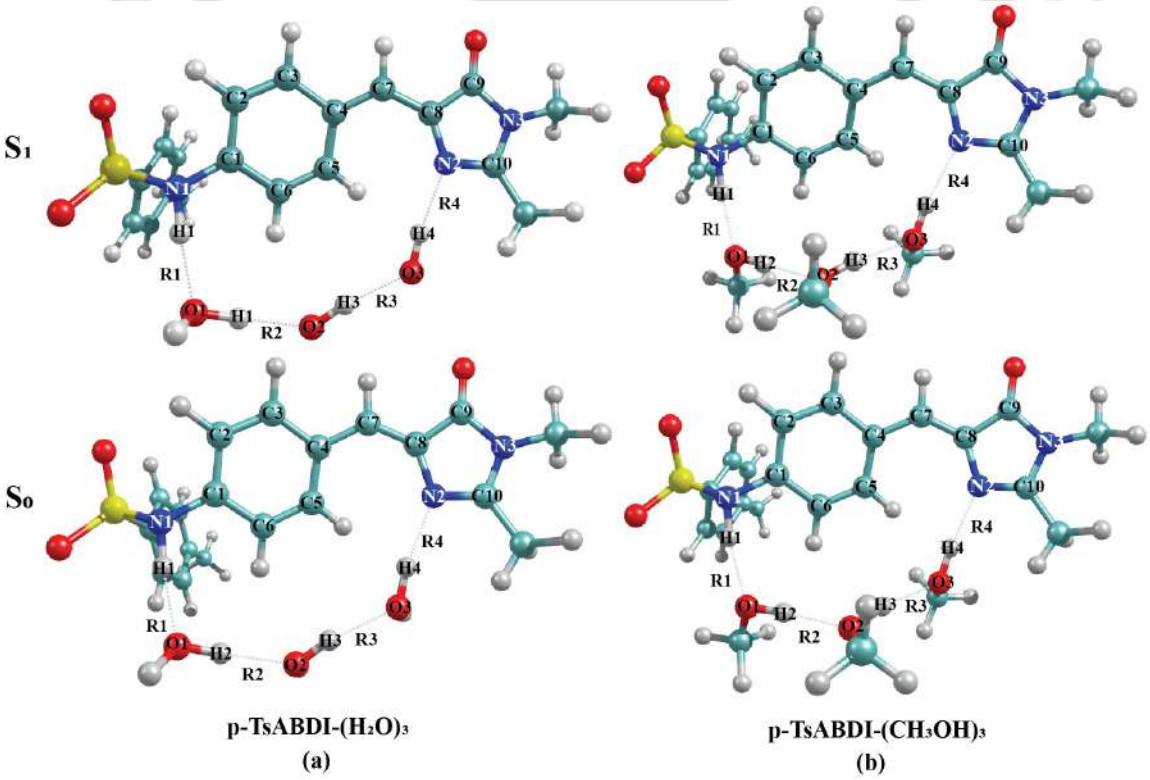


**Figure 3.1:** Molecular geometries of the *p*-TsABDI analogue for $S_0$ and $S_1$ minimum in (a) $H_2O$ and (b) $CH_3OH$ solvents, optimized using CAM-B3LYP/TZVP/IEFPCM level of theoretical accuracy.

All geometric structures were optimized using the CAM-B3LYP/TZVP/IEFPCM method to gain a better understanding of the effect of surrounding active solvent molecules on the hydrogen bonding interactions of the complex. Subsequently, vibrational frequency analyses were performed to ascertain that optimized structures were real minima.

The spectral behavior of *p*-TsABDI has been investigated computationally in solvents having a wider polarity range, as presented in Figure 3.2 employing TDDFT/CAM-B3LYP/TZVP level of theory. As demonstrated in Figure 3.2 and Table 3.1, *p*-TsABDI exhibits one prominent absorption band and two emission bands in all the polar solvents. From the Table 3.1 it has been noted that, in polar solvents such as acetonitrile ($CH_3CN$), dimethylsulfoxide (DMSO), chloroform ($CHCl_3$), methanol ($CH_3OH$), and water ($H_2O$), *p*-TsABDI exhibits an absorption peak, which is comparable with the previously reported experimentally observed values.[231] The emission spectra of *p*-TsABDI, in contrast to the absorption spectra, are significantly reliant on the solvents (Figure 3.2 and Table 3.1). According to the spectral analyses (Figure 3.2 and Table 3.1), it has been observed that for $CH_3CN$ and DMSO the predominant emission peak is located at 427 and 423 nm, while the weak fluorescence is centered at 547 and 543 nm, respectively, results that are comparable with the experimental results at this wavelength. Further, the major emission peaks for polar solvents $CHCl_3$, $CH_3OH$, and $H_2O$ appeared at 429, 448, and 424 nm, whereas the minor peaks are observed at 544 nm ($CHCl_3$), 552 nm ($CH_3OH$), and 581 nm ($H_2O$), respectively. Thus, the agreement between the experimental and simulated excitation and emission results suggests that the TDDFT approach, along with the long-range corrected exchange-correlation hybrid functionals CAM-B3LYP using the TZVP basis set and IEFPCM solvation model, provides an accurate explanation of the optical properties of chromophores during electronic excitations.

Moreover, in recent years, TDDFT has become an effective framework for describing the optical spectra of the organic chromophores, and it has been demonstrated to be specifically effective at describing the electronic excitation of the systems containing transition metals, first and second row elements.[258, 259] Also, to describe the long-range charge-transfer states, we considered CAM-B3LYP functional[260] since other functionals (B3LYP, mPW1PW91, $\omega$B97XD, etc.) fail to describe it and considerably overestimate the excitation energies of the complex with much deviation. Further evidence for the TDDFT calculations comes from the detailed comparison

of the experimental[145, 261, 262] and computational excitation energies of the GFP chromophore (*p*-HBDI) in its neutral, anionic, and cationic forms, as presented in Table A1 and Figure A1 of Appendix A. These calculated $\lambda_{abs}$ and $\lambda_{emis}$ results are in reasonable agreement with the previously reported experimental data.[145, 261, 262] As a result, this approach was believed to be a promising tool to treat the biological processes in their excited-state in different environments, and hence, are suitable for further investigations of *p*-TsABDI in various polar solvents.

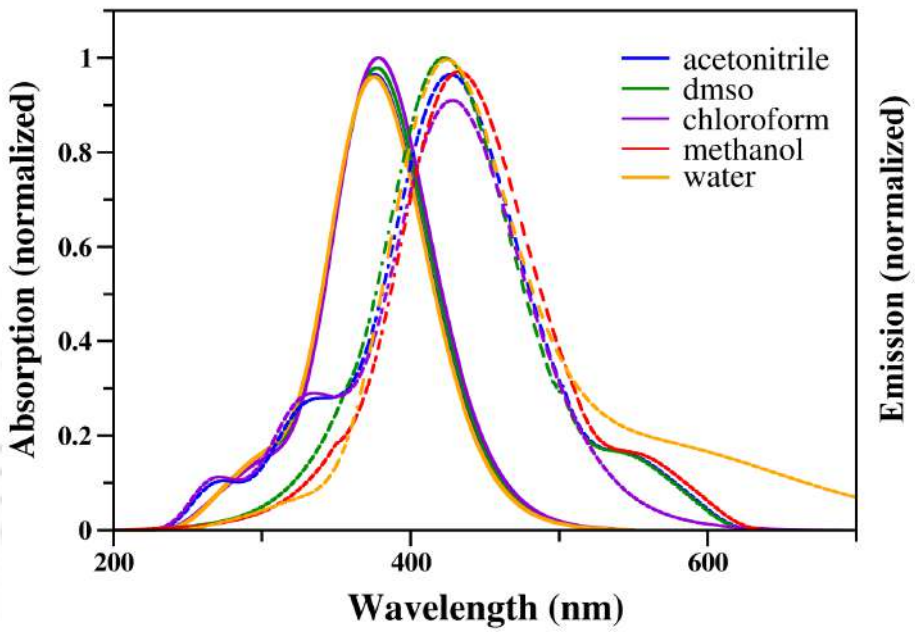


**Figure 3.2:** Simulated absorption (solid) and emission (dotted) spectra of *p*-TsABDI in polar solvents acetonitrile (blue), dimethylsulfoxide (green), chloroform (purple), methanol (red), and water (orange) computed at the TDDFT/CAM-B3LYP/TZVP theoretical level using the IEFPCM model.

**Table 3.1:** Vertical excitation energy (nm), emission energy (nm), and the corresponding oscillator strength ($f$) for transitions of $p$-TsABDI chromophore analogue in polar solvents computed at the TDDFT/CAM-B3LYP/TZVP level of theory using the IEFPCM model. The value in brackets indicates the dielectric constant of the corresponding solvent.

| **Solvent** | $\lambda_{max}{}^{abs}$ (nm) | | | $\lambda_{max}{}^{flu}$ (nm) | | |
|---|---|---|---|---|---|---|
| | **Calc.** | **Expt.**[231] | ***f*** | **Calc.** | **Expt.**[231] | ***f*** |
| **$CH_3CN$** ($\epsilon$=35.7) | 376 | 372 | 0.91 | 427<br>547 | 437<br>512 | 0.83<br>0.15 |
| **DMSO** ($\epsilon$=46.9) | 378 | 378 | 0.92 | 423<br>543 | 425<br>520 | 0.86<br>0.13 |
| **$CHCl_3$** ($\epsilon$=4.8) | 379 | —[a] | 0.94 | 429<br>544 | —[a] | 0.80<br>0.14 |
| **$CH_3OH$** ($\epsilon$=32.6) | 376 | —[a] | 0.90 | 448<br>552 | —[a] | 0.83<br>0.10 |
| **$H_2O$** ($\epsilon$=78.4) | 375 | —[a] | 0.90 | 424<br>581 | —[a] | 0.85<br>0.13 |

[a] **Experimental data not available**

In an effort to define the dual fluorescence in the $p$-TsABDI analogue in the polar media and the reason behind this interesting phenomenon, we tried to explore several aspects playing significant roles. The possible reason for the compound showing the dual emission behavior could be the polarity of the solvents. So, to have an insight into this intriguing dual fluorescence phenomenon and a better representation of the solvent effects, we designated the $p$-TsABDI analogue as its neutral and anionic forms, respectively, and used microsolvation hydration models to explicitly include hydrogen bond effects in quantum chemical calculations. An implicit solvent model poorly describes the electronic characteristics of the hydrogen bonding interactions between the solute and solvents by demonstrating the solvents as a polarizable medium with a specific dielectric constant. Also, explicit models are always size-limited and fail to adequately take into consideration the long-range (or bulk) effects. However, for the most part, a quantum mechanics/molecular mechanics (QM/MM) level is considered to account for bulk solvation on the proton shuttle mechanism in the chromophore, [263, 264] thus providing a reliable description of the solvent effects, but it requires an expensive computation. So, we implemented distinct quantum mechanical (QM) microsolvation augmented with a continuum approach,[265, 266] which enhances the

description of solute-solvent interactions that are cost-effective and represents a good approximation of the solvent effects.[255, 256] Hence, a combined microsolvation continuum model was employed to systematically investigate and improve the description of specific solute-solvent interactions coupled to the bulk effects.

In the present work, we have explicitly included three, four, and five solvent molecules which may significantly interact with the *p*-TsABDI chromophore, with an emphasis on trends of electron affinities influenced by microsolvation. In order to elucidate the mechanistic aspect of the proton transfer pathway, we computed the energy barriers incorporating the hydrogen bond interactions between the *p*-TsABDI analogue and solvent molecules, considering three, four, and five solvent molecules, following the same strategy as by Smith *et al.*[267] In each case, the benzylidene group of the chromophore acts as the proton donor while the imidazolinone moiety acts as a proton acceptor during the process. Figure 3.3 illustrates the energy profiles obtained from the converged stationary points for the neutral states, transition states, and anionic structures computed for three, four, and five solvent models. The proton transfer energy barrier is plotted relative to the optimized energy of the neutral form, and in each case, a single barrier has been observed. It is apparent from Figure 3.3 that for *p*-TsABDI analogue in water solvent the three-solvent model has a lower energy barrier of 18.75 kcal/mol and a faster process than the four and five solvent models with PT energy barrier of 20.75 kcal/mol and 21.20 kcal/mol, respectively. Similarly, the PT process is comparatively more feasible for three-solvent model in methanol solvent. Therefore, in this work, the results of the three-solvent model have been considered for further investigation to explain the ESIPT mechanism of *p*-TsABDI in solvent molecules. Again, since the entire structural studies of the *p*-TsABDI analogue in various polar solvents are far too costly at both the quantum mechanical level and dynamic simulation studies, therefore, we considered the structures in the polar solvents water and methanol to understand the influence of surrounding solvent molecules.

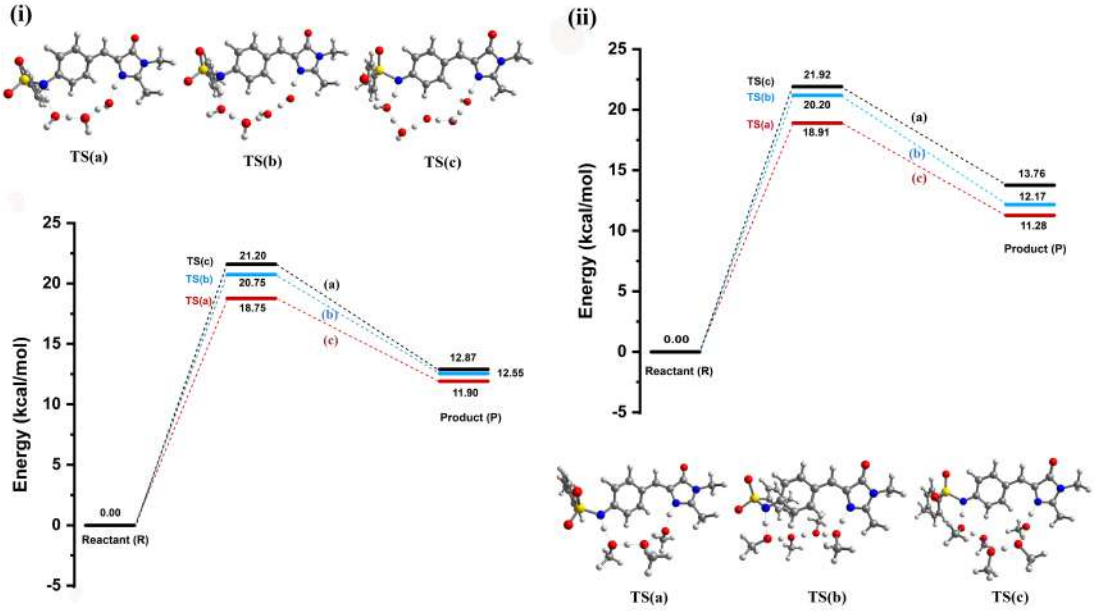


**Figure 3.3:** Potential energy profiles for three (a), four (b), and five (c) solvent model of *p*-TsABDI in (i) water and (ii) methanol solvent.

The chromophore forms an intermolecular H-bonding with the solvent molecules, as depicted by dotted lines in Figure 3.1 to form *p*-TsABDI-(solvent)$_3$ complexes with the labeled numbered atoms involved in the proton transfer (PT) mechanism. Figure 3.1 also illustrates the covalent and intermolecular hydrogen bond distances of *p*-TsABDI-$(H_2O)_3$ and *p*-TsABDI-$(CH_3OH)_3$ complexes. It has been observed that the benzylidene ring of the chromophore behaves as a proton donor in the complexes, whereas the imidazolinone ring behaves as a proton acceptor. The important structural parameters for the complexes *p*-TsABDI-$(H_2O)_3$ and *p*-TsABDI-$(CH_3OH)_3$ in $S_0$ and $S_1$ states involved during the PT activities are summarized in Table 3.2 and Table 3.3. From Figure 3.1 and Table 3.2, the optimized geometries of *p*-TsABDI-$(H_2O)_3$ and *p*-TsABDI-$(CH_3OH)_3$ complexes show the existence of intermolecular H-bonds R1 (H1···O1), R2 (H2···O2), R3 (H3···O3), and R4 (H4···O4) with the bond distances of 1.82, 1.79, 1.85, and 1.94 Å in $S_0$ state and 1.79, 1.78, 1.84, and 1.93 Å in $S_1$ state for *p*-TsABDI-$(H_2O)_3$, respectively. Moreover, in the *p*-TsABDI-$(CH_3OH)_3$ complex, the bond distances of the four intermolecular hydrogen bonds are 1.86, 1.77, 1.79, and 1.98 Å in the $S_0$ state and 1.84, 1.75, 1.78, and 1.88 Å in the $S_1$ state.

**Table 3.2:** Calculated Bond Distances (Å) involved in intermolecular hydrogen bonding of *p*-TsABDI-$(H_2O)_3$ and *p*-TsABDI-$(CH_3OH)_3$ complexes before and after PT processes obtained with DFT/B3LYP and TDDFT/CAM-B3LYP/TZVP levels using IEFPCM model in $S_0$ and $S_1$ states, respectively.

| Complexes | States | N1-H1 | R1[a] | O1-H2 | R2[b] | O2-H3 | R3[c] | O3-H4 | R4[d] |
|---|---|---|---|---|---|---|---|---|---|
| **Before PT** | | | | | | | | | |
| ***p*-TsABDI-$(H_2O)_3$** | $S_0$ | 1.03 | 1.82 | 0.98 | 1.79 | 0.98 | 1.85 | 0.98 | 1.94 |
| | $S_1$ | 1.04 | 1.79 | 0.99 | 1.78 | 0.99 | 1.84 | 0.99 | 1.93 |
| ***p*-TsABDI-$(CH_3OH)_3$** | $S_0$ | 1.03 | 1.86 | 0.98 | 1.77 | 0.98 | 1.79 | 0.98 | 1.98 |
| | $S_1$ | 1.04 | 1.84 | 0.99 | 1.75 | 0.99 | 1.78 | 0.99 | 1.88 |
| **After PT** | | | | | | | | | |
| ***p*-TsABDI-$(H_2O)_3$** | $S_0$ | 1.78 | 0.99 | 1.74 | 0.99 | 1.71 | 0.99 | 1.74 | 1.04 |
| | $S_1$ | 1.84 | 0.98 | 1.75 | 0.98 | 1.72 | 0.98 | 1.78 | 1.03 |
| ***p*-TsABDI-$(CH_3OH)_3$** | $S_0$ | 1.80 | 0.99 | 1.71 | 0.99 | 1.69 | 0.99 | 1.71 | 1.04 |
| | $S_1$ | 1.85 | 0.98 | 1.73 | 0.98 | 1.71 | 0.98 | 1.76 | 1.03 |

[a]R1 = $H_1\cdots O_1$, [b]R2 = $H_2\cdots O_2$, [c]R3 = $H_3\cdots O_3$, and [d]R4 = $H_4\cdots N_2$

The calculated bond distances as shown in Table 3.2 demonstrate that N1-H1 bond in both the complexes *p*-TsABDI-$(H_2O)_3$ and *p*-TsABDI-$(CH_3OH)_3$ marginally increases from 1.03 Å ($S_0$) to 1.04 Å ($S_1$). Furthermore, the other covalent bonds O1-H2, O2-H3, and O3-H4 in the complex *p*-TsABDI-$(H_2O)_3$ show an increase in bond distance value from 0.98 Å ($S_0$) to 0.99 Å ($S_1$). Similarly, in *p*-TsABDI-$(CH_3OH)_3$ complexes, the corresponding bond distances shows similar changes. The hydrogen bond distances R1, R2, R3, and R4 , on the other hand, decrease from 1.82 Å ($S_0$) to 1.79 Å ($S_1$), 1.79 Å ($S_0$) to 1.78 Å ($S_1$), 1.85 Å ($S_0$) to 1.84 Å ($S_1$), and 1.94 Å ($S_0$) to 1.93 Å ($S_1$), respectively, in *p*-TsABDI-$(H_2O)_3$ complexes. Likewise, in *p*-TsABDI-$(CH_3OH)_3$ complexes, the intermolecular H-bonds R1, R2, R3, and R4 decrease from 1.86 Å ($S_0$) to 1.84 Å ($S_1$), 1.77 Å ($S_0$) to 1.75 Å ($S_1$), 1.79 Å ($S_0$) to 1.78 Å ($S_1$), and 1.98 Å ($S_0$) to 1.88 Å ($S_1$), respectively. Although there are no major and prominent changes in bond distances from the $S_0$ to the $S_1$ states, the tendency of increasing or decreasing bond distance is noted.

Simultaneously, the conjugated bonds of the chromophore of *p*-TsABDI analogue in polar solvents undergo a change in the electronic excited-state upon photoexcitation. Table 3.3 compiles the computed structural changes in the bond distances of the chromophore of *p*-TsABDI from the $S_0$-state to the $S_1$-state. The computed

central C4-C7 and C7-C8 bond distances were observed to be 1.46 and 1.36 Å for *p*-TsABDI-$(H_2O)_3$, and 1.45 and 1.36 Å for *p*-TsABDI-$(CH_3OH)_3$ complex in $S_0$ state, indicating that the typical single and double bond characters. However, upon photoexcitation, the corresponding C4-C7 (single) bond distance decreases to 1.41 Å and C7-C8 (double) bond distance increases to 1.43 Å for both *p*-TsABDI-$(H_2O)_3$ and *p*-TsABDI-$(CH_3OH)_3$ complexes, respectively. In additions, the substantial shortening of the C1-N1 bond distance from 1.43 Å in the $S_0$-state to 1.39 Å in the $S_1$-state for *p*-TsABDI-$(H_2O)_3$ complex and from 1.42 Å in the $S_0$-state to 1.39 Å in the $S_1$-state for *p*-TsABDI-$(CH_3OH)_3$ complex are the most notable change in the electronic structure. Moreover, the increase and decrease of the conjugated bond distances of the benzylidene and imidazolinone ring of the chromophore, as shown in Table A2 of Appendix A, suggest that the chromophore experiences a dramatic change upon photoexcitation. Thus, in the $S_1$ state, the shortening of intermolecular H-bonds (R1, R2, R3, and R4) strengthened it, with the simultaneous increase and decrease of the conjugated bonds in the chromophore, implying the involvement of ESIPT process relative to the $S_0$ state.

**Table 3.3:** Calculated conjugated bond distances (Å) of the chromophore for *p*-TsABDI-$(H_2O)_3$ and *p*-TsABDI-$(CH_3OH)_3$ complexes in $S_0$ and $S_1$ states, respectively, involved during the photoexcitation obtained with DFT/B3LYP and TDDFT/CAM-B3LYP/TZVP theoretical accuracies using IEFPCM solvation model.

| **Bond Lengths (Å)** | **States** | ***p*-TsABDI-$(H_2O)_3$** | ***p*-TsABDI-$(CH_3OH)_3$** |
|---|---|---|---|
| **C4-C7** | $S_0$ | 1.46 | 1.45 |
| | $S_1$ | 1.41 | 1.41 |
| **C7-C8** | $S_0$ | 1.36 | 1.36 |
| | $S_1$ | 1.43 | 1.43 |
| **C1-N1** | $S_0$ | 1.43 | 1.42 |
| | $S_1$ | 1.39 | 1.39 |

Furthermore, after PT, the hydrogen bond distances R1, R2, R3, and R4 in the *p*-TsABDI-$(H_2O)_3$ complex subsequently decrease from 0.99Å ($S_0$) to 0.98 Å ($S_1$), 0.99 Å ($S_0$) to 0.98 Å ($S_1$), 0.99 Å ($S_0$) to 0.98 Å ($S_1$), and 1.04 Å ($S_0$) to 1.03 Å ($S_1$), respectively, as demonstrate in Table 3.2. Similarly, the corresponding bond distances (i.e., R1, R2, R3, and R4) in the *p*-TsABDI-$(CH_3OH)_3$ complex shows similar trend. This reveals that upon photoexcitation, the PT process may occur more efficiently

in the $S_1$ state,[268–273] along the hydrogen bond N1-H1···O1 than in the $S_0$ state. Thus, the PT processes of *p*-TsABDI analogue in polar solvents are initiated by the intermolecular H-bonding wire formation in $S_0$ with three solvent molecules, followed by the generation of an excited-state complex upon photoexcitation. Proton transfer proceeds via hydrogen bonding N1-H1···O1 with low-potential energy barrier in $S_1$ state, resulting in the formation of *p*-TsABDI-(solvent)$_3$-PT complexes. Finally, the *p*-TsABDI-(solvent)$_3$-PT complex returns to its $S_0$ state via radiative emission. As demonstrated by the data explained above, we can conclude that photoexcitation induces the lengthening of the covalent bonds in the electronic excited state, subsequently strengthening the intermolecular H-bonds. Consequently, the conjugated bonds of the *p*-TsABDI chromophore, as demonstrated in Figure 3.1 and Table 3.3, experiences a change in the electronic structure in the excited state ($S_1$) upon photoexcitation. Thus, the above explanation represents the strong evidence for the occurrence of excited state intermolecular proton transfer (ESIPT) phenomena in the compound.

The weakening or strengthening of covalent and intermolecular hydrogen bonds in $S_0$ and $S_1$ states are furthermore evaluated by vibrational frequency analysis of the optimized complexes. Figure 3.4 and Table 3.4 represents the N1-H1 and O3-H4 stretching vibrational frequencies for *p*-TsABDI-$(H_2O)_3$ and *p*-TsABDI-$(CH_3OH)_3$ complexes in $S_0$ and $S_1$ states. The computed N1-H1 stretching vibration in $S_0$ and $S_1$ states for *p*-TsABDI-$(H_2O)_3$ complex occurs at 3162 and 3093 $cm^{-1}$, respectively, whereas O3-H4 stretching modes in the $S_0$-state and $S_1$-state are located at 3435 and 3427 $cm^{-1}$, respectively. This small red-shift in vibrational frequencies for N1-H1 and O3-H4 stretching modes (Figure 3.4 and Table 3.4) supports the weakening of N1-H1 and O3-H4 bonds with the simultaneous strengthening of intermolecular hydrogen bonds (i.e., H1···O1 and H4···N2) in $S_1$ state. Similarly, for *p*-TsABDI-$(CH_3OH)_3$ complex, the N1-H1 stretching vibrational modes are observed at 3230 and 3195 $cm^{-1}$ in $S_0$ and $S_1$ states with a smaller red-shift of 35 $cm^{-1}$. Moreover, the O3-H4 vibrational modes in $S_0$ and $S_1$ states for *p*-TsABDI-$(CH_3OH)_3$ complex are observed at 3443 and 3360 $cm^{-1}$, respectively, with a red-shift of 83 $cm^{-1}$, indicating the strengthening of intermolecular H-bonds (i.e., H1···O1 and H4···N2) in the $S_1$ states. As a result of the above discussion, it has been observed that, in the $S_1$ state, the IR spectra of *p*-TsABDI with protic solvent shifts to lower frequencies than in the $S_0$ state, thereby strengthening the intermolecular H-bonds.

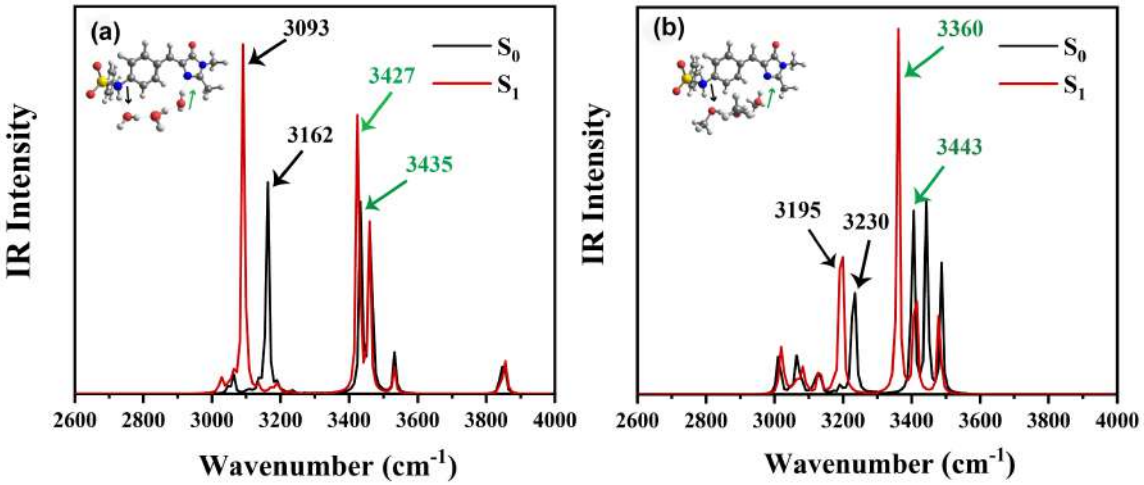


**Figure 3.4:** Simulated IR spectra of (a) *p*-TsABDI-$(H_2O)_3$ and (b) *p*-TsABDI-$(CH_3OH)_3$ complexes for N1-H1 and O3-H4 stretching modes in $S_0$ (black) and $S_1$ (red) states. The stretching vibrational frequencies were calculated at DFT and TDDFT/CAM-B3LYP/TZVP level using IEFPCM model and N1-H1 and O3-H4 stretching bands are labeled in black and green arrows, respectively.

**Table 3.4:** Vibrational frequencies ($cm^{-1}$) of of N1-H1 and O3-H4 stretching modes for *p*-TsABDI-$(H_2O)_3$ and *p*-TsABDI-$(CH_3OH)_3$ complexes involving PT process in $S_0$ and $S_1$ states

| **Vibrational Frequencies** | **States** | **Wavenumber($cm^{-1}$)** | |
|---|---|---|---|
| | | ***p*-TsABDI-$(CH_3OH)_3$** | ***p*-TsABDI-$(CH_3OH)_3$** |
| **N1-H1 Stretching** | $S_0$ | 3162 | 3230 |
| | $S_1$ | 3093 | 3195 |
| $\Delta V$ | | 69 | 35 |
| **O3-H4 Stretching** | $S_0$ | 3435 | 3443 |
| | $S_1$ | 3427 | 3360 |
| $\Delta V$ | | 8 | 83 |

A comprehensive analysis of the electron distributions over the compound has been carried out to reveal an insight into the ESIPT phenomenon caused by photoexcitation with significant changes in the electron density from proton donating to proton accepting groups. Therefore, the frontier molecular orbitals (FMOs) of the compound in polar solvents have been calculated and illustrated in Figure 3.5 to explain the characteristics of electron distribution over the atoms in an electronic excited-state. As illustrated in Figure 3.5, during the electronic transitions, the electron cloud is entirely delocalized on the chromophore in both the highest occupied

molecular orbital (HOMO) and the lowest unoccupied molecular orbital (LUMO), which is attributed to the $\pi \rightarrow \pi^*$ electronic transitions with $\pi$ character of HOMO and $\pi^*$ character of LUMO. On the other hand, no electron density is distributed around the adjacent solvent molecules. This $\pi \rightarrow \pi^*$ electronic transition results in the PT process in the complex. However, the electron density distribution on N1-atom from benzylidene group of the chromophore decreases due to electronic transition from HOMO to LUMO, whereas around N2-atom of the imidazolinone group of the chromophore, the electron density distribution increases significantly causing more acidity to the N1-atom and basicity to the N2-atom of the chromophore, respectively. Furthermore, minor transitions with very low oscillator strength ($f$) less than 0.001 might also occur from the lower level of HOMO to LUMO during the ESIPT process, which corresponds to the n $\rightarrow \pi^*$ character. Thus, FMO analysis suggests that photoexcitation causes the redistribution of electron density over the atoms, which results in the PT process by strengthening the intermolecular H-bonds.

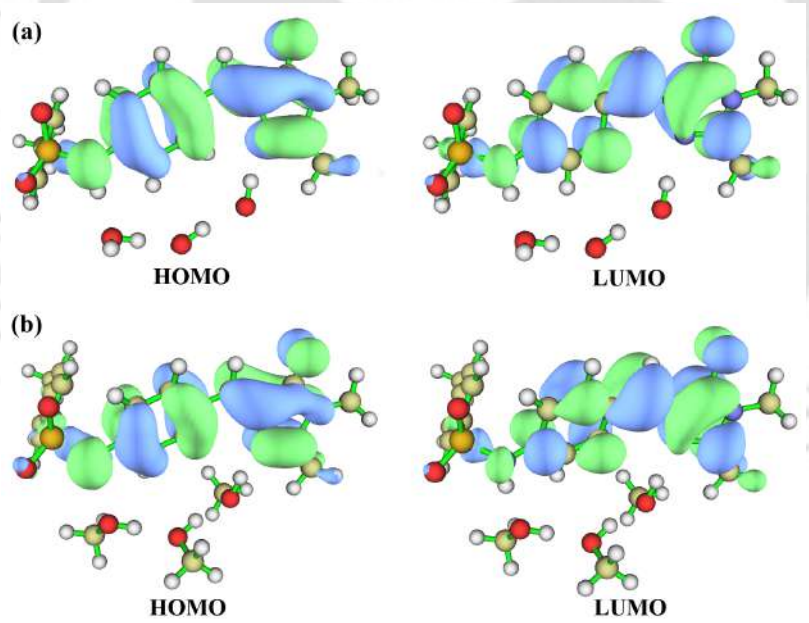


**Figure 3.5:** Frontier molecular orbital (FMOs) showing HOMO and LUMO for (a) *p*-TsABDI-$(H_2O)_3$ and (b) *p*-TsABDI-$(CH_3OH)_3$ complexes that has the major contribution of the wavefunction in the $S_1$ state. The FMOs were computed at CAM-B3LYP/TZVP level using IEFPCM model.

### 3.3.2 Potential Energy Profiles

To assess the occurrence of the ESIPT phenomena of the *p*-TsABDI analogue in the presence of polar solvents, we computed the potential energy curves (PECs) for

the PT pathways from the benzylidene moiety of the chromophore to its imidazolidinone moiety employing DFT and TDDFT approaches with the CAM-B3LYP/TZVP/IEFPCM level of theoretical accuracy in ground- and excited states. Despite the fact that the TDDFT/CAM-B3LYP computed level is unlikely to be precise enough to overcome the correct ordering of the closely spaced excited-states, a majority of the prior research had shown that the method is usually dependable while analyzing the reaction pathways as well as the potential barriers in ESIPT processes.[274] Figure 3.6 depicts the PECs that determine the PT pathway coordinates of $S_0$ and $S_1$ for *p*-TsABDI in water and methanol solvents, and Table 3.5 summarizes the value of relative PT energy barriers ($\Delta V$) and relative reaction energies ($\Delta E$) in $S_0$ and $S_1$ states, respectively. The PT barrier ($\Delta V$) of the complexes is obtained from the difference in the energy of the highest point relative to the energy of the lowest point on PECs [$\Delta V$ = E (highest point on PECs) - E (lowest point on PEC)] for $S_0$ and $S_1$ states, whereas the reaction energy ($\Delta E$) of the complexes is provided by computing the zero-point energy differences (ZPE) of the optimized complexes before and after the PT process [$\Delta E$ = ZPE (after PT) - ZPE (before PT)].

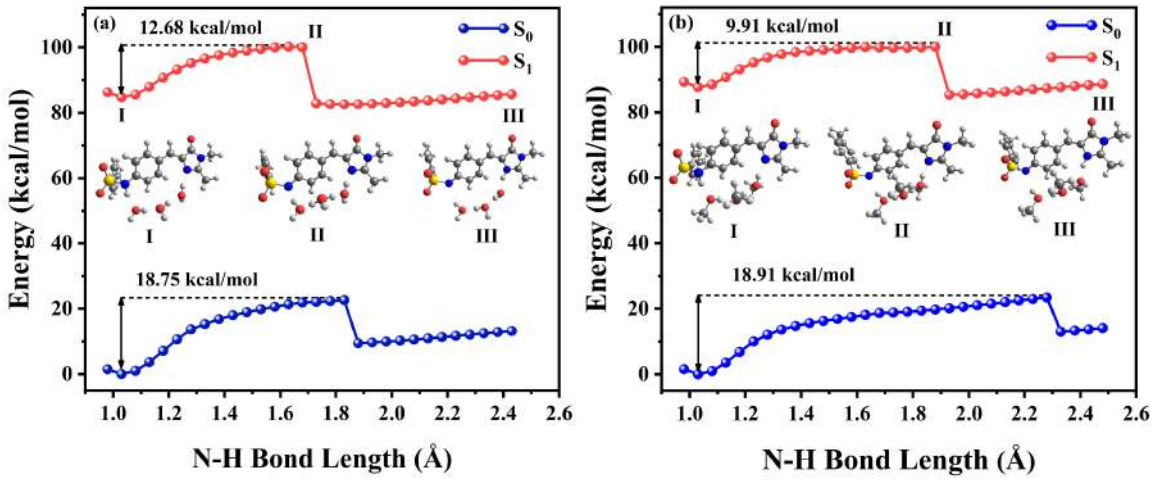


**Figure 3.6:** Potential energy profiles of (a) *p*-TsABDI-$(H_2O)_3$ and (b) *p*-TsABDI-$(CH_3OH)_3$ complexes in $S_0$ and $S_1$ states along the PT coordinate were calculated with CAM-B3LYP/TZVP level of theoretical accuracy using IEFPCM model.

**Table 3.5:** Summary of the PT energy barrier (ΔV) and Reaction Energies (ΔE) on $S_0$ and $S_1$ states for each complexes, respectively.

| Complex | ΔV (kcal/mol) | | ΔE (kcal/mol) | |
|---|---|---|---|---|
| | $S_0$ | $S_1$ | $S_0$ | $S_1$ |
| ***p*-TsABDI-$(H_2O)_3$** | 18.8 | 12.7 | 11.2 | 1.1 |
| ***p*-TsABDI-$(CH_3OH)_3$** | 18.9 | 9.9 | 11.6 | 1.0 |

Figure 3.6 and Table 3.5 reveal that the PT barriers of *p*-TsABDI-$(H_2O)_3$ and *p*-TsABDI-$(CH_3OH)_3$ complexes are high, i.e., 18.8 and 18.9 kcal/mol, respectively, in the $S_0$-state, and are more endothermic (i.e., ΔE are 11.2 kcal/mol and 11.6 kcal/mol, respectively) to enable the proton transfer process. While upon photoexcitation, the PT energy barrier for both *p*-TsABDI-$(H_2O)_3$ and *p*-TsABDI-$(CH_3OH)_3$ complexes reduces to 12.7 and 9.9 kcal/mol, respectively, in the $S_1$-state. Moroever, for both *p*-TsADBI-$(H_2O)_3$ and *p*-TsADBI-$(CH_3OH)_3$ complexes the reaction energy is reduce from 11.2 kcal/mol ($S_0$) to 1.1 kcal/mol ($S_1$), and 11.6 kcal/mol ($S_0$) to 1.0 kcal/mol ($S_1$), respectively, resulting in the $S_1$-state being less endothermic than the $S_0$-state. As a result, the PT process is expected to take place in the $S_1$-state with a relatively smaller PT energy barrier and reaction energy as compared to the $S_0$-state of the complexes. In Figure 3.6, the potential energy curves (PECs) of *p*-TsABDI-$(H_2O)_3$ and *p*-TsABDI-$(CH_3OH)_3$ complexes were scanned by adjusting the N1-H1 bond distance, which is observed to follow a stepwise mechanism.[255] However, considering the detailed PECs alone, it is hard to ascertain whether the ESIPT process occurs in a concerted or sequential manner. Hence, the dynamics simulation in the subsequent section will reveal the ESIPT mechanism.

### 3.3.3 Reduced Density Gradient (RDG) Analysis

The reduced density gradient (RDG) analysis has been implemented to ensure and support the intermolecular H-bonding interactions that are observed to exist between *p*-TsABDI analogue and the surrounding solvent molecules, as noted in the previous sections. The gradient isosurface plot of the reduced density gradient (RDG) verses sign $(\lambda 2)\rho(r)$, as defined by Equation 3.1, in which sign $(\lambda 2)\rho(r)$ signifies the product between the sign of the second Hessian eigenvalues ($\lambda 2$) and total electron density $\rho(r)$, depicts the existence of H-bonding interactions and various non-covalent interactions. The scattering map and RDG isosurface of the *p*-TsADBI-$(H_2O)_3$ and

*p*-TsADBI-$(CH_3OH)_3$ complexes were generated by implementing the DFT approach along with CAM-B3LYP/TZVP method. The 2D and 3D RDG isosurfaces are provided with a coloured surface that signifies the strength of non-covalent interactions based on associated sign($\lambda 2$)$\rho$(r) values.

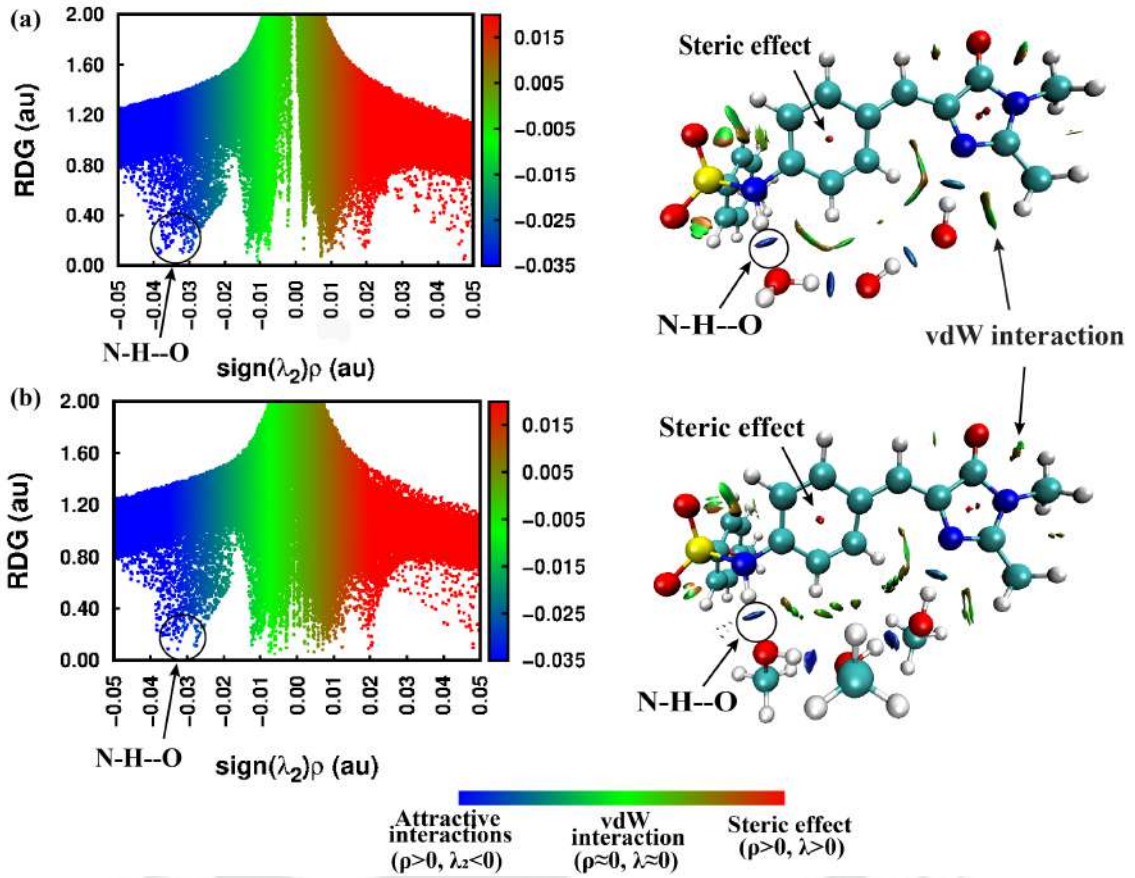


**Figure 3.7:** 2D-RDG scatter plots (left) and NCI isosurfaces (isovalue=0.5) (right) for the *p*-TsABDI compound corresponding to various type of interactions in polar solvent (a) water and (b) methanol. Sign($\lambda 2$)$\rho$(r) (au) values ranges from -0.05 to 0.05 au, and the isosurfaces are coloured accordingly. Blue color indicates the H-bonding interactions, whereas green and red color denotes van der Waals and steric interactions.

The RDG scattered plot represents the attractive interactions like H-bonding, dipole-dipole, halogen-bonds, and so on when the values of sign($\lambda 2$)$\rho$(r) is large and negative ($\rho$>0, $\lambda 2$<0), corresponding to the blue region of the 2D gradient isosurfaces. Whereas the interactions is steric if the value of sign($\lambda 2$)$\rho$(r) is large and positive ($\rho$>0, $\lambda 2$>0) depicted by the red region of the 2D gradient isosurfaces. van der Waals (vdW) interactions always have values near to zero ($\rho \approx 0$, $\lambda 2 \approx 0$) depicted by the green region of the RDG isosurface. Thus, to reveal the type of interactions and to ensure the existence of attractive interactions in between the chromophore

and solvent molecules, we employed the color scheme shown below to depict these functions and plotted on gradient isosurfaces. Figure 3.7 demonstrate the 2D reduced density scatter plots of the complexes *p*-TsABDI-$(H_2O)_3$ and *p*-TsADBI-$(CH_3OH)_3$ along with the 3D isosurfaces. Since Figure 3.7 displays spikes lying in between -0.02 to -0.05 au of sign$(\lambda 2)\rho(r)$ indicates attracti H-bonding which arises due to N–H $\cdots$ O, O–H $\cdots$ O, and O–H $\cdots$ N bonding interactions between the chomophore and solvent molecules. Conversely, there is also a spike lying at the positive values of the gradient map, ranging from 0.01 to 0.05 au, indicative of strong repulsive interactions (steric effect). The vdW interactions occur in the range of -0.01 to 0.01 au.

Subsequently, the color-filled 3D RDG isosurfaces (Figure 3.7, right) signify the type of interactions that exist in the complex. From Figure 3.7 (right, a and b), the four blue elliptical slabs are shown in between hydrogen and oxygen atoms, and in between hydrogen and nitrogen atoms in both the complexes the hydrogen bonding interactions are shown prevailing between the *p*-TsABDI analogue and solvent molecules. Moreover, the interaction regions marked by red and green circles in the isosurface can be identified as the existence of a steric effect within the rings and van der Waals interactions between the atoms of the molecules.

### 3.3.4 Schematic Representation for ESIPT

From the above static calculation analysis, we can conclude a mechanistic representation for the ESIPT process in the *p*-TsABDI analogue as shown in Figure 3.8. Figure 3.8 depicts the basic ESIPT process in the *p*-TsABDI analogue, which begins with photoexcitation of the ground-state neutral form E($S_0$) of the chromophore analogue resulting in the generation of an undissociated electronic excited-state E*($S_1$). Subsequently, the undissociated excited-state E*($S_1$) of *p*-TsABDI undergoes structural rearrangement as a consequence of the excited-state intermolecular proton transfer (ESIPT) phenomena, leading to a dissociated excited-state K*($S_1$). Eventually, the undissociated excited-state E*($S_1$) also returns to its ground-state E($S_0$) by releasing energy as luminescence. The dissociated excited-state K*($S_1$) then relaxes to its ground-state K($S_0$) emitting its energy through radiative and nonradiative transitions. As a consequence, as demonstrated in Figure 3.8, the anionic form of the analogue reverted to its neutral form via a reverse proton transfer process.

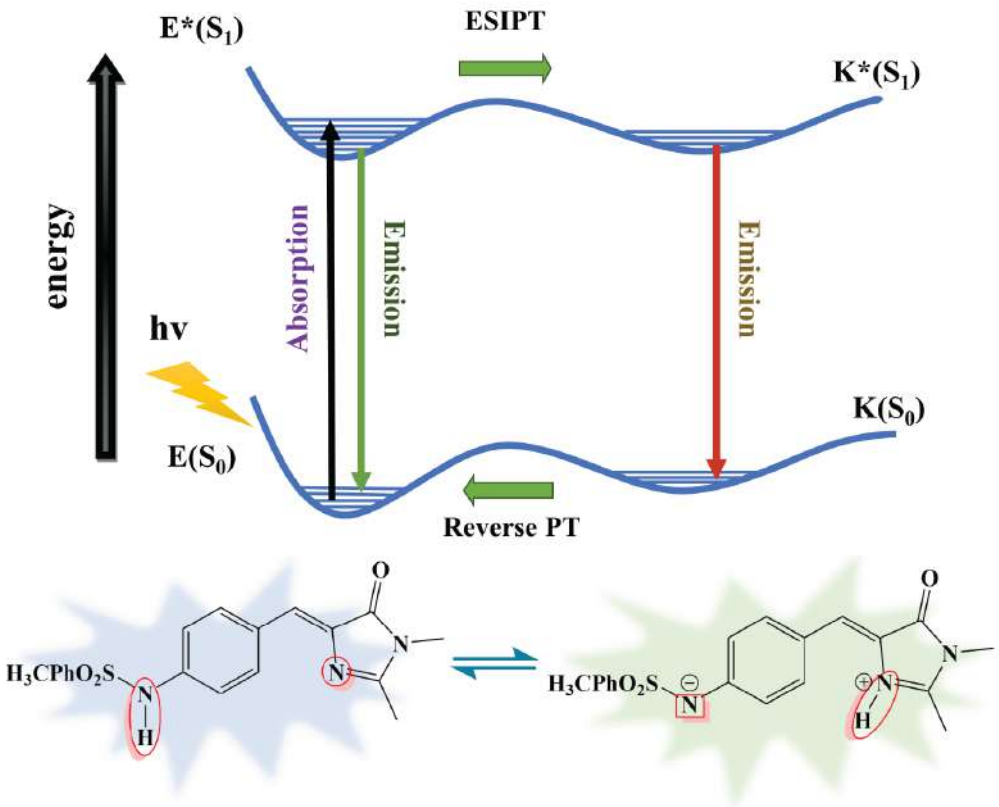


**Figure 3.8:** Schematic illustration for the mechanistic pathway for excited state intermolecular proton transfer (ESIPT) phenomenon of *p*-TsABDI in polar solvents.

### 3.3.5 Excited-State Dynamics Simulation

The dynamics calculations of the compound in polar solvents, water and methanol, i.e., *p*-TsABDI-$(H_2O)_3$ and *p*-TsABDI-$(CH_3OH)_3$, were performed at the TDDFT/CAM-B3LYP/6-31G(d,p) methods to investigate the PT mechanism. For each complex, 100 trajectories with different initial conditions of on-the-fly dynamics simulations were computed with simulation times of 300 fs to uncover the entire mechanism of PT processes and PT probability. The PT time can be defined as the point at which the breaking and forming of bond distances intersect within the given simulation time, averaged based on all active ESIPT trajectories.[254, 255] Depending on the time lag between two successive transfers of protons, the PT mechanism has been categorized as either a concerted or stepwise process.[275] The simulated trajectories for each complex *p*-TsABDI-$(H_2O)_3$ and *p*-TsABDI-$(CH_3OH)_3$ in the $S_1$-state were analyzed and categorized into (a) ESIPT and (b) NO PT. The ratio of the number of active ESIPT trajectories to the total trajectories has been used to determine the PT probability.

**Table 3.6:** Summary for the excited state intermolecular proton transfer (ESIPT) dynamics simulations of *p*-TsABDI chromophore analogue in the polar solvent computed at the TDDFT/CAM-B3LYP/6-31G(d,p) method: number of trajectories showing the PT process or NO PT, PT probability, and PT time, respectively.

| Complex | Reaction | | PT | PT time (fs) | | | |
|---|---|---|---|---|---|---|---|
| | ESIPT | NO PT | probability(%) | PT1 | PT2 | PT3 | PT4 |
| ***p*-TsABDI-$(H_2O)_3$** | 23 | 77 | 23 | 64.3 | 117.5 | 139.5 | 183.8 |
| ***p*-TsABDI-$(CH_30H)_3$** | 28 | 72 | 28 | 74.3 | 104.7 | 196 | 207.4 |

For *p*-TsADBI-$(H_2O)_3$ complexes, out of 100 trajectories, 23 trajectories underwent the ESIPT process through three water molecules, while 77 trajectories show no PT reactions during 300 fs of the simulation time (Table 3.6). Thus, the probability of PT in *p*-TsABDI-$(H_2O)_3$ is 23%, with 77% of trajectories exhibiting no PT process during the given simulation period. This probability of non-PT can be correlated with a considerable PT barrier of 12.68 kcal/mol for the *p*-TsABDI-$(H_2O)_3$ complex in its excited-state, as well as owing to the fact that these reactions are moderately endothermic in the $S_1$-state (Table 3.5 and Figure 3.6).

Figure 3.9(a) illustrates the details of snapshots showing the structural changes along the ESIPT process whereas Figures 3.9(b) and 3.9(c) represent typical trajectories generated for *p*-TsABDI-$(H_2O)_3$ complexes in accordance with the atom numbering scheme of Figure 3.1. Figure 3.9(b) represents the PT processes of the H1 and H2, whereas Figure 3.9(c) denotes the PT processes of H3 and H4 in the *p*-TsABDI-$(H_2O)_3$ complex. In additon, Figure 3.9(d) represents the time evolution of $S_0$ and $S_1$ relative energies, with no crossing between the states owing to the occurrence of the ESIPT mechanism.

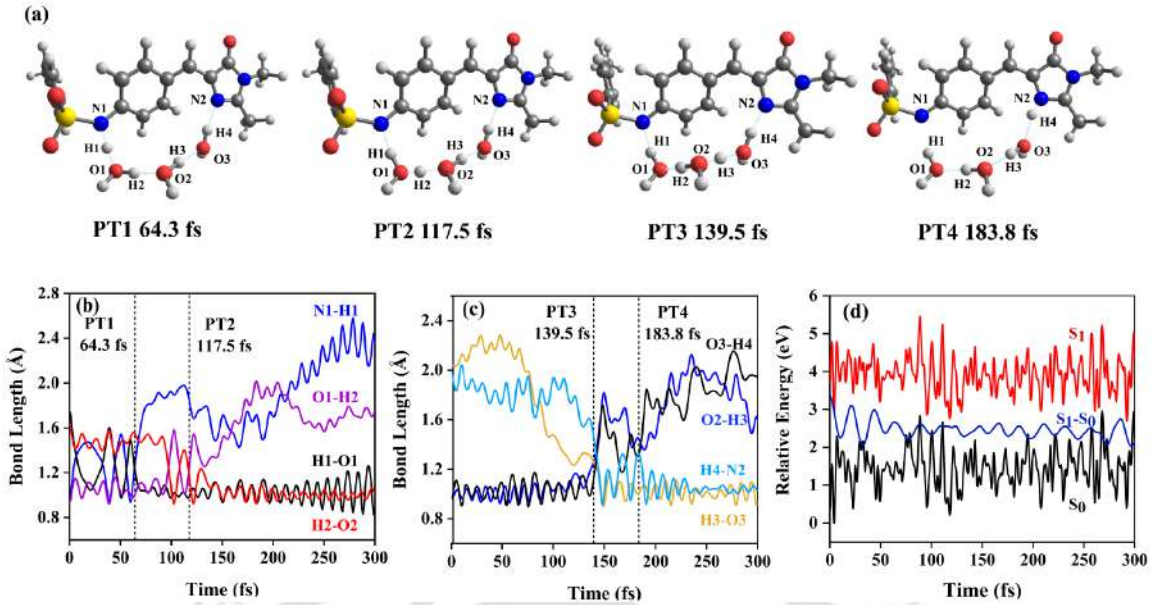


**Figure 3.9:** For the *p*-TsABDI-$(H_2O)_3$ complex in $S_1$ dynamics (a) snapshots along the ESIPT dynamics simulations at corresponding PT time, (b) time evolutions of average breaking (N1-H1 and O1-H2) and forming (H1-O1 and H2-O2) bond distances, (c) time evolutions of average breaking (O2-H3 and O3-H4) and forming (H3-O3 and H4-N2) bond distances, and (d) average relative energies of the $S_0$, $S_1$, and the relative energy difference ($S_1$-$S_0$) between them.

The following steps can be used to characterize the time evolution for the average bond-breaking and bond-forming process along the PT pathway, as demonstrated in 3.9(a). As represented in Figures 3.9(a)-(c), the first proton H1 (PT1) shifts from the N1-atom of the p-TsABDI analogue to the O1-atom (first water molecule) at 64.3 fs, followed by the transfer of the second proton H2 (PT2) from the O1-atom (first water molecule) to the O2-atom (second water molecule) in the complex at 117.5 fs. The third and fourth proton (H3 and H4) depart from the O2-atom (second water molecule) to the O3- atom (third water molecule), and the O3-atom (third water molecule) to the N2-atom of the *p*-TsABDI analogue at 139.5 and 183.8 fs, respectively, demonstrating the stepwise nature of the PT mechanism in the complex. If the time difference between the two consecutive PTs is shorter than the fluctuation period of 10-15 fs corresponding to the vibrational stretching modes of N-H and O-H hydrogen bonds, the PT occurs in a concerted manner, whereas the PT mechanism is stepwise if the time difference of two consecutive PTs is greater than the fluctuation period. Thus, the ESIPT mechanism can be considered to occur in a stepwise manner from the benzylidene moiety of the chromophore to its imidazolinone moiety in accordance with the time lag between all the PT processes. Additionally, Figure

3.9(d) shows that, as the simulation proceeds, the average difference in relative energy between $S_1$- and $S_0$-states begins to decrease. However, the energy still remains above 2 eV at the end of the PT process, indicating that there exists no crossing between the $S_0$- and $S_1$-states as a result of the ESIPT phenomenon and the structure of *p*-TsADBI-$(H_2O)_3$ tends to be planar approximately throughout the mechanism.

Again, Figures A2(a)-(c) of Appendix A depicts a similar event; i.e., all PT occurs in a stepwise manner. As a result, it confirms that PT processes occur in a stepwise manner from the benzylidene moiety of the chromophore to its imidazolinone moiety. Also, the average $S_1$-$S_0$ energy gap gradually decreases but remains above 2 eV after fluctuating substantially, as represented in Figure A2(d), indicating the planar structure of the complex *p*-TsABDI-$(H_2O)_3$ throughout the given simulation time.

Moreover, Figures 3.10(a)-(d) displays the typical trajectories that exhibits no PT during the simulation period.

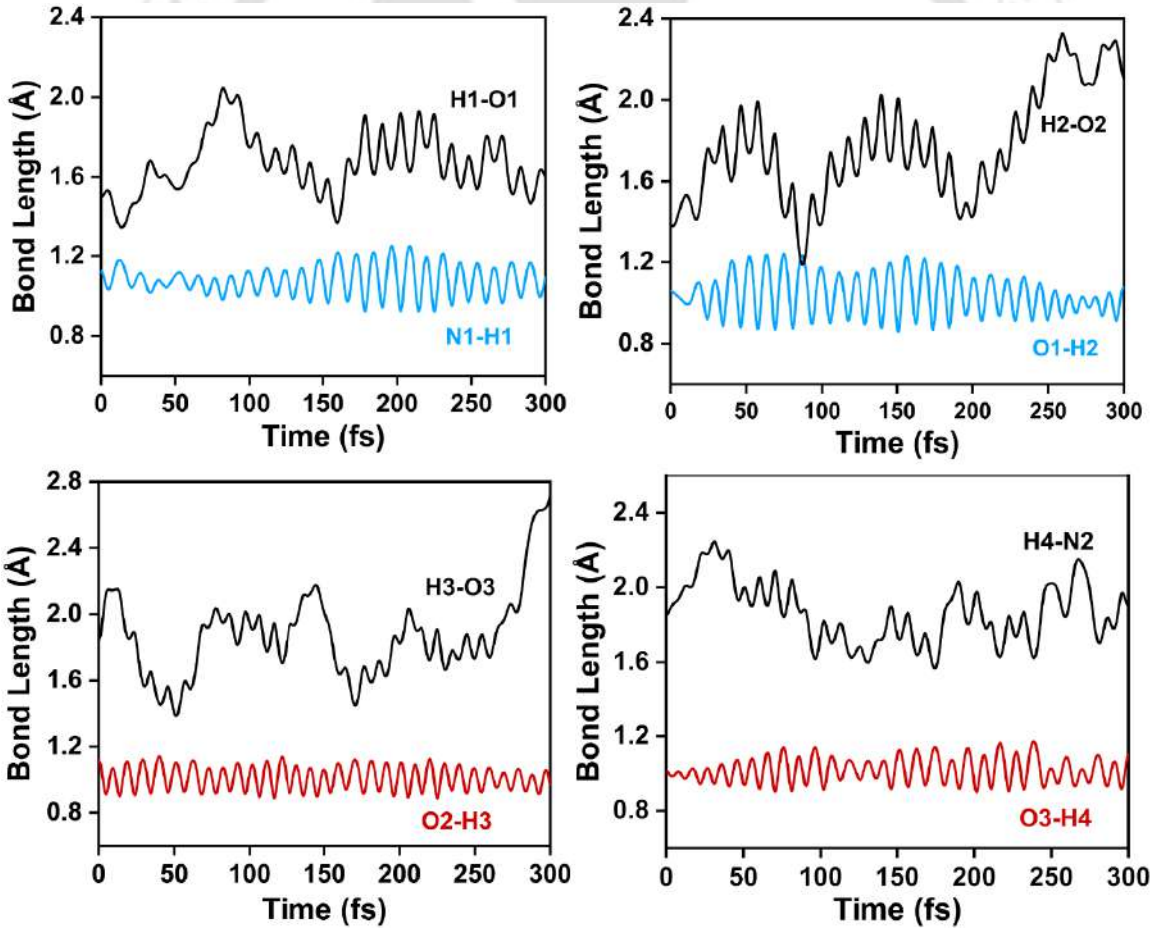


**Figure 3.10:** Time evolution of the breaking bond (N1-H1, O1-H2, O2-H3 and O3-H4) and forming bond (H1-O1, H2-O2, H3-O3 and H4-N2) in the $S_1$ state dynamics for the non-PT characteristics trajectories of the *p*-TsABDI-$(H_2O)_3$ complex at TDDFT/CAM-B3LYP/6-31G(d,p) level.

Similarly, for *p*-TsADBI-$(CH_3OH)_3$ complex, total of 28 (28%) trajectories show the occurrence of the ESIPT reaction via the methanol molecules in the inner shell, while the other 72 (72%) trajectories exhibit no ESIPT reaction during the simulation time of 300 fs. Figure 3.11(a) demonstrates the snapshots of the representative trajectory of proton transfer dynamics for the ESIPT process in *p*-TsABDI-$(CH_3OH)_3$, whereas Figure 3.11(b,c) displays the trajectories exhibiting the PT process. Figure 3.11d shows the time evolutions of the $S_0$- and $S_1$-state relative energies, demonstrating that ESIPT phenomena prevent them from crossing.

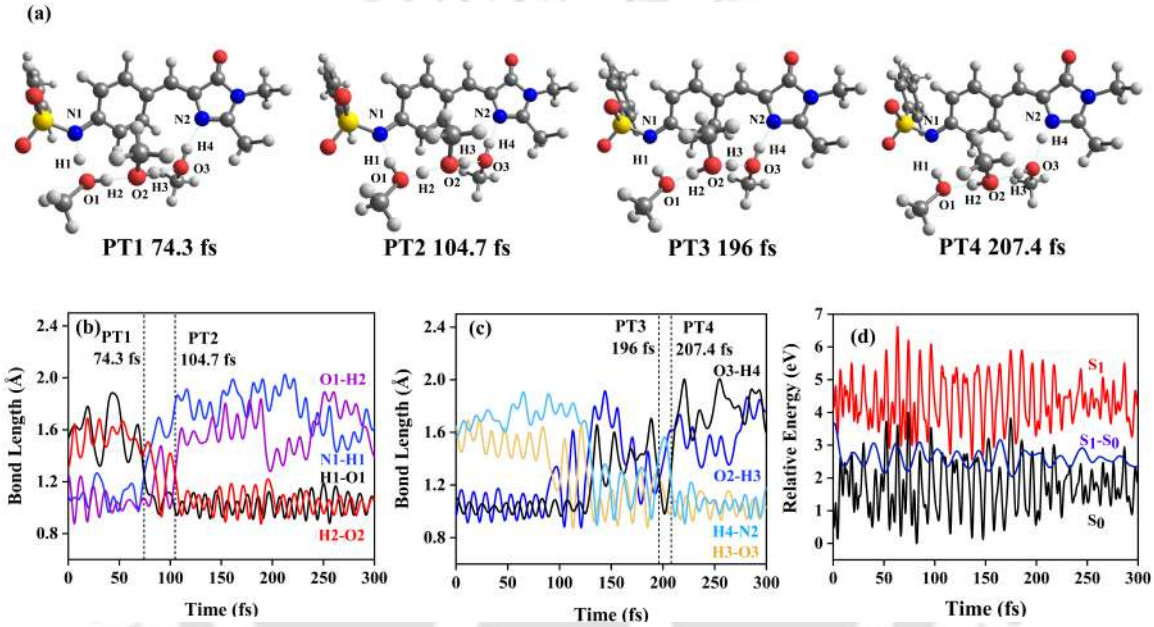


**Figure 3.11:** For the *p*-TsABDI-$(CH_3OH)_3$ complex in $S_1$ dynamics (a) snapshots along the ESIPT dynamics simulations at corresponding PT time, (b) time evolutions of average breaking (N1-H1 and O1-H2) and forming (H1-O1 and H2-O2) bond distances, (c) time evolutions of average breaking (O2-H3 and O3-H4) and forming (H3-O3 and H4-N2) bond distances, and (d) average relative energies of $S_0$, $S_1$, and the relative energy difference ($S_1$-$S_0$) between them.

From Figures 3.11(a)-(c), it has been observed that the first proton H1 (PT1) leaves from the benzylidene part of the chromophore, moving toward the O1-atom (first methanol molecule) at 74.3 fs, eventually followed by the movement of H2 (PT2) from the O2-atom (second methanol molecule) to the O3-atom (third methanol molecule) at 104.7 fs. The PT3 occurs at a time of 196 fs as the third proton H3 (PT3) transfers to the O4-atom (third methanol molecule). Finally, the H4-atom (PT4) transfers from the O4-atom (third methanol molecule) to the N2-atom of the imidazolinone part of the chromophore at 207.4 fs. Thus, there is a considerable time lag of 30.4 fs between PT1 and PT2, 91.3 fs between PT2 and PT3, and 11.4 fs

between PT3 and PT4, thus implying the stepwise nature of the ESIPT mechanism of the complex in the polar solvents.

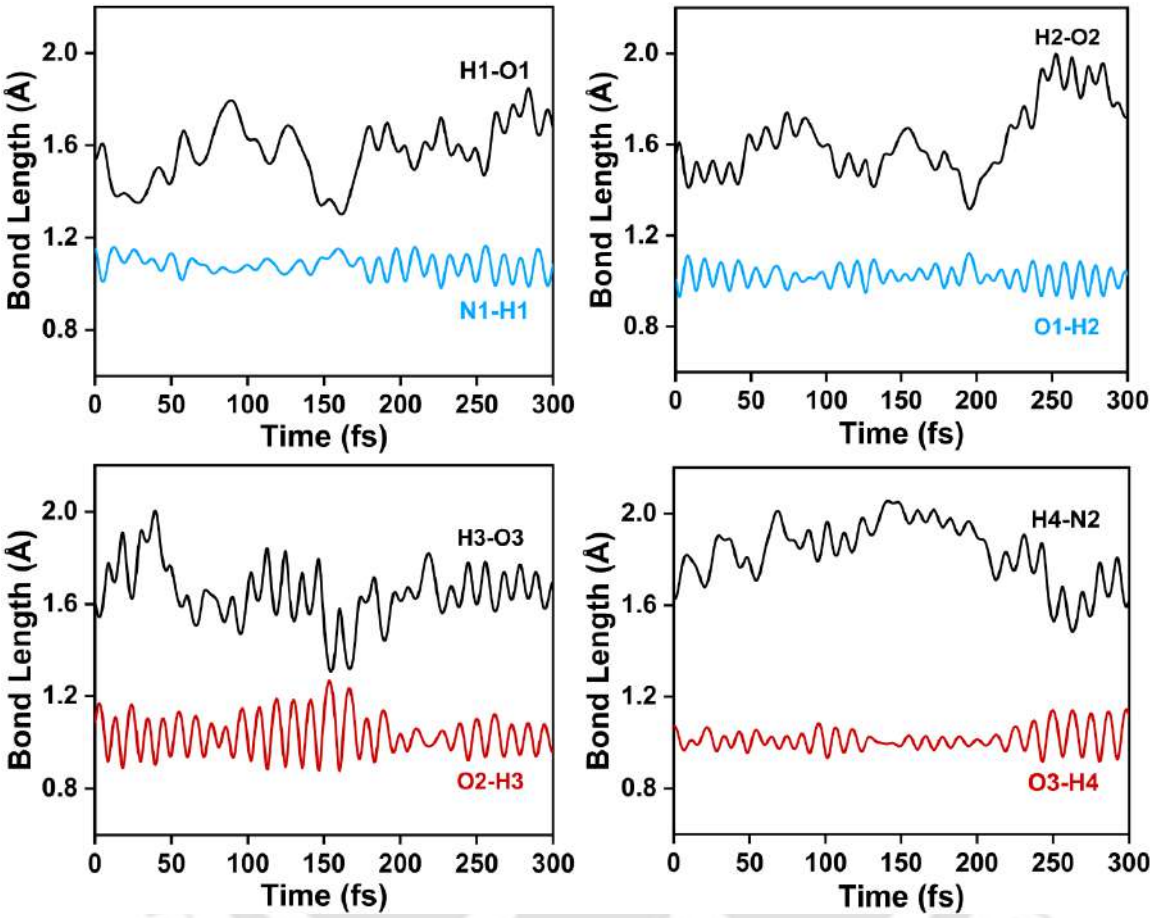


**Figure 3.12:** Time evolution of the breaking bond (N1-H1, O1-H2, O2-H3 and O3-H4) and forming bond (H1-O1, H2-O2, H3-O3 and H4-N2) in the $S_1$ state dynamics for the non-PT characteristics trajectories of the *p*-TsABDI-$(CH_2OH)_3$ complex at TDDFT/CAM-B3LYP/6-31G(d,p) level.

Furthermore, as the simulation proceeds, the average relative energy difference ($S_1$-$S_0$) gradually declines as shown in Figure 3.11(d), but remains above 2 eV after the completion of PT process, implying the occurrence of no crossings between $S_0$ and $S_1$ states and *p*-TsADBI-$(CH_3OH)_3$ complex structure tends to be planar throughout the process. Similarly, Figure A3 (Appendix A) characterizes the stepwise nature of the PT process for the *p*-TsABDI-$(CH_3OH)_3$ complex, while Figure 3.12 illustrates the typical trajectories that do not exhibit any PT transfer during the simulation time.

## 3.4 Conclusions

Photophysics of the para-sulfonamide (*p*-TsADBI) analogue of GFP chromophore that exhibits the unusual dual emissive characteristics in polar solvents have been investigated and probed by combination of quantum and dynamics simulation computational studies. To better understand the origin of this remarkable behavior, we have computed the *p*-TsABDI chromophore analogue in various polar solvents by employing DFT and TDDFT approaches along with the CAM-B3LYP/TZVP/IEFPCM level. The static calculations demonstrated that the *p*-TsABDI analogue undergoes structural rearrangement in the $S_1$-state upon photoexcitation, leading to the strengthening of intermolecular H-bonds (i.e., H1···O1, H2···O2, H3···O3, H4···O2 bonds) that occur. This induces an ultrafast excited-state intermolecular proton transfer (ESIPT) phenomenon in the complexes mediated by solvent molecules. The red-shift of N1-H1 and O3-H4 bond vibrational modes after the photoexcitation further supports the strengthening of H-bonds in the $S_1$-state. According to the PECs, the PT process is unfavorable in the $S_0$-state, whereas it proceeds in the $S_1$-state owing to the comparatively low PT energy barrier and endothermic reactions, signifying the existence of the ESIPT process. Moreover, the strength of hydrogen bonds as well as the occurrence of the ESIPT mechanism in the $S_1$-state is further substantiated by the excited-state dynamics simulation results performed at the TDDFT/CAM-B3LYP/6-31G(d,p) theoretical level. The analysis of the dynamics simulations provides an insight into the PT pathway in the $S_1$-state, as well as gives details on whether the PT mechanism occurs in a concerted or stepwise manner, as measured by their respective time constants. The results thus obtained from the excited-state investigations reveal that the ESIPT reactions are ultrafast, occurring in a stepwise manner in less than 300 fs via three solvent molecules forming a proton-wire pathway. Hence, we hope that the obtained information acquired from both the static calculations in conjunction with the dynamics simulations will pave a way for designing and synthesizing knowledge-based GFP chromophores with improved photophysical properties.

# Chapter 4

# Excited-State Relaxation Mechanisms via Z/E Isomerization in Para-Amino Substituted GFP Chromophore

(The work of this Chapter is published in *J. Chem. Phys.* **2025**, *163*, 054305.)

## 4.1 Introduction

The photoswitchable *cis-trans* behavior of the Green Fluorescent Protein (GFP) chromophore and its derivatives plays a pivotal role in the study of photochemical dynamics and paves the way for the engineering and development of photoreactive compounds.[118, 276–278] These *cis-trans* photoisomerization behaviors of GFP lead to the reversible switching between two distinct stable molecular configurations and are of high interest across various disciplines, with applications ranging from biology to materials science.[76, 119, 278, 279] Aside from this application, the photoswitching behavior of GFP and its derivatives has emerged as a promising technique for optical marking. [280, 281] Such efficient photoisomerization has also been suggested as a key mechanism in the photoswitching of some other photoactivatable fluorescent probes.[282–290] Recently, several investigations have been reported on the reversible photoswitching of GFP-like proteins at the single-molecule level, providing an exciting opportunity in optoelectronics and biological imaging, enabling the development of molecular-scale devices and the detection of rapid protein dynamics within living cells.[291–294] These exceptional light-controlled switching behaviors of GFP-like fluorescent proteins, toggling between a fluorescent "on-state" and nonfluorescent "off-state" or from one color to another, are driven by the rotation of exocyclic single and double bonds within the chromophore.[141, 280, 295] Studies have revealed that *cis-trans* photoisomerization in the chromophore precedes deprotonation and takes

place on the picosecond timescale.[155, 296] Consequently, this *cis-trans* photoisomerization of the neutral chromophore is vital for photoactivation and photoswitching processes of GFP-like chromophores.

Green Fluorescent Protein (GFP) from the jellyfish Aequorea victoria has proved to be one of the significant breakthroughs in scientific research fields.[76, 77, 80, 86, 297] Structural studies have identified that GFP adopts an 11-stranded $\beta$-barrel-like structure, enclosing the chromophore named p-hydroxybenzylideneimidazolinone (*p*-HBDI) at its core, with $\alpha$-helices at both ends.[88, 233] This chromophore is responsible for fluorescence in GFP.[88, 233] Fluorescence is emitted from both the neutral and anionic forms of the chromophore, *p*-HBDI, with the anionic form being generated via excited-state intramolecular proton transfer from the neutral form.[89, 94] Time-resolved spectroscopic investigations have demonstrated the excited-state lifetime of GFP lies in the order of nanoseconds, with a fluorescent quantum yield of 0.8.[76, 77, 89, 94, 101, 298] Nevertheless, fluorescence is quenched when the protein undergoes denaturation or when the chromophore is removed from its protein environment and the quantum yield decreases from 0.8 to $10^{-3}$ (for isolated chromophore).[93] Further, extensive investigation into the photophysical properties of most of the synthetic models GFP chromophore derivatives have been observed to be weakly fluorescent in solution and gas phases.[122–126, 144, 154, 155, 163, 218, 262, 299, 300] Several experimental and theoretical studies have revealed that the ultrafast fluorescence quenching mechanism in *p*-HBDI and its derivatives is associated with the excited state twisting process that leads to internal conversion.[122, 123, 125, 158, 159] The excited state twisting mechanism has been observed to proceed via two primary reaction pathways responsible for the decay mechanism in the p-HBDI chromophore, which involves the significant torsional motions of the exocyclic methine bridge bonds, i.e., either C-C (P) and/or the C=C (I) bond.[93, 158, 159] To achieve a high fluorescence quantum yield ($\Phi_f$) and prevent the nonfluorescent nature, it is important to effectively limit the torsional rotation of the P- and I- bonds in the chromophore.

The simultaneous rotation of the two methine bridge P- and I- bonds, referred to as the *hula-twist*,[157, 301] was initially considered the preferred deactivation pathway due to the limited sensitivity of the excited-state lifetime of the anionic form. However, several quantum-chemical and dynamics simulation studies highlighted that

the imidazolinone-bridged bond channel (I) is the dominant nonadiabatic decay pathway, while the phenol-bridged bond channel (P) contributes to about ∼30% of the total deactivation process.[121–123, 158, 302] It has also been noted that the chromophore (*p*-HBDI) experiences twisted intramolecular charge transfer between imidazolinone (I) and phenolate (P) moieties when the torsional rotations become more pronounced.[124, 126] The torsional dihedral rotation along the I- and P- bonds, denoted as $\Phi_I$ and $\Phi_P$, regulates the direction of the charge transfer process in the excited-state. While the rotation of the I-bonds facilitates the charge transfer from the imidazolinone group to the phenolate group, the rotation of the P-bonds induces charge transfer from the phenolate to the imidazolinone group.[158, 159] Furthermore, on-the-fly surface-hopping dynamics simulations in both the gas and condensed phases using extended multistate multireference second-order perturbation theory (XMS-CASPT2)[122] and high-level quantum mechanics/molecular mechanics (QM/MM) simulations implementing spin-flip time-dependent density functional theory,[160] have further provided strong evidence for this behavior. Martinez and co-workers further corroborate the findings that the excited-state ultrafast internal conversion predominantly proceeds via the I-twisted pathway, with a minor contribution from the competing P-twisted pathway.[158, 159] Over the years, extensive research has led to the synthesis and characterization of several derivatives of *p*-HBDI, exhibiting diverse photophysical properties such as spectral range, fluorescence quantum yield, and photoswitchable behavior.[163, 164, 216–219, 303–306] Notably, the para-amino derivative (*p*-ABDI or $NH_2$-HBDI) of the GFP chromophore was observed to be entirely nonfluorescent.[163, 219, 306]

A para-substituent N-phenyl-amino group has been observed to enhance the fluorescent quantum yield of GFP-like chromophores, which is attributed to "amino conjugation effects," and elevate the Z/E photoisomerization barriers.[219, 306] In contrast, the para-amino group (*p*-$NH_2$) in *p*-ABDI derivative was observed to increase the radiationless decay, thereby decreasing the fluorescence quantum yield.[219, 306] Chen and coworkers[219, 306] found that the *p*-$NH_2$ group engages in a "coherent photoinduced intramolecular charge transfer (ICT) effect" along with "amino conjugation effects" during the Z/E-photoisomerization process in *p*-ABDI. Although amino conjugation effects enhance excited-state stabilization and raise the Z/E photoisomerization barriers, the coherent photoinduced ICT effects pull down the Z/E

photoisomerization barriers[219, 306] in the *p*-ABDI derivative. Thus, the "coherent photoinduced ICT" effect outweighs the "amino conjugation effect" in the para-substituted amino group in the GFP-like chromophore, facilitating photoisomerization phenomena and consequently $S_1/S_0$ deactivation. The *p*-$NH_2$ group is likely to exhibit the same effect on other fluorophores. However, the effect of para-substituent amino groups on $\Phi_I$- and $\Phi_P$- torsional rotations, along with associated competing phenomena in GFP chromophore derivatives, remains poorly understood, and limited studies have been performed on dynamics simulations of the Z/E photoisomerization process. Hence, to address this and characterize the fluorescence-quenching effect, we investigated the photodynamics of the para-amino substituent of the GFP-like chromophore while monitoring key geometric and electronic properties of the system.

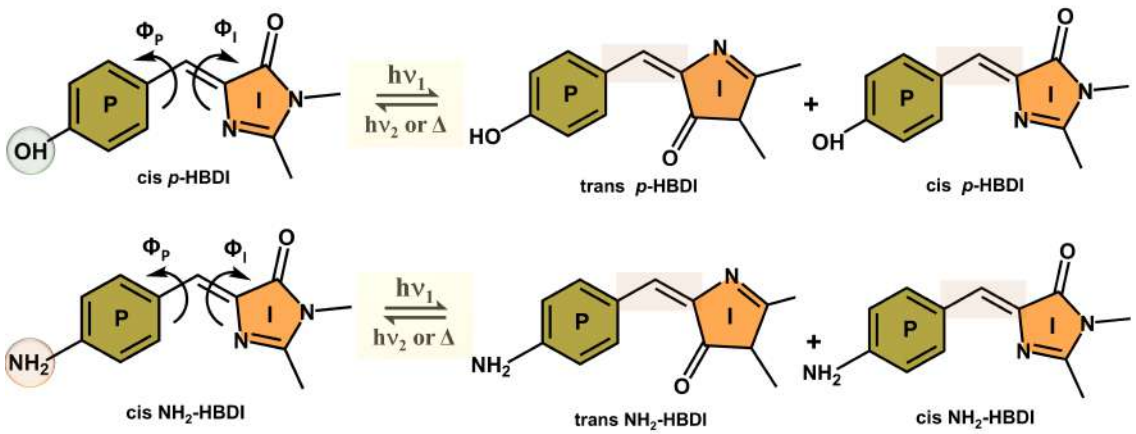


**Figure 4.1:** Cis-trans isomerization of green fluorescent protein (GFP) chromophore (*p*-HBDI) and its para-amino derivative ($NH_2$-HBDI).

## 4.2 Computational Details

### 4.2.1 Electronic Structure Methods

The geometry of the ground-state ($S_0$) and excited-state ($S_1$) minima of $NH_2$-HBDI was obtained using state-average complete active space self-consistent field (SA-CASSCF)[181, 307] and extended multistate complete active space second-order perturbation (XMS-CASPT2) methods[184, 185, 187]. The different active space combinations of 4 electrons in 4 orbitals, 6 electrons in 6 orbitals, and 10 electrons in 9 orbitals were considered, and basis sets 6-31G and cc-pVDZ were employed throughout the calculations. The nature of the active orbitals is represented in Figure 4.2.

The state-averaging procedure considered three singlet states with equal weights. The XMS-CASPT2 calculations utilized the single-state single-reference (SS-SR) contraction scheme, with a real vertical shift of 0.3 a.u. to avoid intruder state problems. In addition, density fitting and frozen core approximations were employed. A frequency calculation on the $S_0$ and $S_1$ minima structure revealed no imaginary frequencies, confirming it as a true minimum. The obtained $S_1/S_0$ minimum energy conical intersections (MECIs) were also optimized at the same levels of theory. Vertical excitation energies of $NH_2$-HBDI were calculated at CASSCF and XMSCASPT2 levels based on the optimized geometry using various active spaces and compared with experimental results to determine the optimal configuration for nonadiabatic dynamics simulations. All the electronic structure calculations were performed using the BAGEL package.[308] Linear interpolation in internal coordinates (LIICs)[309] pathways connecting Franck-Condon (FC), $S_1/S_0$ MECIs, and $S_0$ minimum critical geometries were generated employing CASSCF and XMS-CASPT2 level of theories with the active spaces of (6e,6o) and (4e,4o), respectively, in order to investigate the potential energy surface. LIIC interpolates geometries between two key points in configurational space based on internal coordinates, with single-point energy calculations performed at each geometry.

### 4.2.2 Trajectory Surface Hopping Dynamics

The photodynamics of $NH_2$-HBDI were performed using fewest-switches surface hopping (FSSH) methods by Tully[18, 19, 194] combined with the SA-CASSCF(4,4)/cc-pVDZ electronic structure approach. Similar strategies and combinations of methods have been able to demonstrate accurately the mechanisms of photochemical reaction dynamics involving conical intersections.[282] The optimized ground state geometry and the normal modes were considered to sample the initial conditions (nuclear coordinates and velocities) using a harmonic oscillator Wigner distribution,[310] as implemented in the Newton-X program.[311] A total of 150 initial conditions were generated at 298 K for the nonadiabatic dynamics simulations. The excitation energies and the corresponding oscillator strengths were computed for all initial conditions at the CASSCF(4,4)/cc-pVDZ level and subsequently used to simulate the photoabsorption cross-section of $NH_2$-HBDI. The nuclear ensemble approach (NEA), convoluted by the Lorentzian line shape, and a phenomenological broadening ($\delta$) value of 0.1 eV was employed to construct the photoabsorption cross-section.[310] The initial conditions

were considered without energy restrictions to prevent the inadvertent concentration on an incorrect spectral region. Upon excitation, all the trajectories were propagated starting from the bright $S_1$ state in the FC region using the CASSCF(4,4)/cc-pVDZ level. The trajectories were propagated on-the-fly, where the potential energies, energy gradients, and nonadiabatic couplings were calculated at each time step. The FSSH algorithm takes into account the nonadiabatic coupling (NAC) among $S_2$, $S_1$, and $S_0$ states, and the Velocity Verlet algorithm was employed to integrate Newton's equations of motion with a time step of 0.5 fs. All the trajectories were integrated up to 500 fs. For the correction of the coherence effect in the FSSH dynamics, the energy-based decoherence approach of non-linear decay of mixing by Granucci and Persico was applied, implementing the recommended value of 0.1 au.[195] For the TSH dynamics simulation, we used the Newton-X molecular dynamics simulation program,[252, 311] interfaced with the BAGEL electronic structure package.[308]

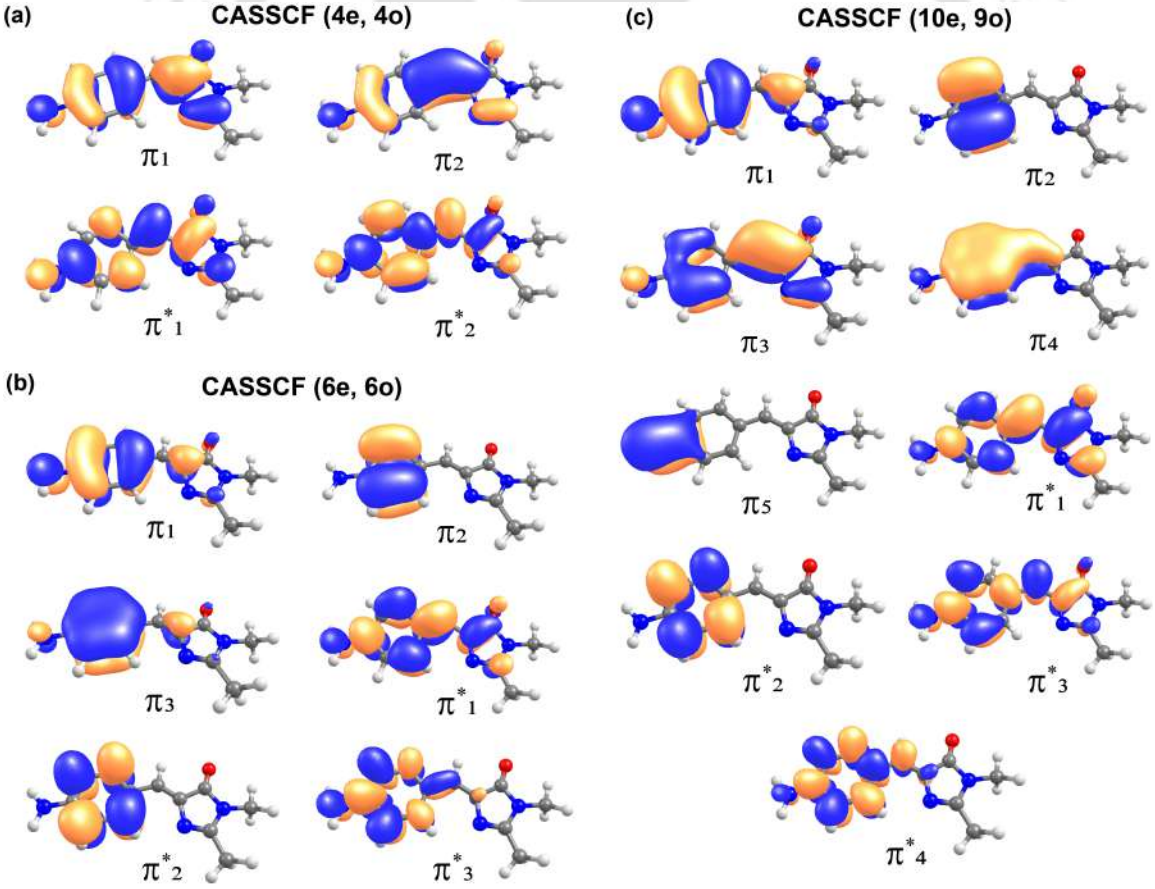


**Figure 4.2:** CASSCF/cc-pVDZ computed natural orbitals utilized in the calculations of $NH_2$-HBDI geometries, with active spaces of (a) CAS(4,4), (b) CAS(6,6), and (c) CAS(10,9). All orbitals are of $\pi$ type.

## 4.3 Results & Discussion

### 4.3.1 Structural and Electronic Properties

The photoisomerization of the $NH_2$-HBDI chromophore occurs due to the twisting of two dihedral angles, labeled as $\Phi_I$ and $\Phi_P$, caused by the exocyclic methine bridge bonds, i.e., phenylamine (P) and imidazolinone (I) bonds, as illustrated in Figure 4.1. The photoisomerization results in the formation of four stereoisomers of the $NH_2$-HBDI chromophore in either "*cis*" or "*trans*" forms. The resulting four *cis* and *trans* stereoisomers are denoted as $S_0$-CS1, $S_0$-CS2, $S_0$-TS1, and $S_0$-TS2 in $S_0$ state and $S_1$-CS1, $S_1$-CS2, $S_1$-TS1, and $S_1$-TS2 in $S_1$ state, as shown in Figure 4.3.

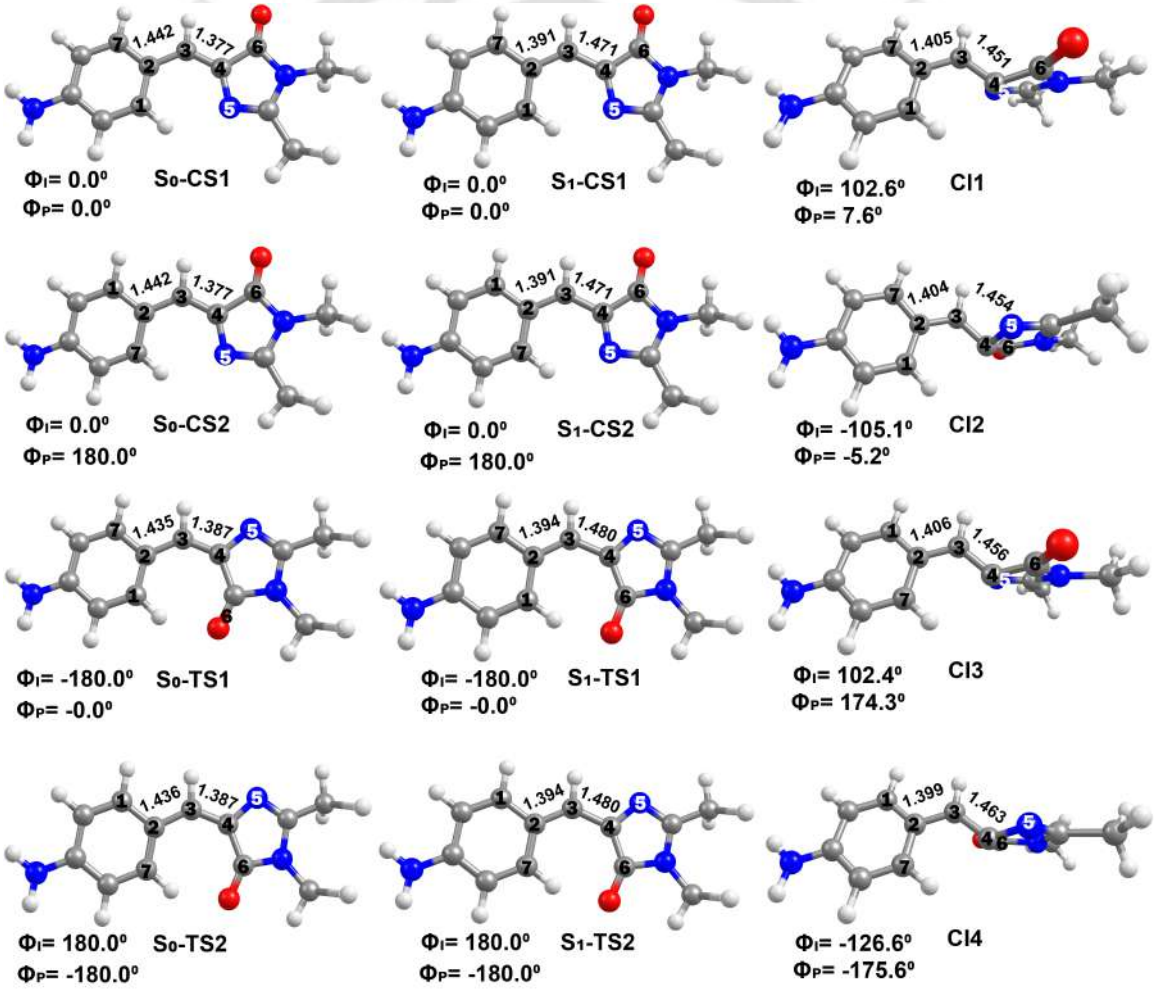


**Figure 4.3:** Molecular geometries of ground ($S_0$) and excited ($S_1$) state minima of all isomers computed at the XMS-CASPT2(6,6)/cc-pVDZ level. The two *cis* isomers are denoted by $S_0$-CS1 and $S_0$-CS2 in the $S_0$ state, and $S_1$-CS1 and $S_1$-CS2 in the $S_1$ state. Similarly, two *trans* isomers are labeled as $S_0$-TS1 and $S_0$-TS2 in the $S_0$ state and $S_1$-TS1 and $S_1$-TS2 in the $S_1$ state. MECIs are CI1, CI2, CI3, and CI4. Bond distances are in angstrom (Å) and dihedral angles in degrees (°).

Figure 4.3 illustrates the optimized geometries of all the cis and trans isomers in $S_0$ and $S_1$ states, along with the atom numbering scheme. The $\Phi_I$ and $\Phi_P$ dihedral angles are defined by the N5-C4-C3-C2 and C1-C2-C3-C4 atoms of the chromophore, respectively. All the stereoisomers exhibit planar geometries in both $S_0$ and $S_1$ states, as observed in the case of the GFP chromophore.[121, 123] Despite their geometrical similarities, the two *cis* and two *trans* isomers are distinguished based on the orientation of the hydrogen atom attached to the amino group and the resulting $\Phi_P$ and $\Phi_I$ dihedral angles. The two *cis* (CS1 and CS2) isomers are characterized by dihedral angles of $\Phi_I = \pm\ 0°$ and $\Phi_P = \pm\ 0°$ or $\pm 180°$, while the *trans* (TS1 and TS2) isomers has dihedral angles of $\Phi_I = \pm\ 180°$ and $\Phi_P = \pm\ 0°$ or $\pm\ 180°$. A comprehensive summary of key geometrical parameters of the minimum energy structures for $S_0$-min and $S_1$-min of all four stereoisomers of the $NH_2$-HBDI chromophore, optimized at different levels, is provided in Figure 4.3 and Table B1 (Appendix B).

The two methine bridge phenylamine (C2-C3 or P-) and imidazolinone (C4–C3 or I-) bonds possess different bond characters in the $S_0$ and $S_1$ state minima. Upon excitation, the C2-C3 bond distance decreases, whereas the bond distance between C3 and C4 elongates in the $S_1$ state (see Figure 4.4 and Table B1). This change in bond distances demonstrates that the C4-C3 bond exhibits a single bond character in the $S_1$ state as compared to the $S_0$ state, which facilitates the imidazolinone bond to twist more significantly, leading to the formation of the *cis* and *trans* isomers. In contrast, the shortening of the C2-C3 bond distance in the $S_1$ state compared to the $S_0$ state minima suggests that the torsional motion around the phenylamine bond may be reduced during the excited state mechanism. The observed increase and decrease in bond distances of imidazolinone and phenylamine bonds in the $S_1$ state may be attributed to the enhanced electron-donating nature of the amino group ($–NH_2$), which increases conjugation. This, in turn, facilitates the electron transfer from the phenylamine to the imidazolinone moieties and vice versa in the $S_1$ state.

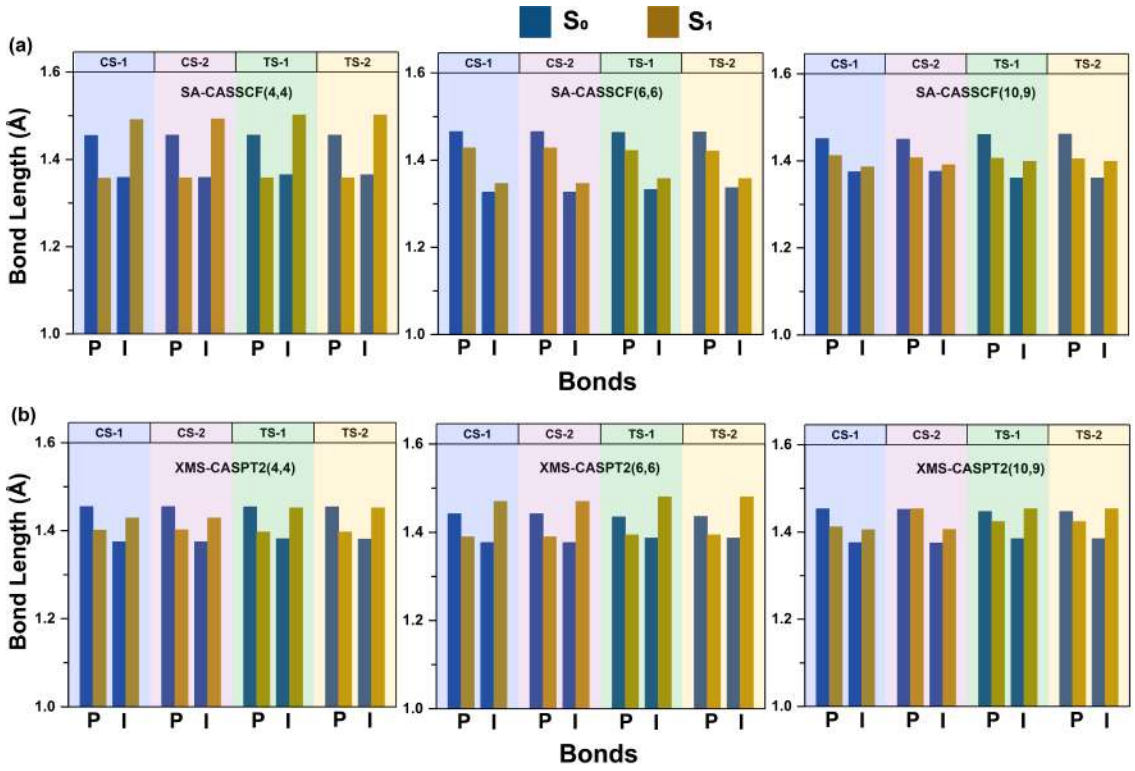


**Figure 4.4:** Phenylamine (C2-C3 or P) and imidazolinone (C4-C3 or I) bond distances of *cis* (CS1 and CS2) and *trans* (TS1 and TS2) isomers at $S_0$ and $S_1$ states of $NH_2$-HBDI chromophore. (a) CASSCF and (b) XMS-CASPT2 methods were implemented using the cc-pVDZ basis set.

### 4.3.2 Relative and Vertical Excitation Energies

A summary of the relative energies of the low-lying excited states at the equilibrium geometry is demonstrated in Table 4.1, with reference to the most stable *cis* isomer ($S_0$-CS1). Table 4.1 shows that the energy levels of the two trans isomers ($S_0$-TS1 and $S_0$-TS2) are observed to be 0.166-0.185 eV at the CASSCF/cc-pVDZ level and 0.116-0.123 eV at the XMS-CASPT2/cc-pVDZ level, respectively, higher than that of the $S_0$-CS1 isomer. Similarly, the $S_0$-CS2 isomer exhibits a negligible higher energy level compared to the $S_0$-CS1 isomer, as demonstrated in Table 4.1. Therefore, the two *cis* isomers exhibit similar energy levels, as do the two *trans* isomers, due to structural similarity, with $S_0$-CS1 being the most stable structure.

**Table 4.1:** Relative energies (eV) of all isomers CS1, CS2, TS1, and TS2 in $S_0$ and $S_1$ states computed at CASSCF and XMS-CASPT2 levels of theory. Active spaces of (4e,4o), (6e,6o), and (10e,9o) were implemented.

| | Methods | $S_0$-CS1 | $S_0$-CS2 | $S_0$-TS1 | $S_0$-TS2 | $S_1$-CS1 | $S_1$-CS2 | $S_1$-TS1 | $S_1$-TS2 |
|---|---|---|---|---|---|---|---|---|---|
| $E_{rel}$ | CASSCF(4,4)[a] | 0 | $6.562\times10^{-6}$ | 0.166 | 0.166 | 4.659 | 4.659 | 4.639 | 4.639 |
| | XMS-CASPT2(4,4)[a] | 0 | $3.533\times10^{-6}$ | 0.123 | 0.123 | 3.345 | 3.345 | 3.322 | 3.322 |
| | CASSCF(6,6)[a] | 0 | $2.479\times10^{-7}$ | 0.185 | 0.184 | 4.333 | 4.333 | 4.510 | 4.510 |
| | XMS-CASPT2(6,6)[a] | 0 | $1.626\times10^{-6}$ | 0.117 | 0.116 | 3.414 | 3.414 | 3.366 | 3.366 |
| | CASSCF(10,9)[a] | 0 | $1.950\times10^{-6}$ | 0.178 | 0.178 | 4.258 | 4.217 | 4.375 | 4.376 |
| | XMS-CASPT2(10,9)[a] | 0 | $2.835\times10^{-6}$ | 0.119 | 0.119 | 3.918 | 3.592 | 3.355 | 3.355 |

[a]**cc-pVDZ basis set**

Moreover, Table 4.2 represents the vertical excitation energies and the corresponding oscillator strengths of the Franck-Condon geometry of the lowest energy isomer of $NH_2$-HBDI at CASSCF/cc-pVDZ and XMS-CASPT2/cc-pVDZ levels of theory with different active spaces. All the excited states were characterized by $\pi \rightarrow \pi^*$ transitions. The vertical excitation energies for two *cis* isomers for the singlet excited states are observed to be 4.43-5.39 eV for the $S_1$ state and 5.167-5.925 eV for the $S_2$ state at the CASSCF/cc-pVDZ level. At the XMS-CASPT2/cc-pVDZ level, these energies are slightly lower, ranging from 3.518 to 4.131 eV for the $S_1$ state and 4.011-4.913 eV for the $S_2$ state. Similarly, for trans isomers, the excitation energies were observed to be located at 4.490-5.274 eV ($S_1$) and 5.142-5.873 eV ($S_2$) at the CASSCF/cc-pVDZ level, with corresponding XMS-CASPT2/cc-pVDZ energies of 3.679-4.046 eV for $S_1$ and 4.268-4.889 eV for $S_2$ state. Furthermore, excitation energies in TD-$\omega$B97XD/cc-pVDZ were observed at 3.739 eV ($S_1$) and 4.137 eV ($S_2$) for *cis* isomers and 3.661 eV ($S_1$) and 4.162 ($S_2$) for *trans* isomers.

The XMS-CASPT2 calculations with different active spaces yield a comparable result, with the most accurate energy (experimental ∼300 nm) for the bright state (3.518 eV) obtained at the XMS-CASPT2/cc-pVDZ level using CAS (4,4) (see Table 4.2). Table 4.2 shows that XMS-CASPT2 results indicate that $S_1$ is the bright state corresponding to a $\pi \rightarrow \pi^*$ excitation, whereas the second excited state, $S_2$, has a smaller oscillator strength and exhibits a dark character. However, it has been observed that the CASSCF/cc-pVDZ methods predict the incorrect ordering of states except when using the (4e,4o) active space, thus resulting in switching of the state character and the variation of energy gaps between $S_1$ and $S_2$ in the case of CASSCF(6,6)/cc-pVDZ and CASSCF(10,9)/cc-pVDZ methods.

**Table 4.2:** Vertical excitation energies (eV) for the first two singlet excited states computed at CASSCF and XMS-CASPT2 levels of theory. Active spaces of (4e,4o), (6e,6o), and (10e,9o) were implemented. "$f$" is the oscillator strength. [a]cc-pVDZ basis set.

| | Methods | $S_1$ | $f$ | $S_2$ | $f$ |
|---|---|---|---|---|---|
| CS1 | CASSCF(4,4)[1] | 5.287 | 1.285 | 5.862 | 0.027 |
| | XMS-CASPT2(4,4)[a] | 3.518 | 1.036 | 4.582 | 0.007 |
| | CASSCF(6,6)[a] | 4.509 | 0.003 | 5.734 | 0.777 |
| | XMS-CASPT2(6,6)[a] | 3.719 | 0.809 | 4.080 | 0.024 |
| | CASSCF(10,9)[a] | 4.477 | 0.013 | 5.167 | 0.887 |
| | XMS-CASPT2(10,9)[a] | 3.649 | 0.796 | 4.011 | 0.071 |
| | TD-$\omega$B97XD[a] | 3.739 | 0.864 | 4.137 | 0.001 |
| | Expt.[2] | 3.24[3] | | | |
| | | 3.12[4] | | | |
| | | 3.15[5] | | | |
| | CASSCF/6-31G(d)[c] | 4.13 | | | |
| CS2 | CASSCF(4,4)[a] | 5.390 | 1.285 | 5.925 | 0.037 |
| | XMS-CASPT2(4,4)[a] | 3.736 | 1.071 | 4.913 | 0.010 |
| | CASSCF(6,6)[a] | 4.536 | 0.004 | 5.862 | 0.727 |
| | XMS-CASPT2(6,6)[a] | 4.131 | 0.601 | 4.314 | 0.131 |
| | CASSCF(10,9)[a] | 4.430 | 0.008 | 5.235 | 0.326 |
| | XMS-CASPT2(10,9)[a] | 4.098 | 0.173 | 4.323 | 0.194 |
| | TD-$\omega$B97XD[a] | 3.739 | 0.864 | 4.137 | 0.001 |
| TS1 | CASSCF(4,4)[a] | 5.274 | 1.237 | 5.873 | 0.028 |
| | XMS-CASPT2(4,4)[a] | 3.679 | 1.017 | 4.889 | 0.009 |
| | CASSCF(6,6)[a] | 4.532 | 0.002 | 5.742 | 0.765 |
| | XMS-CASPT2(6,6)[a] | 4.037 | 0.706 | 4.286 | 0.042 |
| | CASSCF(10,9)[a] | 4.490 | 0.010 | 5.142 | 0.807 |
| | XMS-CASPT2(10,9)[a] | 3.724 | 0.816 | 4.268 | 0.018 |
| | TD-$\omega$B97XD[a] | 3.661 | 0.725 | 4.162 | 0.001 |
| TS2 | CASSCF(4,4)[a] | 5.274 | 1.237 | 5.873 | 0.028 |
| | XMS-CASPT2(4,4)[a] | 3.678 | 1.017 | 4.889 | 0.01 |
| | CASSCF(6,6)[a] | 4.535 | 0.002 | 5.753 | 0.761 |
| | XMS-CASPT2(6,6)[a] | 4.046 | 0.701 | 4.289 | 0.044 |
| | CASSCF(10,9)[a] | 4.491 | 0.010 | 5.143 | 0.806 |
| | XMS-CASPT2(10,9)[a] | 3.725 | 0.815 | 4.269 | 0.019 |
| | TD-$\omega$B97XD[a] | 3.661 | 0.725 | 4.162 | 0.001 |

The CASSCF/cc-pVDZ with (4e,4o) provides the correct state ordering and is consistent with the XMS-CASPT2 and TD-$\omega$B97xD results, with an overestimation of energies. Similar types of issues in switching of state ordering in CASSCF methods have also been observed by Chakraborty *et al.*[282] in the ring opening reaction mechanism of 1,3-cyclooctadiene isomers and various other groups in studies of CHD and BD.[287, 289, 312] These factors have led to the conclusion that studies at the CASSCF(4,4), XMS-CASPT2, and TD-$\omega$B97XD levels provide the most accurate description of the $NH_2$-HBDI chromophore. However, nonadiabatic trajectory surface hopping dynamics simulation for the $NH_2$-HBDI chromophore at the XMS-CASPT2 method with the cc-pVDZ basis set and considering a substantial number of trajectories is computationally very expensive. In addition, the TD-$\omega$B97XD approach cannot compute the nonadiabatic couplings between the excited and ground states and has limitations in accurately describing electronic states near the crossing region. Hence, we opt for the CASSCF(4,4)/cc-pVDZ level of theory for our nonadiabatic dynamics simulation, as it accurately describes the state ordering in the FC region and is comparatively less computationally expensive.

### 4.3.3 Minimum Energy Conical Intersections (MECIs)

Two distinct relaxation pathways, through $\Phi_I$ and $\Phi_P$ dihedral angle rotations, seem to be possible to reach the $S_0$ state after the relaxation from the Franck-Condon region toward the $S_1$ minima, and minimum energy conical intersections (MECIs) are observed to be involved during the photoisomerization mechanism. Multiple conical intersections (CIs) occur between the $S_1$ and $S_0$ states along the dihedral angle rotations. After passing through CIs, the chromophore will decay to the $S_0$ state. To further understand the reaction mechanism, we optimized the MECIs using the XMS-CASPT2(6,6)/cc-pVDZ level of theory, as illustrated in Figure 4.3 and Table B2. Four notable $S_1(^1\pi\pi^*)/S_0$ CIs have been identified, as shown in Figure 4.3 and Table B2, with respect to $\Phi_I$ and $\Phi_P$ dihedral rotations. These four MECIs are denoted as CI1, CI2, CI3, and CI4. In addition, we have also located the occurrence of four CIs at the CASSCF(4,4), CASSCF(6,6), and XMS-CASPT2(4,4) levels of theory using the cc-pVDZ basis set (see Table S2). Polyakov *et al.*[146] and Gao *et al.*[121] reported similar $S_0/S_1$ MECIs for the *p*-HBDI GFP chromophore.

It has been noted that CI1 and CI2 are nearly mirror images of each other, as are CI3 and CI4, which is attributed to the rotation of two bridging P- and I-

bonds. These MECIs exhibit a compression of the C2-C3 bond and an elongation of the C4-C3 bond relative to the $S_0$ state. For the first two MECIs, i.e., CI1 and CI2, the $\Phi_I$ dihedral angles are observed in the range of $\pm 102°$ to $\pm 105°$, while the $\Phi_P$ dihedral angles are around $\pm 5°$ to $\pm 7°$, at the XMS-CASPT2/cc-pVDZ level of theory, as shown in Figure 4.3 and Table B2. This indicates that torsion around the imidazolinone bridge bond (I) plays a crucial role in the excited-state decay process (see Figure 4.3). Similarly, the other two MECIs, CI3 and CI4, display $\Phi_I$ dihedral angles ranging from $\pm 102°$ to $\pm 126°$ and a $\Phi_P$ dihedral angle close to $\pm 175°$ at the same level of theory. Figure 4.3 and Table B2 demonstrate that the two bridging bonds, I- and P-, in the MECIs exhibit covalent characteristics comparable to those of the $S_1$-state minima. Gao *et al.*[121] reported that the $\Phi_I$ and $\Phi_P$ dihedral angles for the CIs of the neutral HBDI chromophore are approximately $\pm 85°$ and $\pm 18°$, respectively. These four CIs geometries are then used to obtain the reaction pathway from the FC region by interpolating structures using linear interpolation in internal coordinates (LIICs). During the photoisomerization process, these pathways will be further validated through our excited-state nonadiabatic molecular dynamics simulations described in section 4.3.6.

### 4.3.4 Relaxation Pathways through Linear Interpolation in Internal Coordinates

To outline the energy profile along the reaction path of $NH_2$-HBDI in the excited state during the deactivation process, linear interpolation in internal coordinates (LIICs) was performed between the geometries at the Franck–Condon point and MECIs, as illustrated in Figure 4.5. These pathways are computed at the CASSCF and XMS-CASPT2 levels (see Fig. 4.5), considering $S_0$ and $S_1$ singlet electronic states. According to both CASSCF and XMS-CASPT2 methods, upon excitation of the chromophore to the $S_1$ state, it decays to the $S_0$ state via $S_1(^1\pi\pi^*/S_0)$ MECIs as a result of $\Phi_I$ and $\Phi_P$ dihedral angle rotations. Here, the rotation of the dihedral angles of $NH_2$-HBDI in the $S_1$ state is induced by the delocalization of electrons between the imidazolinone (I) and phenylamine (P) moieties, resulting in changes in the two methine bridge (C4-C3 and C2-C3) bond characters, as detailed in Table B1. Figure 4.5 illustrates that the decay pathways from the FC structure to the CI1 and CI2 are nearly barrierless (0.078 - 0.167 eV) in the CASSCF(6,6)/cc-pVDZ level, and a

small barrier of ∼0.3 eV is observed at the XMS-CASPT2(6,6)/cc-pVDZ level. However, another pathway leading to CI3 and CI4 proceeds with a comparatively higher energy barrier of 1.186 eV - 2.036 eV in both CASSCF(6,6)/cc-pVDZ and XMS-CASPT2(6,6)/cc-pVDZ levels. In addition, all MECIs possess lower energy than the $S_1$ Franck-Condon point (see Figure 4.5), indicating that excited-state relaxation via pathways through these CIs is energetically feasible. As a result, following excitation to the Franck-Condon region in the $S_1$ state, population transfer to the $S_0$ state via nonradiative relaxation through conical intersections is favorable. Furthermore, Figure 4.5 demonstrates an excellent agreement between the CASSCF and XMS-CASPT2 levels of theory, with only minor differences observed in the estimated barrier height. Additional LIICs pathways connecting the Franck–Condon geometry and $S_1(^1\pi\pi^*)/S_0$ MECIs for CASSCF(4,4)/cc-pVDZ and XMS-CASPT2(4,4)/cc-pVDZ levels of theory are illustrated in Appendix B (see Figure B1), further supporting the evaluation.

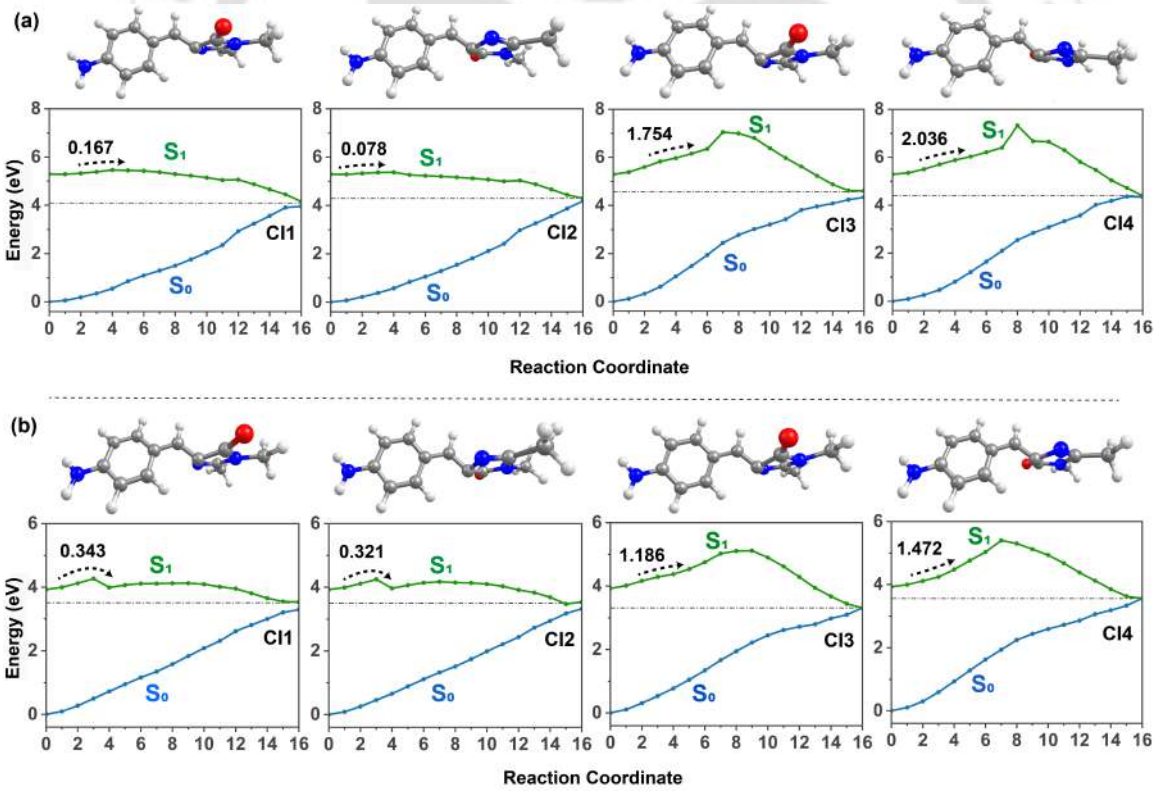


**Figure 4.5:** Linear interpolation in internal coordinates (LIICs) pathways connecting the *cis* ($S_0$-CS1) minimum and $S_1(^1\pi\pi^*)/S_0$ MECI geometries computed at (a) CASSCF(6,6)/cc-pVDZ and (b) XMS-CASPT2(6,6)/cc-pVDZ levels. The top structures display the molecular geometries of the critical points $S_1(^1\pi\pi^*)/S_0$ MECIs along with the dihedral angle rotations at (a) CASSCF(6,6)/cc-pVDZ and (b) XMS-CASPT2(6,6)/cc-pVDZ levels of theory.

### 4.3.5 Photoabsorption Cross-Section Spectra

Based on the excitation energies and their corresponding oscillator strengths (see Table 4.2), we opted for the CASSCF(4,4) method for the further nonadiabatic dynamics simulation of $NH_2$-HBDI chromophore. Accordingly, we generated 150 single-point geometries to sample the initial conditions for $NH_2$-HBDI chromophore in order to simulate the absorption spectrum upon excitation to its first excited ($S_1$) state using the nuclear ensemble approach. The $S_0 \rightarrow S_1$ excitation of $NH_2$-HBDI involves $\pi$–$\pi^*$ transitions corresponding to the bright state. Figure 4.6 represents the simulated photoabsorption cross-section of $NH_2$-HBDI chromophore, computed at the CASSCF(4,4) method using cc-pVDZ basis set and compared with the experimental absorption spectrum (see Table 4.2).

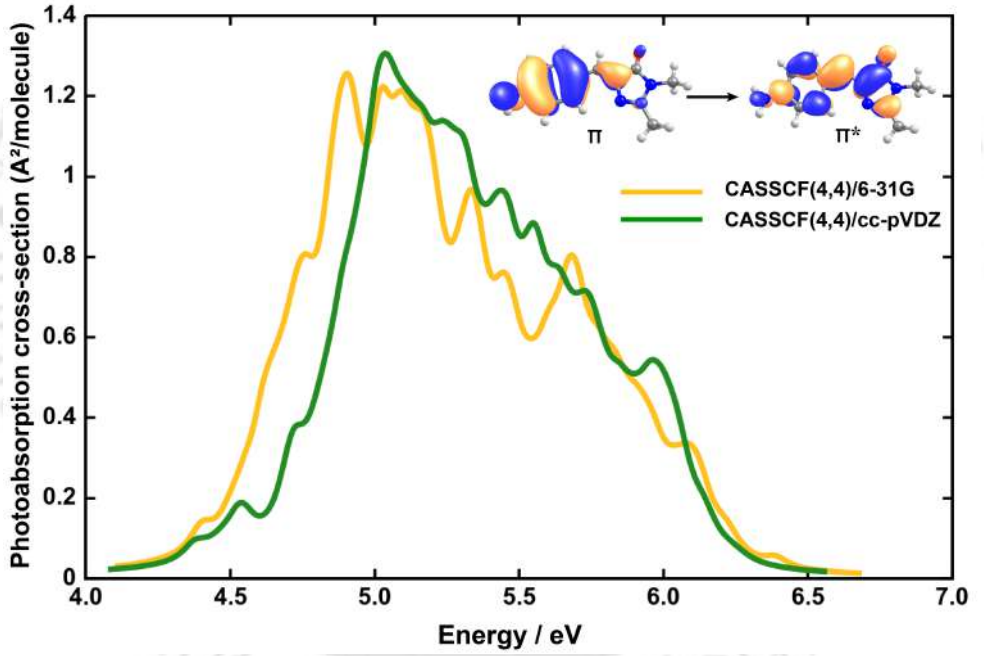


**Figure 4.6:** Simulated photoabsorption cross-section spectra of $NH_2$-HBDI computed at CASSCF(4,4) methods using Wigner distribution, sampling 150 geometries and a Lorentzian line shape with $\delta = 0.1$ eV. The orbitals corresponding to the transition are shown in the inset. 6-31G and cc-pVDZ basis sets are used.

The simulated absorption peak is located at ∼5.03 eV, which is ∼1.7-1.9 eV (Table 4.2) higher than the experimental absorption peak at ∼3.2 eV. This difference in absorption values is typical of CASSCF, as it tends to overestimate excited-state energies in the Franck-Condon region due to the absence of dynamic correlation. Further, this is also consistent with the overestimation of the excitation energy from electronic structure calculation at CASSCF methods (as shown in Table 4.2) with

the brighter $S_1$ state, which has an overestimated excitation energy of ∼5.287 eV compared to the XMS-CASPT2 energies and experimental absorption maximum by ∼ 1.7 - 2.0 eV. A simulated absorption spectrum at the CASSCF(4,4) level using a 6-31G basis set has been computed to compare with the CASSCF(4,4)/cc-pVDZ result.

### 4.3.6 Nonadiabatic Molecular Dynamics Simulations

To investigate the photodynamics of the $NH_2$-HBDI chromophore, we have considered the *cis* isomer for the nonadiabatic simulation of *cis-trans* photoisomerization dynamics upon photoexcitation to the Franck-Condon region. The nonadiabatic dynamics simulations were carried out employing Tully's Fewest Switches Surface Hopping (FSSH) approach in combination with the CASSCF electronic structure method. A total of 150 trajectories were initiated on the $S_1$ state for nonadiabatic trajectory surface hopping dynamics of $NH_2$-HBDI, considering a state average of three electronic states, and propagated for 500 fs. We have carefully examined the trajectories to gain a comprehensive understanding of the photoinduced *cis-trans* isomerization process and the subsequent chemical reaction dynamics of the $NH_2$-HBDI chromophore. As the simulation proceeded, a significant number of trajectories were terminated if the total energy exhibited a change of 0.5 eV or more. This termination of the trajectories resulted from the total energy change is due to convergence instabilities related to structural changes between the two consecutive timescales or orbital rotations between subspaces.[20] Hence, only a limited number of trajectories reached a maximum simulation time of 500 fs. However, we have chosen the TSH/FSSH method over alternative approaches, such as AIMS, MCTDH, etc., which would have avoided the energy drift issue during the simulation due to their significantly higher computational cost compared to TSH in our current limited resources. In addition, similar strategies and combinations of the FSSH approach have been observed to accurately describe the mechanism of photochemical dynamics involving the relaxation mechanism through conical intersections.[282, 290, 313] Therefore, for our relatively large chromophore, the TSH/FSSH method was chosen as an optimal method between accuracy and computational feasibility and was therefore considered for our investigation.

The relaxation mechanism in the $NH_2$-HBDI chromophore, responsible for the radiationless decay from the $S_1$ to $S_0$ electronic states, can be elucidated by analyzing

a few key parameters such as populations, dihedral angles, and bond lengths, along with the trajectory propagation and their behavior at the hopping events. Upon excitation of the chromophore to the $S_1$ singlet excited state in the Franck-Condon region, changes in the imidazolinone (I) and phenylamine (P) bond distances were observed, which in turn led to twisting of the corresponding $\Phi_I$ and $\Phi_P$ dihedral angles as a function of time in several trajectories during the simulation. Therefore, based on the analysis of all these key geometric parameters, the trajectories were categorized as "reactive" and "unreactive." As the simulation proceeds, a "reactive" trajectory shows decreases in the energy gap between $S_1$ and $S_0$ states ($\sim$0.5 eV), an increased in $\Phi_I$ or $\Phi_P$ dihedral angles ($\sim \pm 90°$), and increases and decreases of I- and P- bond distances, all occurring within the maximum simulation time of 500 fs or until the trajectory terminates. In contrast, "unreactive" trajectories exhibit no significant changes in population of the electronic states, dihedral angle rotations, and bond distances during the maximum simulation time of 500 fs or until the trajectory terminates.

Since a significant number of trajectories terminated before reaching the maximum simulation time of 500 fs, we did not represent the average population of the electronic states to avoid misinterpretation of the population decay of $NH_2$-HBDI during the dynamics simulation of the photoisomerization process. Therefore, we have demonstrated the population of the electronic state by a single representative trajectory each for reactive and unreactive pathways, as shown in Figure B2 of the supplementary material. Figures B2(a) and B2(b) demonstrate the time evolution dynamics of the populations for $S_0$, $S_1$, and $S_2$ electronic states of a representative "reactive" and "unreactive" trajectory. From Figure B2(a), it can be seen that the molecule fluctuates in the $S_1$ state and the energy gap between $S_1$ and $S_0$ decreases as the simulation proceeds. However, the trajectories terminate when a drift in total energy of more than 0.5 eV occurs at 332.5 fs, and the energy gap between $S_1$ and $S_0$ reduces nearly to 0.5 eV. Therefore, we identified this region as the occurrence of degeneracy between $S_1$ and $S_0$ states, leading to an $S_1/S_0$ crossing [as shown in Figure B2(a)]. On the other hand, Figure B2(b) shows that the molecules remain in the $S_1$ state until the maximum duration of 500 fs of our simulations, indicating that no photoisomerization reaction is taking place. This suggests that there is still potential for the reaction to occur at longer time scales. Figure B3 illustrates a histogram showing the distribution of termination times of all the reactive and unreactive trajectories

terminated within the simulation time of 500 fs. The histogram time-window depicts that a substantial number of trajectories terminate within the first 150 fs, while only 8 out of 150 trajectories reached a maximum simulation of 500 fs. Moreover, the reactive trajectories predominantly terminate within the range of ∼280-460 fs

To gain more insight into the behavior of the photoinduced mechanism, we analyzed the imidazolinone (C4-C3) and phenylamine (C2-C3) bridged bonds and the corresponding dihedral motions, characterized by N5-C4-C3-C2 (or $\Phi_I$) and C1-C2-C3-C4 ( or $\Phi_P$), respectively, of the representative reactive trajectory initiated from the $S_0$-cis isomer as a function of time. These bond distances and the dihedral motion of the representative trajectory are depicted in Figure 4.7. Figure 4.7(a) demonstrates that the C4-C3 bond initially has a double bond character with a bond length of 1.32 Å, while C2-C3 exhibits a single bond character with a bond length of 1.45 Å. As the simulation proceeds, the C4-C3 bond elongates and acquires the single bond character, whereas the C2-C3 bond is compressed and tends to adopt the double bond character. This change in the C4-C3 and C2-C3 bond characters facilitates the twisting of the $\Phi_I$ dihedral angle rotation in the $S_1$ state upon photoexcitation.

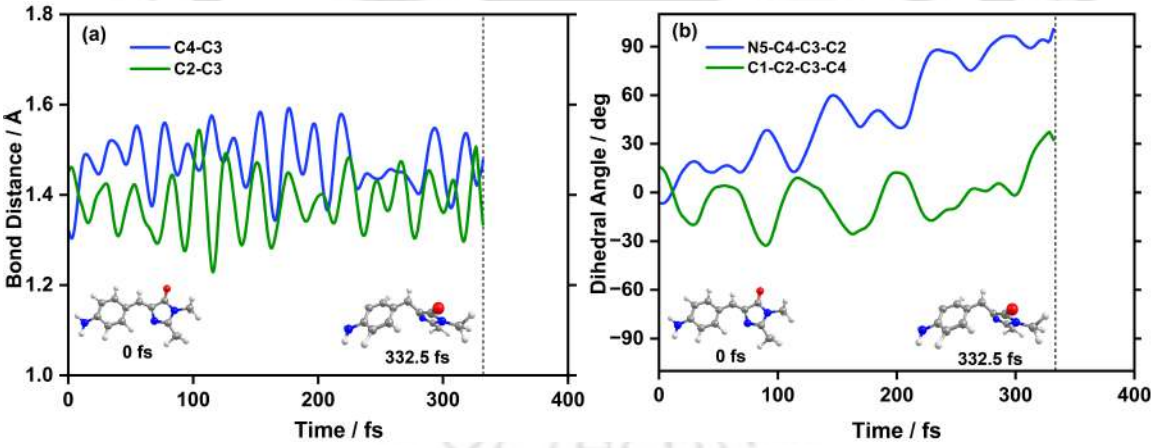


**Figure 4.7:** Time evolution of (a) imidazolinone-bridged C4-C3 (blue) and phenylamine-bridged C2-C3 (green) bond distances, and (b) imidazolinone N5-C4-C3-C2 (blue) and phenylamine C1-C2-C3-C4 (green) dihedral angles, for a representative reactive trajectory at CASSCF(4,4)/cc-pVDZ level of theory. The bond distances are in angstrom (Å), and dihedral angles are in degrees (∘). The inset displays the molecular geometries at the initial of the simulation (0 fs) and end of the simulation (332.5 fs).

Moreover, the torsional rotation as a result of the changes in C4-C3 and C2-C3 bond distances is depicted in Figure 4.7(b). Figure 4.7(b) shows that both the $\Phi_I$ and $\Phi_P$ dihedral angles remain nearly planar till several femtoseconds, after which

the $\Phi_I$ dihedral begins to rotate, simultaneously reducing the energy gap between the $S_1$ and $S_0$ states (Figure B2(a)) as the $\Phi_I$ dihedral torsional angle increases. When the $\Phi_I$ dihedral angle reaches 100° at 332.5 fs, corresponding to a perpendicular orientation of imidazolinone with respect to phenylamine moieties, the $S_1$ and $S_0$ energy gap reduces to 0.5 eV, suggesting the formation of $S_1/S_0$ crossing, which is also been observed previously in the time evolution of the population. However, the $\Phi_P$ dihedral angle shows fluctuation throughout the simulation and remains around 30° by the end, indicating that $\Phi_P$ torsion does not change much in the *cis-trans* isomerization process or requires more simulation time to rotate. Thus, the rotation of the imidazolinone-bridge $\Phi_I$ dihedral angle is the dominant one and is facilitated by the elongation of the C4-C3 bond and compression of the C2-C3 bond, resulting in the internal conversion of the excited state species via MECIs. In addition, the dihedral angle values of the $S_1/S_0$ crossing structure at 332.5 fs obtained from the dynamics simulation are closely aligned with those of the MECI obtained in the electronic structure calculation as shown in Figure 4.3 and Table B2. This indicates that the molecule undergoes nonradiative decay to the $S_0$ state through the $S_1/S_0$ crossing at this point. This aligns with the findings obtained by Chen and coworkers[219] and Huang and coworkers[314], who reported that the nonradiative decay in the para-amino analogue of GFP chromophore occurs within a time-scale of 0.3-1 ps. Thus, the ultrafast decay to the $S_0$ state in $NH_2$-HBDI chromophore has been facilitated by the MECIs, which are governed by the torsional motion around C4-C3 and C2-C3 bonds.

Moreover, the $\Phi_P$ dihedral angle may also be an important pathway on a longer timescale, within 2-5 ps, similar to the effect of $\Phi_P$ torsion in GFP chromophore reported by Martinez and coworkers.[158, 159] In their study, they concluded that the majority of the population decays to the $S_0$ state through the relaxation mechanism via $\Phi_I$-twisted MECIs, whereas ∼34% proceeds via $\Phi_P$-twisted MECIs.[158] The potential insight into the role of $\Phi_I$ and $\Phi_P$ dihedral angle rotations and the reason behind the dominant nature of $\Phi_I$ dihedral rotation can also be explained by the LIIC pathways leading to MECIs corresponding to $\Phi_I$ and $\Phi_P$ dihedral rotations, as shown in Figure 4.5 and Figure B1. The interpolated pathways reveal that the energy barriers leading to CI1 and CI2, corresponding to the prevailing $\Phi_I$ rotation, are lower than those leading to CI3 and CI4, in which $\Phi_P$ rotation is also significant (see Figure 4.3, Figure 4.5, and Figure B1). This indicates that the $\Phi_I$ dihedral

rotation proceeds with a low energy barrier in the $S_1$ state compared to $\Phi_P$ dihedral rotations in both CASSCF and XMS-CASPT2 methods. Therefore, a significant energy barrier associated with $\Phi_P$ rotation compared to $\Phi_I$ rotation causes the slower decay to the $S_0$ states via $\Phi_P$. Besides, due to the higher computational cost in our limited resources, our current study focused on the primary pathways leading to the deactivation to the $S_0$ state, considering a maximum timescale of 500 fs.

To further aid our understanding of the reaction dynamics and the twisting motion of $\Phi_I$ and $\Phi_P$ dihedral angles, we tracked the dihedral angles and bond lengths of all the reactive and unreactive trajectories as a function of time, as illustrated in Figures 4.8 and 4.9. Figure 4.8 depicts the time-dependent evolution of dihedral angles for all the trajectories of the $NH_2$-HBDI chromophore, which includes both the reactive and unreactive pathways. The blue trajectories represent the reactive one in which the key photoinduced event, *cis-trans* isomerization, occurs, whereas the unreactive trajectories are represented by green ones. Four MECI species should be generated with respect to the $\Phi_I$ and $\Phi_P$ dihedral angles during the reaction mechanism according to electronic structure calculations. Figure 4.8 demonstrated that upon photoexcitation, the $\Phi_I$ dihedral angle undergoes torsional motions in both the clockwise and anticlockwise directions, resulting in MECIs located within the range of $\pm$ 90 - 100°. This confirms the occurrence of MECIs with both the positive and negative $\Phi_I$ and $\Phi_P$ values. However, the competitive torsional $\Phi_P$ rotation remains largely unchanged due to the higher energy barrier as compared to the $\Phi_I$ rotation, as shown in Figures 4.5 and B1. Hence, the $\Phi_P$ dihedral angle remains planar throughout the simulations. Furthermore, for another set of unreactive trajectories, indicated by green, both $\Phi_I$ and $\Phi_P$ dihedral angles oscillate between $\pm$ 30° throughout the simulation, suggesting that the molecule remains planar and no *cis-trans* isomerization takes place until the maximum simulation time of 500 fs. This provides a deeper insight into the molecular behavior and potential for photoisomerization.

Similarly, the time evolution of the imidazolinone and phenylamine-bridged bonds during the photoinduced *cis-trans* isomerization for both the reactive and unreactive trajectories is shown in Figure 4.9. Figure 4.9 shows that the C4-C3 average bond distance fluctuates as the reaction proceeds and tends to increase at the end of the simulation. In contrast, the C2-C3 average bond distances also fluctuate but tend to decrease at the end of the simulation. This trend facilitates isomerization, suggesting

that both imidazolinone and phenylamine bonds play crucial roles in the photoisomerization reaction of the $NH_2$-HBDI chromophore analogue.

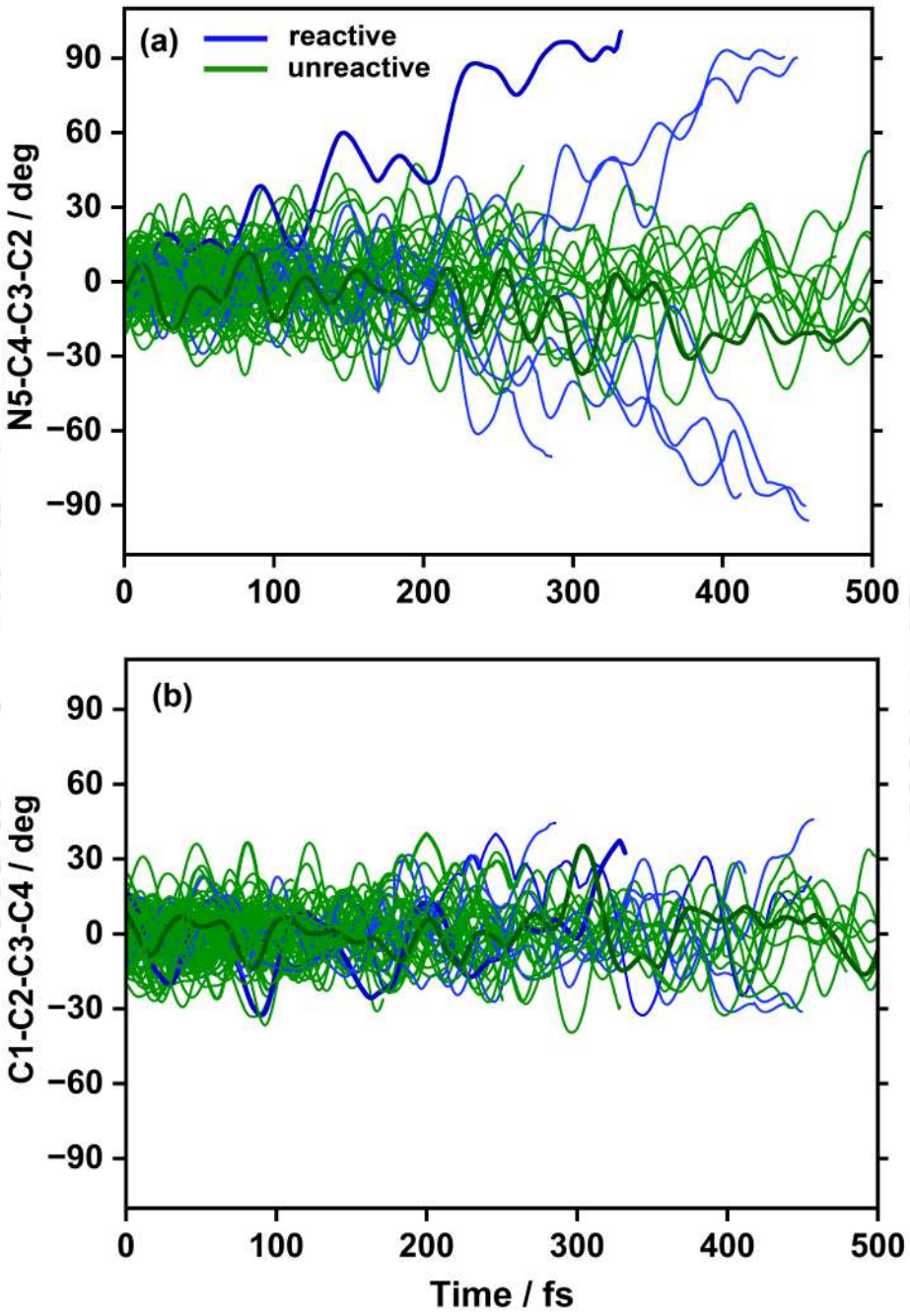


**Figure 4.8:** Time evolution of dihedral angles (a) imidazolinone ($\Phi_I$ or N5-C4-C3-C2), (b) phenylamine ($\Phi_P$ or C1-C2-C3-C4) for both the reactive (blue) and unreactive (green) trajectories at CASSCF(4,4)/cc-pVDZ level of theory. Bold blue indicates representative reactive trajectory and bold green is for for representative unreactive trajectory. The dihedral angles are in degrees.

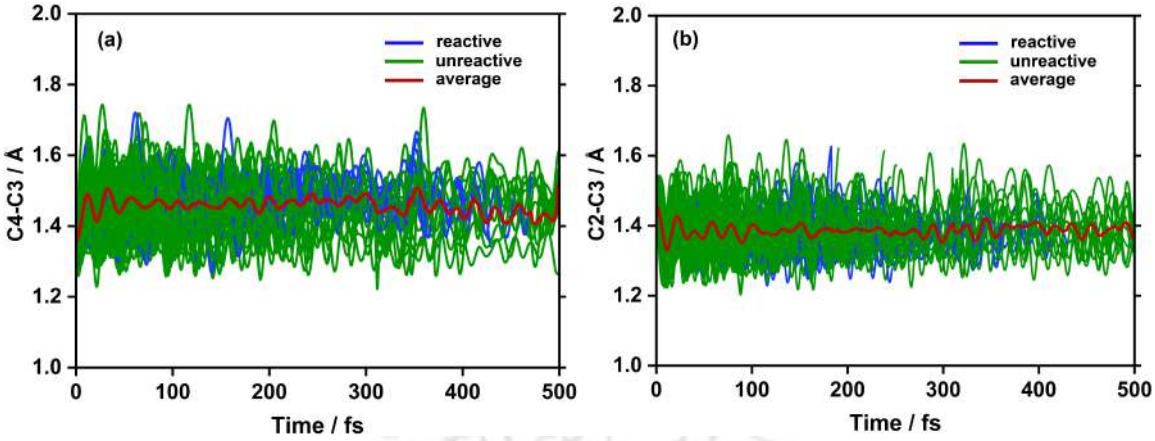


**Figure 4.9:** Time evolution of bond distances (a) imidazolinone ( I or C4-C3) and (b) phenylamine ( P or C2-C3) bridged bonds for both the reactive (blue), unreactive (green), and an average of all (red) trajectories at CASSCF(4,4)/cc-pVDZ level. Bond distances are in angstrom (Å).

## 4.4 Conclusions

In this study, we employed electronic structure calculations, subsequently followed by the CASSCF trajectory surface hopping nonadiabatic simulations, to investigate the photoswitchable *cis-trans* isomerization process of the $NH_2$-HBDI analogue of green fluorescent protein (GFP) chromophore after being excited to $S_1$ state. The electronic structure calculations have suggested that radiationless decay from the excited ($S_1$) state to the ground ($S_0$) state is facilitated by the occurrence of multiple $S_1(^1\pi\pi^*)/S_0$ MECIs involving the distortion of the imidazolinone ($\Phi_I$-) and phenylamine ($\Phi_P$-) bridged dihedral angles. The torsional rotation of the $\Phi_I$- and $\Phi_P$- dihedral angles of $NH_2$-HBDI in the $S_1$ state is caused by the changes in the bond distances of the imidazolinone and phenylamine bridged bonds, i.e., C4-C3 and C2-C3, induced by the delocalization of electrons between the imidazolinone and phenylamine moieties upon photoexcitation. The nonadiabatic dynamics simulation further supports that the radiationless decay of the photoexcited $NH_2$-HBDI chromophore from the $S_1$ excited state to $S_0$ state occurs via $S_1/S_0$ internal conversion, with trajectories exploring many MECIs geometries as a result of torsional rotations with the $\Phi_I$ angle having a major impact. However, due to the energy conservation issue associated with the TSH/FSSH dynamics in combination with CASSCF methods, we were unable to obtain a clear picture of the population decay through the nonadiabatic dynamics

simulation. To accurately capture both the $\Phi_I$ and $\Phi_P$ rotations and the population decay, a more efficient alternative approach with lower computational cost is required. Therefore, nonadiabatic dynamics simulation using a more robust method are currently underway, which is expected to provide deeper insight into nonadiabatic decay.

Hence, our investigation provides insight into the role of conjugation in facilitating the torsional rotation around the imidazolinone and phenylamine bridged bonds in the para-amino derivative of GFP chromophore. These observations contribute to an understanding of the excited-state dynamics of photoexcited chromophores and help to establish a connection between the molecular structure and dynamical behavior.

# Chapter 5

# Ultrafast Hot Exciton Nonadiabatic Excited-State Dynamics in GFP Chromophore Analogue

(The work of this Chapter is published in *J. Phys. Chem. B.* **2024**, *128*, 6786–6796.)

## 5.1 Introduction

Ultrafast excited-state dynamics govern energy transfer and charge formation in some organic and inorganic materials resulting in the generation of excitons. Excitons are predominantly formed as a result of interactions between light and matter, and play a crucial role in numerous fields such as organic and inorganic materials, including optoelectronics, photocatalysis, and nanotechnology.[315–318] The ultrafast excitons diffuse through the material, leading to the charge generation mechanisms in organic $\pi$-electron conjugated donor-acceptor (D-A) interfaces.[319–322] The relaxation processes of excitons were studied at the femtosecond timescale using nonadiabatic excited-state dynamics in $\pi$-conjugated molecules.[323] Over the past decade, a considerable number of efforts have been focused on investigating the dynamics of photoinduced interfacial excitons in various types of organic, inorganic, and hybrid materials that possess donor-acceptor interfaces.[324–329] This has led to significant progress in our comprehension of ultrafast phenomena that governs exciton dynamics and charge generation mechanisms in these materials.[330–333] Nonetheless, certain aspects of the high-energy (hot) exciton and charge generation dynamics at the molecular level remain ambiguous.[334–338] The uncertainty lies in whether hot excitons would facilitate electron-hole charge separation, resulting in enhanced overall charge generation efficiency, or would increase the nonradiative decay through the internal relaxation process to the lower-energy states.

In the past few years, many insightful studies have been reported by Gelinas *et al.*,[339] Najafov *et al.*,[340] Tamura *et al.*,[326, 341] Nelson *et al.*,[333, 342] Rossky *et al.*,[343, 344] and Barbatti *et al.*[323, 329, 345] that explored the nonadiabatic excited-state dynamics and ultrafast exciton relaxation of medium $\pi$-conjugated complexes using various approximations. Despite numerous experimental and theoretical studies on ultrafast exciton relaxation, there has been limited thorough investigation into the accurate description and modeling of the ultrafast exciton and hot charge transfer phenomenon in organic chromophores.[346–348] Inspired by these issues, the present work focuses on the nonadiabatic dynamics of green fluorescent protein (GFP) chromophore based molecular aggregates and explores its excited-state properties and ultrafast exciton dynamics.

Green fluorescent protein (GFP) has ascended as a monarch of fluorescent proteins and remains at the forefront of scientific exploration due to its remarkable adaptability and usefulness.[76, 88, 220, 281, 349–351] It contains a modifiable chromophore, i.e., *p*-hydroxybenzylideneimidazolidinone (*p*-HBDI) at its core, responsible for emitting light.[86–88] Mutation of the chromophore environment results in a remarkable diversity of photophysical properties among GFP chromophore analogues, leading to variations in spectral range, fluorescence quantum yield, and photostability.[78, 291, 352–355] At room temperature outside the protein environment, the GFP chromophore becomes predominantly non-fluorescent due to ultrafast radiationless decay, resulting in its quenching.[93]

Experimental and theoretical investigations revealed that the excited-state ultrafast deactivation occurs through two distinct pathways, which involve rotation around one of the methine bridge bonds i.e., either imidazolinone (I) or phenolate (P) bonds.[124, 126, 152, 302] This ultrafast deactivation coincides with the twisted intramolecular charge transfer (TICT) across the bridge, decreasing fluorescence quantum yield. Significantly, the two torsional pathways mediated by $\Phi_I$-twisted and $\Phi_P$-twisted bonds exhibit intramolecular CT in opposite directions.[124, 126] Internal conversion via $\Phi_I$-twisted conical intersection (CI) seam is the dominant decay pathway leading to the direct formation of the E-stereoisomer, while rotation around $\Phi_P$-twisted channel generates the initial ground-state, potentially restoring the identical $\Phi_P$-flipped configuration.[158, 159] The $\Phi_I$- and $\Phi_P$- dihedral rotations are illustrated in Figure C1 of Appendix C. Thus, when designing a fluorophore derived from *p*-HBDI, it is crucial to minimize the photoisomerization process by restricting

the rotation along the $\Phi_I$-twisted and $\Phi_P$-twisted channels.

Over recent years, several researchers have reported a range of chromophores inspired by the *p*-HBDI that demonstrate diverse photophysical properties.[214–219, 304] Many approaches towards considerable improvement in the fluorescence quantum yield have been attained for structurally constrained derivatives of *p*-HBDI by inhibiting the $\Phi_I$- and $\Phi_P$- torsions simultaneously.[158, 159, 214–219, 304] Yang and coworkers have synthesized the derivative of *p*-HBDI chromophore, i.e., benzylidenedimethylimidazolinone (BDI) analogue.[356] In contrast to naturally occurring *p*-HBDI chromophore which exhibits a high fluorescence quantum yield ($\Phi_f$=0.8) [88], the BDI analogue displayed no fluorescence ($\Phi_f < 0.001$)[356] and attempted to restore fluorescence by imposing structural constraints on the chromophore, simultaneously restricting $\Phi_I$- and $\Phi_P$- torsions.

The primary objective of this investigation is to explore the nature of the excited states in GFP chromophore analogues, i.e., a BDI chromophore, and control the nonradiative decay using first-principles calculations. To gain insights into the generation of high-energy (hot) excitons and its ultrafast relaxation dynamics at an atomistic and time-dependent level, we have carried out nonadiabatic excited-state dynamics simulations using linear-response time-dependent density functional theory (TDDFT)[357, 358] on the BDI-dimer.

## 5.2 Methods

### 5.2.1 Static Calculations

Ground-state and excited-states geometry optimizations for both BDI monomer and dimer were performed with density functional theory (DFT)[234] and time-dependent density functional theory (TDDFT)[235] at long-range dispersion corrected functional $\omega$B97XD[359] level using 6-31G(d), cc-PVTZ, and TZVP basis sets. Earlier studies have demonstrated that this approach, which includes long-range interactions and dispersion effects, has been able to produce reasonably accurate results for this type of system.[360] The vertical excitation energies were computed with the excited-state approaches: linear response time-dependent DFT (TDDFT) employing $\omega$B97XD functional with 6-31G(d) and TZVP basis sets, and second-order algebraic diagrammatic construction [ADC(2)][361, 362] with SV(P), cc-PVTZ, and TZVP basis sets. All the

static calculations were carried out in Gaussian 16[232] and Molpro 2022[363, 364] electronic structure program packages. TheoDore 3.0[365] package by Felix Plasser has been implemented to compute the particle-hole analysis based on a one-electron transition density matrix (1TDM).

### 5.2.2 Dynamics Simulations

The simulation of the absorption cross-section was performed with the nuclear ensemble method based on harmonic-oscillator Wigner distributions,[310] considering a total of 100 points. The $\omega$B97XD density functional and 6-31G(d) basis set were implemented during these spectrum generations. The nonadiabatic dynamics of excited states were performed employing the fewest-switching surface hopping (FSSH)[19] method using TDDFT as implemented in the NEWTON-X program package[252, 311] interfaced with Gaussian 16[232]. A microcanonical ensemble was used to perform the dynamics at the TD-$\omega$B97XD/6-31G(d) level of theory. The classical equations were integrated with a time step of 0.5 fs, while the quantum equations were integrated using interpolated properties between classical steps with 0.025 fs steps. Decoherence effects were accounted for by correcting the time-dependent coefficients based on the approach outlined in the reference.[195] Due to the occurrence of numerous trivial crossings between the weakly interacting or non-interacting states in the dimer, the conventional FSSH approach for nonadiabatic couplings between the excited states becomes computationally expensive requiring very small time-steps.[366, 367] To address this issue, nonadiabatic couplings based on FSSH using the local diabatization approximation,[368, 369] have been employed to determine the diabatic nature of these crossings. In this study, the nonadiabatic couplings between excited states were calculated using time-dependent wave function overlap integrals proposed by Hammes-Schiffer and Tully.[194] This method has been widely implemented to calculate nonadiabatic couplings in dynamics simulations and has been demonstrated to be suitable while encountering trivial crossings.[329, 345, 369] Nonadiabatic couplings between excited and ground states were not computed since the linear-response TDDFT and Kohn-Sham DFT approaches had limitations in providing an accurate description of the electronic states near the crossing region. The trajectories were simulated for a maximum duration of 500 fs or until it reached the $S_1/S_0$ crossing i.e., if the energy gap $\Delta E(S_1\text{-}S_0)$ becomes less than 0.15 eV. In these cases, the final time-step was considered to signify the internal conversion to the $S_0$ state. Based on

this presumption, the occupation of the $S_0$ state at each time step has been calculated, and the $S_1$ occupation was corrected as outlined in reference.[323]

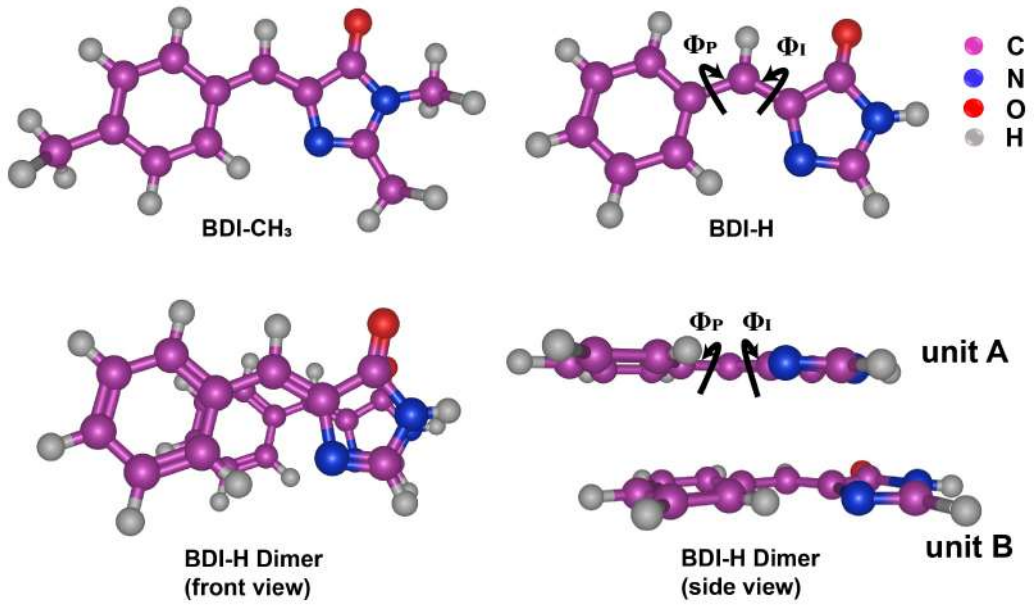


**Figure 5.1:** Optimized ground state ($S_0$) molecular geometries of the BDI-$CH_3$ monomer, BDI-H monomer and BDI-H van der Waals ($v$dW) dimer at TDDFT ($\omega$B97XD/6-31G(d)) method with the illustration of important geometric parameters.

## 5.3 Results & Discussion

The optimized geometries of the BDI chromophores are illustrated in Figure 5.1. The BDI dimer is composed of weak $\pi$–$\pi$ stacking van der Waals ($v$dW) interactions and serves as a model for various organic $\pi$-conjugated fluorescent chromophores. To initiate the investigation, TDDFT[235] vertical excitations and emission energies for the BDI chromophore analogues with -$CH_3$ and -H groups i.e., BDI-$CH_3$ and BDI-H, as shown in Figure 5.1, were computed using $\omega$B97XD[359] functional and 6-31G(d)[370] and TZVP[241] basis sets. The computed TDDFT excitation and emission energies of BDI-$CH_3$ (in ethanol) quantitatively reproduce experimental results as demonstrated in Table 5.1. Considering the significant computational cost associated with the dynamics simulation of the BDI chromophore, we opted to investigate the analogue of -H instead of -$CH_3$, as both exhibit comparable excitation and emission energies (see Table 5.1). To further validate, the vertical excitation energies and absorption cross-section for BDI-$CH_3$ and BDI-H have been computed, and it was observed that both chromophores yield comparable results as represented in Table C1 (see Appendix C)

and Figure 5.2. Hence, the BDI chromophore containing the -H group (BDI-H) has been considered for further studies of higher-energy excited-state dynamics in the $v$dW dimer.

**Table 5.1:** Vertical excitation ($\lambda_{max}{}^{abs}$) and emission ($\lambda_{max}{}^{emis}$) energies (eV) and the corresponding oscillator strength ($f$) for transitions of BDI-$CH_3$ and BDI-H chromophore (monomer) in dielectric medium (ethanol, $\epsilon$=24.3) computed at the TD-$\omega$B97XD/6-31G(d) and TD-$\omega$B97XD/TZVP methods using IEFPCM model. Experimental results[356, 371] (eV) in ethanol (solvent) were given for comparison.

| Complex | $\lambda^{abs}_{max}$ (Calc.) | | | | $\lambda^{abs}_{max}$ | $\lambda^{emis}_{max}$ (Calc.) | | | | $\lambda^{emis}_{max}$ |
|---|---|---|---|---|---|---|---|---|---|---|
| | 6-31G(d) | $f$ | TZVP | $f$ | (Expt.) | 6-31G(d) | $f$ | TZVP | $f$ | (Expt.) |
| BDI-$CH_3$ | 3.77 | 0.84 | 3.73 | 0.83 | 3.56 | 2.83 | 0.98 | 2.66 | 0.91 | 2.64 |
| BDI-H | 3.87 | 0.74 | 3.82 | 0.74 | –[a] | 2.92 | 0.88 | 2.82 | 0.89 | –[a] |

[a]Experimental results not available

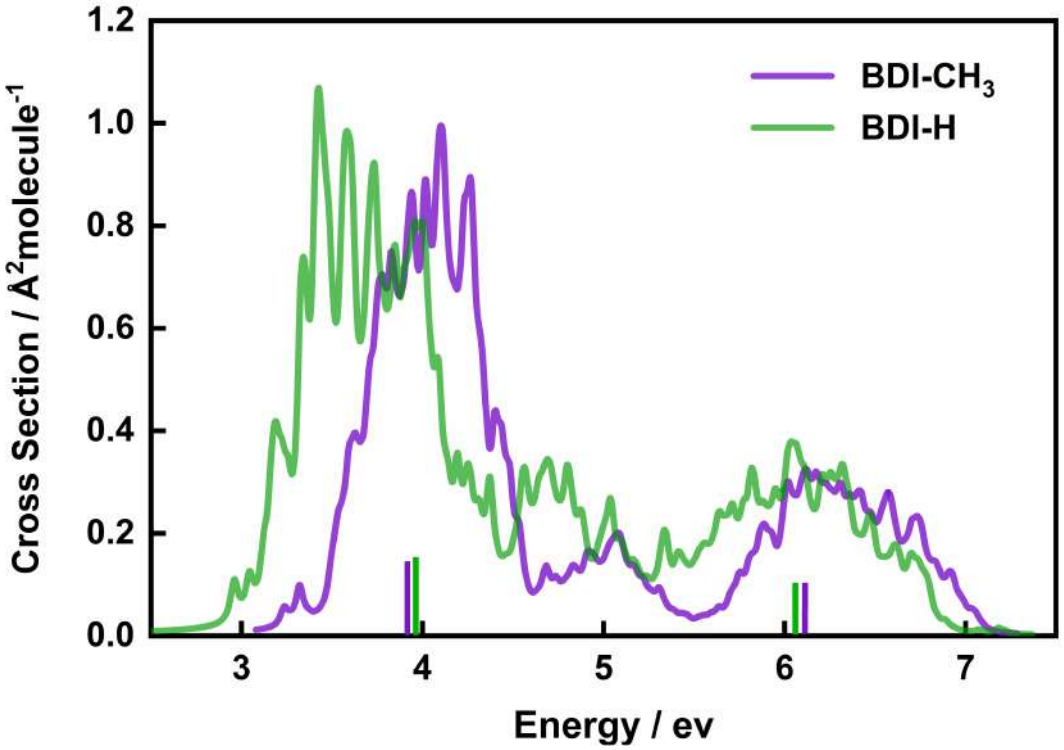


**Figure 5.2:** Absorption cross-sections (Å$^2$ molecule$^{-1}$) of BDI-$CH_3$ monomer (purple) and BDI-H monomer (green) computed using nuclear ensemble approach at TD-$\omega$B97XD/6-31G(d) level of theory. Purple and green vertical bars indicate the most significant oscillator strength for BDI-$CH_3$ and BDI-H monomer.

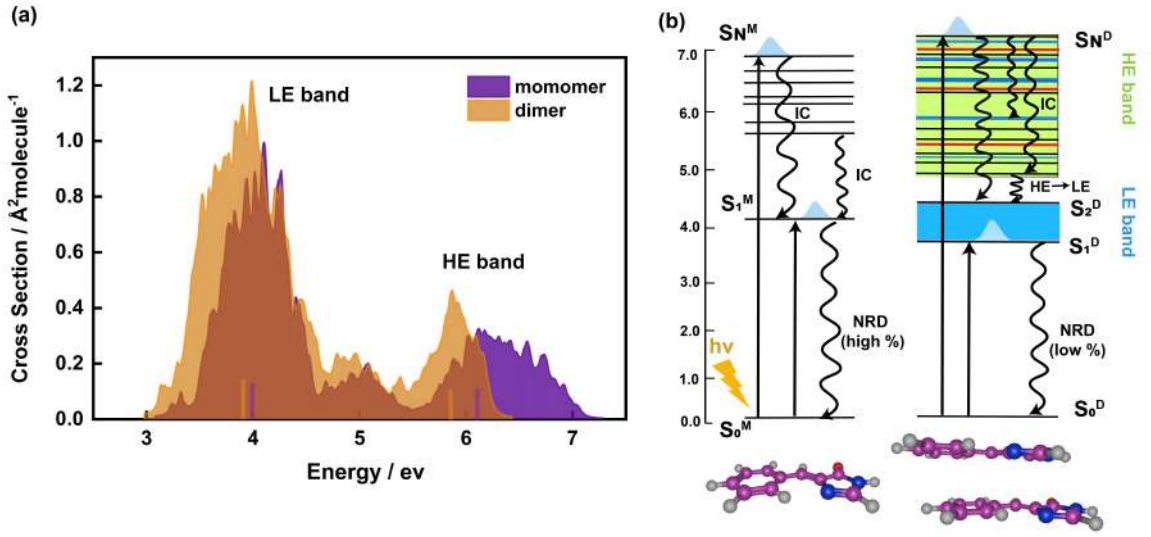


**Figure 5.3:** (a) Absorption cross-sections (Å$^2$ molecule$^{-1}$) of BDI-H dimer (orange) and monomer (purple) computed using a nuclear ensemble approach. Orange and purple vertical bars indicate the most significant oscillator strength for BDI-H dimer and monomer and (b) Upper panel: Schematic representation of vertical transition energies for BDI-H dimer and monomer where $S_N{}^D$ and $S_N{}^M$ indicate the electronic states for the dimer and monomer molecule, NRD and IC denote nonradiative deactivation and internal conversion. Lower panel: Optimized molecular geometries of the BDI-H monomer and dimer. TDDFT ($\omega$B97XD/6-31G(d)) method was implemented.

Figure 5.3(a) illustrates the absorption cross-sections of the BDI-H monomer and $v$dW BDI-H dimer computed using the nuclear ensemble method based on harmonic-oscillator Wigner distributions,[310] whereas Tables C1 and C2 of Appendix C represent the vertical excitation energies and corresponding oscillator strengths. The cross-section derived from the nuclear ensemble simulation was based on 100 points with excitations computed using the TD-$\omega$B97XD/6-31G(d) method ($\delta_J$ = 0.05 eV and eps= 0.005 eV for all electronic states). The vertical excitation energies were calculated at the TDDFT/$\omega$B97XD and ADC(2),[361, 362] methods and 6-31G(d),[370] TZVP,[241] pVTZ,[372] and SV(P),[373] basis sets as detailed in Table C2 of Appendix C. Figure 5.3(a) and Table C2 demonstrate that the absorption cross-section of the BDI-H dimer computed at the TD-$\omega$B97XD/6-31G(d) method exhibits two distinct bands: lower-energy band (LE band, $\sim$ 3.9 eV) and higher-energy band (HE band, $\sim$ 5.7 eV). The HE band is composed of a manifold set of excited states, in which the $S_{15}{}^D$ excited-state possesses a notable oscillator strength ($f$ = 0.018), whereas the LE band arises due to low-lying excited states $S_1{}^D$ and $S_2{}^D$ as depicted in Figure 5.3(b) and Table C2. Due to the asymmetrical ground-state ($S_0$) structure of the BDI-dimer, similar to other noncovalent organic dimers,[329, 374] the low-lying

excited state is split into $S_1{}^D$ state and $S_2{}^D$ state as shown in Figure 5.3(b). However, for monomer, the HE and LE bands are observed at ∼3.9 and ∼6.1 eV, respectively, with $S_6{}^M$ excited-state exhibiting a notable oscillator strength of 0.113 (see Figure 5.3a and Table C1). Figure 5.3(b) illustrates a schematic representation of the mechanistic pathway of the nonradiative deactivation process in the BDI-H dimer and monomer chromophore after photoabsorption to higher-energy excited states.

Nonadiabatic excited-state dynamics of the BDI-H dimer employing the FSSH[19, 194] approach with the TDDFT method was initiated in the higher-energy (HE) excitation window (5.7 ± 0.5 eV) as depicted in Figure 5.3a. FSSH approach by Tully and coworkers,[18, 194] have been widely implemented for the photoinduced ultrafast excited-state nonadiabatic dynamics simulations of biological, organic, and material complexes.[319, 323, 329, 375–377] To simulate the higher-energy excitation of the BDI-H dimer with the FSSH/TDDFT method, a total of 15 excited states were considered, which makes it computationally very expensive. Hence, the simulations were limited to only a few trajectories (i.e., $N_{traj} = 22$). A total of 22 trajectories were run from the $S_{15}$ excited states for a maximum of 500 fs or until reaching a $S_0/S_1$ gap of 0.15 eV. Three (3) trajectories reached the $S_0/S_1$ crossing during the simulation, whereas 19 trajectories still had a significant $S_0/S_1$ energy gap and remained in excited states at 500 fs.

Figure 5.4 illustrates the occupations of the higher-energy excited states ($S_3$-$S_{15}$, HE band) and lower-energy excited states ($S_1$-$S_2$, LE band), along $S_0$ occupation as a function of time. Due to the involvement of more excited states, Figure 5.4 is split into two parts (Figure 5.4, top: $S_0$-$S_8$ and bottom: $S_9$-$S_{15}$). The ultrafast deactivation of the higher-energy excited states is initiated at 16 fs and begins to decay with the subsequent transfer of population to the lower-energy excited states through nonadiabatic transitions. After 100 fs, the occupation of the lower-energy excited states ($S_1$ and $S_2$) increases, with the occupation of $S_1$ reaching ∼45% and $S_2$ reaching about ∼30% within 250 fs. After 300 fs, the occupation of the excited states further oscillates between the LE and HE states and remains nearly constant after 400 fs. Subsequently, the $S_0$ state starts to populate after 125 fs and contains a fraction of ∼13% of the total occupations within 265 fs and remains constant until the end of the simulation. This indicates that nearly 13% of the total population is transferred to the $S_0$ state.

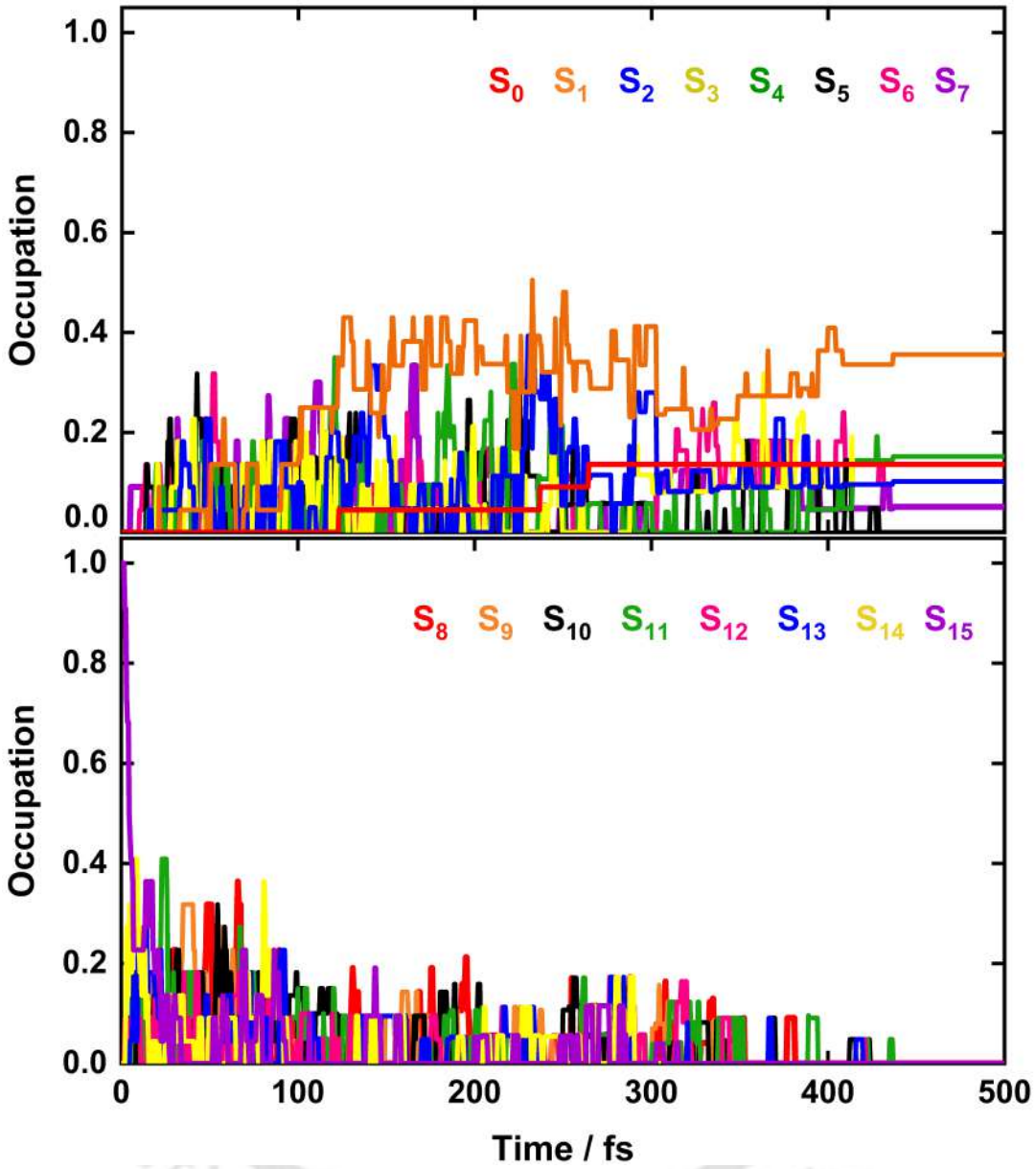


**Figure 5.4:** Occupation of each electronic state of the BDI-H dimer for 500 fs from the nonadiabatic excited-state dynamics at the TD-$\omega$B97XD/6-31G(d) level of theory. Higher-energy states (HE band) comprise excited states from $S_3$ to $S_{15}$, while the lower-energy states (LE band) include $S_1$ and $S_2$ excited states. Excited-state dynamics were initiated by populating higher-energy states (HE band) after 5.7 $\pm$ 0.5 eV excitation.

To acquire a deeper insight into the photophysics and nonadiabatic excited-state dynamics within the BDI-H dimer, Figure 5.5 displays two representative trajectories (TrX and TrY) from the FSSH/TD-$\omega$B97XD dynamics simulation. In Figure 5.5a, TrX represents the trajectories that stopped at $S_0/S_1$ crossing, i.e., $\Delta E(S_1–S_0) <$ 0.15 eV whereas the TrY (Figure 5.5b) represents those that reached the maximum simulation time of 500 fs without reaching the $S_0$ state.

For TrX, at t=0 fs as shown in Figure 5.5Ia, the dimer is asymmetrically linear and lies one above another. As time proceeds, the photoexcited dimer gradually decays from the HE state ($S_3$-$S_{15}$) to the LE state ($S_1$-$S_2$). At t = 32.5 fs, the dimer experiences an initial relaxation from the HE state to the LE state, accompanied by a slight distortion of the complex. However, at t = 52 fs, it reverts to the HE state and remains in this state until t = 118 fs. Furthermore, at t=118 fs, the dimer relaxes back to the LE state, and this behavior continues until t = 265 fs, when the energy difference between $S_1$ and $S_0$ diminishes to less than 0.15 eV, resulting in $S_1/S_0$ intersection, as illustrated in Figure 5.5Ia. As a result, the BDI-H dimer undergoes deformation as shown in Figure 5.5Ia (top), involving the minor rotation of $\Phi_I$- and $\Phi_P$-dihedral angles of the monomer units of the BDI-H dimer accompanied by the transfer of a proton from unit A to unit B. Subsequently, the dimer undergoes radiationless deactivation to the $S_0$ state. This radiationless deactivation process to the $S_0$-state resembles the hula-twist ultrafast internal conversion decay that proceeds through $\Phi_I$-twisted and $\Phi_P$-twisted rotation for the GFP chromophore monomer as reported in several studies.[156, 158, 159, 217]

However, the photoexcited dimer for TrY oscillates between the HE and LE states for a duration ranging from 33.5 to 228.5 fs after which it remains localized in the LE region and does not reach the $S_0$ state with no dihedral angle rotation or proton transfer (PT) process as shown in Figure 5.5Ib.

The time evolution of the hot exciton dynamics is thus primarily influenced by ultrafast nuclear oscillation, specifically, the rotation of the $\Phi_I$- and $\Phi_P$- dihedral angles of each monomer unit within the BDI-H dimer. These torsional dihedral angle rotations are the major nuclear oscillations that lead to nonadiabatic relaxation. To better understand the significance of ultrafast nuclear oscillations in the hot exciton dynamics, we discuss the impact of $\Phi_I$- and $\Phi_P$- dihedral rotations of each monomer unit within the BDI-H dimer as demonstrated in Figure 5.5II and 5.5III.

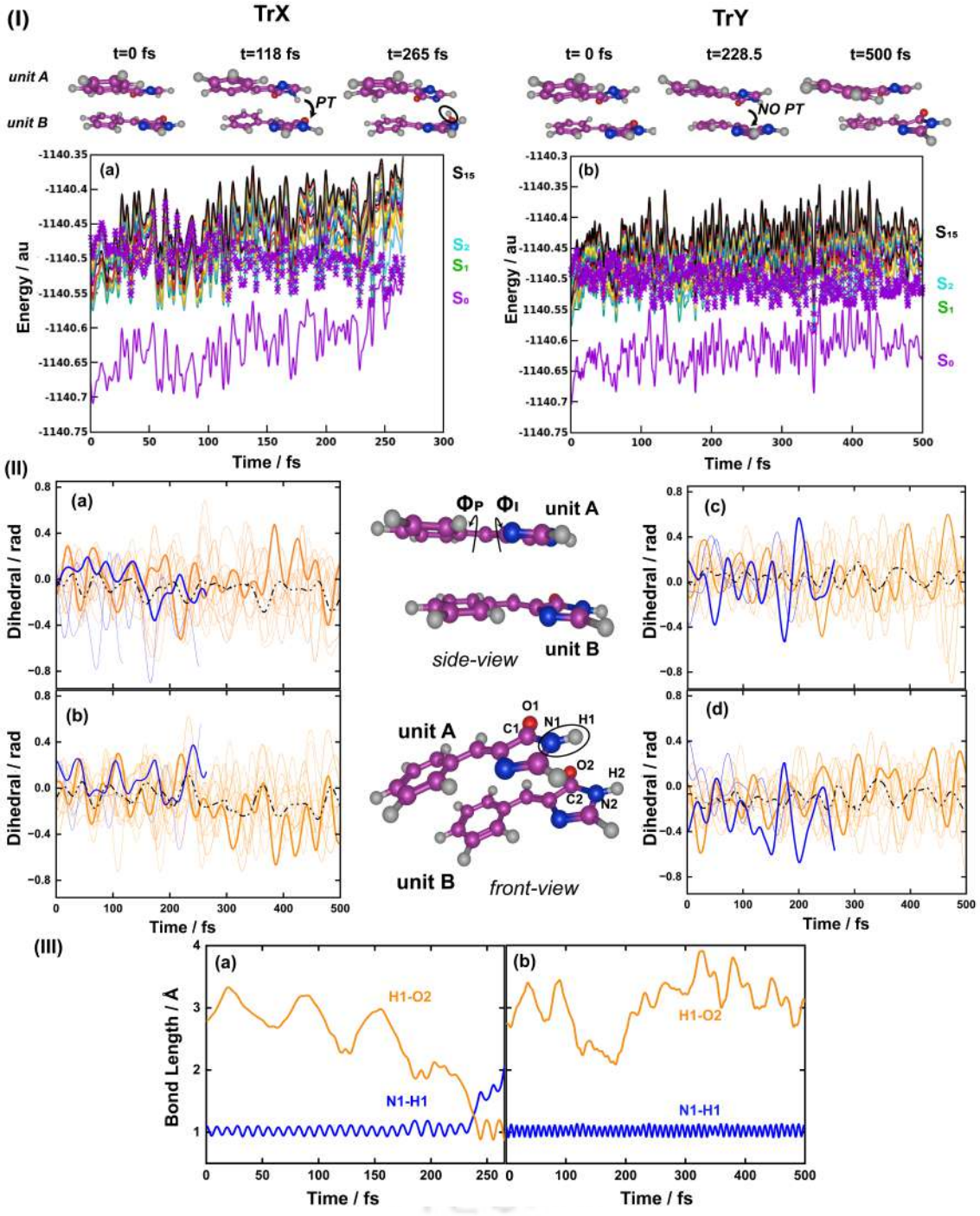


**Figure 5.5:** (I) Time evolution of ground ($S_0$) and excited states ($S_1$-$S_{15}$) energies for two representative trajectories (a) TrX and (b) TrY, computed at the TD-$\omega$B97XD/6-31G(d) level. The dotted purple color signifies the current state. Top: Snapshots of the molecular geometries at the major time steps. PT: proton transfer, NO PT: no-proton transfer. (II) Time evolution of dihedral angle rotations $\Phi_I$- (a & c) and $\Phi_P$- (b & d) within BDI-H dimer. For unit A: (a) & (b), and for unit B: (c) & (d). Blue and orange color indicates trajectories type TrX and TrY, respectively. (III) Time evolutions of average bond distances (N1–H1 and H1–O2) showing (a) PT and (b) No PT process.

In Figure 5.5II, the $\Phi_I$- and $\Phi_P$- dihedral rotations have been illustrated for all

trajectories for the monomer unit A (Figures 5.5IIa and 5.5IIb) and unit B (Figure 5.5IIc and 5.5IId) of the BDI-H dimer. Figure 5.5II shows two distinct behaviors observed for two different types of trajectories. The blue color indicates trajectories of type TrX, while orange is for type TrY, with two bold dihedral angles (representative trajectories for types TrX and TrY). The $\Phi_I$- and $\Phi_P$- dihedral angles are defined by the bridged-bond of the BDI-H chromophore, as illustrated in the middle column of Figure 5.5II. Figures 5.5II (a-d) illustrate that for TrX, upon photoexcitation, the chromophore remains planar for several hundreds of femtoseconds, subsequently followed by the transfer of excitons from the HE to LE states after 118 fs. This causes an increase in the degree of oscillations for both $\Phi_I$- and $\Phi_P$-dihedral angles (for unit A and unit B), as indicated by the blue bold representative TrX. The increase in the degree of oscillations leads to the twisting of the $\Phi_I$- and $\Phi_P$- dihedral angles with the simultaneous transfer of a proton from unit A to unit B, as illustrated in Figure 5.5Ia (top, molecular geometries) and Figure 5.5III(a). Upon PT, the oscillation of $\Phi_I$- and $\Phi_P$- dihedral angles decreases, and the chromophore retains its planar geometry. This phenomenon resulted in exciton localization and subsequent radiationless decay via crossing between $S_1$ and $S_0$ states at t = 265 fs.

On the other hand, for trajectory TrY, the chromophore remains planar for the initial few femtoseconds similar to TrX, as the exciton fluctuates between the HE to LE regions until 228.5 fs. After 228.5 fs, the exciton remains localized in the LE region, and the degree of oscillations for dihedral angles increases but the complex remains planar until the end of the simulation without distorting the structure and no PT between the monomer units occurs, as shown by the orange (bold) plot of Figures 5.5Ib (top, molecular geometries), 5.5II, and 5.5IIIb. This observation indicates that the planarity in TrY reduces the probability of radiationless deactivation in the BDI-H dimer complex.

To gain a profound comprehension of the photophysics and the nature of the exciton dynamics, we have computed the electron-hole analysis of the BDI-H dimer for all the excited states and plotted the natural transition orbitals (NTOs) along with the Ω-plots (or electron-hole correlation plot) for the corresponding times of the simulations as represented in the Figure 5.6. Also, Tables 5.2(a-b) and Table C3 represent the summaries of various parameters of exciton properties for 15 singlet excited states of the BDI-H dimer for two representative trajectories, TrX and TrY, at three corresponding times.

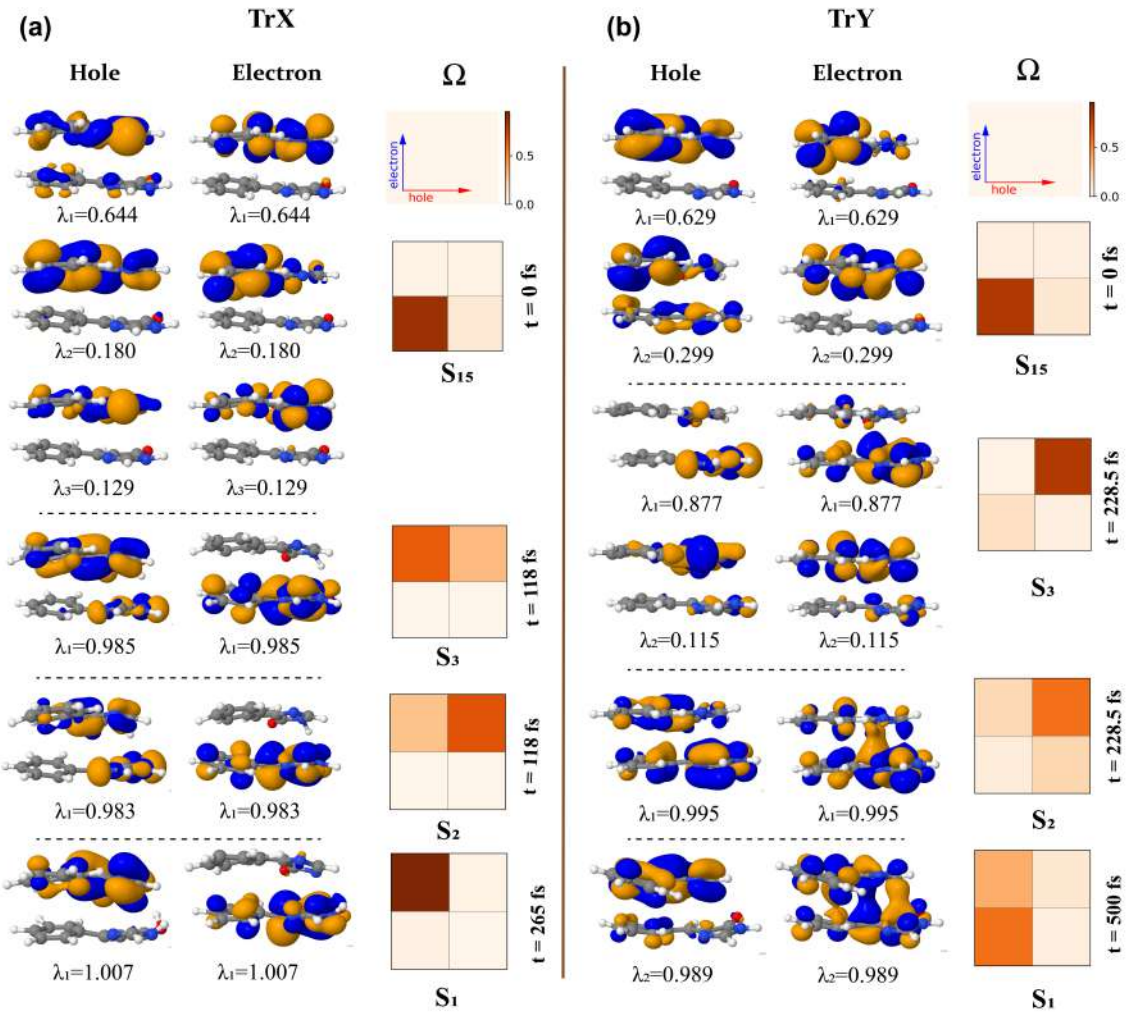


**Figure 5.6:** Natural transition orbitals (NTOs) of the running excited state of the exciton of BDI-H van der Waals ($v$dW) dimer for the two representative trajectories (a) TrX and (b) TrY, computed at the TD-$\omega$B97XD/6-31G(d) level of theory. Isosurface value of 0.03 was considered. Ω column: Plot of the Ω matrix (or electron-hole correlation plot).

For electron-hole analysis, the complex is divided into two fragments and labeled as unit A (fragment 1) and unit B (fragment 2), and the NTOs for the cases of two representative trajectories (TrX and TrY) at different simulation times are shown in Figure 5.6. For the trajectory TrX, initially at t = 0 fs, there are three transitions with amplitude $\lambda_1 = 0.644$, $\lambda_2 = 0.180$, and $\lambda_3 = 0.129$, whereas, TrY exhibits two transitions with amplitude $\lambda_1 = 0.629$ and $\lambda_2 = 0.299$, $\lambda_1$ being the dominant one in both cases as depicted in Figure 5.6. For both trajectories, at the initial simulations (t = 0 fs) the excitation (both hole and electron) may be entirely localized on the same fragment i.e., a Frenkel exciton[365, 378] as demonstrated by the NTOs of the $S_{15}$ (running) state and Ω- plot as shown in Figure 5.6. The pure Frenkel exciton character at t = 0 fs is further proved by the CT character ($\omega_{CT}$) and coherence

length ($\omega_{COH}$) values of 0.12($\approx$ 0) and 1.14 for TrX, and 0.14($\approx$ 0) and 1.19 for TrY, respectively, as characterized in Table C3. However, for TrX at t = 118 fs (see Figure 5.6a), the NTOs and Ω-plots suggest the delocalization of the exciton within units A and B with amplitude of transitions $\lambda_1$= 0.985 ($S_3$) and $\lambda_1$=0.983 ($S_2$). This is further validated by CT character ($\omega_{CT}$, $S_3$=0.67 and $S_2$=0.30) and coherence length ($\omega_{COH}$, $S_3$=1.30 and $S_2$=1.28) as shown in Table C3 of the Appendix C, signifying an even mixture between Frenkel and CT character.[379] In contrast, for TrY at t=228.5 fs (see Figure 5.6b), both the electron and hole in the $S_3$ state are localized in either unit A or B ($\omega_{CT}$ = 0.07 and $\omega_{COH}$ = 1.10, Table C3) with a major contribution of $\lambda_1$=0.877, indicating the Frenkel nature of exciton. Meanwhile, the $S_2$ state ($\lambda_1$=0.995) exhibits a mixture of Frenkel and CT characters ($\omega_{CT}$ = 0.38 and $\omega_{COH}$ = 1.61, Table C3) with both the electron and hole delocalized in unit A and B.[379] Thus, there are significant qualitative differences in wavefunction character between the two trajectories (i.e., TrX and TrY) while going from HE to LE region. At time t=118 fs (TrX) and t=228.5 fs (TrY), we considered the excitonic properties in $S_2$ and $S_3$ states, as the exciton is transferred from $S_3$ state (HE state) to $S_2$ state (LE state).

Subsequently, the $S_1 \rightarrow S_0$ nonadiabatic deactivation occurs at t = 264 fs for TrX, resulting in the localization of electron in unit B and hole in unit A, indicating the CT character which is further supported by the Ω-plot and excitonic properties ($\omega_{CT}$= 0.947 $\approx$ 1 and $\omega_{COH}$ = 1.06), as demonstrated in Figure 5.6a and Table 5.2a. On the other hand, for TrY at t=500 fs, the electron density is delocalized between units A and B with hole intensity in unit A, suggesting the existence of a Frenkel-type excitonic resonance state ($\omega_{CT}$ = 0.38 $\approx$ 0 and $\omega_{COH}$ = 1.54) (see Figure 5.6b and Table 5.2b). Thus, this discussion concludes that at the end of simulation, in TrX, there is $S_1 \rightarrow S_0$ nonadiabatic deactivation due to the CT nature of the exciton, whereas for TrY, the electron and hole density is delocalized leading to the localization of exciton within the LE states. Further, the change in wavefunction character for TrX and TrY is also reflected through the exciton size ($\tilde{d}_{exc}$) i.e., the averaged distance between the electron and hole quasiparticles. An exciton size with values higher than 4 Å is indicative of CT contribution while below or equal reflects pure local excitation. Thus, Table 5.2a and Table C3(I) demonstrates that TrX exhibits $\tilde{d}_{exc}$ values of 3.17 at t=0 fs, 3.82 ($S_2$) and 4.28 ($S_3$) at t=118 fs, and 4.26 at t=264 fs, indicating the CT character during the $S_1 \rightarrow S_0$ nonadiabatic deactivation. For TrY, $\tilde{d}_{exc}$ is 3.87 at

t=0 fs, 3.91 ($S_2$) and 3.27 ($S_3$) at t=229 fs, and 3.89 at t=500 fs as tabulated in Table 5.2b and Table C3(II), indicating the Frenkel excitonic state at the end of simulation.

**Table 5.2:** Mean position of hole and electron (POS), Excitonic participation ratio (PR), charge transfer ratio ($\omega_{CT}$), coherence length ($\omega_{COH}$), natural transition orbital participation ratio ($PR_{NTO}$), number of entangled states ($Z_{HE}$) and exciton size ($\tilde{d}_{exc}$, Å) for singlet excited states of the BDI-H *v*dW dimer for two representative trajectories (a) TrX, t=265 fs and (b) TrY, t=500 fs.

**(a) TrX**

| state | POS | PR | $\omega_{CT}$ | $\omega_{COH}$ | $PR_{NTO}$ | $Z_{HE}$ | $\tilde{d}_{exc}$ |
|---|---|---|---|---|---|---|---|
| **$S_1$** | **1.49** | **1.06** | **0.95** | **1.06** | **1.00** | **1.01** | **4.26** |
| $S_2$ | 1.48 | 1.05 | 0.95 | 1.05 | 1.00 | 1.02 | 4.03 |
| $S_3$ | 1.49 | 1.07 | 0.93 | 1.07 | 1.02 | 1.05 | 4.46 |
| $S_4$ | 1.49 | 1.07 | 0.93 | 1.07 | 1.01 | 1.04 | 3.98 |
| $S_5$ | 1.49 | 1.09 | 0.91 | 1.09 | 1.01 | 1.04 | 5.68 |
| $S_6$ | 1.15 | 1.33 | 0.08 | 1.10 | 1.35 | 1.65 | 3.27 |
| $S_7$ | 1.49 | 1.99 | 0.11 | 1.23 | 2.05 | 2.21 | 3.33 |
| $S_8$ | 1.31 | 1.74 | 0.08 | 1.15 | 1.83 | 2.06 | 3.25 |
| $S_9$ | 1.95 | 1.09 | 0.09 | 1.09 | 1.04 | 1.13 | 3.95 |
| $S_{10}$ | 1.97 | 1.07 | 0.06 | 1.06 | 1.02 | 1.07 | 3.09 |
| $S_{11}$ | 1.49 | 1.06 | 0.94 | 1.06 | 1.10 | 1.25 | 4.62 |
| $S_{12}$ | 1.52 | 1.16 | 0.86 | 1.16 | 1.09 | 1.24 | 4.06 |
| $S_{13}$ | 1.53 | 1.17 | 0.85 | 1.17 | 2.10 | 2.28 | 4.49 |
| $S_{14}$ | 1.54 | 1.15 | 0.87 | 1.14 | 2.02 | 2.09 | 4.64 |
| $S_{15}$ | 1.21 | 1.48 | 0.34 | 1.35 | 2.59 | 3.02 | 4.07 |

**(b) TrY**

| state | POS | PR | $\omega_{CT}$ | $\omega_{COH}$ | $PR_{NTO}$ | $Z_{HE}$ | $\tilde{d}_{exc}$ |
|---|---|---|---|---|---|---|---|
| **$S_1$** | **1.28** | **1.64** | **0.38** | **1.54** | **1.05** | **1.15** | **3.89** |
| $S_2$ | 1.67 | 1.74 | 0.34 | 1.59 | 1.15 | 1.37 | 3.91 |
| $S_3$ | 1.17 | 1.39 | 0.26 | 1.34 | 1.54 | 1.79 | 3.64 |
| $S_4$ | 1.28 | 1.59 | 0.42 | 1.48 | 1.43 | 1.74 | 3.90 |
| $S_5$ | 1.86 | 1.34 | 0.23 | 1.25 | 1.57 | 1.88 | 3.55 |
| $S_6$ | 1.74 | 1.61 | 0.33 | 1.49 | 1.22 | 1.51 | 3.97 |
| $S_7$ | 1.74 | 1.56 | 0.44 | 1.44 | 1.41 | 1.72 | 4.01 |
| $S_8$ | 1.08 | 1.18 | 0.06 | 1.07 | 1.41 | 1.84 | 3.66 |
| $S_9$ | 1.18 | 1.42 | 0.11 | 1.16 | 1.43 | 1.89 | 3.53 |
| $S_{10}$ | 1.64 | 1.59 | 0.57 | 1.54 | 1.787 | 2.21 | 4.04 |
| $S_{11}$ | 1.84 | 1.36 | 0.24 | 1.31 | 1.51 | 1.89 | 3.78 |
| $S_{12}$ | 1.49 | 1.16 | 0.87 | 1.15 | 1.08 | 1.22 | 4.21 |
| $S_{13}$ | 1.22 | 1.52 | 0.26 | 1.36 | 2.17 | 2.75 | 4.08 |
| $S_{14}$ | 1.53 | 1.85 | 0.36 | 1.74 | 2.29 | 3.12 | 3.59 |
| $S_{15}$ | 1.14 | 1.32 | 0.17 | 1.22 | 1.76 | 2.49 | 3.49 |

This ultrafast higher-energy excited-state nonradiative deactivation pathway closely resembles the $S_1 \rightarrow S_0$ ring opening mechanism previously observed for bithiophene monomers and dimer complexes.[323, 329, 377] As noted in the previous section, the fraction of trajectories reaching the $S_0$ state is significantly lower in the BDI-H dimer due to the hindrance in torsional dihedral angle rotations caused by $\pi$-$\pi$ stacking van der Waals interactions. Thus, excited-state nonradiative pathways in the BDI-H dimer are influenced by $\Phi_I$- and $\Phi_P$-torsional rotation followed by the transfer of a proton from one monomer unit to another unit of the dimer, resulting in deactivation of the exciton to its $S_0$-state.

Further to validate the mechanistic insights into the occurrence of reduced radiationless deactivation in the dimer, we analyzed the single-point TDDFT [$\omega$B97XD/6-31G(d)] potential energy profiles of the ground ($S_0$) and excited ($S_1$, $S_2$, $S_3$, and $S_{15}$ for dimer; $S_1$, $S_2$, $S_3$, and $S_6$ for monomer) states along $\Phi_I$- and $\Phi_P$-dihedral angles of BDI-H dimer and monomer as depicted in Figure 5.7. Since for monomer, the HE band and LE band are observed at ~3.9 eV and ~6.1 eV, respectively, with $S_6$ exhibiting a notable oscillator strength of 0.113 (see Figure 5.3 and Table C1), so the monomer analysis was focused up to the $S_6$ excited states. Figure 5.7Ia and Table 5.3 demonstrate that for $\Phi_I$- dihedral rotation of a monomer unit within the BDI-H

dimer, a substantial energy barrier of 4.661 eV ($S_1$) must be surmounted. In contrast, the rotation process in the monomer proceeds with a very low energy barrier of 0.316 eV ($S_1$), and there involves the occurrence of an intersection at 90° between the $S_1$ and $S_0$ states (Figure 5.7Ib and Table 5.3). A significant energy barrier in the $S_1$ profile of the dimer hinders nonradiative transitions, which accounts for a comparatively slower return to the $S_0$ state. On the other hand, the existence of a low energy barrier in the $S_1$ state and the occurrence of $S_1/S_0$ crossing facilitate the nonadiabatic radiationless deactivation in the monomer. Further, the dimer exhibits notably higher excited-state energy barriers of 3.548 eV ($S_2$), 3.545 eV ($S_3$), and 4.795 eV ($S_{15}$), compared to the monomer, which has energy barriers of 1.259 eV ($S_2$), 1.892 eV ($S_3$), and 1.308 eV ($S_6$), as depicted in Figures 5.7Ia, 5.7Ib, and Table 5.3.

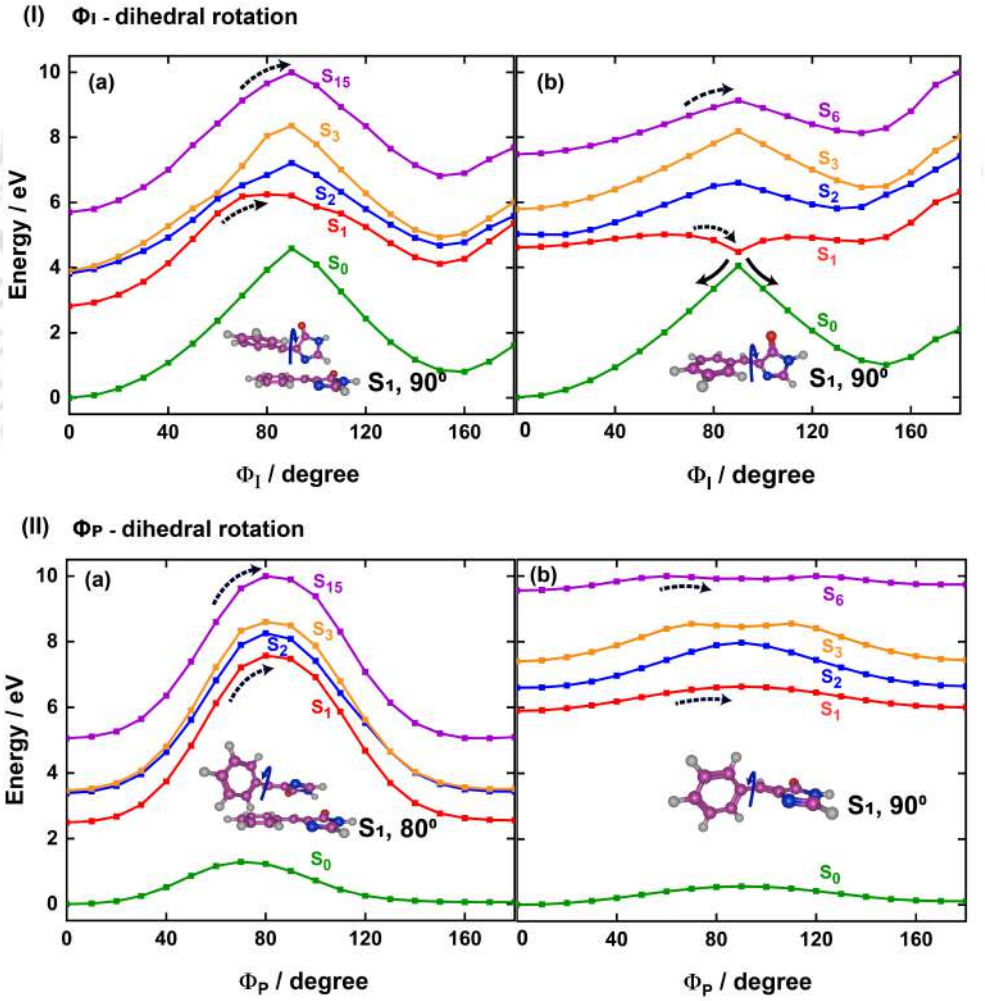


**Figure 5.7:** Single-point potential energy profiles of BDI-H dimer and monomer along (I) $\Phi_I$- dihedral rotation and (II) $\Phi_P$- dihedral rotation, at the ground ($S_0$) and excited states ($S_1$, $S_2$, $S_3$, $S_6$, and $S_{15}$) computed at the TD-$\omega$B97XD/6-31G(d) level of theory. For dimer, LE states ($S_1$ and $S_2$) and HE states ($S_3$ and $S_{15}$) are considered (a) and (c), whereas for monomer LE state ($S_1$) and HE states ($S_2$, $S_3$, and $S_6$) are considered (b) and (d).

Similarly, to occur $\Phi_P$-torsional rotation in BDI-H dimer, higher potential energy barriers of 5.987 eV ($S_1$), 5.743 eV ($S_2$), 6.056 eV ($S_3$), and 5.826 eV ($S_{15}$) are required (see Figure 5.7IIa and Table 5.3), while in monomer relatively lower energy barriers of 0.457 eV ($S_1$), 0.849 eV ($S_2$), 0.652 eV ($S_3$), and 0.272 eV ($S_6$) are needed (see Figure 5.7IIb and Table 5.3). As a result, dihedral rotation plays a pivotal role and predominantly drives the exciton relaxation from the excited states to the ground state.

**Table 5.3:** Summary of $\Phi_I$- and $\Phi_P$- torsional energy barrier ground ($S_0$) and excited states ($S_N$). $S_N$ for monomer: $S_1$, $S_2$, $S_3$, and $S_6$, whereas $S_N$ for dimer: $S_1$, $S_2$, $S_3$, and $S_{15}$, respectively. Note: Due to the expensive computational cost of higher energy excited states energy barrier calculation, our focus has been directed towards analyzing the most significant states. All values are in eV.

| | | | **$\Phi_I$-dihedral** | | | |
|---|---|---|---|---|---|---|
| **BDI-H** | $\Delta S_0$ | $\Delta S_1$ | $\Delta S_2$ | $\Delta S_3$ | $\Delta S_6$ | $\Delta S_{15}$ |
| **Dimer** | 4.494 | 4.661 | 3.548 | 3.545 | - | 4.795 |
| **Monomer** | 3.198 | 0.316 | 1.259 | 1.892 | 1.308 | - |
| | | | **$\Phi_P$-dihedral** | | | |
| **Dimer** | 1.451 | 5.987 | 5.743 | 6.056 | - | 5.826 |
| **Monomer** | 0.348 | 0.457 | 0.849 | 0.652 | 0.272 | - |

Thus, the energetics of the lowest $\pi\pi^*$ state within the proximity of the $S_1/S_0$ region is responsible for significant variation in reaction pathways in the BDI-H dimer and monomer along $\Phi_I$- and $\Phi_P$- dihedral rotations. The low-energy barrier of the $\Phi_I$- and $\Phi_P$- dihedral angle in the $S_1$ state leads to $S_1/S_0$ deactivation in the monomer, while for the dimer the energy dramatically increases due to hindered $\Phi_I$- and $\Phi_P$- dihedral rotations. This hindrance in rotation occurred as a result of weak $\pi$–$\pi$ stacking interactions in the dimer. Hence, the interactions associated with $\pi$–$\pi$ stacking alter the configuration of the potential energy surfaces in the excited states, which in turn regulate the exciton dynamics in the BDI-H chromophore. Therefore, higher potential energy barriers of excited states can be attributed to the hindered torsional dihedral angle rotations that arise due to the $\pi$–$\pi$ stacking interaction in the dimer. This collectively leads to an elongation in the duration of low-lying excited states, i.e., $S_1$ and $S_2$ which in turn reduces the nonadiabatic radiationless deactivation to the $S_0$ state in the BDI-H dimer.

## 5.4 Conclusions

In conclusion, we have investigated the photophysics of high energy (hot) excitons and their ultrafast nonadiabatic deactivation processes of GFP chromophore analogue, i.e., BDI-H chromophore. The results provide a rationalization of the ultrafast behavior of the exciton in a dimer after photoabsorption of light to higher-energy excited states. The time evolution and relaxation process evidenced that the ultrafast relaxation of hot excitons to the $S_0$-state is mainly driven by $\Phi_I$- and $\Phi_P$- dihedral rotations within the monomer units of BDI-H dimer. As it has been known that the GFP chromophore analogue, outside the protein environment, undergoes efficient $S_1 \rightarrow S_0$ deactivation through the $S_1/S_0$ intersection due to $\Phi_I$- and $\Phi_P$- dihedral rotation, the formation of the $\pi$-$\pi$ stacking complex might serve as an initial step in the nonadiabatic mechanisms that enhance the photostability of the chromophore. Our findings are consistent with exciton dynamics governing charge generation and energy transfer in photoreactive $\pi$-electron conjugated systems. Hence, this study demonstrates the usefulness of the quantitative electronic structure method combined with surface-hopping analysis to unravel the higher-energy nonadiabatic excited-state dynamics for a GFP chromophore dimer and provides a route to design efficient photoactive biological chromophores.

# Chapter 6

# Multidimensional Excited-State Dynamics of an Ortho Derivative GFP Chromophore

(The work of this Chapter will be communicated soon.)

## 6.1 Introduction

The photoinduced excited-state intra and intermolecular proton transfer (ESIPT) process has gathered numerous experimental and computational studies, since it plays a fundamental role in several chemical and biological phenomena.[94, 380–386] Proton transfer in the excited state can proceed adiabatically or non-adiabatically upon photoexcitation, depending on the nature of the respective systems. However, the excited-state intramolecular proton transfer (ESIPT) is particularly significant in photochemistry due to its remarkably large Stokes' shift fluorescence, which occurs without self-reabsorption.[385–388] It also possesses other unique characteristics, such as ultrafast dynamics,[389–391] dual emission,[388] and spectral sensitivity to the surrounding environment.[392] Molecules exhibiting ESIPT phenomena have been found applicability in a wide range of fields, including organic light-emitting diodes (OLEDs),[393] proton-transfer laser,[394, 395] photostabilizers,[396, 397] white light generation,[208, 398, 399] thermally activated delayed fluorescence (TADF) based devices,[400, 401] photochromic switching,[380, 402] optoelectronics materials,[388, 403] anions and cations sensing,[404, 405] and information storage device.

During the ESIPT process, the $\pi$-conjugated moieties or molecules are interconnected through hydrogen bonding, and the system predominantly exists in its normal enol form (N) in the ground state. Upon photoexcitation, intramolecular proton transfer occurs, leading to the formation of tautomer (T) in keto form. The energy

barrier associated with ESIPT governs the equilibrium between these two forms, resulting in various intriguing photophysical properties of the molecules, including the occurrence of either single or dual fluorescence.[268, 388, 406] By facilitating the proton exchange between two electronegative centers of $\pi$-conjugated moieties along the pre-existing intramolecular hydrogen bonds, the ESIPT phenomena has been considered as an effective mechanism to provide an photostability to such systems. The energy barrier of the ESIPT is influenced by several factors such as hydrogen bonding, electron donating or withdrawing groups, solvent, and pH.[388, 406–411] Thus, the reaction dynamics and potential energy barrier of the proton transfer have been a subject of extensive studies. ESIPT typically occurs in ultrafast time scale, often within 100 fs.[382, 386, 412–414] In recent years, tremendous progress on the detailed mechanism of ESIPT has been made both experimentally and theoretically.

Recent research has extensively investigated the excited-state proton transfer reactions in Green Fluorescent Protein (GFP) chromophore and its derivatives, which emerge as a potential application for bioimaging technique.[94, 95, 116, 127, 230, 304, 415–417] These fundamental insights into the proton transfer process in GFP chromophores have inspired rational design strategies and further exploration of their derivatives. Thus, we focus on the unique excited-state intramolecular proton transfer (ESIPT) mechanism in ortho derivatives of GFP chromophore.[229, 230, 303, 417–419] Since the chromophore, *p*-hydroxybenzylideneimidazolinone (*p*-HBDI), located at the core is conformationally locked within the protein $\beta$-barrel through covalent and hydrogen bonding, and is responsible for its high fluorescence quantum yield ($\Phi_f$ = 0.8).[88] And excited state proton transfer (ESPT) from the chromophore occurs via a proton relay involving water molecules and the remote E222 residue. However, outside the protein environment, the chromophore is observed to be nonemissive ($\Phi_f$ < $10^{-3}$) at room temperature due to the ultrafast exocyclic methine-bridged single and double bond rotations in excited-state.[95, 104, 124, 152]

Extensive experimental and theoretical investigations have been reported over the past few decades to mimic and enhance the photophysical properties of GFP chromophore without the confinement effect of the $\beta$-barrel. Various strategies have been explored to improve the fluorescence quantum yield by inhibiting *cis-trans* photoisomerization. These include the incorporation of bulky groups into the benzylidene or imidazolinone moieties,[420–422] metal complexation,[167, 415] intermolecular or intramolecular hydrogen-bonded cyclization,[164, 229, 230, 304, 415, 416] complexing

with BODIPY,[217, 415] etc. In light of these, Chao and co-workers,[418] synthesized ortho-hydroxy GFP analogue, 4-(2-hydroxybenzylidene)- 1H-imidazol-5(4H)-one denoted as *o*-HBDI, which showed a distinct photophysical behavior characterized by ultrafast excited-state intramolecular proton transfer (ESIPT) upon excitation, followed by *cis-trans* isomerization. The ESIPT process between the hydroxyphenyl and imidazolinone group hinders the exocyclic single and double bond rotations, thereby reducing the radiationless deactivation. Following this finding, several groups has further reported a range of ortho-hydroxy HBDI and investigated their photophysical properties, elucidating the role of the electronic effects of the substituent on the fluorescence quantum yield.[215, 218, 229, 230, 303, 416, 417, 419, 423] Moreover, Cui and coworkers investigated the photoinduced dynamics of *o*-HBDI and identified the occurrence of six minimum energy conical intersection geometries (MECIs) between the excited ($S_1$) and ground ($S_0$) states.[303, 417] They also reported that the ultrafast ESIPT occurs within 20 fs based on the semi-empirical methods, with the excited-state dynamical results depending on the number of beads used in the simulations.[417] Despite many experimental and theoretical studies, a comprehensive investigation of the excited-state dynamics of *o*-HBDI through various channels using ab initio methods remains limited. Hence, in the present work, we explore the photoinduced reaction mechanism along with the possibilities of various internal conversion pathways and excited-state dynamics using the ab initio CASSCF/XMS-CASPT2 methods.

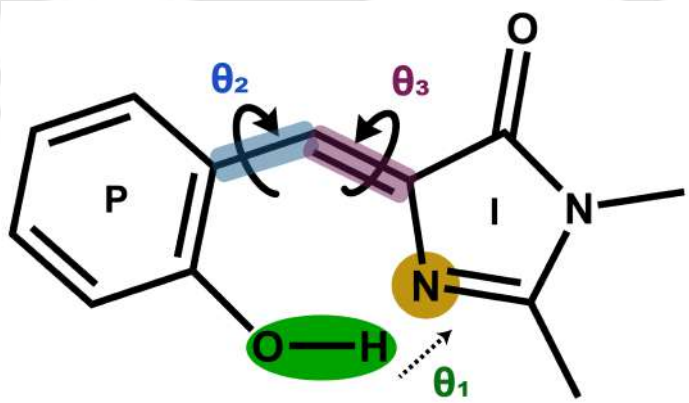


**Figure 6.1:** Molecular representation of the *o*-HBDI chromophore demonstrating the key reaction mechanisms. $\theta_1$ denotes the PT reaction from hydroxyphenyl to imidazolinone ring while $\theta_2$, and $\theta_3$ represent the torsional motion associated with exocyclic single and double bond rotations, respectively.

## 6.2 Methods

### 6.2.1 Electronic Structure Calculations

The electronic structure of *o*-HBDI chromophore and its configurational isomers in ground and excited states was mainly described by state-average complete active space self-consistent field (SA-CASSCF)[181, 307] and extended multistate complete active space second-order perturbation (XMS-CASPT2) [185, 187] methods. The state-averaging approach includes the three singlet electronic states with equal weights. The XMS-CASPT2 method was implemented to incorporate the dynamic correlation effects, providing more accurate energies for all optimized geometries and minimum energy potential energy profiles that CASSCF cannot provide. An active space combination of ten electrons in nine orbitals and four electrons in four orbitals were considered, comprising $\pi$ and $\pi^*$ type orbitals, as shown in Figure S1. All the calculations employed cc-pVDZ basis set combined with the cc-pVDZ-jkfit auxiliary basis for density fitting. We perform XMS-CASPT2 calculations using the CASSCF reference wavefunction with a real vertical shift of 0.3 au to address an intruder state problem.[424] The single-state single-reference (SS-SR) contraction scheme was used during the calculations.[425] The vibrational frequency calculation at the optimized ground and excited state minima showed no imaginary frequencies, confirming their characterization as true minima. The minimum energy conical intersections (MECIs) obtained between the $S_1$ and $S_0$ states were also optimized using both the CASSCF and XMS-CASPT2 levels of theory. The vertical excitation energies of *o*-HBDI chromophore were calculated using varying active space and different theoretical methods, with results compared against the experimental data to identify the optimal approach for further calculations. Subsequently, the linear interpolation in internal coordinates (LIICs)[309] between the critical geometries and the minimum-energy conical structures (MECIs) were implemented to investigate the potential energy surface and explore the reaction pathways of the *o*-HBDI chromophore. All these electronic structure calculations were performed using the BAGEL[308] and Turbomole[426, 427] program packages.

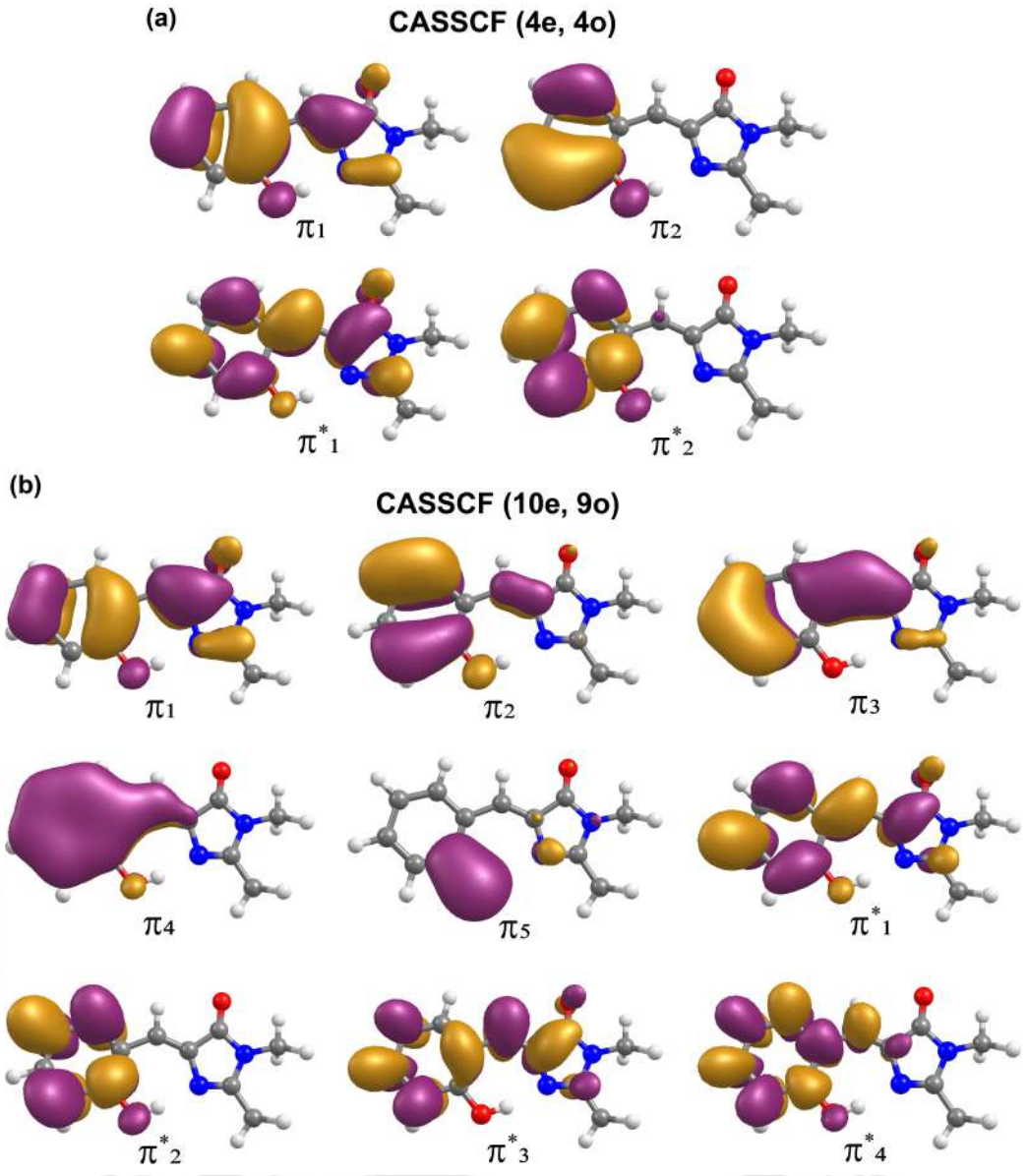


**Figure 6.2:** SA-CASSCF/cc-pVDZ computed natural orbitals utilized in the calculation of *o*-HBDI geometries, with active spaces of (a) CAS(4,4), and (c) CAS(10,9). All orbitals are of $\pi$ type.

### 6.2.2 Dynamics Simulations

We employed the nuclear ensemble approach (NEA) based on harmonic-oscillator Wigner distributions[310] to simulate the photoabsorption cross-section of the o-HBDI chromophore and generate the initial conditions for subsequent nonadiabatic dynamics simulations. A total of 100 ground-state geometries at 298 K, representing its nuclear probability density, were considered to sample the initial conditions. The excitation energies and the corresponding oscillator strength were computed for all

the geometries to simulate the photoabsorption cross-section of *o*-HBDI. The photoabsorption cross-section was constructed by employing a Lorentzian line shape and a phenomenological broadening ($\delta$) value of 0.1 eV[310] at the CASSCF(4,4)/cc-pVDZ level of theory, subsequently followed by the nonadiabatic dynamics simulation. To avoid inadvertent concentration on an incorrect spectral region, the initial conditions were considered without any energy restrictions. The ultrafast nonadiabatic dynamics simulation of *o*-HBDI is computed using Tully's fewest-switches surface hopping (FSSH)[18, 19, 194] method at the same level. During FSSH dynamics, the energy-based decoherence approach was applied to account for the coherence effect using the recommended value of 0.1 au.[195] The Velocity-Verlet algorithm was implemented to integrate Newton's classical equation of motion with the time-step of 0.5 fs, while the unitary propagation method was used to solve the time-dependent electronic Schrödinger equation of motion. Upon excitation to $S_1$ state, all the trajectories were propagated on-the-fly, with the potential energies, energy gradients, and nonadiabatic couplings computed at each time step. The trajectories were computed to a maximum simulation of 300 fs, since the ab initio dynamics of such larger molecules is computationally very expensive. Hence, this study mainly focused on the ESIPT reaction. The entire FSSH dynamics were carried out in Newton-X[311] molecular dynamics simulation program interfaced with the BAGEL[308] electronic structure package.

## 6.3 Results & Discussion

### 6.3.1 Molecular Geometries and Electronic Properties

Due to the unique photophysical properties, the photophysics of the GFP chromophore and its derivatives have been extensively investigated. We start the discussion by characterizing the key geometries and electronic states involved during photoexcitation of the ortho-hydroxy substituted derivative (*o*-HBDI) of GFP chromophore. The photoinduced reaction of *o*-HBDI was observed to proceed along three distinct configurational channels: $\theta_1$ corresponding to the proton transfer reactions along O9-H10 bond coordinate, $\theta_2$ and $\theta_3$ denoting the torsional motions associated with exocyclic single (C2-C3) and double (C4-C3) bond rotations, respectively, as shown in Figure 6.1. The optimized ground state minimum ($S_0$) has the enol (E)

structural isomeric form, whereas the excited state minimum ($S_1$) exhibits the keto (K) form. The $S_0$ and $S_1$ state minima, and the corresponding enol and keto isomers, are calculated at both the CASSCF and XMS-CASPT2 levels of theory using cc-pVDZ basis sets. These relevant geometries at XMS-CASPT2(10,9)/cc-pVDZ level are illustrated in Figure 6.3, highlighting the significant geometric parameters and atom numbering scheme. It shows that both the $S_0$-min and $S_1$-min adopt a planar configuration with Cs symmetry, characterized by the hydroxyphenyl (C1-C2-C3-C4 or $\Phi_P$-) and imidazolinone (N5-C4-C3-C2 or $\Phi_I$-) dihedral angle of 0°. In the $S_0$-min state isomer of *o*-HBDI, the phenol (C2-C3) bond exhibits single bond character with a bond length of 1.452 Å, whereas the imidazolinone (C4-C3) bond possesses double bond character with a bond length of 1.378 Å . Unlike the GFP chromophore, where the C2-C3 bond compresses to form a double bond character and the C4-C3 bond elongates adopting a single bond character upon photoexcitation, both C2-C3 and C4-C3 bonds in *o*-HBDI remain unchanged in $S_1$ state minima, as shown in Figure 6.3 and Table D1. The lengths of C2-C3 and C4-C3 bonds are measured to be 1.462 Å and 1.401 Å respectively, in $S_1$ state. Moreover, in the $S_0$-min of *o*-HBDI, the ortho-hydroxy (O9-H10) group of hydroxyphenyl moiety was observed to form an intramolecular hydrogen bonding with the neighbouring N5-atom of the imidazolinone moiety. Upon photoexcitation, the redistribution of the electronic charge leads to a fast proton (-H10 atom) transfer from the phenolic to the imidazolinone moiety, thereby forming the H10-N5 bond (1.113 Å) in $S_1$-min. This results in the conversion of enol tautomer to keto form in $S_1$ excited state minimum (see Figure 6.3). Moreover, Table D1 also summarized the key geometric parameters of $S_0$-min, $S_1$-min, and corresponding enol and keto isomers calculated at various levels of theory. These geometrical parameters are consistent with the previous studies using single-reference and semi-empirical methods.[303, 417]

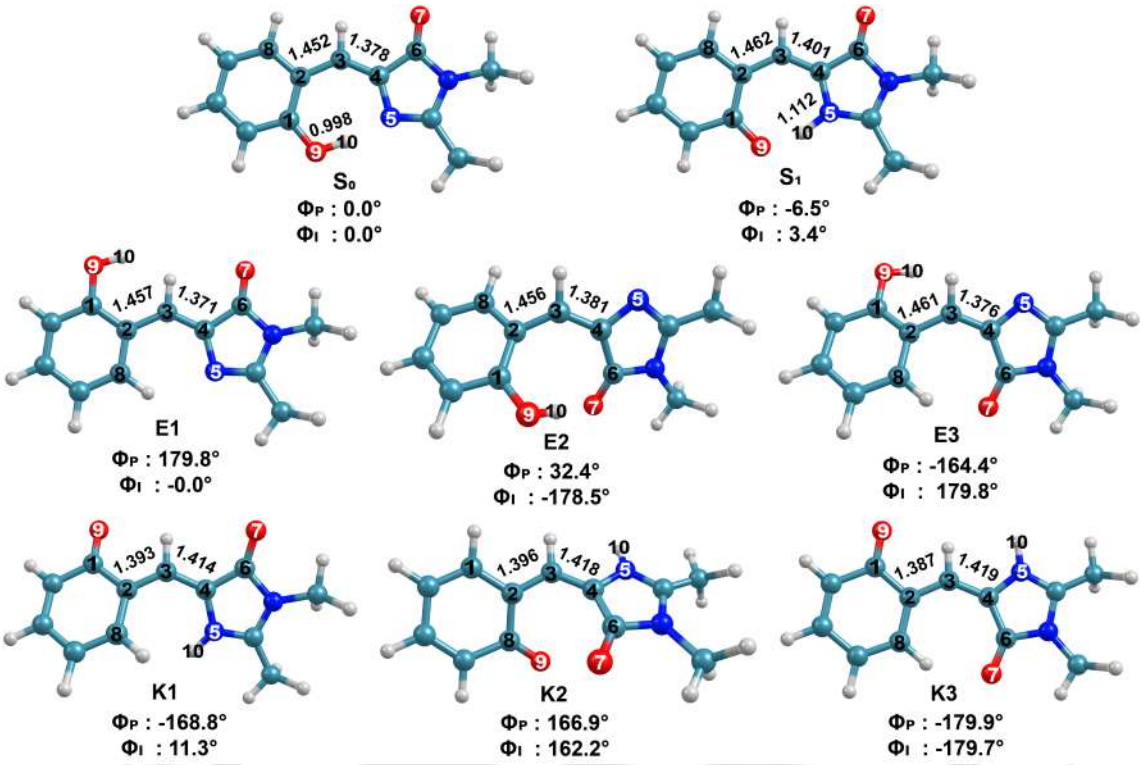


**Figure 6.3:** Molecular geometries of ground-state ($S_0$) and excited-state ($S_1$) minima, and the corresponding enol (E1, E2 and E3) and keto (K1, K2 and K3) isomers, optimized at XMS-CASPT2(10,9)/cc-pVDZ level of theory. Phenolic ($\Phi_P$) dihedral is defined by C1-C2-C3-C4, while imidazolinone ($\Phi_I$) is representated by N5-C4-C3-C2.

Along with *enol-keto* isomerization, photoexcitation of the *o*-HBDI fluorophore induces *cis-trans* isomerization. The cis-trans photoisomerization occurs via hydroxyphenyl bridged ($\Phi_P$) and imidazolinone bridged ($\Phi_I$) torsional rotations along $\theta_2$ and $\theta_3$ channels, which competes with the PT reaction in $\theta_1$ channel. This *cis-trans* photoisomerization yields three enol isomers (E1, E2, and E3) and three keto isomers (K1, K2, and K3), as depicted in Figure 6.3. Figure 6.3 reveals that the C2-C3 and C4-C3 bond distances in the enolic (E1, E2, and E3) tautomers remain unchanged from the $S_0$-min. In contrast, in the keto (K1, K2, and K3) tautomeric isomers, the C4-C3 bond changes its character to a single bond while the C2-C3 bond becomes a double bond, as shown in Figure 6.3 and Table D1. This suggests that *cis-trans* isomerization is more favourable in keto isomers. Furthermore, CASSCF and XMS-CASPT2 couldn't locate the $S_1$-min in the enolic form and $S_0$-min in the keto form of the tautomer. This is attributed to the ultrafast proton transfer reaction upon photoexcitation resulting in $S_1$-keto isomer and barrierless keto-enol tautomerization in the $S_0$ state, which enables the rapid proton back transfer to its enolic form. Thus,

a total of eight configurational isomers were obtained from *enol-keto* and *cis-trans* isomerization occurring through $\theta_1$, $\theta_2$, and $\theta_3$ pathways.

### 6.3.2 Relative and Vertical Excitation Energies

Table 6.1 shows the relative energies (REs) of *o*-HBDI at the $S_0$ and $S_1$ minima, along with its configurational isomers, identifying $S_0$-min as the most stable that exists in enolic form. So, the minimum energy of $S_0$ enol was considered as the reference energy. For keto isomers, the K3 form with phenolate oxygen (-O9) attached to hydroxyphenyl meioty and ketonic oxygen (-O7) to imidazolinone moiety have *anti* orientation are observed to be more stable than the K1 and K2 isomers. In contrast, the K2 form, where the groups adopt a *syn* orientation, exhibits higher energy and reduced stability due to the steric hindrance between the two groups. However, enol isomers have a relatively less stable E3 form, with E1 being the most stable in CASSCF and E2 in the XMS-CASPT2 methods (see Table 6.1).

**Table 6.1:** Relative Energies (RE, eV) *o*-HBDI chromophore at $S_0$-min and $S_1$-min along with all the configurational isomers in its enol (E1, E2 and E3) and keto (K1, K2, and K3) forms at CASSCF and XMS-CASPT2 levels of theory. The basis set cc-pVDZ was used.

| Methods | $S_0$-min | $S_1$-min | E1 | E2 | E3 | K1 | K2 | K3 |
|---|---|---|---|---|---|---|---|---|
| **CASSCF(10,9)** | 0 | 3.811 | 0.229 | 0.263 | 0.388 | 1.854 | 2.285 | 1.549 |
| **CASSCF(4,4)** | 0 | 3.811 | 0.262 | 0.354 | 0.404 | 1.805 | 2.185 | 1.692 |
| **XMS-CASPT2(10,9)** | 0 | 2.793 | 0.349 | 0.302 | 0.502 | 1.347 | 1.553 | 1.275 |
| **XMS-CASPT2(4,4)** | 0 | 3.348 | 0.397 | 0.288 | 0.544 | 1.404 | 1.642 | 1.325 |

The Franck-Condon (FC) excitation of *o*-HBDI was calculated using the equilibrium enol geometry ($S_0$). Table 6.2 demonstrates the vertical excitation energies (VEEs) and the corresponding oscillator strength at various electronic structure methods. All transition corresponds to the $^1\pi\pi^*$ character. The calculated VEEs and their corresponding oscillator strengths from different electronic structure methods, ADC(2), XMS-CASPT2, and TDDFT, are close to each other, indicating $S_1$ as the bright state while $S_2$ exhibits a dark character. A comparison with experimental results demonstrates a strong agreement, further validating the accuracy of these methods. However, as observed in Table 6.2, the CASSCF methods overestimated the excitation energies of both $S_1$ and $S_2$ states because of its inherent tendency to

neglect the dynamic correlation. Additionally, a switching of state character has been observed, with $S_2$ having significantly higher oscillator strength than $S_1$, similar to the issue reported in previous studies.[282, 287, 289, 312] The VEEs at CASSCF(10,9) and CASSCF(4,4) levels were observed to be 4.31 and 5.03 eV for $S_1$ state and 5.62 and 5.82 eV for $S_2$ state, respectively. Hence, $S_1$ state has been considered spectroscopically bright for further calculations.

**Table 6.2:** Vertical Excitation Energies (VEEs, eV) of *o*-HBDI chromophore for the first two singlet exited states at ADC(2), CASSCF, XMS-CASPT2 and TDDFT methods. The basis set cc-pVDZ was used. "$f$ " is the oscillator strength.

| Methods | $S_1$ | $f$ | $S_2$ | $f$ |
|---|---|---|---|---|
| **ADC(2)** | 3.39 | 0.41 | 4.01 | 0.00 |
| **CASSCF(10,9)** | 4.31 | 0.05 | 5.62 | 0.69 |
| **CASSCF(4,4)** | 5.03 | 0.15 | 5.82 | 1.02 |
| **XMS-CASPT2(10,9)** | 3.40 | 0.23 | 4.34 | 0.29 |
| **XMS-CASPT2(4,4)** | 3.36 | 0.53 | 4.25 | 0.47 |
| **TD-B3LYP** | 3.17 | 0.28 | 3.75 | 0.32 |
| **TD-$\omega$B97xD** | 3.59 | 0.49 | 4.34 | 0.00 |
| **Expt. ($\Phi_f$)[418, 419]** | 3.22 ($3.1\times10^{-3}$)[a] | | | |
| | 3.21 ($2.2\times10^{-3}$)[b] | | | |
| | 3.24 ($1.5\times10^{-3}$)[c] | | | |
| | 3.23 ($0.2\times10^{-3}$)[d] | | | |

[a] in Cycohexane, [b] in Dichloromethane, [c] in ACN, and [d] MeOH

### 6.3.3 Excited State Intramolecular Proton Transfer (ESIPT)

The photoexcitation of *o*-HBDI to low-lying excited state induces the intramolecular transfer of proton –H10 from the ortho position of the hydroxyphenyl moiety to the imidazolinone unit, breaking the O9-H10 bond and forming the N5-H10 bond. This process results in *enol-keto* tautomerization within the $\theta_1$ channel. To evaluate the feasibility of the PT process, the potential energy profile was computed along the PT coordinate for $S_0$, $S_1$, and $S_2$ electronic coordinates at both CASSCF and XMS-CASPT2 levels, as shown in Figure 6.4 and Table 6.3. Figure 6.4 and Table 6.3 indicate that the O9-H10 bond-breaking process in $S_1$ state exhibits a lower PT energy

barrier of 0.77 eV and 0.91 eV at CASSCF(4,4)/cc-pVDZ and CASSCF(10,9)/cc-pVDZ levels, and 0.29 eV and 0.21 eV at XMS-CASPT2(4,4)/cc-pVDZ and XMS-CASPT2(10,9)/cc-pVDZ levels, respectively. However, the PT energy barrier in the $S_0$ and $S_2$ states is notably higher compared to the $S_1$ state. At CASSCF(4,4)/cc-pVDZ level, the PT barriers are 1.83 eV for $S_0$ and 1.26 eV for $S_2$, whereas at CASSCF(10,9)/cc-pVDZ level, they are 2.34 eV for $S_0$ and 1.08 eV for $S_2$ state. A similar trend is observed at XMS-CASPT2 level using both (10e,9o) and (4e,4o) active spaces, where the PT energy barrier in the $S_0$ state remains higher than in the $S_1$ state, as presented in Table 6.3. This confirms that the *enol-keto* tautomerization is highly favourable in the excited state upon photoexcitation within the $\theta_1$ channel.

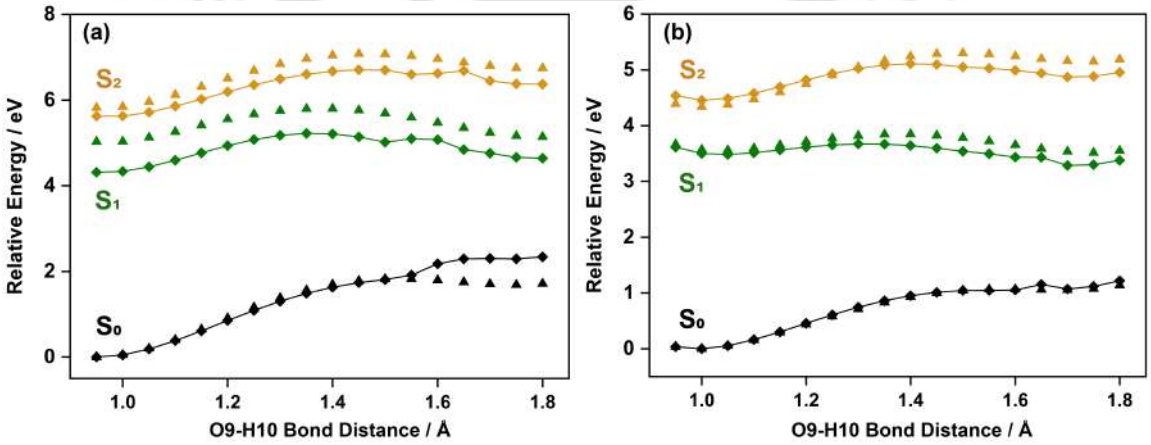


**Figure 6.4:** Potential energy profiles of *o*-HBDI chromophore along the proton transfer coordinate in $S_0$, $S_1$, and $S_2$ states, computed at (a) CASSCF and (b) XMS-CASPT2 levels of theory using (10e,9o) and (4e,4o) active spaces. Solid lines denote (10e,9o), and dotted lines correspond to (4e,4o) active spaces. cc-pVDZ basis set is used.

**Table 6.3:** Summary of the proton transfer (PT) energy barrier along the O9-H10 bond at $S_0$, $S_1$, and $S_2$ electronic states. Energies are in eV.

| **Methods** | $\Delta S_0$ | $\Delta S_1$ | $\Delta S_2$ |
|---|---|---|---|
| **CASSCF (10,9)** | 2.34 | 0.91 | 1.08 |
| **CASSCF (4,4)** | 1.83 | 0.77 | 1.26 |
| **XMS-CASPT2 (10,9)** | 1.22 | 0.21 | 0.65 |
| **XMS-CASPT2 (4,4)** | 1.14 | 0.29 | 0.96 |

### 6.3.4 Minimum Energy Conical Intersections (MECIs)

Upon excitation to the $S_1$ state, multiple $S_1(^1\pi\pi^*)/S_0$ minimum energy conical intersections (MECIs) were observed in the enol and keto isomeric form due to torsional rotation along exocyclic hydroxyphenyl-bridged and imidazolinone-bridged, i.e., single- and double- bonds, as shown in Figures 6.5 and Table D3. These torsional rotations along $\theta_2$ and $\theta_3$ channels compete with the ESIPT reaction occurring along the $\theta_1$. In the photodynamics study of *o*-HBDI in OM2/MRCI method, Liu *et al.*[417] have observed the occurrence of the six MECIs. However, our calculation using CASSCF and XMS-CASPT2 methods identified a total of eight $S_1(^1\pi\pi^*)/S_0$ MECIs, four in keto form and four in enol form, as shown in Figure 6.5 and Table D3. The MECIs in the keto form of MECI were labeled as K-CI1, K-CI2, K-CI3, and K-CI4, while those in enol form of MECIs were denoted as E-CI1, E-CI2, E-CI3, and E-CI4, respectively. All MECIs were optimized at the CASSCF/cc-pVDZ and XMS-CASPT2/cc-pVDZ levels of theory, and a more detailed comparison of the key geometrical parameters has been demonstrated in Table D3. The two keto MECIs, K-CI1 and K-CI2, possess nearly the same energy (see Table 6.1) and exist as chiral isomers (see Figure 6.5), differing in imidazolinone-bridged torsional rotation ($\Phi_I$) in clockwise and anti-clockwise directions. In both K-CI1 and K-CI2, the imidazolinone moiety adopts a perpendicular orientation to the phenolic moiety. The $\Phi_I$ dihedral angles for K-CI1 and K-CI2 are around $\pm102°$ to $\pm103°$, whereas the $\Phi_P$ dihedral angles are $\pm3°$ to $\pm4°$, at XMS-CASPT2 level of theory as shown in Figure 6.5. Similarly, K-CI3 and K-CI4 form a chiral isomeric pair and have comparable energy, distinguished by $\Phi_I$ of $\pm0°$ and $\Phi_P$ of $\pm81°$ to $\pm82°$ dihedral angle rotations in the opposite directions with the hydroxyphenyl moiety perpendicular to the imidazolinone unit (see Figure 6.5). The enolic MECIs (i.e., E-CI1, E-CI2, E-CI3, and E-CI4) possess characteristics similar to keto MECIs, with E-CI1/E-CI2 and E-CI3/E-CI4 forming mirror-image counterparts, making them chiral isomers.

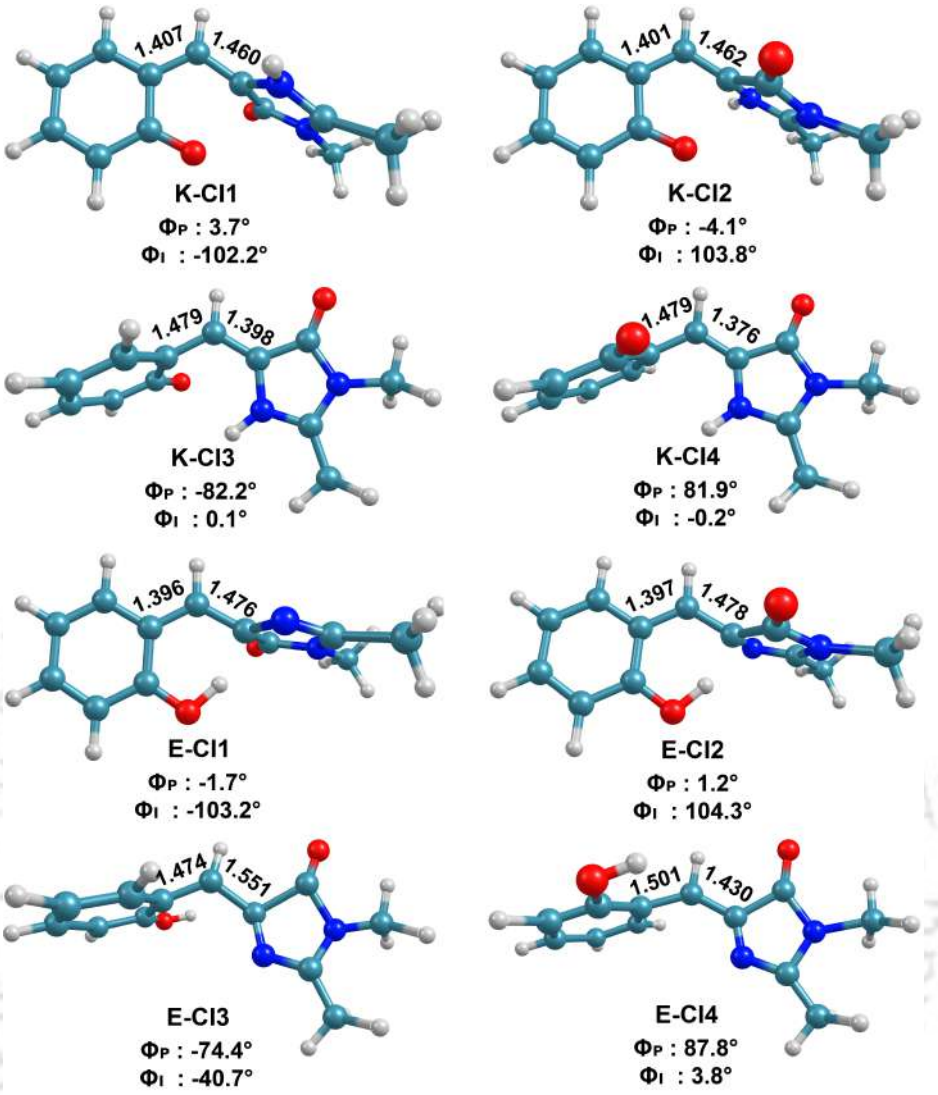


**Figure 6.5:** Molecular geometries of four keto (K-CI1, K-CI2, K-CI3, and K-CI4) and four enol (E-CI1, E-CI2, E-CI3, and E-CI4) minimum energy conical intersections (MECIs) of *o*-HBDI optimized at XMS-CASPT2(10,9)/cc-pVDZ level of theory. Phenolic ($\Phi_P$ ) dihedral is defined by C1-C2-C3-C4, while imidazolinone ($\Phi_I$ ) is represented by N5-C4-C3-C2.

At both CASSCF and XMS-CASPT2 levels, the energies of six MECIs, i.e., K-CI1, K-CI2, K-CI3, K-CI4, E-CI1, and E-CI2 were observed to have lower energy than the $S_1$-FC geometry, except in case of CASSCF(10,9) levels, as shown in Figure 6.6 and Table D2. On the other hand, the other two enolic MECIs E-CI3 and E-CI4, possess significantly higher energies, ranging from 6 to 12 eV relative to the $S_1$ FC geometry, in both CASSCF and XMS-CASPT2 levels. Hence, these two enolic MECIs are particularly challenging to locate, which explains why Liu *et al.*[417] were able to identify only six MECIs at the OM2/MRCI level.

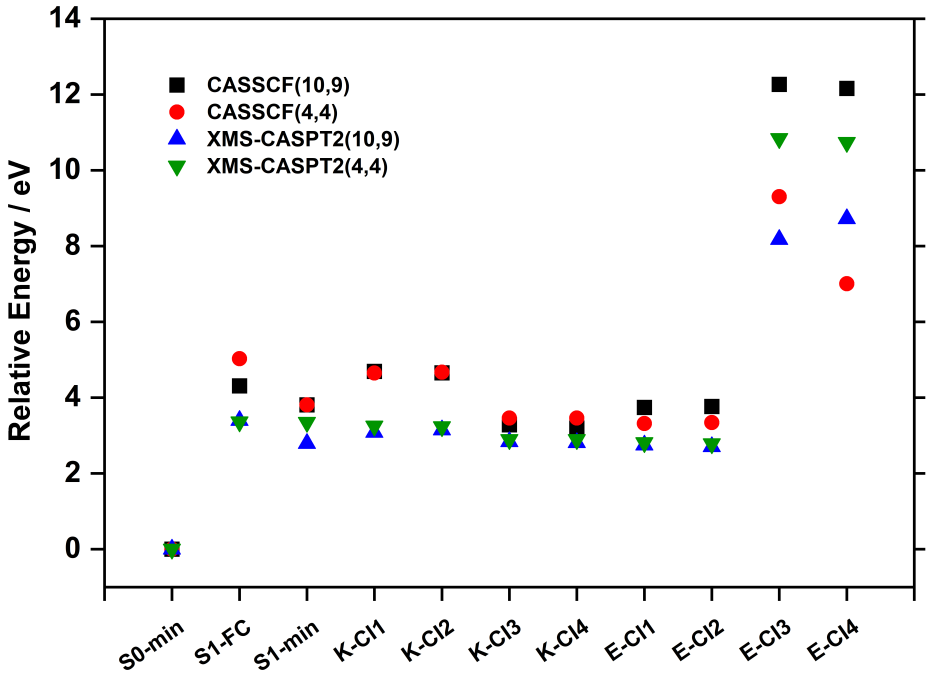


**Figure 6.6:** Relative energies of $S_0$, $S_1$, and all the MECIs corresponding to keto and enol forms at CASSCF/cc-pVDZ and XMS-CASPT2(10,9)/cc-pVDZ levels of theory. Active spaces (10e,9o) and (4e,4o) are used.

### 6.3.5 Relaxation Pathways Through LIICs

To map out the possible photochemical pathways and assess the potential involvement of single (C2-C3) and double (C4-C3) bond rotations, we compute the energies along the reaction pathways connecting the Franck-Condon geometry to the MECIs between $S_0$ and $S_1$ electronic states. The geometries along the pathways between FC geometries and MECIs are generated by linear interpolation of internal coordinates (LIICs). These pathways were computed using CASSCF(10,9)/cc-pVDZ and CASSCF(4,4)/cc-pVDZ levels for keto and enol MECIs. Figure 6.7 illustrates that upon excitation of *o*-HBDI to the $S_1$ state, it undergoes relaxation to the $S_0$ state via the $S_1(^1\pi\pi^*)/S_0$ intersection, which emerges due to the torsional rotation of the C2-C3 and C4-C3 bonds. The torsional rotation of C2-C3 and C4-C3 bonds in *o*-HBDI is facilitated by the delocalization of electrons between imidazolinone and hydroxyphenyl moieties, resulting in a change in exocyclic hydroxymethyl- and imidazolinone-bridged, C2-C3 and C4-C3 bonds character, as presented in Table D3.

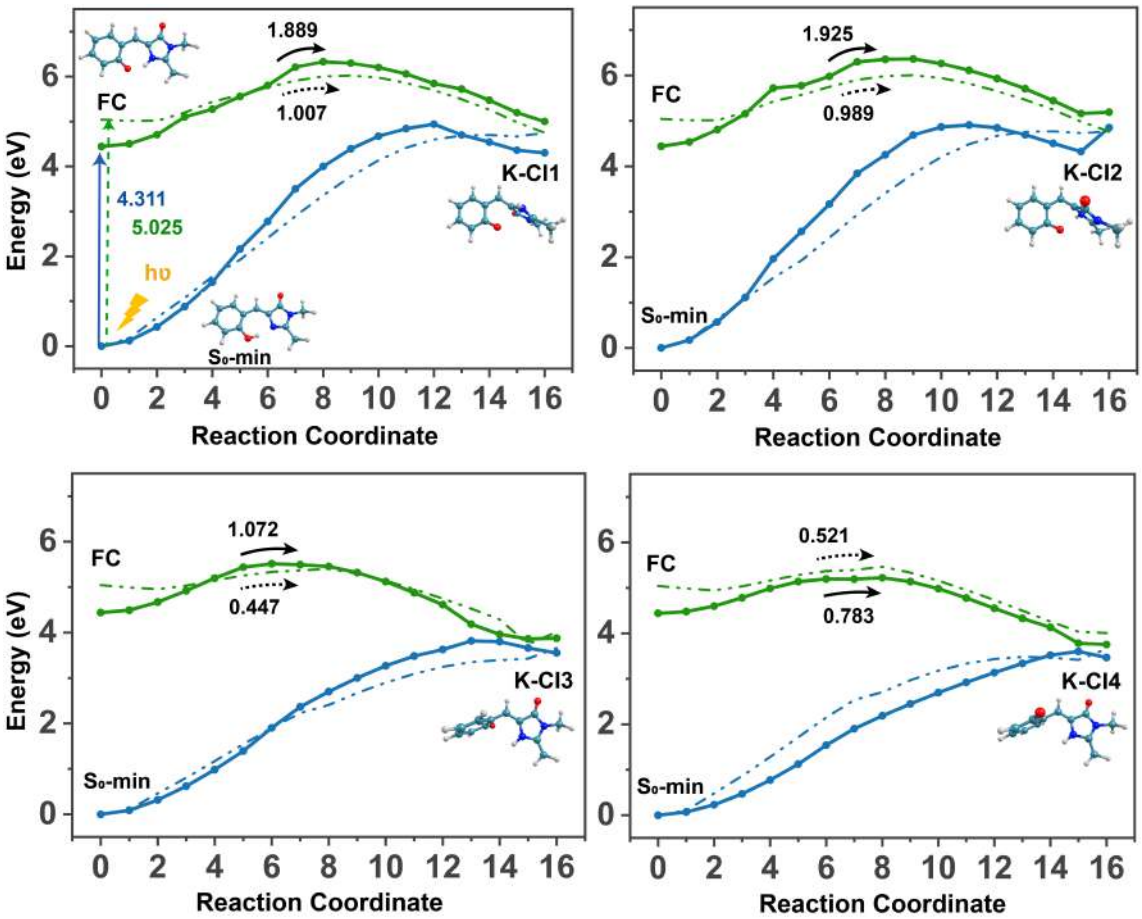


**Figure 6.7:** Linear interpolation in internal coordinates (LIICs) pathways connecting the $S_0$-min (enol) and keto $S_1(^1\pi\pi^*)/S_0$ MECI geometries computed at (a) CASSCF(10,9)/cc-pVDZ and (b) CASSCF(4,4)/cc-pVDZ levels. Solid lines represent the CASSCF(10,9) method, while dotted lines correspond to the CASSCF(4,4) method.

The CASSCF(10,9) method indicates that the deactivation pathways from the Franck Condon region to the two keto MECIs K-CI1 and K-CI2 have energy barriers of 1.889 and 1.925 eV, respectively. In the CASSCF (4,4) method, these barriers are significantly reduced to 1.007 eV and 0.989 eV. Similarly, the relaxation pathway leading to another two keto MECIs, K-CI3 and K-CI4, exhibits comparatively low energy barriers of 1.072 eV and 0.783 eV in the CASSCF(10,9) method, which further decreases to 0.447 eV and 0.521 eV in the CASSCF(4,4) method. However, since K-CI1 and K-CI2 possess higher energy than the $S_1$-FC point, the excited-state relaxation via pathway through these MECIs is not energetically feasible in CASSCF (10,9) method, but was observed to be feasible in CASSCF(4,4) method, whereas the pathway leading to K-CI3 and K-CI4, which lies at lower energies than $S_1$-FC point, is observed to be the favourable deactivation route in both CASSCF(4,4) and CASSCF (10,9) levels.

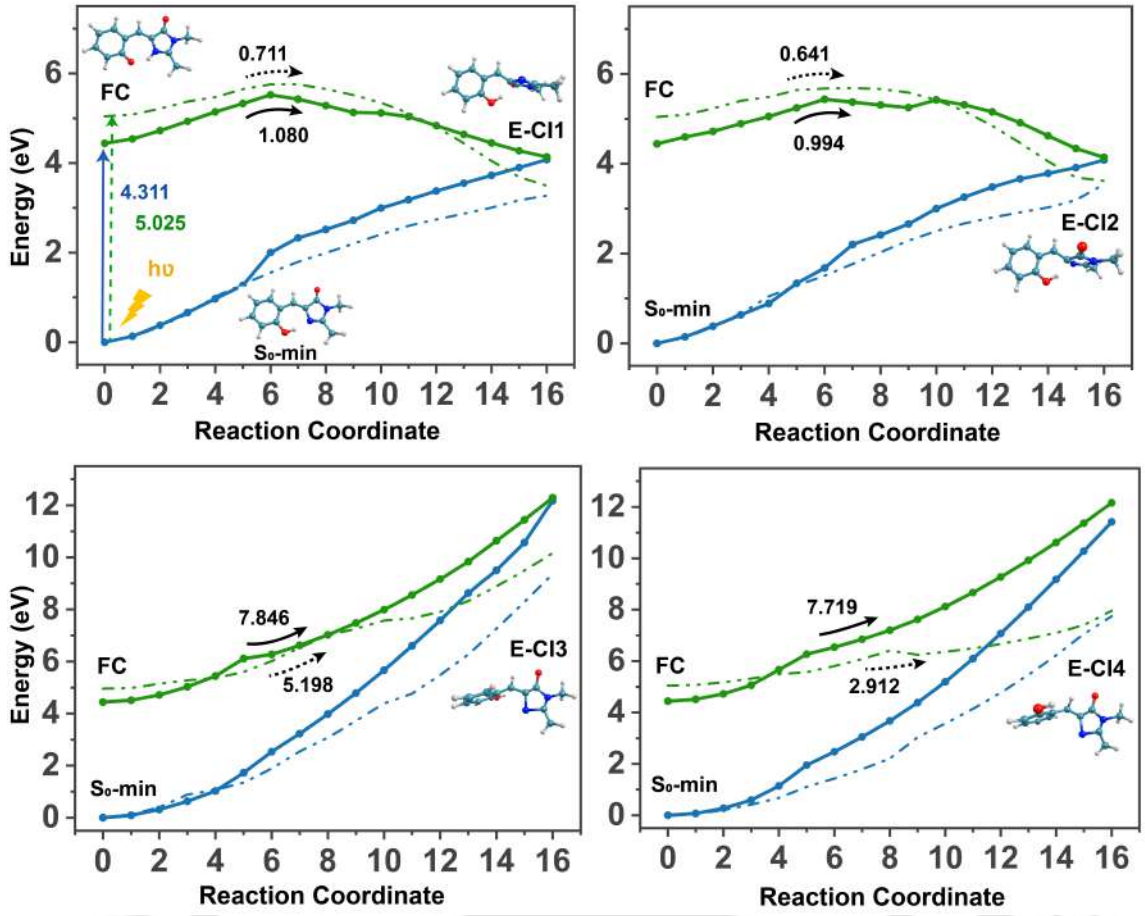


**Figure 6.8:** Linear interpolation in internal coordinates (LIICs) pathways connecting the $S_0$-min (enol) and enol $S_1(^1\pi\pi^*)/S_0$ MECI geometries computed at (a) CASSCF(10,9)/cc-pVDZ and (b) CASSCF(4,4)/cc-pVDZ levels. Solid lines represent the CASSCF(10,9) method, while dotted lines correspond to the CASSCF(4,4) method.

Further, for enolic MECIs, the deactivation barriers for E-CI1 and E-CI2, associated with I- bond rotation, are calculated to be 1.080 eV and 0.994 eV in CASSCF(10,9) level, and 0.711 eV and 0.641 eV in CASSCF(4,4) level. On the other hand, the pathway leading to the E-CI3 and E-CI4 exhibits significantly higher energy barriers of 7.846 eV and 7.719 eV at CASSCF(10,9) and 5.198 eV and 2.912 eV at CASSCF(4,4) levels of theory, with these MECIs positioned at much higher energy above the $S_1$ FC point. This suggests that the relaxation mechanism via internal conversion through the $S_1(^1\pi\pi^*)/S_0$ enol MECIs (E-CI1 and E-CI2) is structurally and energetically favourable following excitation to the $S_1$ electronic state. However, deactivation through E-CI3 and E-CI4 MECIs involves significant structural distortion and higher energy, making it an unfavorable pathway during the photochemical process.

### 6.3.6 Photoabsorption Cross-section Spectra

The photoabsorption cross-section of *o*-HBDI was simulated using the nuclear ensemble approach, employing harmonic-oscillator Wigner distributions to sample the initial conditions for nonadiabatic molecular dynamics simulations. We generate a total of 100 single-point geometries to sample the initial conditions of o-HBDI in order to simulate the absorption cross-section upon excitation to the excited states. The simulated absorption spectra of *o*-HBDI at the CASSCF(4,4)/cc-pVDZ level are presented in Figure 6.9 and compared with the experimental excitation energies from Table 6.2. The simulated absorption peak appears around ∼5.00 eV and ∼5.85 eV (Figure 6.9), which corresponds to the $S_0 \rightarrow S_1$ and $S_0 \rightarrow S_2$ transitions. These values aligns with the overestimated values of excitation energies from electronic structure CASSCF results (Table 6.2) along with the swapping of state characters. Further, these characteristics are also evident when compared with the overestimation of excitation energies with experimental results, which shows a discrepancy of about ∼2.0 eV, as shown in Table 6.2. Such an overestimation of excitation energies in the Franck Condon region is a well-documented limitation of CASSCF methods arising from the lack of dynamic correlation treatment. This $S_0 \rightarrow S_1$ and $S_0 \rightarrow S_2$ excitation in o-HBDI involves the $\pi$-$\pi^*$ transition localized on the imidazolinone and phenolic ring meioty. Hence, we considered both transitions and whole spectral window without any energy restriction for our further nonadiabatic simulation dynamics.

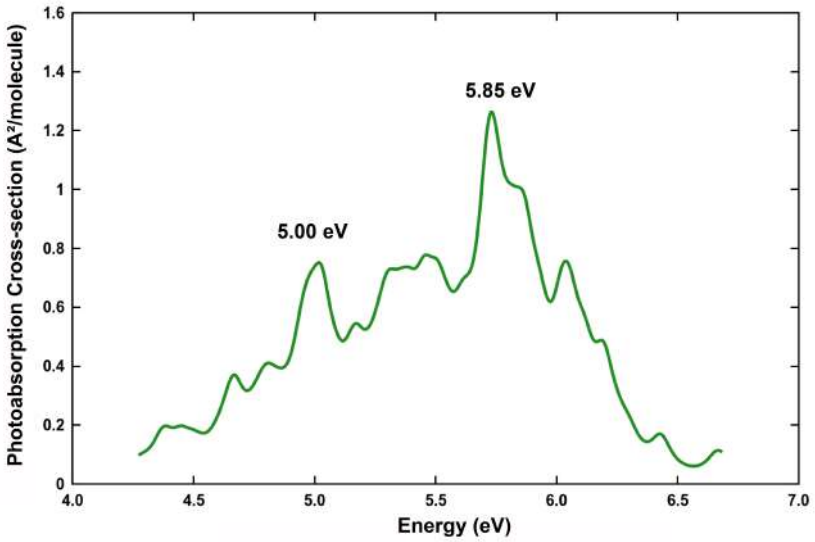


**Figure 6.9:** Simulated photoabsorption cross-section spectra of *o*-HBDI at CASSCF(4,4) methods using Wigner distribution, sampling 100 geometries. A Lorentzian line shape with $\delta = 0.1$ eV and cc-pVDZ basis set is used.

### 6.3.7 Nonadiabatic Molecular Dynamics Simulations

Considering all the above-mentioned factors, the trajectory surface hopping dynamics simulation was performed based on CASSCF(4,4)/cc-pVDZ level to gain more insight into the photodynamics of *o*-HBDI, including three electronic states. A total of 100 trajectories were considered for the nonadiabatic simulation for a maximum time of 300 fs. Out of 100 trajectories, only 19 underwent excited state proton transfer phenomenon, which can be correlated with the considerable energy barrier of 0.77 eV during the PT pathways in its excited ($S_1$) state (see Figure 6.4 and Table 6.3). The proton transfer (PT) time can be defined as the time at which the breaking bond and forming bond become equal and intersect with each other. Figure 6.10 illustrates the average of all the active trajectories in which the ESIPT occurs. The details of the snapshots of the geometries showing the structural change along the ESIPT process are also displayed at the top of Figure 6.10. The atom numbering scheme is in accordance with Figure 6.3.

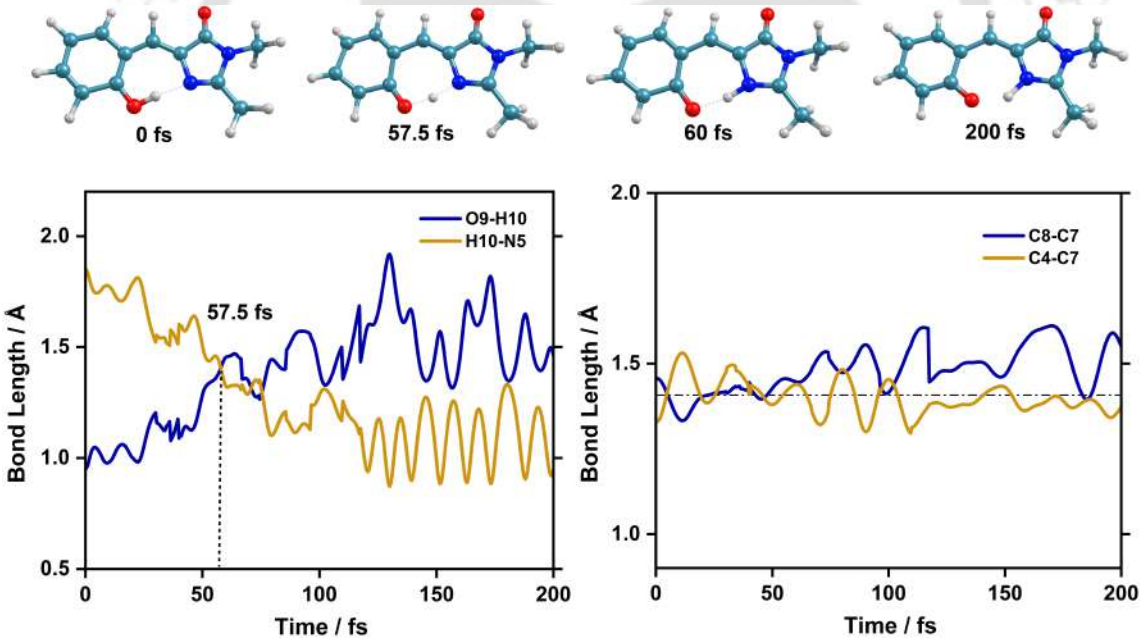


**Figure 6.10:** Time evolutions of bond distances of *o*-HBDI, average of all the active PT trajectories, showing (a) breaking bond O9-H10 and forming bond H10-N5, and (b) methine-bridge C8-C7 single bond and C4-C7 double-bond, at CASSCF(4,4)/cc-pVDZ level. The top structure displays the molecular geometries corresponding 0 fs, 57.5 fs, 60 fs, and 200 fs.

The following observation can be deduced from the time evolution of the average bond-breaking and bond-forming representative trajectories, as depicted in Figure 6.10. As represented in Figure 6.10, the O9-H10 bond of the hydroxyphenyl moiety

breaks at the time-scale of 57.5 fs, simultaneously forming the H10-N5 bonds of the imidazolinone moiety of the *o*-HBDI chromophore. This suggests that the ESIPT of the ortho-proton occurs from the hydroxyphenyl moiety to the imidazolinone moiety of *o*-HBDI within the first 100 fs. However, Cui *et. al* [303] have reported that the first PT occurs within 10-15 fs at the OM2/MRCI level of theory. Thus, it can be concluded that at the CASSCF level, the PT phenomena occur with a slight delay compared to the OM2/MRCI level.

Furthermore, quantum chemical calculations revealed that the tortional motion of the exocyclic single (C2-C3) and double (C4-C3) bond along the $\theta_2$ and $\theta_3$ channels (see Figure 6.1), plays an important role in the photodynamics of *o*-HBDI, leading to different photochemical pathways. We also tried to locate the torsional rotation around the C2-C3 and C4-C3 bonds during the nonadiabatic simulations. Among 100 trajectories, very few completed the maximum simulation time of 300 fs, while the remaining trajectories terminated before the maximum simulation time. This termination of the trajectories is attributed to the total energy change caused by the convergence instabilities, which arise due to the structural change between the two consecutive timescales or orbital rotations between subspaces.[20] This indicates that a longer timescale is required for *o*-HBDI to undergo torsional rotations. However, since our focus is on the ESIPT phenomena occurring in *o*-HBDI, we limit our current analysis to nonadiabatic simulation up to 300 fs. We plan to extend these preliminary findings through CASSCF and CASPT2 dynamics simulation to gain a comprehensive insight into other deactivation pathways.

## 6.4 Conclusions

The static electronic structure calculations, subsequently followed by trajectory surface hopping dynamics, were performed to investigate the photodynamics of ortho-hydroxy GFP-based chromophore upon photoabsorption of light. Our analysis revealed that on photoexcitation, the ESIPT process occurs from the hydroxyphenyl group of the *o*-HBDI chromophore to the imidazolinone group, leading to the formation of keto tautomers. This enol-keto tautomerization is then followed by the cis-trans isomerization process along the exocyclic methine-bridged bonds, resulting in the radiationless deactivation of the chromophore from the $S_1$ to $S_0$ state. Based on the potential energy profiles of $S_0$, $S_1$, and $S_2$ states, we observed that the ESIPT

phenomena have a lower energy barrier, making it energetically feasible upon photoexcitation. After the ESIPT process, the chromophore decays to the $S_0$ state via $S_1(^1\pi\pi^*)/S_0$ MECIs as a result of the *cis-trans* isomerization process. According to our nonadiabatic dynamics simulation, the proton transfer occurs within the first 100 fs at the CASSCF level and is thus intrinsically fast. However, no *cis-trans* isomerization reaction was detected till 300 fs, which implies that the simulation requires a picosecond timescale for this phenomenon to occur.

# Chapter 7

# Conclusions and Outlook

## 7.1 Conclusions

This thesis focuses on the photophysical and photochemical behavior of the Green Fluorescent Protein (GFP) chromophore and its derivatives upon photoabsorption of light. Theoretical and computational chemistry have played a pivotal role in deepening our understanding and characterizing the properties of a system upon photoabsorption. Thus, these approaches have enabled the researchers to address the unresolved questions and foster a new research avenue across diverse fields, including environmental chemistry, materials science, and biology. So, in this thesis, we aim to elucidate how steric and electronic environments significantly influence the photophysical behaviour of GFP chromophore derivatives and map out the factors governing the stereochemical outcome of key photoinduced processes by employing the electronic structure methods coupled with mixed quantum-classical dynamics. In recent decades, a wide range of GFP chromophore derivatives has been synthesized, exhibiting diverse spectral characteristics and distinct photophysical properties. While the wt-GFP chromophore exhibits green fluorescence, some variants display blue, orange, and yellow emission. Further, certain derivatives of the GFP chromophore exhibit a dual fluorescent nature, and some possess nonfluorescent properties. In this thesis, we initiate our investigation by exploring the unusual dual emissive nature of a para-sulfonamide analogue of GFP chromophore, aiming to uncover the underlying mechanism, which is then subsequently followed by the study of the nonfluorescent behaviour of GFP chromophore and its derivatives, along with the factors responsible for its quenching. The study then proceeds to explore both nonconventional and conventional approaches aimed at reducing the nonfluorescent behaviour and enhancing

the photostability and excited-state lifetime of the chromophore. To facilitate clarity, the explanation has thus been structured into the following subsections.

- In chapter 3, we observed that the para-sulfonamide analogue exhibits dual emissive behaviour in polar solvents. Studies based on static calculations and dynamics simulations revealed that, upon photoexcitation, the chromophore undergoes structural rearrangement in the polar solvent, resulting in an ultrafast excited-state intermolecular proton transfer (ESIPT) process in the $S_1$ state. This ESIPT phenomenon is responsible for the dual emissive behaviour of the para-sulfonamide analogue. On-the-fly dynamics simulation further demonstrates that the proton transfer process is ultrafast and proceeds in a stepwise manner within 300 fs from the benzylidene moiety of the chromophore to its imidazolinone moiety.

- Chapter 4 is based on the ab initio electronic structure approaches in conjunction with trajectory surface hopping dynamics, where we investigated the ultrafast photoinduced cis-trans isomerization phenomenon in the para-amino derivative of GFP chromophore, which is intrinsically nonfluorescent. Our investigation demonstrates that upon excitation to the $S_1$ excited state, the chromophore undergoes nonselective structural distortion along the exocyclic methine-bridged imidazolinone (I) and phenylamine (P) bonds, leading to the ultrafast nonradiative decay via $S_1/S_0$ internal conversion. This internal conversion is facilitated by the multiple $S_1(^1\pi\pi^*)/S_0$ conical intersections as a result of both $\Phi_I$ and $\Phi_P$ tortional rotations corresponding to I and P bonds, respectively, with $\Phi_I$ rotation playing a dominant role.

- Since GFP chromophore and its derivatives were known to efficiently undergo $S_1$-$S_0$ nonradiative decay due to $\Phi_I$ and $\Phi_P$ dihedral rotations, our study (Chapter 5) is further extended to explore a nonconventional approach to restrict the dihedral angle rotations by forming a dimer, thereby enhancing the photostability and exploring the nature of the excited states. First principles nonadiabatic excited state dynamics were implemented to study the photophysics of the higher energy (hot) exciton of the dimer and its relaxation dynamics at an atomistic and time-dependent level. The time evolution and relaxation processes emerging from our nonadiabatic excited state dynamics evidenced the long-lived exciton in the dimer. Thus, the formation of van der Waals $\pi$-$\pi$

stacked dimer restricts the $\Phi_I$- and $\Phi_P$- dihedral rotation, resulting in an energetically uphill pathway towards the $\Phi_I$-twisted and $\Phi_P$-twisted intersection seam. This enhances the photostability of the chromophore by limiting the access to nonradiative decay channels between S1 and $S_0$, thereby restricting the $\Phi_I$- and $\Phi_P$-dihedral rotation.

- Finally, in Chapter 6, we proceed with an alternate approach to enhance the photostability of GFP chromophore derivatives by considering an ortho-hydroxy analogue, which possesses a distinct photophysical behaviour upon photoexcitation. This behaviour is characterized by excited-state intramolecular proton transfer (ESIPT) phenomena, followed by cis-trans isomerization. Our electronic structure calculation, along with mixed quantum-chemical dynamics simulations, demonstrates that the ESIPT processes between the hydroxyphenyl and imidazolinone group occur in an ultrafast manner within 100 fs, thereby resulting in keto-enol isomers and thus, hinders the exocyclic I- and P- bond rotation for a few femtoseconds initially. However, the cis-trans isomerization process proceeds along the rotations of exocyclic methine-bridged bonds, resulting in radiationless deactivation of the chromophore to the $S_0$ state via multiple $S_1(^1\pi\pi^*)/S_0$ MECIs.

Thus, depending on the molecular structures and substituent groups, different chromophore exhibits distinct photoinduced processes, such as excited state intermolecular and intramolecular proton transfer (ESIPT), *cis-trans* isomerization, and *keto-enol* tautomerization, thereby governing their fluorescent properties. Thus, this thesis offers molecular-level insights into ultrafast photoinduced excited-state dynamics of biological and organic chromophores, resolving an interplay between molecular structure and dynamical behaviour.

## 7.2 Outlook

The theoretical and computational investigations based on electronic structure methods, along with the quantum-classical dynamics simulations, have proven to have great potential in deepening our understanding of the mechanistic aspects of photochemical reactivity. Our work on Green Fluorescent Protein (GFP) derivatives is the beginning of our attempt to comprehend the photochemistry in biological and organic

chromophores, by elucidating how structural configurations modulate their photophysics. Despite the advancement of theoretical and computational chemistry, the study of excited state dynamics and behaviour of GFP chromophore and its derivatives in a complex environment, such as encapsulated within the protein or embedded with DNA probes, has always posed a nontrivial task. Hence, a more comprehensive study involving a complex environment with strategic functionalization to modulate the properties of the adduct is crucial. Such investigations are currently underway in our group, which would provide a route to understand the excited state behaviour of biological and organic chromophores in complex environments. Moreover, since trajectory surface hopping dynamics based on CASSCF methods have explicitly failed to provide an accurate description of the population dynamics and time evolution of electronically excited states, a more efficient and computationally affordable alternative approach is required. Such approaches are currently being explored in our group and are expected to provide a deeper insight into the photophysics of the chromophores, potentially addressing the existing limitations of dynamics simulations.

# References


(1) Orton, R. J.; Sturm, O. E.; Vyshemirsky, V.; Calder, M.; Gilbert, D. R.; Kolch, W. Computational modelling of the receptor-tyrosine-kinase-activated MAPK pathway. *Biochem. J.* **2005**, *392*, 249–261.

(2) Esposito, L.; Banyasz, A.; Douki, T.; Perron, M.; Markovitsi, D.; Improta, R. Effect of C5-methylation of cytosine on the photoreactivity of DNA: a joint experimental and computational study of TCG trinucleotides. *J. Am. Chem. Soc.* **2014**, *136*, 10838–10841.

(3) Jones, C. M.; List, N. H.; Martínez, T. J. Steric and Electronic Origins of Fluorescence in GFP and GFP-like Proteins. *J. Am. Chem. Soc.* **2022**, *144*, 12732–12746.

(4) Blouin, N.; Michaud, A.; Gendron, D.; Wakim, S.; Blair, E.; Neagu-Plesu, R.; Belletete, M.; Durocher, G.; Tao, Y.; Leclerc, M. Toward a rational design of poly (2, 7-carbazole) derivatives for solar cells. *J. Am. Chem. Soc.* **2008**, *130*, 732–742.

(5) Jain, A.; Shin, Y.; Persson, K. A. Computational predictions of energy materials using density functional theory. *Nat. Rev. Mater.* **2016**, *1*, 1–13.

(6) Kholil, M.; Bhuiyan, M. Electronic, elastic, vibrational and superconducting properties of a ternary superconductors LaIrP (P= P, As): insights from DFT. *"Solid State Commun.* **2020**, *322*, 114053.

(7) Serrano-Andrés, L.; Serrano-Pérez, J. J. In *Handbook of computational chemistry*; Springer: 2015, pp 1–88.

(8) González, L.; Lindh, R., *Quantum chemistry and dynamics of excited states: methods and applications*; John Wiley & Sons: 2020.

(9) Domcke, W.; Koppel, H.; Yarkony, D. R., *Conical intersections: electronic structure, dynamics & spectroscopy*; World Scientific: 2004; Vol. 15.

(10) Schuurman, M. S.; Domcke, W.; Yarkony, D. R.; Koppel, H., *Conical Intersections: Theory, Computation and Experiment*; World Scientific: 2011; Vol. 17.

(11) Nelson, T. R.; White, A. J.; Bjorgaard, J. A.; Sifain, A. E.; Zhang, Y.; Nebgen, B.; Fernandez-Alberti, S.; Mozyrsky, D.; Roitberg, A. E.; Tretiak, S. Non-adiabatic excited-state molecular dynamics: Theory and applications for modeling photophysics in extended molecular materials. *Chem. Rev.* **2020**, *120*, 2215–2287.

(12) Mai, S.; González, L. Molecular photochemistry: recent developments in theory. *Angew. Chem. Int. Ed.* **2020**, *59*, 16832–16846.

(13) Mai, S.; Marquetand, P.; González, L. Nonadiabatic dynamics: The SHARC approach. *WIREs Comput. Mol. Sci.* **2018**, *8*, e1370.

(14) Beck, M. H.; Jäckle, A.; Worth, G. A.; Meyer, H.-D. The multiconfiguration time-dependent Hartree (MCTDH) method: a highly efficient algorithm for propagating wavepackets. *Phys. Rep.* **2000**, *324*, 1–105.

(15) Meyer, H.-D.; Gatti, F.; Worth, G. A., *Multidimensional quantum dynamics: MCTDH theory and applications*; John Wiley & Sons: 2009.

(16) Wang, H.; Thoss, M. Multilayer formulation of the multiconfiguration time-dependent Hartree theory. *J. Chem. Phys.* **2003**, *119*, 1289–1299.

(17) Wang, H. Multilayer multiconfiguration time-dependent Hartree theory. *J. Phys. Chem. A* **2015**, *119*, 7951–7965.

(18) Tully, J. C.; Preston, R. K. Trajectory surface hopping approach to nonadiabatic molecular collisions: the reaction of H+ with D2. *J. Chem. Phys.* **1971**, *55*, 562–572.

(19) Tully, J. C. Molecular dynamics with electronic transitions. *J. Chem. Phys.* **1990**, *93*, 1061–1071.

(20) Barbatti, M. Nonadiabatic dynamics with trajectory surface hopping method. *WIREs Comput. Mol. Sci.* **2011**, *1*, 620–633.

(21) Richter, M.; Marquetand, P.; González-Vázquez, J.; Sola, I.; González, L. SHARC: ab initio molecular dynamics with surface hopping in the adiabatic representation including arbitrary couplings. *J. Chem. Theory Comput.* **2011**, *7*, 1253–1258.

(22) Wang, L.; Akimov, A.; Prezhdo, O. V. Recent progress in surface hopping: 2011–2015. *J. Phys. Chem. Lett.* **2016**, *7*, 2100–2112.

(23) Shalashilin, D. V. Nonadiabatic dynamics with the help of multiconfigurational Ehrenfest method: Improved theory and fully quantum 24D simulation of pyrazine. *J. Chem. Phys.* **2010**, *132*.

(24) Marx, D.; Hutter, J., *Ab initio molecular dynamics: basic theory and advanced methods*; Cambridge University Press: 2009.

(25) Ben-Nun, M.; Quenneville, J.; Martínez, T. J. Ab initio multiple spawning: Photochemistry from first principles quantum molecular dynamics. *J. Phys. Chem. A* **2000**, *104*, 5161–5175.

(26) Ben-Nun, M.; Martínez, T. J. Ab initio quantum molecular dynamics. *Adv. Chem. Phys.* **2002**, *121*, 439–512.

(27) Kapral, R.; Ciccotti, G. Mixed quantum-classical dynamics. *J. Chem. Phys.* **1999**, *110*, 8919–8929.

(28) Kapral, R. Progress in the theory of mixed quantum-classical dynamics. *Annu. Rev. Phys. Chem.* **2006**, *57*, 129–157.

(29) Min, S. K.; Agostini, F.; Gross, E. K. Coupled-trajectory quantum-classical approach to electronic decoherence in nonadiabatic processes. *Phys. Rev. Lett.* **2015**, *115*, 073001.

(30) Agostini, F.; Min, S. K.; Abedi, A.; Gross, E. K. Quantum-classical nonadiabatic dynamics: Coupled-vs independent-trajectory methods. *J. Chem. Theory Comput.* **2016**, *12*, 2127–2143.

(31) Crespo-Otero, R.; Barbatti, M. Recent advances and perspectives on nonadiabatic mixed quantum–classical dynamics. *Chem. Rev.* **2018**, *118*, 7026–7068.

(32) Curchod, B. F.; Martínez, T. J. Ab initio nonadiabatic quantum molecular dynamics. *Chem. Rev.* **2018**, *118*, 3305–3336.

(33) Agostini, F.; Curchod, B. F. Different flavors of nonadiabatic molecular dynamics. *WIREs Comput. Mol. Sci.* **2019**, *9*, e1417.

(34) Mukherjee, B.; Naskar, K.; Mukherjee, S.; Ghosh, S.; Sahoo, T.; Adhikari, S. Beyond Born–Oppenheimer theory for spectroscopic and scattering processes. *Int. Rev. Phys. Chem.* **2019**, *38*, 287–341.

(35) Matsika, S.; Krause, P. Nonadiabatic events and conical intersections. *Annu. Rev. Phys. Chem.* **2011**, *62*, 621–643.

(36) Mukherjee, S.; Fedorov, D. A.; Varganov, S. A. Modeling spin-crossover dynamics. *Annu. Rev. Phys. Chem.* **2021**, *72*, 515–540.

(37) Neves-Petersen, M. T.; Klitgaard, S.; Pascher, T.; Skovsen, E.; Polivka, T.; Yartsev, A.; Sundström, V.; Petersen, S. B. Flash photolysis of cutinase: identification and decay kinetics of transient intermediates formed upon UV excitation of aromatic residues. *Biophys. J.* **2009**, *97*, 211–226.

(38) Soorkia, S.; Jouvet, C.; Grégoire, G. UV photoinduced dynamics of conformer-resolved aromatic peptides. *Chem. Rev.* **2019**, *120*, 3296–3327.

(39) Harris, D. C.; Bertolucci, M. D., *Symmetry and spectroscopy: an introduction to vibrational and electronic spectroscopy*; Courier Corporation: 1989.

(40) Ng, C.-Y., *Vacuum ultraviolet photoionization and photodissociation of molecules and clusters*; World Scientific: 1991.

(41) Brixner, T.; Pfeifer, T.; Gerber, G.; Wollenhaupt, M.; Baumert, T. Optimal control of atomic, molecular and electron dynamics with tailored femtosecond laser pulses. *Femtosecond Laser Spectroscopy* **2005**, 225–266.

(42) Iqbal, A.; Stavros, V. G. Active participation of $1\pi\sigma^*$ states in the photodissociation of tyrosine and its subunits. . *Phys. Chem. Lett.* **2010**, *1*, 2274–2278.

(43) Kowalewski, M.; Fingerhut, B. P.; Dorfman, K. E.; Bennett, K.; Mukamel, S. Simulating coherent multidimensional spectroscopy of nonadiabatic molecular processes: From the infrared to the x-ray regime. *Chem. Rev.* **2017**, *117*, 12165–12226.

(44) Tajti, A.; Fogarasi, G.; Szalay, P. G. Reinterpretation of the UV spectrum of cytosine: only two electronic transitions? *ChemPhysChem* **2009**, *10*, 1603–1606.

(45) Barbatti, M.; Szymczak, J. J.; Aquino, A. J.; Nachtigallová, D.; Lischka, H. The decay mechanism of photoexcited guanine- A nonadiabatic dynamics study. *J. Chem. Phys.* **2011**, *134*.

(46) Ruckenbauer, M.; Mai, S.; Marquetand, P.; González, L. Photoelectron spectra of 2-thiouracil, 4-thiouracil, and 2, 4-dithiouracil. *J. Chem. Phys.* **2016**, *144*.

(47) Nogueira, J. J.; Plasser, F.; González, L. Electronic delocalization, charge transfer and hypochromism in the UV absorption spectrum of polyadenine unravelled by multiscale computations and quantitative wavefunction analysis. *Chem. Sci.* **2017**, *8*, 5682–5691.

(48) Mai, S.; Mohamadzade, A.; Marquetand, P.; González, L.; Ullrich, S. Simulated and experimental time-resolved photoelectron spectra of the intersystem crossing dynamics in 2-thiouracil. *Molecules* **2018**, *23*, 2836.

(49) Zobel, J. P.; Heindl, M.; Nogueira, J. J.; González, L. Vibrational sampling and solvent effects on the electronic structure of the absorption spectrum of 2-nitronaphthalene. *J. Chem. Theory Comput.* **2018**, *14*, 3205–3217.

(50) Barbatti, M.; Aquino, A. J.; Lischka, H. Ultrafast two-step process in the nonadiabatic relaxation of the CH2 molecule. *Mol. Phys.* **2006**, *104*, 1053–1060.

(51) Schapiro, I.; Roca-Sanjuán, D.; Lindh, R.; Olivucci, M. A surface hopping algorithm for nonadiabatic minimum energy path calculations. *J. Comput. Chem.* **2015**, *36*, 312–320.

(52) Mai, S.; Richter, M.; Marquetand, P.; González, L. The DNA nucleobase thymine in motion–Intersystem crossing simulated with surface hopping. *Chem. Phys.* **2017**, *482*, 9–15.

(53) Heim, P.; Mai, S.; Thaler, B.; Cesnik, S.; Avagliano, D.; Bella-Velidou, D.; Ernst, W. E.; González, L.; Koch, M. Revealing ultrafast population transfer between nearly degenerate electronic states. *J. Phys. Chem. Lett.* **2020**, *11*, 1443–1449.

(54) Horton, S. L.; Liu, Y.; Forbes, R.; Makhija, V.; Lausten, R.; Stolow, A.; Hockett, P.; Marquetand, P.; Rozgonyi, T.; Weinacht, T. Excited state dynamics of CH2I2 and CH2BrI studied with UV pump VUV probe photoelectron spectroscopy. *J. Chem. Phys.* **2019**, *150*.

(55) Brunk, E.; Rothlisberger, U. Mixed quantum mechanical/molecular mechanical molecular dynamics simulations of biological systems in ground and electronically excited states. *Chem. Rev.* **2015**, *115*, 6217–6263.

(56) Gozem, S.; Luk, H. L.; Schapiro, I.; Olivucci, M. Theory and simulation of the ultrafast double-bond isomerization of biological chromophores. *Chem. Rev.* **2017**, *117*, 13502–13565.

(57) Cerullo, G.; Polli, D.; Lanzani, G.; De Silvestri, S.; Hashimoto, H.; Cogdell, R. J. Photosynthetic light harvesting by carotenoids: detection of an intermediate excited state. *Science* **2002**, *298*, 2395–2398.

(58) Cheng, Y.-C.; Fleming, G. R. Dynamics of light harvesting in photosynthesis. *Annu. Rev. Phys. Chem.* **2009**, *60*, 241–262.

(59) Romero, E.; Novoderezhkin, V. I.; Van Grondelle, R. Quantum design of photosynthesis for bio-inspired solar-energy conversion. *Nature* **2017**, *543*, 355–365.

(60) Herbst, J.; Heyne, K.; Diller, R. Femtosecond infrared spectroscopy of bacteriorhodopsin chromophore isomerization. *Science* **2002**, *297*, 822–825.

(61) Tapavicza, E.; Tavernelli, I.; Rothlisberger, U. Trajectory Surface Hopping within Linear Response Time-Dependent<? format?> Density-Functional Theory. *Phys. Rev. Lett.* **2007**, *98*, 023001.

(62) Warshel, A. Bicycle-pedal model for the first step in the vision process. *Nature* **1976**, *260*, 679–683.

(63) Schoenlein, R. W.; Peteanu, L. A.; Mathies, R. A.; Shank, C. V. The first step in vision: femtosecond isomerization of rhodopsin. *Science* **1991**, *254*, 412–415.

(64) Ernst, O. P.; Lodowski, D. T.; Elstner, M.; Hegemann, P.; Brown, L. S.; Kandori, H. Microbial and animal rhodopsins: structures, functions, and molecular mechanisms. *Chem. Rev.* **2014**, *114*, 126–163.

(65) Domcke, W.; Sobolewski, A. L. Spectroscopy meets theory. *Nat. Chem.* **2013**, *5*, 257–258.

(66) Pattison, D. I.; Rahmanto, A. S.; Davies, M. J. Photo-oxidation of proteins. *Photochem. Photobiol. Sci.* **2012**, *11*, 38–53.

(67) Correia, M.; Neves-Petersen, M. T.; Jeppesen, P. B.; Gregersen, S.; Petersen, S. B. UV-light exposure of insulin: pharmaceutical implications upon covalent insulin dityrosine dimerization and disulphide bond photolysis. *PloS one* **2012**, *7*, e50733.

(68) Sanchez-Lengeling, B.; Aspuru-Guzik, A. Inverse molecular design using machine learning: Generative models for matter engineering. *Science* **2018**, *361*, 360–365.

(69) Mathew, S.; Yella, A.; Gao, P.; Humphry-Baker, R.; Curchod, B. F.; Ashari-Astani, N.; Tavernelli, I.; Rothlisberger, U.; Nazeeruddin, M. K.; Grätzel, M. Dye-sensitized solar cells with 13% efficiency achieved through the molecular engineering of porphyrin sensitizers. *Nat. Chem.* **2014**, *6*, 242–247.

(70) Bartók, A. P.; De, S.; Poelking, C.; Bernstein, N.; Kermode, J. R.; Csányi, G.; Ceriotti, M. Machine learning unifies the modeling of materials and molecules. *Sci. Adv.* **2017**, *3*, e1701816.

(71) Bochenkova, A. V.; Klærke, B.; Rahbek, D. B.; Rajput, J.; Toker, Y.; Andersen, L. H. UV Excited-State Photoresponse of Biochromophore Negative Ions. *Angew. Chem.* **2014**, *126*, 9955–9959.

(72) West, C. W.; Bull, J. N.; Hudson, A. S.; Cobb, S. L.; Verlet, J. R. Excited state dynamics of the isolated green fluorescent protein chromophore anion following UV excitation. *J. Phys. Chem. B.* **2015**, *119*, 3982–3987.

(73) Gamiz-Hernandez, A. P.; Angelova, I. N.; Send, R.; Sundholm, D.; Kaila, V. R. Protein-Induced Color Shift of Carotenoids in $\beta$-Crustacyanin. *Angew. Chem. Int. Ed.* **2015**, *54*, 11564–11566.

(74) Peng, H.-Q.; Niu, L.-Y.; Chen, Y.-Z.; Wu, L.-Z.; Tung, C.-H.; Yang, Q.-Z. Biological applications of supramolecular assemblies designed for excitation energy transfer. *Chem. Rev.* **2015**, *115*, 7502–7542.

(75) Miyawaki, A.; Shcherbakova, D. M.; Verkhusha, V. V. Red fluorescent proteins: chromophore formation and cellular applications. *Curr. Opin. Struct. Biol.* **2012**, *22*, 679–688.

(76) Tsien, R. Y. The green fluorescent protein. *Annu. Rev. Biochem.* **1998**, *67*, 509–544.

(77) Zimmer, M. Green fluorescent protein (GFP): applications, structure, and related photophysical behavior. *Chem. Rev.* **2002**, *102*, 759–782.

(78) Acharya, A.; Bogdanov, A. M.; Grigorenko, B. L.; Bravaya, K. B.; Nemukhin, A. V.; Lukyanov, K. A.; Krylov, A. I. Photoinduced chemistry in fluorescent proteins: curse or blessing? *Chem. Rev.* **2017**, *117*, 758–795.

(79) Davenport, D.; Nicol, J. Luminescence in hydromedusae. *Proc. R. Soc. Lond. B.* **1955**, *144*, 399–411.

(80) Shimomura, O.; Johnson, F. H.; Saiga, Y. Extraction, purification and properties of aequorin, a bioluminescent protein from the luminous hydromedusan, Aequorea. *J. Cell. Comp. Physiol.* **1962**, *59*, 223–239.

(81) Shimomura, O. Discovery of green fluorescent protein. *Methods Biochem. Anal.* **2005**, *47*, 1–13.

(82) Shimomura, O.; Musicki, B.; Kishi, Y. Semi-synthetic aequorin. An improved tool for the measurement of calcium ion concentration. *Biochemical Journal* **1988**, *251*, 405–410.

(83) Morin, J. G.; Hastings, J. W. Energy transfer in a bioluminescent system. *J. Cell. Physiol.* **1971**, *77*, 313–318.

(84) Morise, H.; Shimomura, O.; Johnson, F. H.; Winant, J. Intermolecular energy transfer in the bioluminescent system of Aequorea. *Biochem.* **1974**, *13*, 2656–2662.

(85) Ward, W.; Cormier, M. Energy transfer protein in coelenterate bioluminescence. *J. Biol. Chem.* **1979**, *254*.

(86) Shimomura, O. Structure of the chromophore of Aequorea green fluorescent protein. *FEBS Lett.* **1979**, *104*, 220–222.

(87) Cody, C. W.; Prasher, D. C.; Westler, W. M.; Prendergast, F. G.; Ward, W. W. Chemical structure of the hexapeptide chromophore of the Aequorea green-fluorescent protein. *Biochem.* **1993**, *32*, 1212–1218.

(88) Ormö, M.; Cubitt, A. B.; Kallio, K.; Gross, L. A.; Tsien, R. Y.; Remington, S. J. Crystal structure of the Aequorea victoria green fluorescent protein. *Science* **1996**, *273*, 1392–1395.

(89) Brejc, K.; Sixma, T. K.; Kitts, P. A.; Kain, S. R.; Tsien, R. Y.; Ormö, M.; Remington, S. J. Structural basis for dual excitation and photoisomerization of the Aequorea victoria green fluorescent protein. *Proc. Natl. Acad. Sci. U.S.A.* **1997**, *94*, 2306–2311.

(90) Heim, R.; Prasher, D. C.; Tsien, R. Y. Wavelength mutations and posttranslational autoxidation of green fluorescent protein. *Proc. Natl. Acad. Sci. U.S.A.* **1994**, *91*, 12501–12504.

(91) Cubitt, A. B.; Heim, R.; Adams, S. R.; Boyd, A. E.; Gross, L. A.; Tsien, R. Y. Understanding, improving and using green fluorescent proteins. *Trends Biochem Sci.* **1995**, *20*, 448–455.

(92) Craggs, T. D. Green fluorescent protein: structure, folding and chromophore maturation. *Chem. Soc.* **2009**, *38*, 2865–2875.

(93) Niwa, H.; Inouye, S.; Hirano, T.; Matsuno, T.; Kojima, S.; Kubota, M.; Ohashi, M.; Tsuji, F. I. Chemical nature of the light emitter of the Aequorea green fluorescent protein. *Proc. Natl. Acad. Sci. U.S.A.* **1996**, *93*, 13617–13622.

(94) Chattoraj, M.; King, B. A.; Bublitz, G. U.; Boxer, S. G. Ultra-fast excited state dynamics in green fluorescent protein: multiple states and proton transfer. *Proc. Natl. Acad. Sci. U.S.A.* **1996**, *93*, 8362–8367.

(95) Meech, S. R. Excited state reactions in fluorescent proteins. *Chem. Soc. Rev.* **2009**, *38*, 2922–2934.

(96) Van Thor, J. J. Photoreactions and dynamics of the green fluorescent protein. *Chem. Soc. Rev.* **2009**, *38*, 2935–2950.

(97) Bravaya, K. B.; Grigorenko, B. L.; Nemukhin, A. V.; Krylov, A. I. Quantum chemistry behind bioimaging: insights from ab initio studies of fluorescent proteins and their chromophores. *Acc. Chem. Res.* **2012**, *45*, 265–275.

(98) Creemers, T.; Lock, A.; Subramaniam, V.; Jovin, T.; Völker, S. Three photoconvertible forms of green fluorescent protein identified by spectral hole-burning. *Nat. Struct. Biol.* **1999**, *6*, 557–560.

(99) Kennis, J. T.; Larsen, D. S.; van Stokkum, I. H.; Vengris, M.; van Thor, J. J.; van Grondelle, R. Uncovering the hidden ground state of green fluorescent protein. *Proc. Natl. Acad. Sci. U. S. A.* **2004**, *101*, 17988–17993.

(100) Seebacher, C.; Deeg, F.; Bräuchle, C.; Wiehler, J.; Steipe, B. Stable low-temperature photoproducts and hole burning of green fluorescent protein (GFP). *J. Phys. Chem. B* **1999**, *103*, 7728–7732.

(101) Striker, G.; Subramaniam, V.; Seidel, C. A.; Volkmer, A. Photochromicity and fluorescence lifetimes of green fluorescent protein. *J. Phys. Chem. B* **1999**, *103*, 8612–8617.

(102) Voityuk, A. A.; Michel-Beyerle, M.-E.; Rösch, N. Structure and rotation barriers for ground and excited states of the isolated chromophore of the green fluorescent protein. *Chem. Phys. Lett.* **1998**, *296*, 269–276.

(103) Chen, M. C.; Lambert, C. R.; Urgitis, J. D.; Zimmer, M. Photoisomerization of green fluorescent protein and the dimensions of the chromophore cavity. *Chem. Phys.* **2001**, *270*, 157–164.

(104) Weber, W.; Helms, V.; McCammon, J. A.; Langhoff, P. W. Shedding light on the dark and weakly fluorescent states of green fluorescent proteins. *Proc. Natl. Acad. Sci. U. S. A.* **1999**, *96*, 6177–6182.

(105) Leiderman, P.; Huppert, D.; Agmon, N. Transition in the temperature-dependence of GFP fluorescence: from proton wires to proton exit. *Biophys. J.* **2006**, *90*, 1009–1018.

(106) Agmon, N. Kinetics of switchable proton escape from a proton-wire within green fluorescence protein. *J. Phys. Chem. B* **2007**, *111*, 7870–7878.

(107) Van Thor, J. J.; Pierik, A. J.; Nugteren-Roodzant, I.; Xie, A.; Hellingwerf, K. J. Characterization of the photoconversion of green fluorescent protein with FTIR spectroscopy. *Biochem.* **1998**, *37*, 16915–16921.

(108) Kummer, A. D.; Wiehler, J.; Rehaber, H.; Kompa, C.; Steipe, B.; Michel-Beyerle, M. E. Effects of threonine 203 replacements on excited-state dynamics and fluorescence properties of the green fluorescent protein (GFP). *J. Phys. Chem. B* **2000**, *104*, 4791–4798.

(109) Voityuk, A. A.; Michel-Beyerle, M.-E.; Rösch, N. Quantum chemical modeling of structure and absorption spectra of the chromophore in green fluorescent proteins. *Chem. Phys.* **1998**, *231*, 13–25.

(110) Bell, A. F.; He, X.; Wachter, R. M.; Tonge, P. J. Probing the ground state structure of the green fluorescent protein chromophore using Raman spectroscopy. *Biochem.* **2000**, *39*, 4423–4431.

(111) Yoo, H.-Y.; Boatz, J. A.; Helms, V.; McCammon, J. A.; Langhoff, P. W. Chromophore protonation states and the proton shuttle mechanism in green fluorescent protein: inferences drawn from ab initio theoretical studies of chemical structures and vibrational spectra. *J. Phys. Chem. B* **2001**, *105*, 2850–2857.

(112) Laino, T.; Nifosı`, R.; Tozzini, V. Relationship between structure and optical properties in green fluorescent proteins: a quantum mechanical study of the chromophore environment. *Chem. Phys.* **2004**, *298*, 17–28.

(113) Helms, V.; Straatsma, T.; McCammon, J. A. Internal dynamics of green fluorescent protein. *J. Phys. Chem. B* **1999**, *103*, 3263–3269.

(114) Tozzini, V.; Nifosı`, R. Ab initio molecular dynamics of the green fluorescent protein (GFP) chromophore: an insight into the photoinduced dynamics of green fluorescent proteins. *J. Phys. Chem. B* **2001**, *105*, 5797–5803.

(115) Reuter, N.; Lin, H.; Thiel, W. Green fluorescent proteins: Empirical force field for the neutral and deprotonated forms of the chromophore. Molecular dynamics simulations of the wild type and S65T mutant. *J. Phys. Chem. B* **2002**, *106*, 6310–6321.

(116) Lill, M. A.; Helms, V. Proton shuttle in green fluorescent protein studied by dynamic simulations. *Proc. Natl. Acad. Sci. U. S. A.* **2002**, *99*, 2778–2781.

(117) Patnaik, S. S.; Trohalaki, S.; Naik, R. R.; Stone, M. O.; Pachter, R. Computational study of the absorption spectra of green fluorescent protein mutants. *Biopolymers* **2007**, *85*, 253–263.

(118) Voliani, V.; Bizzarri, R.; Nifosi, R.; Abbruzzetti, S.; Grandi, E.; Viappiani, C.; Beltram, F. Cis- trans photoisomerization of fluorescent-protein chromophores. *J. Phys. Chem. B* **2008**, *112*, 10714–10722.

(119) Addison, K.; Conyard, J.; Dixon, T.; Bulman Page, P. C.; Solntsev, K. M.; Meech, S. R. Ultrafast studies of the photophysics of Cis and trans states of the green fluorescent protein chromophore. *J. Phys. Chem. Lett.* **2012**, *3*, 2298–2302.

(120) Rather, S. R.; Rajbongshi, B. K.; Nair, N. N.; Sen, P.; Ramanathan, G. Excited state relaxation dynamics of model green fluorescent protein chromophore analogs: Evidence for cis–trans isomerism. *J. Phys. Chem. A* **2011**, *115*, 13733–13742.

(121) Gao, A.; Wang, M.; Ding, J. Ultrafast trans-cis photoisomerization of the neutral chromophore in green fluorescent proteins: Surface-hopping dynamics simulation. *J. Chem. Phys.* **2018**, *149*.

(122) Park, J. W.; Shiozaki, T. On-the-fly CASPT2 surface-hopping dynamics. *J. Chem. Theory Comput.* **2017**, *13*, 3676–3683.

(123) Zhao, L.; Zhou, P.-W.; Li, B.; Gao, A.-H.; Han, K.-L. Non-adiabatic dynamics of isolated green fluorescent protein chromophore anion. *J. Chem. Phys.s* **2014**, *141*.

(124) Martin, M. E.; Negri, F.; Olivucci, M. Origin, nature, and fate of the fluorescent state of the green fluorescent protein chromophore at the CASPT2//CASSCF resolution. *J. Am. Chem. Soc.* **2004**, *126*, 5452–5464.

(125) Toniolo, A.; Olsen, S.; Manohar, L.; Martinez, T. Conical intersection dynamics in solution: the chromophore of green fluorescent protein. *Faraday Discuss.* **2004**, *127*, 149–163.

(126) Olsen, S.; Lamothe, K.; Martinez, T. J. Protonic gating of excited-state twisting and charge localization in GFP chromophores: a mechanistic hypothesis for reversible photoswitching. *J. Am. Chem. Soc.* **2010**, *132*, 1192–1193.

(127) Stoner-Ma, D.; Jaye, A. A.; Matousek, P.; Towrie, M.; Meech, S. R.; Tonge, P. J. Observation of excited-state proton transfer in green fluorescent protein using ultrafast vibrational spectroscopy. *J. Am. Chem. Soc.* **2005**, *127*, 2864–2865.

(128) Vendrell, O.; Gelabert, R.; Moreno, M.; Lluch, J. M. Potential energy landscape of the photoinduced multiple proton-transfer process in the green fluorescent protein: classical molecular dynamics and multiconfigurational electronic structure calculations. *J. Am. Chem. Soc.* **2006**, *128*, 3564–3574.

(129) Bourne-Worster, S.; Worth, G. A. Quantum dynamics of excited state proton transfer in green fluorescent protein. *J. Chem. Phys.* **2024**, *160*.

(130) Lavoie-Cardinal, F.; Jensen, N. A.; Westphal, V.; Stiel, A. C.; Chmyrov, A.; Bierwagen, J.; Testa, I.; Jakobs, S.; Hell, S. W. Two-color RESOLFT nanoscopy with green and red fluorescent photochromic proteins. *ChemPhysChem* **2014**, *15*, 655–663.

(131) Mizuno, H.; Mal, T. K.; Wälchli, M.; Kikuchi, A.; Fukano, T.; Ando, R.; Jeyakanthan, J.; Taka, J.; Shiro, Y.; Ikura, M., et al. Light-dependent regulation of structural flexibility in a photochromic fluorescent protein. *Proc. Natl. Acad. Sci. U.S.A.* **2008**, *105*, 9227–9232.

(132) Dedecker, P.; Hotta, J.-i.; Ando, R.; Miyawaki, A.; Engelborghs, Y.; Hofkens, J. Fast and reversible photoswitching of the fluorescent protein Dronpa as evidenced by fluorescence correlation spectroscopy. *Biophys. J.* **2006**, *91*, L45–L47.

(133) Hayashi, I.; Mizuno, H.; Tong, K. I.; Furuta, T.; Tanaka, F.; Yoshimura, M.; Miyawaki, A.; Ikura, M. Crystallographic evidence for water-assisted photoinduced peptide cleavage in the stony coral fluorescent protein Kaede. *J. Mol. Biol.* **2007**, *372*, 918–926.

(134) Kogure, T.; Karasawa, S.; Araki, T.; Saito, K.; Kinjo, M.; Miyawaki, A. A fluorescent variant of a protein from the stony coral Montipora facilitates dual-color single-laser fluorescence cross-correlation spectroscopy. *Nat. Biotechnol.* **2006**, *24*, 577–581.

(135) Tay, J.; Parkes, M. A.; Addison, K.; Chan, Y.; Zhang, L.; Hailes, H. C.; Bulman Page, P. C.; Meech, S. R.; Blancafort, L.; Fielding, H. H. The Effect of conjugation on the competition between internal conversion and electron detachment: a comparison between green fluorescent and red Kaede protein chromophores. *J. Phys. Chem. Lett.* **2017**, *8*, 765–771.

(136) Bulina, M. E.; Chudakov, D. M.; Britanova, O. V.; Yanushevich, Y. G.; Staroverov, D. B.; Chepurnykh, T. V.; Merzlyak, E. M.; Shkrob, M. A.; Lukyanov, S.; Lukyanov, K. A. A genetically encoded photosensitizer. *Nat. Biotechnol.* **2006**, *24*, 95–99.

(137) Sample, V.; Newman, R. H.; Zhang, J. The structure and function of fluorescent proteins. *Chem. Soc. Rev.* **2009**, *38*, 2852–2864.

(138) Wachter, R. M. The family of GFP-like proteins: Structure, function, photophysics and biosensor applications. Introduction and perspective. *Photochem. Photobiol.* **2006**, *82*, 339–344.

(139) Nemukhin, A.; Grigorenko, B.; Savitsky, A. Computer modeling of the structure and spectra of fluorescent proteins. *Acta Nat.* **2009**, *1*, 33–43.

(140) Seward, H. E.; Bagshaw, C. R. The photochemistry of fluorescent proteins: implications for their biological applications. *Chem. Soc. Rev.* **2009**, *38*, 2842–2851.

(141) Lukyanov, K. A.; Chudakov, D. M.; Lukyanov, S.; Verkhusha, V. V. Photoactivatable fluorescent proteins. *Nat. Rev. Mol. Cell Biol.* **2005**, *6*, 885–890.

(142) Lukyanov, K. A.; Serebrovskaya, E. O.; Lukyanov, S.; Chudakov, D. M. Fluorescent proteins as light-inducible photochemical partners. *Photochem. Photobiol. Sci.* **2010**, *9*, 1301–1306.

(143) Subach, F. V.; Verkhusha, V. V. Chromophore transformations in red fluorescent proteins. *Chem. Rev.* **2012**, *112*, 4308–4327.

(144) Tolbert, L. M.; Baldridge, A.; Kowalik, J.; Solntsev, K. M. Collapse and recovery of green fluorescent protein chromophore emission through topological effects. *Acc. Chem. Res.* **2012**, *45*, 171–181.

(145) Conyard, J.; Kondo, M.; Heisler, I. A.; Jones, G.; Baldridge, A.; Tolbert, L. M.; Solntsev, K. M.; Meech, S. R. Chemically modulating the photophysics of the GFP chromophore. *J. Phys. Chem. B* **2011**, *115*, 1571–1577.

(146) Polyakov, I.; Grigorenko, B.; Epifanovsky, E.; Krylov, A.; Nemukhin, A. Potential energy landscape of the electronic states of the GFP chromophore in different protonation forms: Electronic transition energies and conical intersections. *J. Chem. Theory Comput.* **2010**, *6*, 2377–2387.

(147) Kojima, S.; Ohkawa, H.; Hirano, T.; Maki, S.; Niwa, H.; Ohashi, M.; Inouye, S.; Tsuji, F. I. Fluorescent properties of model chromophores of tyrosine-66 substituted mutants of Aequorea green fluorescent protein (GEP). *Tetrahedron Lett.* **1998**, *39*, 5239–5242.

(148) Svendsen, A.; Kiefer, H. V.; Pedersen, H. B.; Bochenkova, A. V.; Andersen, L. H. Origin of the intrinsic fluorescence of the green fluorescent protein. *J. Am. Chem. Soc.* **2017**, *139*, 8766–8771.

(149) Bochenkova, A. V.; Andersen, L. H. Ultrafast dual photoresponse of isolated biological chromophores: link to the photoinduced mode-specific nonadiabatic dynamics in proteins. *Faraday Discuss.* **2013**, *163*, 297–319.

(150) Olsen, S.; Smith, S. C. Bond selection in the photoisomerization reaction of anionic green fluorescent protein and kindling fluorescent protein chromophore models. *J. Am. Chem. Soc.* **2008**, *130*, 8677–8689.

(151) Mori, T.; Martínez, T. J. Exploring the conical intersection seam: the seam space nudged elastic band method. *J. Chem. Theory Comput.* **2013**, *9*, 1155–1163.

(152) Taylor, M. A.; Zhu, L.; Rozanov, N. D.; Stout, K. T.; Chen, C.; Fang, C. Delayed vibrational modulation of the solvated GFP chromophore into a conical intersection. *Phys. Chem. Chem. Phys.* **2019**, *21*, 9728–9739.

(153) Carrascosa, E.; Bull, J. N.; Scholz, M. S.; Coughlan, N. J.; Olsen, S.; Wille, U.; Bieske, E. J. Reversible photoisomerization of the isolated green fluorescent protein chromophore. *J. Phys. Chem. Lett.* **2018**, *9*, 2647–2651.

(154) Mandal, D.; Tahara, T.; Meech, S. R. Excited-state dynamics in the green fluorescent protein chromophore. *J. Phys. Chem. B* **2004**, *108*, 1102–1108.

(155) Webber, N. M.; Litvinenko, K. L.; Meech, S. R. Radiationless relaxation in a synthetic analogue of the green fluorescent protein chromophore. *J. Phys. Chem. B* **2001**, *105*, 8036–8039.

(156) Baffour-Awuah, N. Y. A.; Zimmer, M. Hula-twisting in green fluorescent protein. *Chem. Phys.* **2004**, *303*, 7–11.

(157) Liu, R. S.; Hammond, G. S. Examples of Hula-Twist in Photochemical cis–trans Isomerization. *Chem. Eur. J.* **2001**, *7*, 4536–4545.

(158) Jones, C. M.; List, N. H.; Martínez, T. J. Resolving the ultrafast dynamics of the anionic green fluorescent protein chromophore in water. *Chem. Sci.* **2021**, *12*, 11347–11363.

(159) List, N. H.; Jones, C. M.; Martínez, T. J. Internal conversion of the anionic GFP chromophore: in and out of the I-twisted S 1/S 0 conical intersection seam. *Chem. Sci.* **2022**, *13*, 373–385.

(160) Minezawa, N.; Nakajima, T. Quantum mechanical/molecular mechanical trajectory surface hopping molecular dynamics simulation by spin-flip time-dependent density functional theory. *J. Chem. Phys.* **2020**, *152*.

(161) Toniolo, A.; Ben-Nun, M.; Martinez, T. Optimization of conical intersections with floating occupation semiempirical configuration interaction wave functions. *The Journal of Physical Chemistry A* **2002**, *106*, 4679–4689.

(162) Toniolo, A.; Granucci, G.; Martínez, T. J. Conical intersections in solution: a QM/MM study using floating occupation semiempirical configuration interaction wave functions. *J. Phys. Chem. A* **2003**, *107*, 3822–3830.

(163) Yang, J.-S.; Huang, G.-J.; Liu, Y.-H.; Peng, S.-M. Photoisomerization of the green fluorescence protein chromophore and the meta-and para-amino analogues. *Chem. Commun.* **2008**, 1344–1346.

(164) Chen, Y.-H.; Sung, R.; Sung, K. Insights into excited state intramolecular proton transfer: an alternative model for excited state proton transfer of green fluorescence protein. *J. Phys. Chem. A* **2018**, *122*, 5931–5944.

(165) Fang, X.; Wang, Y.; Wang, D.; Zhao, G.; Zhang, W.; Ren, A.; Wang, H.; Xu, J.; Gao, B.-R.; Yang, W. Synthesized blue fluorescent protein analogue with tunable colors from excited-state intramolecular proton transfer through an N–H $\cdots$ N hydrogen bond. *J. Phys. Chem. Lett.* **2014**, *5*, 92–98.

(166) Nam, K. H. Fluorescent protein-based metal biosensors. *Chemosensors* **2023**, *11*, 216.

(167) Baldridge, A.; Solntsev, K. M.; Song, C.; Tanioka, T.; Kowalik, J.; Hardcastle, K.; Tolbert, L. M. Inhibition of twisting of a green fluorescent protein-like chromophore by metal complexation. *Chem. Commun.* **2010**, *46*, 5686–5688.

(168) An undulatory theory of the mechanics of atoms and molecules. *Phys. Rev.* **1926**, *28*, 1049.

(169) Szabo, A.; Ostlund, N. S., *Modern quantum chemistry: introduction to advanced electronic structure theory*; Courier Corporation: 1996.

(170) Born, M.; Huang, K., *Dynamical theory of crystal lattices*; Oxford university press: 1955.

(171) Born, M.; Oppenheimer, R. Zur Quantentheorie der Molekeln. *Ann. Phys.* **1927**, *389*, 457–484.

(172) Bruus, H.; Flensberg, K., *Many-body quantum theory in condensed matter physics: an introduction*; Oxford university press: 2004.

(173) Hohenberg, P.; Kohn, W. Inhomogeneous electron gas. *Phys. Rev.* **1964**, *136*, B864.

(174) Kohn, W.; Sham, L. J. Self-consistent equations including exchange and correlation effects. *Phys. Rev.* **1965**, *140*, A1133.

(175) Runge, E. Density-functional theory for time-dependent systems. *Phys. Rev. Lett.* **1984**, *52*, 997.

(176) Olsen, J.; Yeager, D. L.; Jørgensen, P. Optimization and Characterization of a Multiconfigurational Self-Consistent Field (MCSCF) State. *Adv. Chem. Phys.* **1983**, 1–176.

(177) Shepard, R. The multiconfiguration self-consistent field method. *Advances in Chemical Physics: Ab Initio Methods in Quantum Chemistry Part 2* **1987**, *69*, 63–200.

(178) Dalgaard, E.; Jo/rgensen, P. Optimization of orbitals for multiconfigurational reference states. *J. Chem. Phys.* **1978**, *69*, 3833–3844.

(179) Lischka, H.; Nachtigallova, D.; Aquino, A. J.; Szalay, P. G.; Plasser, F.; Machado, F. B.; Barbatti, M. Multireference approaches for excited states of molecules. *Chem. Rev.* **2018**, *118*, 7293–7361.

(180) Roos, B. O.; Taylor, P. R.; Sigbahn, P. E. A complete active space SCF method (CASSCF) using a density matrix formulated super-CI approach. *Chem. Phys.* **1980**, *48*, 157–173.

(181) Roos, B. O. et al. The complete active space self-consistent field method and its applications in electronic structure calculations. *Adv. Chem. Phys.* **2007**, *69*, 399–445.

(182) Jensen, F., *Introduction to computational chemistry*; John wiley & sons: 2017.

(183) Andersson, K.; Malmqvist, P. A.; Roos, B. O.; Sadlej, A. J.; Wolinski, K. Second-order perturbation theory with a CASSCF reference function. *J. Phys. Chem.* **1990**, *94*, 5483–5488.

(184) Andersson, K.; Malmqvist, P.-Å.; Roos, B. O. Second-order perturbation theory with a complete active space self-consistent field reference function. *J. Chem. Phys.* **1992**, *96*, 1218–1226.

(185) Finley, J.; Malmqvist, P.-Å.; Roos, B. O.; Serrano-Andrés, L. The multi-state CASPT2 method. *Chem. Phys. Lett.* **1998**, *288*, 299–306.

(186) Granovsky, A. A. Extended multi-configuration quasi-degenerate perturbation theory: The new approach to multi-state multi-reference perturbation theory. *J. Chem. Phys.* **2011**, *134*.

(187) Shiozaki, T.; Győrffy, W.; Celani, P.; Werner, H.-J. Communication: Extended multi-state complete active space second-order perturbation theory: Energy and nuclear gradients. *J. Chem. Phys.* **2011**, *135*.

(188) Schirmer, J. Beyond the random-phase approximation: A new approximation scheme for the polarization propagator. *Phys. Rev. A* **1982**, *26*, 2395.

(189) Schirmer, J.; Cederbaum, L. S.; Walter, O. New approach to the one-particle Green's function for finite Fermi systems. *Phys. Rev. A* **1983**, *28*, 1237.

(190) Trofimov, A. B.; Krivdina, I.; Weller, J.; Schirmer, J. Algebraic-diagrammatic construction propagator approach to molecular response properties. *Chem. Phys.* **2006**, *329*, 1–10.

(191) Trofimov, A.; Stelter, G.; Schirmer, J. A consistent third-order propagator method for electronic excitation. *J. Chem. Phys.* **1999**, *111*, 9982–9999.

(192) Trofimov, A.; Stelter, G.; Schirmer, J. Electron excitation energies using a consistent third-order propagator approach: Comparison with full configuration interaction and coupled cluster results. *J. Chem. Phys.* **2002**, *117*, 6402–6410.

(193) Schirmer, J.; Trofimov, A. B. Intermediate state representation approach to physical properties of electronically excited molecules. *J. Chem. Phys.* **2004**, *120*, 11449–11464.

(194) Hammes-Schiffer, S.; Tully, J. C. Proton transfer in solution: Molecular dynamics with quantum transitions. *J. Chem. Phys.* **1994**, *101*, 4657–4667.

(195) Granucci, G.; Persico, M. Critical appraisal of the fewest switches algorithm for surface hopping. *J. Chem. Phys.* **2007**, *126*.

(196) Jain, A.; Sindhu, A. Pedagogical overview of the fewest switches surface hopping method. *ACS Omega* **2022**, *7*, 45810–45824.

(197) Brancato, G.; Signore, G.; Neyroz, P.; Polli, D.; Cerullo, G.; Abbandonato, G.; Nucara, L.; Barone, V.; Beltram, F.; Bizzarri, R. Dual fluorescence through Kasha's rule breaking: an unconventional Photomechanism for intracellular probe design. *J. Phys. Chem. B* **2015**, *119*, 6144–6154.

(198) Eber, G.; Grüneis, F.; Schneider, S.; Dörr, F. Dual fluorescence emission of azulene derivatives in solution. *Chem. Phys. Lett.* **1974**, *29*, 397–404.

(199) Bettermann, H.; Bienioschek, M.; Ippendorf, H.; Martin, H.-D. Dual fluorescence of novel modified carotenoids. *Angew. Chem. Int. Ed.* **1992**, *31*, 1042–1044.

(200) Feng, X.; Qi, C.; Feng, H.-T.; Zhao, Z.; Sung, H. H.; Williams, I. D.; Kwok, R. T.; Lam, J. W.; Qin, A.; Tang, B. Z. Dual fluorescence of tetraphenylethylene-substituted pyrenes with aggregation-induced emission characteristics for white-light emission. *Chem. Sci.* **2018**, *9*, 5679–5687.

(201) Grabowski, Z. R.; Rotkiewicz, K.; Rettig, W. Structural changes accompanying intramolecular electron transfer: focus on twisted intramolecular charge-transfer states and structures. *Chem. Rev.* **2003**, *103*, 3899–4032.

(202) Haidekker, M. A.; Theodorakis, E. A. Environment-sensitive behavior of fluorescent molecular rotors. *J. Biol. Eng.* **2010**, *4*, 1–14.

(203) Zachariasse, K. A.; Von Der Haar, T.; Hebecker, A.; Leinhos, U.; Kuhnle, W. Intramolecular charge transfer in aminobenzonitriles: requirements for dual fluorescence. *Pure Appl. Chem.* **1993**, *65*, 1745–1750.

(204) Ghosh, S.; Girish, K.; Ghosh, S. Evaluation of intramolecular charge transfer state of 4-N, N-dimethylamino cinnamaldehyde using time-dependent density functional theory. *J. Chem. Sci.* **2013**, *125*, 933–938.

(205) Grabowski, Z. R.; Rotkiewicz, K.; Siemiarczuk, A. Dual fluorescence of donor-acceptor molecules and the twisted intramolecular charge transfer (TICT) states. *J. Lumin.* **1979**, *18*, 420–424.

(206) Chrayteh, A.; Ewels, C.; Jacquemin, D. Dual fluorescence in strap ESIPT systems: a theoretical study. *Phys. Chem. Chem. Phys.* **2020**, *22*, 854–863.

(207) Czernel, G.; Budziak, I.; Oniszczuk, A.; Karcz, D.; Pustuła, K.; Górecki, A.; Matwijczuk, A.; Gładyszewska, B.; Gagoś, M.; Niewiadomy, A., et al. ESIPT-related origin of dual fluorescence in the selected model 1, 3, 4-thiadiazole derivatives. *Molecules* **2020**, *25*, 4168.

(208) Tang, K.-C.; Chang, M.-J.; Lin, T.-Y.; Pan, H.-A.; Fang, T.-C.; Chen, K.-Y.; Hung, W.-Y.; Hsu, Y.-H.; Chou, P.-T. Fine tuning the energetics of excited-state intramolecular proton transfer (ESIPT): white light generation in a single ESIPT system. *J. Am. Chem. Soc* **2011**, *133*, 17738–17745.

(209) Nandhikonda, P.; Heagy, M. D. Dual fluorescent N-aryl-2, 3-naphthalimides: applications in ratiometric DNA detection and white organic light-emitting devices. *Org. Lett.* **2010**, *12*, 4796–4799.

(210) Gui, R.; Jin, H.; Bu, X.; Fu, Y.; Wang, Z.; Liu, Q. Recent advances in dual-emission ratiometric fluorescence probes for chemo/biosensing and bioimaging of biomarkers. *Coord. Chem. Rev.* **2019**, *383*, 82–103.

(211) Haidekker, M. A.; Theodorakis, E. A. Ratiometric mechanosensitive fluorescent dyes: design and applications. *J. Mater. Chem. C* **2016**, *4*, 2707–2718.

(212) Wu, L.; Huang, C.; Emery, B. P.; Sedgwick, A. C.; Bull, S. D.; He, X.-P.; Tian, H.; Yoon, J.; Sessler, J. L.; James, T. D. Förster resonance energy transfer (FRET)-based small-molecule sensors and imaging agents. *Chem. Soc. Rev.* **2020**, *49*, 5110–5139.

(213) Huang, X.; Song, J.; Yung, B. C.; Huang, X.; Xiong, Y.; Chen, X. Ratiometric optical nanoprobes enable accurate molecular detection and imaging. *Chem. Soc. Rev.* **2018**, *47*, 2873–2920.

(214) Chatterjee, T.; Mandal, M.; Das, A.; Bhattacharyya, K.; Datta, A.; Mandal, P. K. Dual fluorescence in GFP chromophore analogues: Chemical modulation of charge transfer and proton transfer bands. *J. Phys. Chem. B* **2016**, *120*, 3503–3510.

(215) Chatterjee, S.; Ahire, K.; Karuso, P. Room-temperature dual fluorescence of a locked green fluorescent protein chromophore analogue. *J. Am. Chem. Soc.* **2019**, *142*, 738–749.

(216) Nemukhin, A. V.; Grigorenko, B. L.; Khrenova, M. G.; Krylov, A. I. Computational challenges in modeling of representative bioimaging proteins: GFP-like proteins, flavoproteins, and phytochromes. *J. Phys. Chem. B* **2019**, *123*, 6133–6149.

(217) Wu, L.; Burgess, K. Syntheses of highly fluorescent GFP-chromophore analogues. *J. Am. Chem. Soc.* **2008**, *130*, 4089–4096.

(218) Hsu, Y.-H.; Chen, Y.-A.; Tseng, H.-W.; Zhang, Z.; Shen, J.-Y.; Chuang, W.-T.; Lin, T.-C.; Lee, C.-S.; Hung, W.-Y.; Hong, B.-C., et al. Locked ortho- and para-Core chromophores of green fluorescent protein; dramatic emission

enhancement via structural constraint. *J. Am. Chem. Soc.* **2014**, *136*, 11805–11812.

(219) Chen, Y.-H.; Sung, R.; Sung, K. Why does a para-amino group make the green fluorescent protein chromophore non-fluorescent: coherent intramolecular charge transfer reduces the Z/E-photoisomerization barrier. *Chem. Commun.* **2019**, *55*, 8991–8994.

(220) Chalfie, M.; Tu, Y.; Euskirchen, G.; Ward, W. W.; Prasher, D. C. Green fluorescent protein as a marker for gene expression. *Science* **1994**, *263*, 802–805.

(221) Cai, L.; Li, H.; Yu, X.; Wu, L.; Wei, X.; James, T. D.; Huang, C. Green Fluorescent Protein GFP-Chromophore-Based Probe for the Detection of Mitochondrial Viscosity in Living Cells. *ACS Appl. Bio Mater.* **2021**, *4*, 2128–2134.

(222) Branchini, B. R.; Lusins, J. O.; Zimmer, M. A molecular mechanics and database analysis of the structural preorganization and activation of the chromophore-containing hexapeptide fragment in green fluorescent protein. *J. Biomol. Struct. Dyn.* **1997**, *14*, 441–448.

(223) Stoner-Ma, D.; Jaye, A. A.; Ronayne, K. L.; Nappa, J.; Meech, S. R.; Tonge, P. J. An alternate proton acceptor for excited-state proton transfer in green fluorescent protein: rewiring GFP. *J. Am. Chem. Soc.* **2008**, *130*, 1227–1235.

(224) Sen, T.; Ma, Y.; Polyakov, I. V.; Grigorenko, B. L.; Nemukhin, A. V.; Krylov, A. I. Interplay between locally excited and charge transfer states governs the photoswitching mechanism in the fluorescent protein Dreiklang. *J. Phys. Chem. B* **2021**, *125*, 757–770.

(225) Dong, J.; Solntsev, K. M.; Poizat, O.; Tolbert, L. M. The meta-green fluorescent protein chromophore. *J. Am. Chem. Soc.* **2007**, *129*, 10084–10085.

(226) Shu, X.; Leiderman, P.; Gepshtein, R.; Smith, N. R.; Kallio, K.; Huppert, D.; Remington, S. J. An alternative excited-state proton transfer pathway in green fluorescent protein variant S205V. *Protein Sci.* **2007**, *16*, 2703–2710.

(227) Wineman-Fisher, V.; Simkovitch, R.; Shomer, S.; Gepshtein, R.; Huppert, D.; Saif, M.; Kallio, K.; Remington, S. J.; Miller, Y. Insight into the structure and the mechanism of the slow proton transfer in the GFP double mutant T203V/S205A. *Phys. Chem. Chem. Phys.* **2014**, *16*, 11211–11223.

(228) Shinobu, A.; Agmon, N. Proton wire dynamics in the green fluorescent protein. *J. Chem. Theory Comput.* **2017**, *13*, 353–369.

(229) Hsieh, C.-C.; Chou, P.-T.; Shih, C.-W.; Chuang, W.-T.; Chung, M.-W.; Lee, J.; Joo, T. Comprehensive studies on an overall proton transfer cycle of the ortho-green fluorescent protein chromophore. *J. Am. Chem. Soc.* **2011**, *133*, 2932–2943.

(230) Chuang, W.-T.; Hsieh, C.-C.; Lai, C.-H.; Lai, C.-H.; Shih, C.-W.; Chen, K.-Y.; Hung, W.-Y.; Hsu, Y.-H.; Chou, P.-T. Excited-state intramolecular proton transfer molecules bearing o-hydroxy analogues of green fluorescent protein chromophore. *J. Org. Chem.* **2011**, *76*, 8189–8202.

(231) Chen, Y.-H.; Sung, R.; Sung, K. Synthesis and properties of the p-sulfonamide analogue of the green fluorescent protein (GFP) chromophore: the mimic of GFP chromophore with very strong N–H photoacid strength. *Org. Lett.* **2018**, *20*, 1768–1772.

(232) Frisch, M. et al. Gaussian 16, Revision C. 01. Gaussian, Inc., Wallingford CT. 2016.

(233) Yang, F.; Moss, L. G.; Phillips, G. N. The molecular structure of green fluorescent protein. *Nat. Biotechnol.* **1996**, *14*, 1246–1251.

(234) Parr, R. G. In *Horizons of quantum chemistry*; Springer: 1980, pp 5–15.

(235) Adamo, C.; Jacquemin, D. The calculations of excited-state properties with Time-Dependent Density Functional Theory. *Chem. Soc. Rev.* **2013**, *42*, 845–856.

(236) Lu, L.; Hu, H.; Hou, H.; Wang, B. An improved B3LYP method in the calculation of organic thermochemistry and reactivity. *Comput. Theor. Chem.* **2013**, *1015*, 64–71.

(237) Yanai, T.; Tew, D. P.; Handy, N. C. A new hybrid exchange–correlation functional using the Coulomb-attenuating method (CAM-B3LYP). *Chem. Phys. Lett.* **2004**, *393*, 51–57.

(238) Zhao, Y.; Truhlar, D. G. The M06 suite of density functionals for main group thermochemistry, thermochemical kinetics, noncovalent interactions, excited states, and transition elements: two new functionals and systematic testing of four M06-class functionals and 12 other functionals. *Theor. Chem. Acc.* **2008**, *120*, 215–241.

(239) Petersson, G.; Al-Laham, M. A. A complete basis set model chemistry. II. Open-shell systems and the total energies of the first-row atoms. *J. Chem. Phys.* **1991**, *94*, 6081–6090.

(240) Francl, M. M.; Pietro, W. J.; Hehre, W. J.; Binkley, J. S.; Gordon, M. S.; DeFrees, D. J.; Pople, J. A. Self-consistent molecular orbital methods. XXIII. A polarization-type basis set for second-row elements. *J. Chem. Phys.* **1982**, *77*, 3654–3665.

(241) Schäfer, A.; Huber, C.; Ahlrichs, R. Fully optimized contracted Gaussian basis sets of triple zeta valence quality for atoms Li to Kr. *J. Chem. Phys.* **1994**, *100*, 5829–5835.

(242) Mennucci, B.; Cances, E.; Tomasi, J. Evaluation of solvent effects in isotropic and anisotropic dielectrics and in ionic solutions with a unified integral equation method: theoretical bases, computational implementation, and numerical applications. *J. Phys. Chem. B* **1997**, *101*, 10506–10517.

(243) Cances, E.; Mennucci, B.; Tomasi, J. A new integral equation formalism for the polarizable continuum model: Theoretical background and applications to isotropic and anisotropic dielectrics. *J. Chem. Phys.* **1997**, *107*, 3032–3041.

(244) Cossi, M.; Barone, V. Time-dependent density functional theory for molecules in liquid solutions. *J. Chem. Phys.* **2001**, *115*, 4708–4717.

(245) Improta, R.; Barone, V.; Scalmani, G.; Frisch, M. J. A state-specific polarizable continuum model time dependent density functional theory method for excited state calculations in solution. *J. Chem. Phys.* **2006**, *125*, 054103 (1–9).

(246) Improta, R.; Scalmani, G.; Frisch, M. J.; Barone, V. Toward effective and reliable fluorescence energies in solution by a new state specific polarizable continuum model time dependent density functional theory approach. *J. Chem. Phys.* **2007**, *127*, 074504 (1–9).

(247) Johnson, E. R.; Keinan, S.; Mori-Sánchez, P.; Contreras-García, J.; Cohen, A. J.; Yang, W. Revealing noncovalent interactions. *J. Am. Chem. Soc.* **2010**, *132*, 6498–6506.

(248) Tang, W.; Sanville, E.; Henkelman, G. A grid-based Bader analysis algorithm without lattice bias. *J. Phys.: Condens. Matter* **2009**, *21*, 084204.

(249) Lu, T.; Chen, F. Multiwfn: a multifunctional wavefunction analyzer. *J. Comput. Chem.* **2012**, *33*, 580–592.

(250) Humphrey, W.; Dalke, A.; Schulten, K. VMD: visual molecular dynamics. *J. Mol. Graphics* **1996**, *14*, 33–38.

(251) Barbatti, M.; Aquino, A. J.; Lischka, H. The UV absorption of nucleobases: semi-classical ab initio spectra simulations. *Phys. Chem. Chem. Phys.* **2010**, *12*, 4959–4967.

(252) Barbatti, M.; Granucci, G.; Persico, M.; Ruckenbauer, M.; Vazdar, M.; Eckert-Maksić, M.; Lischka, H. The on-the-fly surface-hopping program system Newton-X: Application to ab initio simulation of the nonadiabatic photodynamics of benchmark systems. *J. Photochem. Photobiol. A: Chem.* **2007**, *190*, 228–240.

(253) Prommin, C.; Kanlayakan, N.; Chansen, W.; Salaeh, R.; Kerdpol, K.; Daengngern, R.; Kungwan, N. Theoretical insights on solvent control of intramolecular and intermolecular proton transfer of 2-(2′-hydroxyphenyl) benzimidazole. *J. Phys. Chem. A* **2017**, *121*, 5773–5784.

(254) Barbatti, M.; Aquino, A. J.; Lischka, H.; Schriever, C.; Lochbrunner, S.; Riedle, E. Ultrafast internal conversion pathway and mechanism in 2-(2′-hydroxyphenyl) benzothiazole: a case study for excited-state intramolecular proton transfer systems. *Phys. Chem. Chem. Phys.* **2009**, *11*, 1406–1415.

(255) Chansen, W.; Kungwan, N. Theoretical Insights into Excited-State Intermolecular Proton Transfers of 2, 7-Diazaindole in Water Using a Microsolvation Approach. *J. Phys. Chem. A* **2021**, *125*, 5314–5325.

(256) Li, Y.; Siddique, F.; Aquino, A. J.; Lischka, H. Molecular dynamics simulation of the excited-state proton transfer mechanism in 3-hydroxyflavone using explicit hydration models. *J. Phys. Chem. A* **2021**, *125*, 5765–5778.

(257) Swope, W. C.; Andersen, H. C.; Berens, P. H.; Wilson, K. R. A computer simulation method for the calculation of equilibrium constants for the formation of physical clusters of molecules: Application to small water clusters. *J. Chem. Phys.* **1982**, *76*, 637–649.

(258) Marques, M. A.; López, X.; Varsano, D.; Castro, A.; Rubio, A. Time-dependent density-functional approach for biological chromophores: the case of the green fluorescent protein. *Phys. Rev. Lett.* **2003**, *90*, 258101.

(259) Jacquemin, D.; Mennucci, B.; Adamo, C. Excited-state calculations with TD-DFT: from benchmarks to simulations in complex environments. *Phys. Chem. Chem. Phys.* **2011**, *13*, 16987–16998.

(260) Cai, Z.-L.; Crossley, M. J.; Reimers, J. R.; Kobayashi, R.; Amos, R. D. Density functional theory for charge transfer: The nature of the N-bands of porphyrins and chlorophylls revealed through CAM-B3LYP, CASPT2, and SAC-CI calculations. *J. Phys. Chem. B* **2006**, *110*, 15624–15632.

(261) Webber, N. M.; Meech, S. R. Electronic spectroscopy and solvatochromism in the chromophore of GFP and the Y66F mutant. *Photochem. Photobiol. Sci.* **2007**, *6*, 976–981.

(262) Dong, J.; Solntsev, K. M.; Tolbert, L. M. Solvatochromism of the green fluorescence protein chromophore and its derivatives. *J. Am. Chem. Soc.* **2006**, *128*, 12038–12039.

(263) Kina, D.; Nakayama, A.; Noro, T.; Taketsugu, T.; Gordon, M. S. Ab initio QM/MM molecular dynamics study on the excited-state hydrogen transfer of 7-azaindole in water solution. *J. Phys. Chem. A* **2008**, *112*, 9675–9683.

(264) Raucci, U.; Chiariello, M. G.; Rega, N. Modeling excited-state proton transfer to solvent: A dynamics study of a super photoacid with a hybrid implicit/explicit solvent model. *J. Chem. Theory Comput.* **2020**, *16*, 7033–7043.

(265) Da Silva, C. O.; Mennucci, B.; Vreven, T. Combining microsolvation and polarizable continuum studies: New insights in the rotation mechanism of amides in water. *J. Phys. Chem. A* **2003**, *107*, 6630–6637.

(266) Simm, G. N.; Türtscher, P. L.; Reiher, M. Systematic microsolvation approach with a cluster-continuum scheme and conformational sampling. *J. Comput. Chem.* **2020**, *41*, 1144–1155.

(267) Wang, S.; Smith, S. C. Mechanistic aspects of proton chain transfer in the green fluorescent protein Part II. A comparison of minimal quantum chemical models. *Phys. Chem. Chem. Phys.* **2007**, *9*, 452–458.

(268) Zhao, G.-J.; Han, K.-L. Hydrogen bonding in the electronic excited state. *Acc. Chem. Res.* **2012**, *45*, 404–413.

(269) Guo, Y.; Zhong, Y.; Wu, Z.; Wang, C.; Wang, Y.; Zhang, J.; Wang, H.; Zhao, G. The hydrogen bond effect on excited state mechanism for 2-isopropyl thioxanone in protic solvents: Experimental and theoretical investigation. *J. Mol. Liq.* **2022**, *345*, 117012.

(270) Li, P.; Guo, Y.; Jia, Y.; Guan, H.; Wang, C.; Wu, Z.; Sun, S.; Qu, Z.; Zhou, P.; Zhao, G. Achieving metal-free phosphorescence in dilute solutions for imaging hypoxia in cells and tumors. *Mater. Chem. Front.* **2021**, *5*, 7170–7175.

(271) Wang, C.; Liu, Y.; Feng, X.; Zhou, C.; Liu, Y.; Yu, X.; Zhao, G. Phase regulation strategy of perovskite nanocrystals from 1D orthomorphic $NH_4PbI_3$ to 3D cubic $(NH_4)_{0{\cdot}5}$ $Cs_{0{\cdot}5}Pb(I_{0{\cdot}5}Br_{0{\cdot}5})_3$ phase enhances photoluminescence. *Angew. Chem. Int. Ed.* **2019**, *58*, 11642–11646.

(272) Cao, P.; Zheng, H.; Wu, P. Multicolor ultralong phosphorescence from perovskite-like octahedral $\alpha$-AlF3. *Nat. Commun.* **2022**, *13*, 1–9.

(273) Guo, Y.; Guan, H.; Li, P.; Wang, C.; Wu, Z.; Wang, Y.; Yu, Z.; Zhang, Z.; Wang, S.; Zhao, G. Thermally activated delayed fluorescence enabled by reversed conformational distortion for blue emitters. *J. Phys. Chem. Lett.* **2021**, *12*, 9501–9507.

(274) Cui, Y.; Zhao, H.; Zhao, J.; Li, P.; Song, P.; Xia, L. The excited-state multiple proton transfer mechanism of the 7-hydroxyquinoline–$(CH_3OH)_3$ cluster. *New J. Chem.* **2015**, *39*, 9910–9917.

(275) Dewar, M. J. Multibond reactions cannot normally be synchronous. *J. Am. Chem. Soc.* **1984**, *106*, 209–219.

(276) Abbandonato, G.; Signore, G.; Nifosı`, R.; Voliani, V.; Bizzarri, R.; Beltram, F. Cis–trans photoisomerization properties of GFP chromophore analogs. *Eur. Biophys. J.* **2011**, *40*, 1205–1214.

(277) He, X.; Bell, A. F.; Tonge, P. J. Ground state isomerization of a model green fluorescent protein chromophore. *FEBS Lett.* **2003**, *549*, 35–38.

(278) Warren, M. M.; Kaucikas, M.; Fitzpatrick, A.; Champion, P.; Timothy Sage, J.; Van Thor, J. J. Ground-state proton transfer in the photoswitching reactions of the fluorescent protein Dronpa. *Nat. Commun.* **2013**, *4*, 1461.

(279) Chudakov, D. M.; Matz, M. V.; Lukyanov, S.; Lukyanov, K. A. Fluorescent proteins and their applications in imaging living cells and tissues. *Physiol. Rev.* **2010**, *90*, 1103–1163.

(280) Lippincott-Schwartz, J.; Altan-Bonnet, N.; Patterson, G. H. Photobleaching and photoactivation: following protein dynamics in living cells. *Nat. Cell Biol.* **2003**, *5*, S7–14.

(281) Lippincott-Schwartz, J.; Patterson, G. H. Development and use of fluorescent protein markers in living cells. *Science* **2003**, *300*, 87–91.

(282) Chakraborty, P.; Liu, Y.; Weinacht, T.; Matsika, S. Excited state dynamics of cis, cis-1, 3-cyclooctadiene: Non-adiabatic trajectory surface hopping. *J. Chem. Phys.* **2020**, *152*, 174302.

(283) Barbatti, M.; Paier, J.; Lischka, H. Photochemistry of ethylene: A multireference configuration interaction investigation of the excited-state energy surfaces. *J. Chem. Phys.* **2004**, *121*, 11614–11624.

(284) Tao, H.; Levine, B. G.; Martínez, T. J. Ab initio multiple spawning dynamics using multi-state second-order perturbation theory. *J. Phys. Chem. A* **2009**, *113*, 13656–13662.

(285) Olivucci, M.; Ragazos, I. N.; Bernardi, F.; Robb, M. A. A conical intersection mechanism for the photochemistry of butadiene. A MC-SCF study. *J. Am. Chem. Soc.* **1993**, *115*, 3710–3721.

(286) Dou, Y.; Torralva, B. R.; Allen, R. E. Detailed Mechanism for Trans- Cis Photoisomerization of Butadiene Following a Femtosecond-Scale Laser Pulse. *J. Phys. Chem. A* **2003**, *107*, 8817–8824.

(287) Glover, W. J.; Mori, T.; Schuurman, M. S.; Boguslavskiy, A. E.; Schalk, O.; Stolow, A.; Martínez, T. J. Excited state non-adiabatic dynamics of the smallest polyene, trans 1, 3-butadiene. II. Ab initio multiple spawning simulations. *J. Chem. Phys.* **2018**, *148*, 164303.

(288) Celani, P.; Ottani, S.; Olivucci, M.; Bernardi, F.; Robb, M. A. What happens during the picosecond lifetime of 2A1 cyclohexa-1, 3-diene? A CAS-SCF study of the cyclohexadiene/hexatriene photochemical interconversion. *J. Am. Chem. Soc.* **1994**, *116*, 10141–10151.

(289) Kim, J.; Tao, H.; White, J. L.; Petrovic, V. S.; Martinez, T. J.; Bucksbaum, P. H. Control of 1, 3-cyclohexadiene photoisomerization using light-induced conical intersections. *J. Phys. Chem. A* **2012**, *116*, 2758–2763.

(290) Polyak, I.; Hutton, L.; Crespo-Otero, R.; Barbatti, M.; Knowles, P. J. Ultrafast photoinduced dynamics of 1, 3-cyclohexadiene using XMS-CASPT2 surface hopping. *J. Chem. Theory Comput.* **2019**, *15*, 3929–3940.

(291) Dickson, R. M.; Cubitt, A. B.; Tsien, R. Y.; Moerner, W. E. On/off blinking and switching behaviour of single molecules of green fluorescent protein. *Nature* **1997**, *388*, 355–358.

(292) Jung, G.; Wiehler, J.; Steipe, B.; Bräuchle, C.; Zumbusch, A. Single-molecule microscopy of the green fluorescent protein using simultaneous two-color excitation. *ChemPhysChem* **2001**, *2*, 392–396.

(293) Ando, R.; Mizuno, H.; Miyawaki, A. Regulated fast nucleocytoplasmic shuttling observed by reversible protein highlighting. *Science* **2004**, *306*, 1370–1373.

(294) Hutchison, C. D.; Baxter, J. M.; Fitzpatrick, A.; Dorlhiac, G.; Fadini, A.; Perrett, S.; Maghlaoui, K.; Lefèvre, S. B.; Cordon-Preciado, V.; Ferreira, J. L., et al. Optical control of ultrafast structural dynamics in a fluorescent protein. *Nat. Chem.* **2023**, *15*, 1607–1615.

(295) Andresen, M.; Stiel, A. C.; Trowitzsch, S.; Weber, G.; Eggeling, C.; Wahl, M. C.; Hell, S. W.; Jakobs, S. Structural basis for reversible photoswitching in Dronpa. *Proc. Natl. Acad. Sci. U. S. A.* **2007**, *104*, 13005–13009.

(296) Mandal, D.; Tahara, T.; Webber, N. M.; Meech, S. R. Ultrafast fluorescence of the chromophore of the green fluorescent protein in alcohol solutions. *Chem. Phys. Lett.* **2002**, *358*, 495–501.

(297) Johnson, F. H.; Shimomura, O.; Saiga, Y.; Gershman, L. C.; Reynolds, G. T.; Waters, J. R. Quantum efficiency of Cypridina luminescence, with a note on that of Aequorea. *J. Cell. Comp. Physiol.* **1962**, *60*, 85–103.

(298) Perozzo, M.; Ward, K. B.; Thompson, R.; Ward, W. X-ray diffraction and time-resolved fluorescence analyses of Aequorea green fluorescent protein crystals. *J. Biol. Chem.* **1988**, *263*, 7713–7716.

(299) Solntsev, K. M.; Poizat, O.; Dong, J.; Rehault, J.; Lou, Y.; Burda, C.; Tolbert, L. M. Meta and para effects in the ultrafast excited-state dynamics of the green fluorescent protein chromophores. *J. Phys. Chem. B* **2008**, *112*, 2700–2711.

(300) Litvinenko, K. L.; Webber, N. M.; Meech, S. R. Internal conversion in the chromophore of the green fluorescent protein: Temperature dependence and isoviscosity analysis. *J. Phys. Chem. A* **2003**, *107*, 2616–2623.

(301) Liu, R.; Asato, A. E. The primary process of vision and the structure of bathorhodopsin: a mechanism for photoisomerization of polyenes. *Proc. Natl. Acad. Sci. U. S. A.* **1985**, *82*, 259–263.

(302) Forbes, M. W.; Jockusch, R. A. Deactivation pathways of an isolated green fluorescent protein model chromophore studied by electronic action spectroscopy. *J. Am. Chem. Soc.* **2009**, *131*, 17038–17039.

(303) Cui, G.; Lan, Z.; Thiel, W. Intramolecular hydrogen bonding plays a crucial role in the photophysics and photochemistry of the GFP chromophore. *J. Am. Chem. Soc.* **2012**, *134*, 1662–1672.

(304) Lama, B.; Sarma, M. Unraveling the mechanistic pathway for the dual fluorescence in green fluorescent protein (GFP) chromophore analogue: a detailed theoretical investigation. *J. Phys. Chem. B* **2022**, *126*, 9930–9944.

(305) Lama, B.; Sarma, M. Ultrafast Hot Exciton Nonadiabatic Excited-State Dynamics in Green Fluorescent Protein Chromophore Analogue. *J. Phys. Chem. B* **2024**, *128*, 6786–6796.

(306) Chen, Y.-H.; Sung, R.; Sung, K. Dramatic changes in the excited-state behaviour of the green fluorescent protein chromophore by a strong $\pi$-donating group through significantly lowering the excited-state potential energy surface with photoinduced intramolecular charge transfer. *Phys. Chem. Chem. Phys.* **2020**, *22*, 2424–2428.

(307) Werner, H.-J.; Meyer, W. A quadratically convergent MCSCF method for the simultaneous optimization of several states. *J. Chem. Phys.* **1981**, *74*, 5794–5801.

(308) Shiozaki, T. BAGEL: brilliantly advanced general electronic-structure library. , *Wiley Interdiscip. Rev.: Comput. Mol. Sci.* **2018**, *8*, e1331.

(309) Zhu, X.; Thompson, K. C.; Martínez, T. J. Geodesic interpolation for reaction pathways. *J. Chem. Phys.* **2019**, *150*.

(310) Crespo-Otero, R.; Barbatti, M. Spectrum simulation and decomposition with nuclear ensemble: formal derivation and application to benzene, furan and 2-phenylfuran. *Theor. Chem. Acc.* **2012**, *131*, 1237.

(311) Barbatti, M.; Ruckenbauer, M.; Plasser, F.; Pittner, J.; Granucci, G.; Persico, M.; Lischka, H. Newton-X: a surface-hopping program for nonadiabatic molecular dynamics. *Wiley Interdiscip. Rev.: Comput. Mol. Sci.* **2014**, *4*, 26–33.

(312) Levine, B. G.; Martínez, T. J. Ab initio multiple spawning dynamics of excited butadiene: Role of charge transfer. *J. Phys. Chem. A* **2009**, *113*, 12815–12824.

(313) Papineau, T. V.; Jacquemin, D.; Vacher, M. Which electronic structure method to choose in trajectory surface hopping dynamics simulations? Azomethane as a case study. *J. Phys. Chem. Lett.* **2024**, *15*, 636–643.

(314) Huang, G.-J.; Cheng, C.-W.; Hsu, H.-Y.; Prabhakar, C.; Lee, Y.-P.; Diau, E. W.-G.; Yang, J.-S. Effects of hydrogen bonding on internal conversion of GFP-like chromophores. I. The para-amino systems. *J. Phys. Chem. B* **2013**, *117*, 2695–2704.

(315) Long, R.; Prezhdo, O. V. Asymmetry in the electron and hole transfer at a polymer–carbon nanotube heterojunction. *Nano Lett.* **2014**, *14*, 3335–3341.

(316) Bang, J.; Meng, S.; Sun, Y.-Y.; West, D.; Wang, Z.; Gao, F.; Zhang, S. Regulating energy transfer of excited carriers and the case for excitation-induced hydrogen dissociation on hydrogenated graphene. *Proc. Natl. Acad. Sci. USA* **2013**, *110*, 908–911.

(317) Oldani, N.; Tretiak, S.; Bazan, G.; Fernandez-Alberti, S. Modeling of internal conversion in photoexcited conjugated molecular donors used in organic photovoltaics. *Energy Environ. Sci.* **2014**, *7*, 1175–1184.

(318) Collini, E. Spectroscopic signatures of quantum-coherent energy transfer. *Chem. Soc. Rev.* **2013**, *42*, 4932–4947.

(319) Nelson, T.; Fernandez-Alberti, S.; Roitberg, A. E.; Tretiak, S. Nonadiabatic excited-state molecular dynamics: Modeling photophysics in organic conjugated materials. *Acc. Chem. Res.* **2014**, *47*, 1155–1164.

(320) Brédas, J.-L.; Beljonne, D.; Coropceanu, V.; Cornil, J. Charge-transfer and energy-transfer processes in $\pi$-conjugated oligomers and polymers: a molecular picture. *Chem. Rev.* **2004**, *104*, 4971–5004.

(321) Beaujuge, P. M.; Fréchet, J. M. Molecular design and ordering effects in $\pi$-functional materials for transistor and solar cell applications. *J. Am. Chem. Soc.* **2011**, *133*, 20009–20029.

(322) Brédas, J.-L.; Norton, J. E.; Cornil, J.; Coropceanu, V. Molecular understanding of organic solar cells: the challenges. *Acc. Chem. Res.* **2009**, *42*, 1691–1699.

(323) Fazzi, D.; Barbatti, M.; Thiel, W. Modeling ultrafast exciton deactivation in oligothiophenes via nonadiabatic dynamics. *Phys. Chem. Chem. Phys.* **2015**, *17*, 7787–7799.

(324) Chapman, C. T.; Liang, W.; Li, X. Ultrafast coherent electron–hole separation dynamics in a fullerene derivative. *J. Phys. Chem. Lett.* **2011**, *2*, 1189–1192.

(325) Bakulin, A. A.; Rao, A.; Pavelyev, V. G.; van Loosdrecht, P. H.; Pshenichnikov, M. S.; Niedzialek, D.; Cornil, J.; Beljonne, D.; Friend, R. H. The role of driving energy and delocalized states for charge separation in organic semiconductors. *Science* **2012**, *335*, 1340–1344.

(326) Tamura, H.; Burghardt, I. Ultrafast charge separation in organic photovoltaics enhanced by charge delocalization and vibronically hot exciton dissociation. *J. Am. Chem. Soc.* **2013**, *135*, 16364–16367.

(327) Akimov, A. V.; Prezhdo, O. V. Nonadiabatic dynamics of charge transfer and singlet fission at the pentacene/C60 interface. *J. Am. Chem. Soc.* **2014**, *136*, 1599–1608.

(328) Jakowetz, A. C.; Böhm, M. L.; Zhang, J.; Sadhanala, A.; Huettner, S.; Bakulin, A. A.; Rao, A.; Friend, R. H. What controls the rate of ultrafast charge transfer and charge separation efficiency in organic photovoltaic blends. *J. Am. Chem. Soc.* **2016**, *138*, 11672–11679.

(329) Fazzi, D.; Barbatti, M.; Thiel, W. Unveiling the role of hot charge-transfer states in molecular aggregates via nonadiabatic dynamics. *J. Am. Chem. Soc.* **2016**, *138*, 4502–4511.

(330) Collini, E.; Scholes, G. D. Coherent intrachain energy migration in a conjugated polymer at room temperature. *Science* **2009**, *323*, 369–373.

(331) Akimov, A. V.; Neukirch, A. J.; Prezhdo, O. V. Theoretical insights into photoinduced charge transfer and catalysis at oxide interfaces. *Chem. Rev.* **2013**, *113*, 4496–4565.

(332) Clarke, T. M.; Durrant, J. R. Charge photogeneration in organic solar cells. *Chem. Rev.* **2010**, *110*, 6736–6767.

(333) Clark, J.; Nelson, T.; Tretiak, S.; Cirmi, G.; Lanzani, G. Femtosecond torsional relaxation. *Nat. Phys.* **2012**, *8*, 225–231.

(334) Noriega, R.; Rivnay, J.; Vandewal, K.; Koch, F. P.; Stingelin, N.; Smith, P.; Toney, M. F.; Salleo, A. A general relationship between disorder, aggregation and charge transport in conjugated polymers. *Nat. Mater.* **2013**, *12*, 1038–1044.

(335) Song, Y.; Clafton, S. N.; Pensack, R. D.; Kee, T. W.; Scholes, G. D. Vibrational coherence probes the mechanism of ultrafast electron transfer in polymer–fullerene blends. *Nat. Commun.* **2014**, *5*, 4933 (1–7).

(336) Provencher, F.; Bérubé, N.; Parker, A. W.; Greetham, G. M.; Towrie, M.; Hellmann, C.; Côté, M.; Stingelin, N.; Silva, C.; Hayes, S. C. Direct observation of ultrafast long-range charge separation at polymer–fullerene heterojunctions. *Nat. Commun.* **2014**, *5*, 4288 (1–11).

(337) Vázquez, H.; Troisi, A. Calculation of rates of exciton dissociation into hot charge-transfer states in model organic photovoltaic interfaces. *Phys. Rev. B* **2013**, *88*, 205304 (1–5).

(338) Bera, S.; Gheeraert, N.; Fratini, S.; Ciuchi, S.; Florens, S. Impact of quantized vibrations on the efficiency of interfacial charge separation in photovoltaic devices. *Phys. Rev. B* **2015**, *91*, 041107 (1–5).

(339) Gélinas, S.; Rao, A.; Kumar, A.; Smith, S. L.; Chin, A. W.; Clark, J.; Van Der Poll, T. S.; Bazan, G. C.; Friend, R. H. Ultrafast long-range charge separation in organic semiconductor photovoltaic diodes. *Science* **2014**, *343*, 512–516.

(340) Najafov, H.; Lyu, B.; Biaggio, I.; Podzorov, V. Investigating the origin of the high photoconductivity of rubrene single crystals. *Phys. Rev. B* **2008**, *77*, 125202 (1–12).

(341) Tamura, H.; Bittner, E. R.; Burghardt, I. Exciton dissociation at donor-acceptor polymer heterojunctions: Quantum nonadiabatic dynamics and effective-mode analysis. *J. Chem. Phys.* **2007**, *126*, 021103 (1–5).

(342) Nelson, T.; Fernandez-Alberti, S.; Chernyak, V.; Roitberg, A. E. Nonadiabatic excited-state molecular dynamics: Numerical tests of convergence and parameters. *J. Chem. Phys.* **2012**, *136*, 054108 (1–12).

(343) Sterpone, F.; Rossky, P. J. Molecular modeling and simulation of conjugated polymer oligomers: Ground and excited state chain dynamics of PPV in the gas phase. *J. Phys. Chem. B* **2008**, *112*, 4983–4993.

(344) Jailaubekov, A. E.; Willard, A. P.; Tritsch, J. R.; Chan, W.-L.; Sai, N.; Gearba, R.; Kaake, L. G.; Williams, K. J.; Leung, K.; Rossky, P. J., et al. Hot charge-transfer excitons set the time limit for charge separation at donor/acceptor interfaces in organic photovoltaics. *Nat. Mater.* **2013**, *12*, 66–73.

(345) Cardozo, T. M.; Galliez, A. P.; Borges, I.; Plasser, F.; Aquino, A. J.; Barbatti, M.; Lischka, H. Dynamics of benzene excimer formation from the parallel-displaced dimer. *Phys. Chem. Chem. Phys.* **2019**, *21*, 13916–13924.

(346) Dimitriev, O. P. Dynamics of excitons in conjugated molecules and organic semiconductor systems. *Chem. Rev.* **2022**, *122*, 8487–8593.

(347) Brixner, T.; Hildner, R.; Köhler, J.; Lambert, C.; Würthner, F. Exciton transport in molecular aggregates–from natural antennas to synthetic chromophore systems. *Adv. Energy Mater.* **2017**, *7*, 1700236 (1–33).

(348) Pershin, A.; Hall, D.; Lemaur, V.; Sancho-Garcia, J.-C.; Muccioli, L.; Zysman-Colman, E.; Beljonne, D.; Olivier, Y. Highly emissive excitons with reduced exchange energy in thermally activated delayed fluorescent molecules. *Nat. Commun.* **2019**, *10*, 597 (1–5).

(349) Feilmeier, B. J.; Iseminger, G.; Schroeder, D.; Webber, H.; Phillips, G. J. Green fluorescent protein functions as a reporter for protein localization in Escherichia coli. *J. Bacteriol.* **2000**, *182*, 4068–4076.

(350) Giepmans, B. N.; Adams, S. R.; Ellisman, M. H.; Tsien, R. Y. The fluorescent toolbox for assessing protein location and function. *Science* **2006**, *312*, 217–224.

(351) Rodriguez, E. A.; Campbell, R. E.; Lin, J. Y.; Lin, M. Z.; Miyawaki, A.; Palmer, A. E.; Shu, X.; Zhang, J.; Tsien, R. Y. The growing and glowing toolbox of fluorescent and photoactive proteins. *Trends Biochem. Sci.* **2017**, *42*, 111–129.

(352) Andresen, M.; Stiel, A. C.; Fölling, J.; Wenzel, D.; Schönle, A.; Egner, A.; Eggeling, C.; Hell, S. W.; Jakobs, S. Photoswitchable fluorescent proteins enable monochromatic multilabel imaging and dual color fluorescence nanoscopy. *Nat. Biotechnol.* **2008**, *26*, 1035–1040.

(353) Grotjohann, T.; Testa, I.; Leutenegger, M.; Bock, H.; Urban, N. T.; Lavoie-Cardinal, F.; Willig, K. I.; Eggeling, C.; Jakobs, S.; Hell, S. W. Diffraction-unlimited all-optical imaging and writing with a photochromic GFP. *Nature* **2011**, *478*, 204–208.

(354) Pakhomov, A. A.; Martynov, V. I. GFP family: structural insights into spectral tuning. *Chem. Biol.* **2008**, *15*, 755–764.

(355) Lin, C.-Y.; Romei, M. G.; Oltrogge, L. M.; Mathews, I. I.; Boxer, S. G. Unified model for photophysical and electro-optical properties of green fluorescent proteins. *J. Am. Chem. Soc.* **2019**, *141*, 15250–15265.

(356) Tsai, M.-S.; Ou, C.-L.; Tsai, C.-J.; Huang, Y.-C.; Cheng, Y.-C.; Sun, S.-S.; Yang, J.-S. Fluorescence enhancement of unconstrained GFP chromophore analogues based on the push–pull substituent effect. *J. Org. Chem.* **2017**, *82*, 8031–8039.

(357) Tavernelli, I. Nonadiabatic molecular dynamics simulations: Synergies between theory and experiments. *Acc. Chem. Res.* **2015**, *48*, 792–800.

(358) Tapavicza, E.; Bellchambers, G. D.; Vincent, J. C.; Furche, F. Ab initio non-adiabatic molecular dynamics. *Phys. Chem. Chem. Phys.* **2013**, *15*, 18336–18348.

(359) Chai, J.-D.; Head-Gordon, M. Long-range corrected hybrid density functionals with damped atom–atom dispersion corrections. *Phys. Chem. Chem. Phys.* **2008**, *10*, 6615–6620.

(360) Sen, K.; Crespo-Otero, R.; Weingart, O.; Thiel, W.; Barbatti, M. Interfacial states in donor–acceptor organic heterojunctions: computational insights into thiophene-oligomer/fullerene junctions. *J. Chem. Theory Comput.* **2013**, *9*, 533–542.

(361) Trofimov, A. B.; Schirmer, J. An efficient polarization propagator approach to valence electron excitation spectra. *J. Phys. B: At. Mol. Opt. Phys.* **1995**, *28*, 2299.

(362) Dreuw, A.; Wormit, M. The algebraic diagrammatic construction scheme for the polarization propagator for the calculation of excited states. *WIREs: Comp. Mol. Sci.* **2015**, *5*, 82–95.

(363) Werner, H.-J.; Knowles, P. J.; Knizia, G.; Manby, F. R.; Schütz, M. Molpro: a general-purpose quantum chemistry program package. *WIREs: Comp. Mol. Sci.* **2012**, *2*, 242–253.

(364) Werner, H.-J.; Knowles, P. J.; Manby, F. R.; Black, J. A.; Doll, K.; Heßelmann, A.; Kats, D.; Köhn, A.; Korona, T.; Kreplin, D. A., et al. The Molpro quantum chemistry package. *J. Chem. Phys.* **2020**, *152*, 144107 (1–24).

(365) Plasser, F. TheoDORE: A toolbox for a detailed and automated analysis of electronic excited state computations. *J. Chem. Phys.* **2020**, *152*, 084108 (1–14).

(366) Fernandez-Alberti, S.; Roitberg, A. E.; Nelson, T.; Tretiak, S. Identification of unavoided crossings in nonadiabatic photoexcited dynamics involving multiple electronic states in polyatomic conjugated molecules. *J. Chem. Phys.* **2012**, *137*, 014512 (1–10).

(367) Wang, L.; Prezhdo, O. V. A simple solution to the trivial crossing problem in surface hopping. *J. Phys. Chem. Lett.* **2014**, *5*, 713–719.

(368) Granucci, G.; Persico, M.; Toniolo, A. Direct semiclassical simulation of photochemical processes with semiempirical wave functions. *J. Chem. Phys.* **2001**, *114*, 10608–10615.

(369) Plasser, F.; Granucci, G.; Pittner, J.; Barbatti, M.; Persico, M.; Lischka, H. Surface hopping dynamics using a locally diabatic formalism: Charge transfer in the ethylene dimer cation and excited state dynamics in the 2-pyridone dimer. *J. Chem. Phys.* **2012**, *137*, 22A514 (1–13).

(370) Petersson, a.; Bennett, A.; Tensfeldt, T. G.; Al-Laham, M. A.; Shirley, W. A.; Mantzaris, J. A complete basis set model chemistry. I. The total energies of closed-shell atoms and hydrides of the first-row elements. *J. Chem. Phys.* **1988**, *89*, 2193–2218.

(371) Lee, J.-S.; Baldridge, A.; Feng, S.; SiQiang, Y.; Kim, Y. K.; Tolbert, L. M.; Chang, Y.-T. Fluorescence response profiling for small molecule sensors utilizing the green fluorescent protein chromophore and its derivatives. *ACS Comb. Sci.* **2011**, *13*, 32–38.

(372) Dunning Jr, T. H. Gaussian basis sets for use in correlated molecular calculations. I. The atoms boron through neon and hydrogen. *J. Chem. Phys.* **1989**, *90*, 1007–1023.

(373) Schäfer, A.; Horn, H.; Ahlrichs, R. Fully optimized contracted Gaussian basis sets for atoms Li to Kr. *J. Chem. Phys.* **1992**, *97*, 2571–2577.

(374) Schnell, M.; Erlekam, U.; Bunker, P.; von Helden, G.; Grabow, J.-U.; Meijer, G.; Van Der Avoird, A. Structure of the benzene dimer—governed by dynamics. *Angew. Chem. Int. Ed.* **2013**, *52*, 5180–5183.

(375) Barbatti, M.; Aquino, A. J.; Szymczak, J. J.; Nachtigallová, D.; Hobza, P.; Lischka, H. Relaxation mechanisms of UV-photoexcited DNA and RNA nucleobases. *Proc. Natl. Acad. Sci. USA* **2010**, *107*, 21453–21458.

(376) Liu, X.-Y.; Li, Z.-W.; Fang, W.-H.; Cui, G. Nonadiabatic exciton and charge separation dynamics at interfaces of zinc phthalocyanine and fullerene: orientation does matter. *J. Phys. Chem. A* **2020**, *124*, 7388–7398.

(377) Prlj, A.; Curchod, B. F.; Corminboeuf, C. Excited state dynamics of thiophene and bithiophene: new insights into theoretically challenging systems. *Phys. Chem. Chem. Phys* **2015**, *17*, 14719–14730.

(378) Plasser, F.; Lischka, H. Analysis of excitonic and charge transfer interactions from quantum chemical calculations. *J. Chem. Theory Comput.* **2012**, *8*, 2777–2789.

(379) Plasser, F. Entanglement entropy of electronic excitations. *J. Chem. Phys.* **2016**, *144*, 194107 (1–9).

(380) Sobolewski, A. L.; Domcke, W. Ab initio potential-energy functions for excited state intramolecular proton transfer: a comparative study of o-hydroxybenzaldehyde, salicylic acid and 7-hydroxy-1-indanone. *Phys. Chem. Chem. Phys.* **1999**, *1*, 3065–3072.

(381) Jacquemin, D.; Zuniga, J.; Requena, A.; Céron-Carrasco, J. P. Assessing the importance of proton transfer reactions in DNA. *Acc. Chem. Res.* **2014**, *47*, 2467–2474.

(382) Lee, J.; Kim, C. H.; Joo, T. Active role of proton in excited state intramolecular proton transfer reaction. *J. Phys. Chem. A* **2013**, *117*, 1400–1405.

(383) Mawa, I.; Panda, A. N. Insights into the Excited-State Processes in 1-Hydroxy-2-acetonaphthone at ADC (2) and CASSCF Levels. *J. Phys. Chem. A* **2021**, *125*, 3015–3024.

(384) Zhao, G.-J.; Han, K.-L. Role of intramolecular and intermolecular hydrogen bonding in both singlet and triplet excited states of aminofluorenones on internal conversion, intersystem crossing, and twisted intramolecular charge transfer. *J. Phys. Chem. A* **2009**, *113*, 14329–14335.

(385) Padalkar, V. S.; Seki, S. Excited-state intramolecular proton-transfer (ESIPT)-inspired solid state emitters. *Chem. Soc. Rev.* **2016**, *45*, 169–202.

(386) Zhou, P.; Han, K. Unraveling the detailed mechanism of excited-state proton transfer. *Acc. Chem. Res.* **2018**, *51*, 1681–1690.

(387) Zhao, G.-J.; Han, K.-L. Ultrafast hydrogen bond strengthening of the photoexcited fluorenone in alcohols for facilitating the fluorescence quenching. *J. Phys. Chem. A* **2007**, *111*, 9218–9223.

(388) Kwon, J. E.; Park, S. Y. Advanced organic optoelectronic materials: Harnessing excited-state intramolecular proton transfer (ESIPT) process. *Adv. Mater.* **2011**, *23*, 3615–3642.

(389) Arzhantsev, S. Y.; Takeuchi, S.; Tahara, T. Ultrafast excited-state proton transfer dynamics of 1, 8-dihydroxyanthraquinone (chrysazin) studied by femtosecond time-resolved fluorescence spectroscopy. *Chem. Phys. Lett.* **2000**, *330*, 83–90.

(390) Nag, P.; Anand, N.; Vennapusa, S. R. Ultrafast nonadiabatic excited-state intramolecular proton transfer in 3-hydroxychromone: A surface hopping approach. *J. Chem. Phys.* **2021**, *155*.

(391) Nag, P.; Bera, A.; Vennapusa, S. R. Rapid intersystem crossing induced by ultrafast excited-state intramolecular proton transfer in 3-Mercaptopyran-4-one. *J. Phys. Chem. A* **2022**, *126*, 6407–6415.

(392) Cheng, J.; Liu, D.; Bao, L.; Xu, K.; Yang, Y.; Han, K. A Single 2-(2′-Hydroxyphenyl) benzothiazole Derivative Can Achieve Pure White-Light Emission. *Chem. Asian J.* **2014**, *9*, 3215–3220.

(393) Zhang, Z.; Chen, Y.-A.; Hung, W.-Y.; Tang, W.-F.; Hsu, Y.-H.; Chen, C.-L.; Meng, F.-Y.; Chou, P.-T. Control of the reversibility of excited-state intramolecular proton transfer (ESIPT) reaction: host-polarity tuning white organic light emitting diode on a new thiazolo [5, 4-d] thiazole ESIPT system. *Chem. Mater.* **2016**, *28*, 8815–8824.

(394) Chou, P.; McMorrow, D.; Aartsma, T.; Kasha, M. The proton-transfer laser. Gain spectrum and amplification of spontaneous emission of 3-hydroxyflavone. *J. Phys. Chem.* **1984**, *88*, 4596–4599.

(395) Yan, C.-C.; Wang, X.-D.; Liao, L.-S. Organic lasers harnessing excited state intramolecular proton transfer process. *ACS Photonics* **2020**, *7*, 1355–1366.

(396) Catalan, J.; Fabero, F.; Soledad Guijarro, M.; Claramunt, R. M.; Santa Maria, M. D.; Foces-Foces, M. d. l. C.; Hernandez Cano, F.; Elguero, J.; Sastre, R. Photoinduced intramolecular proton transfer as the mechanism of ultraviolet stabilizers: a reappraisal. *J. Am. Chem. Soc.* **1990**, *112*, 747–759.

(397) Fluegge, A. P.; Waiblinger, F.; Stein, M.; Keck, J.; Kramer, H. E.; Fischer, P.; Wood, M. G.; DeBellis, A. D.; Ravichandran, R.; Leppard, D. Probing the intramolecular hydrogen bond of 2-(2-hydroxyphenyl) benzotriazoles in polar environment: a photophysical study of UV absorber efficiency. *J. Phys. Chem. A* **2007**, *111*, 9733–9744.

(398) Serdiuk, I. E. Design and emissive features of ionic white-light fluorophore. *J. Phys. Chem. C* **2018**, *122*, 18615–18620.

(399) Moraes, E. S.; Teixeira Alves Duarte, L. G.; Germino, J. C.; Atvars, T. D. Z. Near attack conformation as strategy for ESIPT modulation for white-light generation. *J. Phys. Chem. C* **2020**, *124*, 22406–22415.

(400) Long, Y.; Mamada, M.; Li, C.; Dos Santos, P. L.; Colella, M.; Danos, A.; Adachi, C.; Monkman, A. Excited state dynamics of thermally activated delayed fluorescence from an excited state intramolecular proton transfer system. *J. Phys. Chem. Lett.* **2020**, *11*, 3305–3312.

(401) Jiang, G.; Li, F.; Fan, J.; Song, Y.; Wang, C.-K.; Lin, L. Theoretical perspective for luminescent mechanism of thermally activated delayed fluorescence emitter with excited-state intramolecular proton transfer. *J. Mater. Chem. C* **2020**, *8*, 98–108.

(402) Lim, S.-J.; Seo, J.; Park, S. Y. Photochromic switching of excited-state intramolecular proton-transfer (ESIPT) fluorescence: a unique route to high-contrast memory switching and nondestructive readout. *J. Am. Chem. Soc.* **2006**, *128*, 14542–14547.

(403) Park, S.; Seo, J.; Kim, S. H.; Park, S. Y. Tetraphenylimidazole-based excited-state intramolecular proton-transfer molecules for highly efficient blue electroluminescence. *Adv. Funct. Mater.* **2008**, *18*, 726–731.

(404) Wu, Y.; Peng, X.; Fan, J.; Gao, S.; Tian, M.; Zhao, J.; Sun, S. Fluorescence sensing of anions based on inhibition of excited-state intramolecular proton transfer. *J. Org. Chem.* **2007**, *72*, 62–70.

(405) Sedgwick, A. C.; Wu, L.; Han, H.-H.; Bull, S. D.; He, X.-P.; James, T. D.; Sessler, J. L.; Tang, B. Z.; Tian, H.; Yoon, J. Excited-state intramolecular proton-transfer (ESIPT) based fluorescence sensors and imaging agents. *Chem. Soc. Rev.* **2018**, *47*, 8842–8880.

(406) Zhao, J.; Ji, S.; Chen, Y.; Guo, H.; Yang, P. Excited state intramolecular proton transfer (ESIPT): from principal photophysics to the development of new chromophores and applications in fluorescent molecular probes and luminescent materials. *Phys. Chem. Chem. Phys.* **2012**, *14*, 8803–8817.

(407) Tseng, H.-W.; Liu, J.-Q.; Chen, Y.-A.; Chao, C.-M.; Liu, K.-M.; Chen, C.-L.; Lin, T.-C.; Hung, C.-H.; Chou, Y.-L.; Lin, T.-C., et al. Harnessing excited-state intramolecular proton-transfer reaction via a series of amino-type hydrogen-bonding molecules. *J. Phys. Chem. Lett.* **2015**, *6*, 1477–1486.

(408) Hsieh, C.-C.; Jiang, C.-M.; Chou, P.-T. Recent experimental advances on excited-state intramolecular proton coupled electron transfer reaction. *Acc. Chem. Res.* **2010**, *43*, 1364–1374.

(409) Demchenko, A. P.; Tang, K.-C.; Chou, P.-T. Excited-state proton coupled charge transfer modulated by molecular structure and media polarization. *Chem. Soc. Rev.* **2013**, *42*, 1379–1408.

(410) Azarias, C.; Budzák, Š.; Laurent, A. D.; Ulrich, G.; Jacquemin, D. Tuning ESIPT fluorophores into dual emitters. *Chem. Sci.* **2016**, *7*, 3763–3774.

(411) Liu, W.; Wang, Y.; Tang, L.; Oscar, B. G.; Zhu, L.; Fang, C. Panoramic portrait of primary molecular events preceding excited state proton transfer in water. *Chem. Sci.* **2016**, *7*, 5484–5494.

(412) Ameer-Beg, S.; Ormson, S. M.; Brown, R. G.; Matousek, P.; Towrie, M.; Nibbering, E. T.; Foggi, P.; Neuwahl, F. V. Ultrafast measurements of excited state intramolecular proton transfer (ESIPT) in room temperature solutions of 3-hydroxyflavone and derivatives. *J. Phys. Chem. A* **2001**, *105*, 3709–3718.

(413) Winkler, V. S.; Fournier, J. A. Characterizing excited-state intramolecular proton transfer in 3-hydroxyflavone with ultrafast transient infrared spectroscopy. *Chem. Commun.* **2024**, *60*, 12417–12420.

(414) Rodríguez-Córdoba, W.; Zugazagoitia, J. S.; Collado-Fregoso, E.; Peon, J. Excited state intramolecular proton transfer in schiff bases. Decay of the locally excited enol state observed by femtosecond resolved fluorescence. *J. Phys. Chem. A* **2007**, *111*, 6241–6247.

(415) Baranov, M. S.; Lukyanov, K. A.; Borissova, A. O.; Shamir, J.; Kosenkov, D.; Slipchenko, L. V.; Tolbert, L. M.; Yampolsky, I. V.; Solntsev, K. M. Conformationally locked chromophores as models of excited-state proton transfer in fluorescent proteins. *J. Am. Chem. Soc.* **2012**, *134*, 6025–6032.

(416) Liu, X.-Y.; Chang, X.-P.; Xia, S.-H.; Cui, G.; Thiel, W. Excited-state proton-transfer-induced trapping enhances the fluorescence emission of a locked GFP chromophore. *J. Chem. Theory Comput.* **2016**, *12*, 753–764.

(417) Liu, X.-Y.; Wang, S.-R.; Fang, W.-H.; Cui, G. Nuclear Quantum Effects on Nonadiabatic Dynamics of a Green Fluorescent Protein Chromophore Analogue: Ring-Polymer Surface-Hopping Simulation. *J. Chem. Theory Comput.* **2024**, *20*, 3426–3439.

(418) Chen, K.-Y.; Cheng, Y.-M.; Lai, C.-H.; Hsu, C.-C.; Ho, M.-L.; Lee, G.-H.; Chou, P.-T. Ortho green fluorescence protein synthetic chromophore; excited-state intramolecular proton transfer via a seven-membered-ring hydrogen-bonding system. *J. Am. Chem. Soc.* **2007**, *129*, 4534–4535.

(419) Boulanger, S. A.; Chen, C.; Myasnyanko, I. N.; Baranov, M. S.; Fang, C. Fluorescence modulation of ortho-green fluorescent protein chromophores following ultrafast proton transfer in solution. *J. Phys. Chem. B* **2022**, *126*, 5081–5093.

(420) Ge, S.; Deng, H.; Su, Y.; Zhu, X. Emission enhancement of GFP chromophore in aggregated state via combination of self-restricted effect and supramolecular host–guest complexation. *RSC Adv.* **2017**, *7*, 17980–17987.

(421) Povarova, N. V.; Zaitseva, S. O.; Baleeva, N. S.; Smirnov, A. Y.; Myasnyanko, I. N.; Zagudaylova, M. B.; Bozhanova, N. G.; Gorbachev, D. A.; Malyshevskaya, K. K.; Gavrikov, A. S., et al. Red-Shifted Substrates for FAST Fluorogen-Activating Protein Based on the GFP-Like Chromophores. *Chem. Eur. J.* **2019**, *25*, 9592–9596.

(422) Muselli, M.; Baudequin, C.; Perrio, C.; Hoarau, C.; Bischoff, L. Pd (0)-Catalyzed Direct C- H Functionalization of 2-H-4-Benzylidene Imidazolones: Friendly and Large-Scale Access to GFP and Kaede Protein Fluorophores. *Chem. Eur. J.* **2016**, *22*, 5520–5524.

(423) Paul, D.; Sahoo, P.; Sengupta, A.; Tripathy, U.; Chatterjee, S. Revealing the Role of Electronic Effect to Modulate the Photophysics and Z-Scan Responses of o-Locked GFP Chromophores. *J. Phys. Chem. B* **2024**, *129*, 692–711.

(424) Forsberg, N.; Malmqvist, P.-Å. Multiconfiguration perturbation theory with imaginary level shift. *Chem. Phys. Lett.* **1997**, *274*, 196–204.

(425) Park, J. W. Single-state single-reference and multistate multireference zeroth-order Hamiltonians in MS-CASPT2 and conical intersections. *J. Chem. Theory Comput.* **2019**, *15*, 3960–3973.

(426) Balasubramani, S. G.; Chen, G. P.; Coriani, S.; Diedenhofen, M.; Frank, M. S.; Franzke, Y. J.; Furche, F.; Grotjahn, R.; Harding, M. E.; Hättig, C., et al. TURBOMOLE: Modular program suite for ab initio quantum-chemical and condensed-matter simulations. *J. Chem. Phys.* **2020**, *152*.

(427) Franzke, Y. J.; Holzer, C.; Andersen, J. H.; Begušić, T.; Bruder, F.; Coriani, S.; Della Sala, F.; Fabiano, E.; Fedotov, D. A.; Fürst, S., et al. TURBOMOLE: Today and tomorrow. *J. Chem. Theory Comput.* **2023**, *19*, 6859–6890.

# Appendix A

**Table A1:** Vertical excitation energy (nm), emission energy (nm) and the corresponding oscillator strength ($f$) for transitions of the GFP chromophore ($p$-HBDI) in its neutral, anionic, and cationic forms computed at the TDDFT/CAM-B3LYP/TZVP level of theoretical accuracy. For the solvent phase, we implemented the IEFPCM solvation model.

| **Solvent** | **Forms** | $\lambda_{max}{}^{abs}$ (nm) | | | $\lambda_{max}{}^{flu}$ (nm) | | |
|---|---|---|---|---|---|---|---|
| | | **Calc.** | **Expt.** [145, 261, 262] | $f$ | **Calc.** | **Expt.** [145, 261, 262] | $f$ |
| **$CH_3CN$** ($\epsilon$=35.7) | Neutral | 366 | 367 | 0.8 | 415 | –[a] | 1.1 |
| | Anion | 440 | 441 | 0.5 | 413 | –[a] | 0.7 |
| | Cation | 352 | 393 | 0.5 | 335 | –[a] | 0.6 |
| **$H_2O$** ($\epsilon$=78.4) | Neutral | 366 | 367 | 0.8 | 412 | –[a] | 1.1 |
| | Anion | 441 | 424 | 0.5 | 414 | –[a] | 0.7 |
| | Cation | 351 | 393 | 0.5 | 336 | –[a] | 0.6 |
| **$CH_3OH$** ($\epsilon$=32.6) | Neutral | 365 | 368 | 0.8 | 414 | –[a] | 1.1 |
| | Anion | 440 | 428 | 0.5 | 419 | –[a] | 0.7 |
| | Cation | 352 | 395 | 0.5 | 335 | –[a] | 0.6 |
| **$C_2H_5OH$** ($\epsilon$=24.5) | Neutral | 366 | 372 | 0.8 | 412 | 418 | 0.9 |
| | Anion | 441 | 442 | 0.5 | 456 | 448 | 0.5 |
| | Cation | 352 | 401 | 0.4 | 389 | 442 | 0.5 |
| **Gas** | Neutral | 351 | –[a] | 0.8 | 378 | –[a] | 0.8 |
| | Anion | 413 | –[a] | 0.4 | 376 | –[a] | 0.4 |
| | Cation | 427 | –[a] | 0.3 | 325 | –[a] | 0.2 |

[a] **Experimental data not available**

[f] **Oscillator Strength**

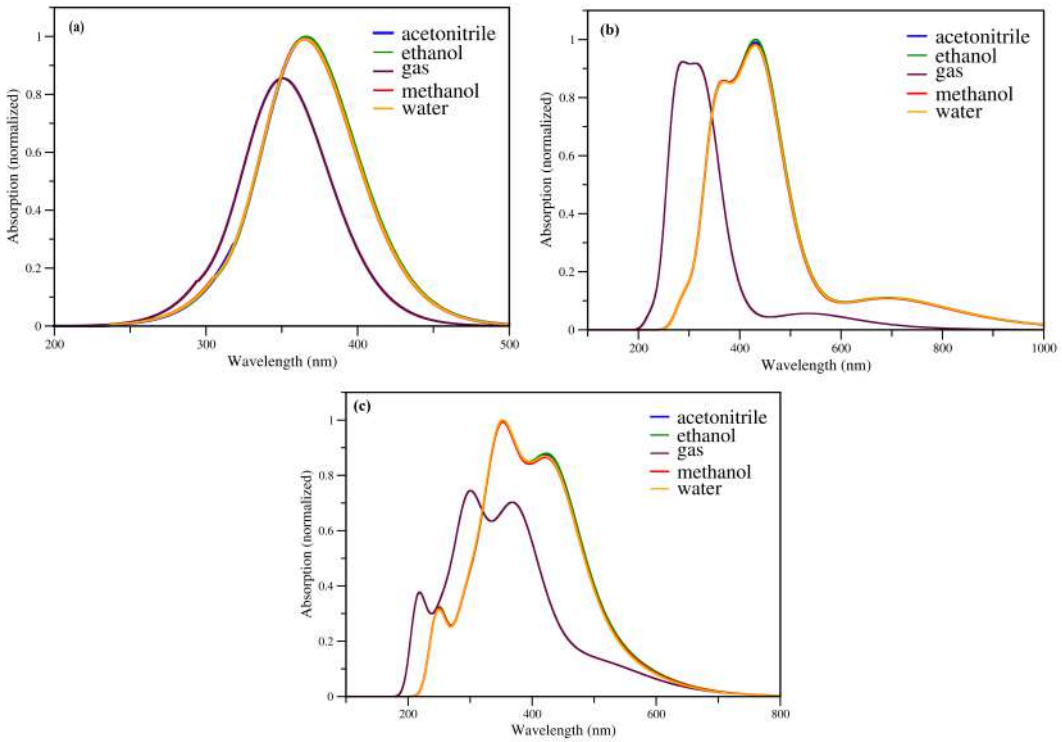


**Figure A1:** Simulated absorption spectra for (a) neutral, (b) anionic, and (c) cationic form of GFP chromophore (*p*-HBDI) in acetonitrile (blue), ethanol (green), gas (purple), methanol (red), and water (orange) computed at the TDDFT/CAM-B3LYP/TZVP/IEFPCM level.

**Table A2:** Calculated conjugated bond distances (Å) of the chromophore for *p*-TsABDI-$(H_2O)_3$ and *p*-TsABDI-$(CH_3OH)_3$ complexes in $S_0$ and $S_1$ states, respectively, involved during the photoexcitation obtained with DFT/B3LYP and TDDFT/CAM-B3LYP/TZVP theoretical accuracies using IEFPCM solvation model.

| **Bond Lengths** (Å) | **States** | ***p*-TsABDI-$(H_2O)_3$** | ***p*-TsABDI-$(CH_3OH)_3$** |
|---|---|---|---|
| C1-C2 | $S_0$ | 1.46 | 1.45 |
| | $S_1$ | 1.41 | 1.41 |
| C2-C3 | $S_0$ | 1.36 | 1.36 |
| | $S_1$ | 1.43 | 1.43 |
| C3-C4 | $S_0$ | 1.43 | 1.42 |
| | $S_1$ | 1.39 | 1.39 |
| C4-C5 | $S_0$ | 1.43 | 1.42 |
| | $S_1$ | 1.39 | 1.39 |
| C5-C6 | $S_0$ | 1.43 | 1.42 |
| | $S_1$ | 1.39 | 1.39 |
| C6-C1 | $S_0$ | 1.43 | 1.42 |
| | $S_1$ | 1.39 | 1.39 |
| C8-N2 | $S_0$ | 1.43 | 1.42 |
| | $S_1$ | 1.39 | 1.39 |
| N2-C10 | $S_0$ | 1.43 | 1.42 |
| | $S_1$ | 1.39 | 1.39 |
| C10-N3 | $S_0$ | 1.43 | 1.42 |
| | $S_1$ | 1.39 | 1.39 |
| N3-C9 | $S_0$ | 1.43 | 1.42 |
| | $S_1$ | 1.39 | 1.39 |
| C9-C8 | $S_0$ | 1.43 | 1.42 |
| | $S_1$ | 1.39 | 1.39 |

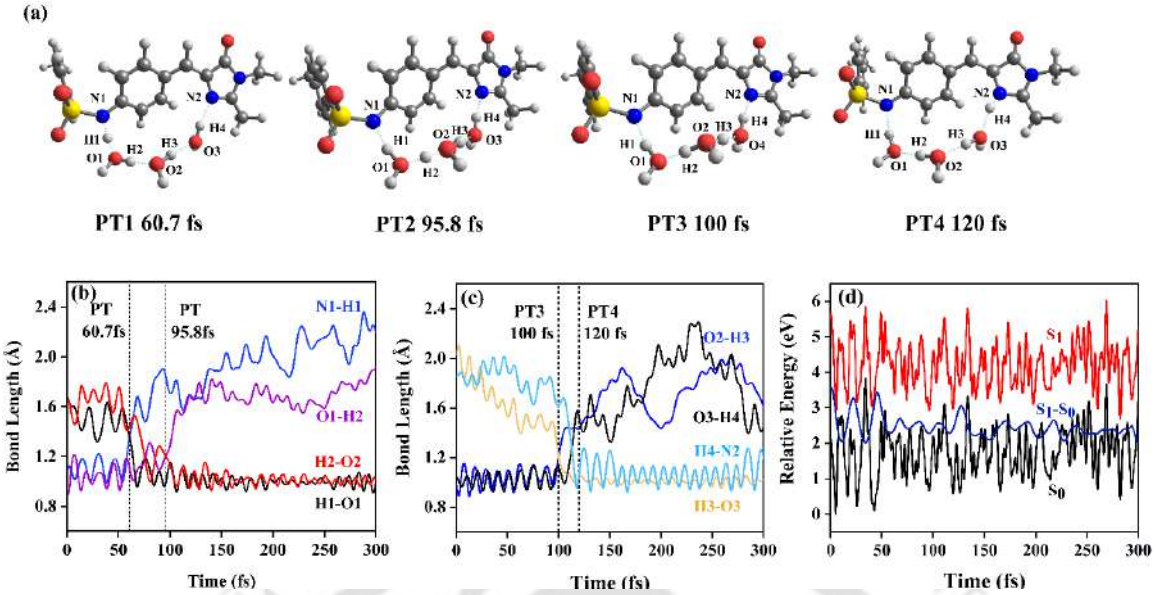


**Figure A2:** For the *p*-TsABDI-$(H_2O)_3$ complex in $S_1$ dynamics (a) snapshots along the ESIPT dynamics simulations at corresponding PT time, (b) time evolutions of average breaking (N1-H1 and O1-H2) and forming (H1-O1 and H2-O2) bond distances, (c) time evolution of average breaking (O2-H3 and O3-H4) and forming (H3-O3 and H4-N2) bond distances, and (d) average relative energies of the $S_0$ and $S_1$, and the energy difference ($S_1$-$S_0$) between them.

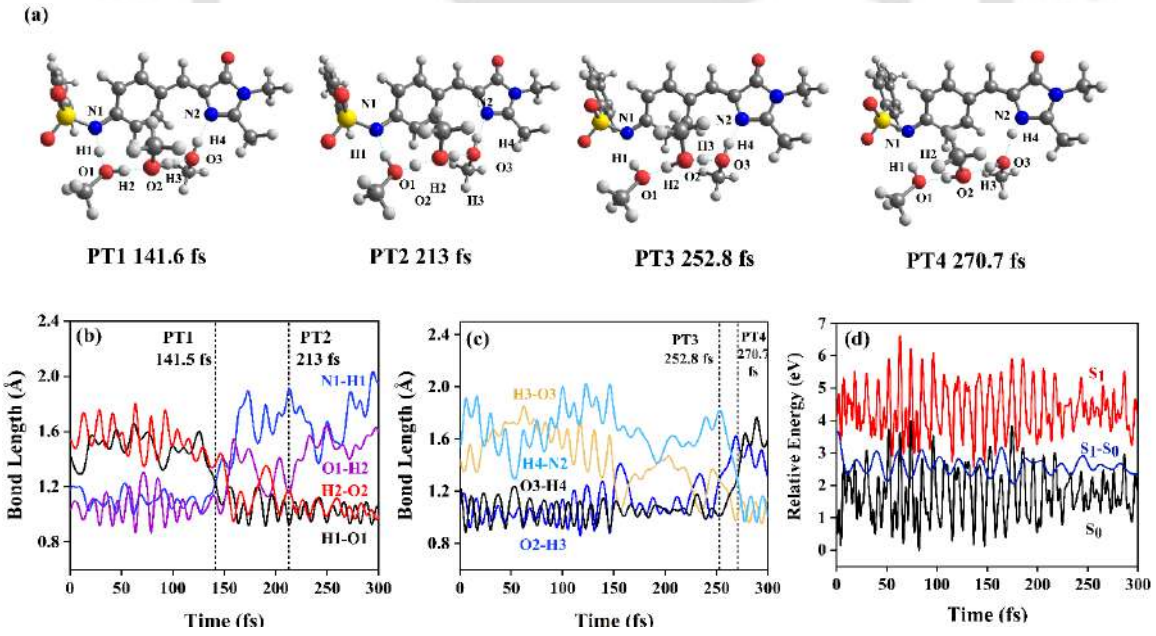


**Figure A3:** For the *p*-TsABDI-$(CH_3OH)_3$ complex in $S_1$ state dynamics (a) snapshots along the ESIPT dynamics simulations at corresponding PT time, (b) time evolutions of average breaking (N1-H1 and O1-H2) and forming (H1-O1 and H2-O2) bond distances, (c) time evolutions of average breaking bonds (O2-H3 and O3-H4) and forming (H3-O3 and H4-N2) bond distances, and (d) average relative energies of the $S_0$ and $S_1$, and the energy difference ($S_1$-$S_0$) between them.

# Appendix B

**Table B1:** Geometrical parameters of optimized cis and trans isomers: CS1, CS2, TS1, and TS2, in the ground ($S_0$) and excited ($S_1$) states at different levels of theory. Atom numbering is in accordance with Figure 4.3. Bond distances are in angstrom (Å) and dihedral angles in degrees (°). The cc-pVDZ basis set is used. $\Phi_I$ = N5-C4-C3-C2 and $\Phi_P$ = C1-C2-C3-C4.

| Structure | Method | C2-C3 | C3-C4 | C1-C2-C3 | C2-C3-C4 | N5-C4-C3 | $\Phi_I$ | $\Phi_P$ |
|---|---|---|---|---|---|---|---|---|
| $S_0$-CS1 | **CASSCF(4,4)** | 1.456 | 1.359 | 124.29 | 130.37 | 129.05 | 0 | 0 |
| | **CASSCF(6,6)** | 1.466 | 1.327 | 124.01 | 131.12 | 129.71 | 0 | 0 |
| | **CASSCF(10,9)** | 1.451 | 1.375 | 124.65 | 130.66 | 129.10 | 0 | 0 |
| | **XMS-CASPT2(4,4)** | 1.455 | 1.375 | 123.44 | 129.26 | 128.16 | 0 | 0 |
| | **XMS-CASPT2(6,6)** | 1.442 | 1.377 | 123.64 | 129.39 | 128.10 | 0 | 0 |
| | **XMS-CASPT2(10,9)** | 1.453 | 1.376 | 123.59 | 129.4 | 128.16 | 0 | 0 |
| $S_0$-CS2 | **CASSCF(4,4)** | 1.456 | 1.359 | 118.99 | 130.38 | 129.05 | 0 | 180 |
| | **CASSCF(6,6)** | 1.466 | 1.327 | 118.26 | 131.12 | 129.71 | 0 | 180 |
| | **CASSCF(10,9)** | 1.450 | 1.375 | 118.16 | 130.66 | 129.08 | 0 | 180 |
| | **XMS-CASPT2(4,4)** | 1.455 | 1.375 | 118.83 | 129.26 | 128.16 | 0 | 180 |
| | **XMS-CASPT2(6,6)** | 1.442 | 1.377 | 118.93 | 129.39 | 128.10 | 0 | 180 |
| | **XMS-CASPT2(10,9)** | 1.452 | 1.375 | 118.78 | 129.33 | 128.10 | 0 | 180 |
| $S_0$-TS1 | **CASSCF(4,4)** | 1.456 | 1.365 | 126.24 | 134.88 | 119.64 | -180 | -0 |
| | **CASSCF(6,6)** | 1.464 | 1.333 | 126.09 | 135.69 | 120.17 | -180 | -0 |
| | **CASSCF(10,9)** | 1.461 | 1.361 | 126.23 | 134.87 | 119.61 | -180 | -0 |
| | **XMS-CASPT2(4,4)** | 1.454 | 1.382 | 125.58 | 133.67 | 118.31 | -180 | -0 |
| | **XMS-CASPT2(6,6)** | 1.435 | 1.387 | 125.63 | 133.79 | 118.3 | -180 | -0 |
| | **XMS-CASPT2(10,9)** | 1.447 | 1.385 | 125.51 | 133.86 | 118.39 | -180 | -0 |
| $S_0$-TS2 | **CASSCF(4,4)** | 1.456 | 1.365 | 117.35 | 134.87 | 119.68 | 180 | -180 |
| | **CASSCF(6,6)** | 1.466 | 1.333 | 116.42 | 135.81 | 120.22 | 180 | -180 |
| | **CASSCF(10,9)** | 1.462 | 1.361 | 116.74 | 134.85 | 119.63 | 180 | -180 |
| | **XMS-CASPT2(4,4)** | 1.454 | 1.381 | 117.05 | 133.67 | 118.42 | 180 | -180 |
| | **XMS-CASPT2(6,6)** | 1.436 | 1.387 | 117.21 | 133.84 | 118.31 | 180 | -180 |
| | **XMS-CASPT2(10,9)** | 1.447 | 1.385 | 117.07 | 133.87 | 118.4 | 180 | -180 |
| $S_1$-CS1 | **CASSCF(4,4)** | 1.357 | 1.491 | 122.93 | 130.09 | 127.31 | 0 | 0 |
| | **CASSCF(6,6)** | 1.428 | 1.347 | 123.89 | 130.31 | 129.79 | 0 | 0 |
| | **CASSCF(10,9)** | 1.412 | 1.386 | 124.19 | 129.83 | 129.37 | 0 | 0 |
| | **XMS-CASPT2(4,4)** | 1.401 | 1.429 | 122.21 | 128.09 | 128.13 | 0 | 0 |
| | **XMS-CASPT2(6,6)** | 1.391 | 1.471 | 122.36 | 128.64 | 126.81 | 0 | 0 |
| | **XMS-CASPT2(10,9)** | 1.412 | 1.405 | 123.87 | 127.82 | 128.78 | 0 | 0 |

| Structure | Method | C2-C3 | C3-C4 | C1-C2-C3 | C2-C3-C4 | N5-C4-C3 | $\Phi_I$ | $\Phi_P$ |
|---|---|---|---|---|---|---|---|---|
| $S_1$-CS2 | **CASSCF(4,4)** | 1.358 | 1.493 | 120.56 | 129.83 | 127.13 | 0 | 180 |
| | **CASSCF(6,6)** | 1.428 | 1.347 | 118.09 | 130.30 | 129.79 | 0 | 180 |
| | **CASSCF(10,9)** | 1.407 | 1.391 | 117.91 | 130.14 | 129.26 | 0 | 180 |
| | **XMS-CASPT2(4,4)** | 1.401 | 1.429 | 120.06 | 128.09 | 128.13 | 0 | 180 |
| | **XMS-CASPT2(6,6)** | 1.391 | 1.471 | 120.04 | 128.64 | 126.81 | 0 | 180 |
| | **XMS-CASPT2(10,9)** | 1.453 | 1.407 | 122.26 | 125.11 | 128.76 | 0 | 180 |
| $S_1$-TS1 | **CASSCF(4,4)** | 1.358 | 1.502 | 123.39 | 132.01 | 115.11 | -180 | -0 |
| | **CASSCF(6,6)** | 1.422 | 1.358 | 126.02 | 134.55 | 119.25 | -180 | -0 |
| | **CASSCF(10,9)** | 1.405 | 1.399 | 125.86 | 134.28 | 118.52 | -180 | -0 |
| | **XMS-CASPT2(4,4)** | 1.397 | 1.452 | 123.25 | 130.84 | 130.84 | -180 | -0 |
| | **XMS-CASPT2(6,6)** | 1.394 | 1.480 | 123.07 | 131.04 | 114.81 | -180 | -0 |
| | **XMS-CASPT2(10,9)** | 1.425 | 1.453 | 123.57 | 129.15 | 115.54 | -180 | -0 |
| $S_1$-TS2 | **CASSCF(4,4)** | 1.358 | 1.502 | 120.02 | 132.01 | 115.11 | 180 | -180 |
| | **CASSCF(6,6)** | 1.421 | 1.358 | 116.83 | 134.59 | 119.26 | 180 | -180 |
| | **CASSCF(10,9)** | 1.404 | 1.399 | 116.63 | 134.25 | 118.46 | 180 | -180 |
| | **XMS-CASPT2(4,4)** | 1.397 | 1.452 | 123.25 | 130.84 | 115.48 | 180 | -180 |
| | **XMS-CASPT2(6,6)** | 1.394 | 1.480 | 119.33 | 131.06 | 114.80 | 180 | -180 |
| | **XMS-CASPT2(10,9)** | 1.425 | 1.453 | 123.57 | 129.15 | 115.55 | 180 | -180 |

**Table B2:** Geometrical parameters of optimized four minimum energy conical intersections (MECIs): CI1, CI2, CI3, and CI4 at different levels of theory. Atom numbering is in accordance with Figure 4.3. Bond distances are in angstrom (Å) and dihedral angles in degrees (°). The cc-pVDZ basis set is used. $\Phi_I$ = N5-C4-C3-C2 and $\Phi_P$ = C1-C2-C3-C4.

| Structure | Method | C2-C3 | C3-C4 | C1-C2-C3 | C2-C3-C4 | N5-C4-C3 | $\Phi_I$ | $\Phi_P$ |
|---|---|---|---|---|---|---|---|---|
| CI1 | **CASSCF(4,4)** | 1.367 | 1.455 | 119.51 | 125.57 | 114.33 | 108.9 | 1.4 |
| | **CASSCF(6,6)** | 1.369 | 1.456 | 120.33 | 125.59 | 111.63 | 110.6 | 1.8 |
| | **XMS-CASPT2(4,4)** | 1.397 | 1.457 | 118.89 | 124.25 | 96.97 | 102.2 | 6.9 |
| | **XMS-CASPT2(6,6)** | 1.405 | 1.451 | 118.62 | 124.03 | 93.82 | 102.6 | 7.6 |
| CI2 | **CASSCF(4,4)** | 1.367 | 1.455 | 119.51 | 125.57 | 114.32 | -108.9 | -1.6 |
| | **CASSCF(6,6)** | 1.367 | 1.459 | 118.29 | 125.60 | 112.79 | -110.0 | -2.1 |
| | **XMS-CASPT2(4,4)** | 1.396 | 1.456 | 118.99 | 124.22 | 96.88 | -102.3 | -6.9 |
| | **XMS-CASPT2(6,6)** | 1.404 | 1.454 | 119.37 | 125.78 | 95.11 | -105.1 | -5.2 |
| CI3 | **CASSCF(4,4)** | 1.367 | 1.455 | 119.51 | 125.58 | 114.24 | 108.9 | 179.9 |
| | **CASSCF(6,6)** | 1.376 | 1.458 | 121.39 | 126.76 | 102.44 | 112.4 | -174.8 |
| | **XMS-CASPT2(4,4)** | 1.397 | 1.457 | 118.91 | 124.29 | 96.95 | 102.2 | -174.6 |
| | **XMS-CASPT2(6,6)** | 1.406 | 1.456 | 121.71 | 123.99 | 97.03 | 102.4 | 174.3 |
| CI4 | **CASSCF(4,4)** | 1.375 | 1.459 | 120.21 | 127.52 | 109.26 | -113.8 | -177.4 |
| | **CASSCF(6,6)** | 1.372 | 1.462 | 119.60 | 125.92 | 120.64 | -126.4 | -175.6 |
| | **XMS-CASPT2(4,4)** | 1.397 | 1.457 | 118.75 | 124.16 | 97.32 | -102.7 | 174.6 |
| | **XMS-CASPT2(6,6)** | 1.399 | 1.463 | 121.49 | 123.97 | 124.43 | -126.6 | -175.6 |

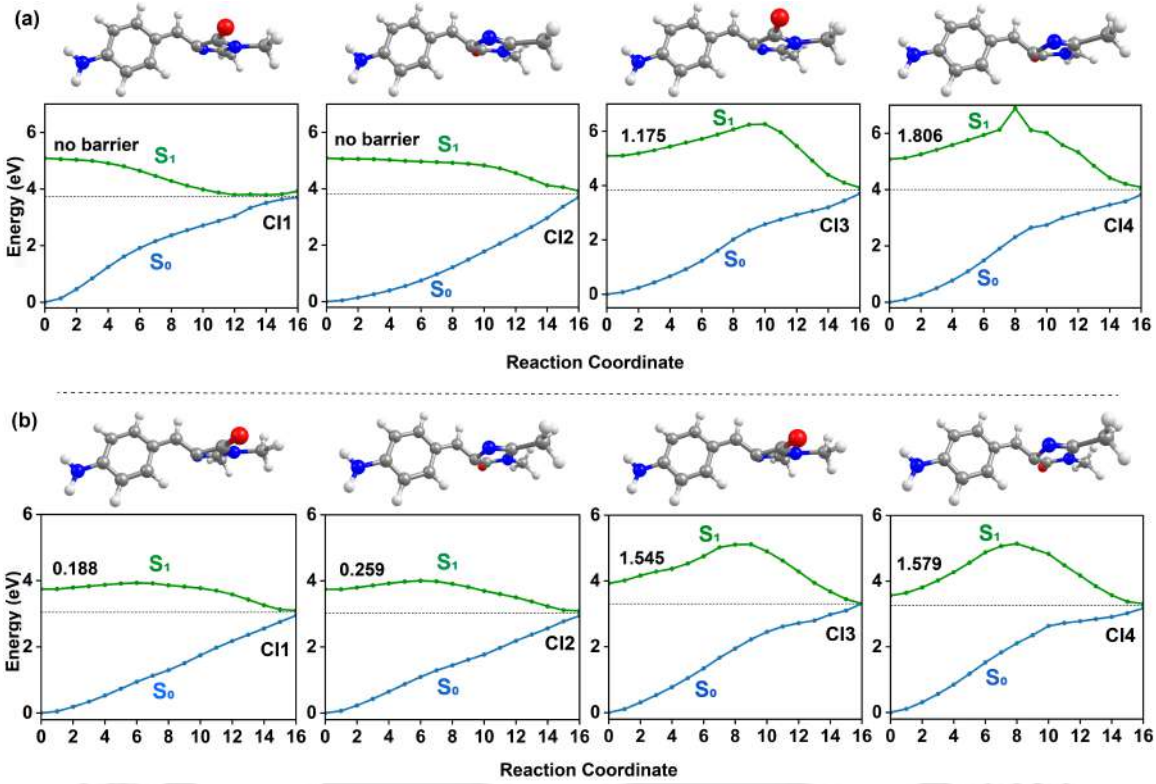


**Figure B1:** Linear interpolation in internal coordinates (LIICs) pathways connecting *cis* ($S_0$-CS1) minimum and $S_1(^1\pi\pi^*)/S_0$ MECI geometries computed at (a) CASSCF(4,4)/cc-pVDZ and (b) XMS-CASPT2(4,4)/cc-pVDZ levels. The top structures display molecular geometries of the critical points $S_1(^1\pi\pi^*)/S_0$ MECIs along with the dihedral angle rotations at (a) CASSCF(4,4)/cc-pVDZ and (b) XMS-CASPT2(4,4)/cc-pVDZ levels of theory.

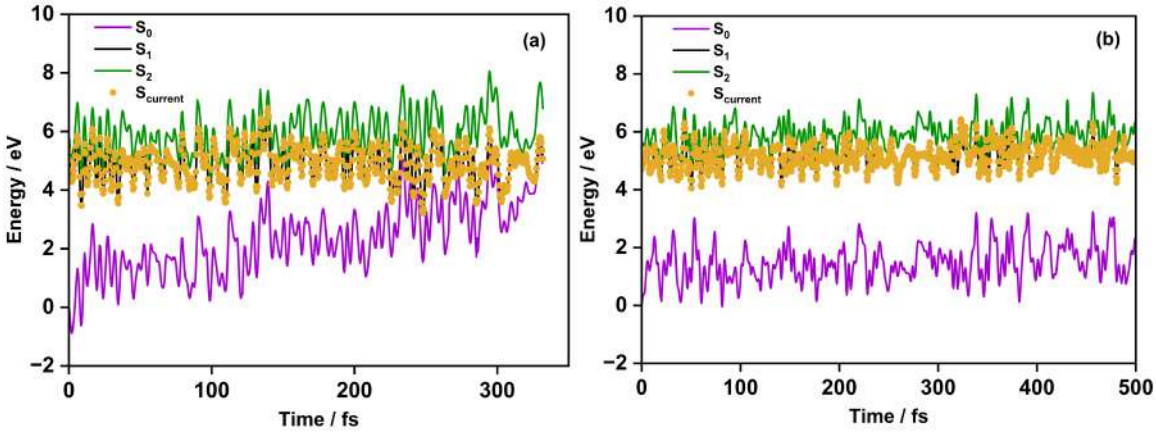


**Figure B2:** Time evolution of ground ($S_0$) and excited ($S_1$ and $S_2$) electronic states for a representative (a) reactive and (b) unreactive trajectory computed at CASSCF(4,4)/cc-pVDZ level of theory. The dotted yellow color signifies the current state ($S_{current}$) during the simulation.

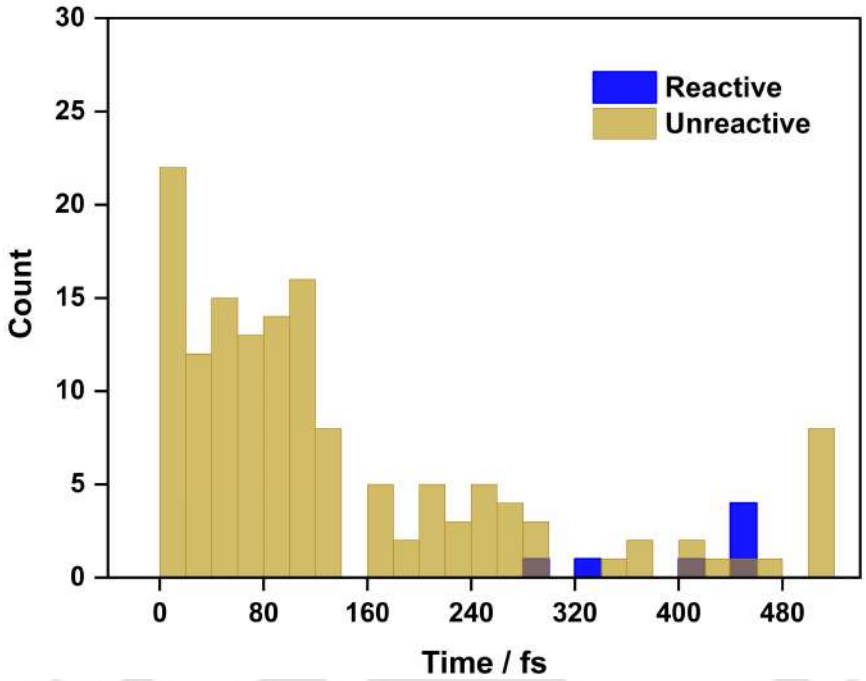


**Figure B3:** Histogram of the time window for reactive (blue) and unreactive (yellow) trajectories showing termination event.

# Appendix C

**Figure C1:** Structure of the GFP ($p$-HBDI$^-$) chromophore model demonstrating $\Phi_I$- (formed by the five-membered ring) and $\Phi_P$- (formed by six-membered ring) of the chromophore.

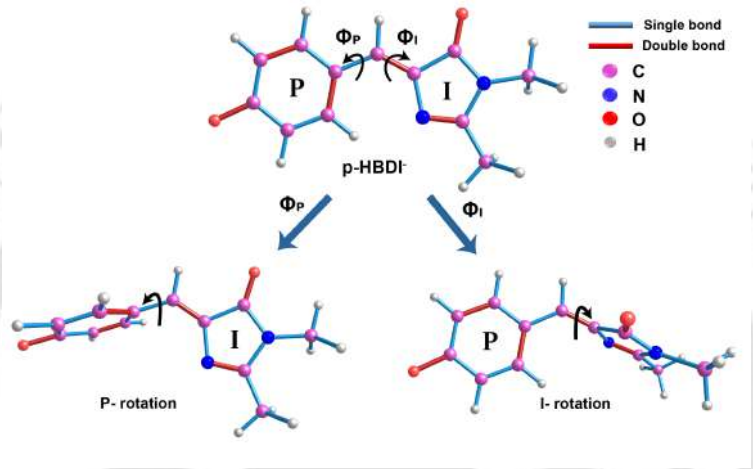


**Table C1:** Vertical excitation ($\lambda_{max}^{abs}$) energies (eV) and the corresponding oscillator strength (f) for transitions of BDI-$CH_3$ and BDI-H chromophore (monomer) computed at the TD-$\omega$B97XD level with different basis sets, in vacuum.

| Excited States | BDI-H | | | | BDI-$CH_3$ | | | |
|---|---|---|---|---|---|---|---|---|
| | 6-31G(d) | | TZVP | | 6-31G(d) | | TZVP | |
| | $\lambda_{max}^{abs}$ | $f$ | $\lambda_{max}^{abs}$ | $f$ | $\lambda_{max}^{abs}$ | $f$ | $\lambda_{max}^{abs}$ | $f$ |
| $S_1$ | 3.971 | 0.654 | 3.936 | 0.654 | 3.919 | 0.753 | 3.882 | 0.744 |
| $S_2$ | 4.033 | 0.001 | 3.961 | 0.001 | 4.087 | 0.001 | 4.108 | 0.001 |
| $S_3$ | 4.798 | 0.011 | 4.727 | 0.012 | 4.831 | 0.014 | 4.804 | 0.015 |
| $S_4$ | 5.196 | 0.069 | 5.119 | 0.061 | 4.973 | 0.136 | 4.938 | 0.121 |
| $S_5$ | 5.595 | 0.001 | 5.555 | 0.001 | 5.580 | 0.001 | 5.597 | 0.001 |
| **$S_6$** | **6.102** | **0.113** | **5.934** | **0.127** | **5.968** | **0.111** | **5.827** | **0.137** |
| $S_7$ | 6.471 | 0.042 | 6.298 | 0.059 | 6.391 | 0.065 | 6.259 | 0.090 |
| $S_8$ | 6.642 | 0.081 | 6.529 | 0.078 | 6.454 | 0.057 | 6.415 | 0.045 |
| $S_9$ | 6.776 | 0.001 | 6.680 | 0.001 | 6.82 | 0.001 | 6.774 | 0.001 |
| $S_{10}$ | 7.021 | 0.003 | 6.926 | 0.083 | 6.937 | 0.115 | 6.882 | 0.149 |

**Table C2:** Vertical excitation ($\lambda_{max}^{abs}$) energies (eV) and the corresponding oscillator strength ($f$) for the transition of BDI-H chromophore (dimer) computed at the TD-$\omega$B97XD and ADC(2) methods using different basis sets.

| States | $\omega$B97XD/ 6-31G(d) ($\lambda_{max}^{abs}$) | $f$ | $\omega$B97XD/ TZVP ($\lambda_{max}^{abs}$) | $f$ | ADC(2)/ SVP ($\lambda_{max}^{abs}$) | $f$ | ADC(2)/ pVTZ ($\lambda_{max}^{abs}$) | $f$ | ADC(2)/ TZVP ($\lambda_{max}^{abs}$) | $f$ |
|---|---|---|---|---|---|---|---|---|---|---|
| $S_1$ | 3.701 | 0.122 | 3.698 | 0.134 | 3.685 | 0.024 | 3.574 | 0.054 | 3.575 | 0.083 |
| $S_2$ | 3.965 | 0.103 | 3.947 | 0.492 | 3.739 | 0.089 | 3.636 | 0.097 | 3.633 | 0.071 |
| $S_3$ | 3.977 | 0.281 | 3.981 | 0.012 | 3.81 | 0.127 | 3.714 | 0.026 | 3.694 | 0.029 |
| $S_4$ | 4.037 | 0.123 | 4.028 | 0.115 | 3.977 | 0.754 | 3.888 | 0.751 | 3.854 | 0.744 |
| $S_5$ | 4.175 | 0.289 | 4.137 | 0.183 | 4.202 | 0.091 | 4.046 | 0.098 | 4.026 | 0.095 |
| $S_6$ | 4.407 | 0.069 | 4.379 | 0.042 | 4.462 | 0.026 | 4.337 | 0.031 | 4.32 | 0.022 |
| $S_7$ | 4.683 | 0.019 | 4.670 | 0.017 | 4.488 | 0.026 | 4.389 | 0.037 | 4.395 | 0.033 |
| $S_8$ | 4.815 | 0.009 | 4.786 | 0.009 | 4.673 | 0.009 | 4.534 | 0.007 | 4.53 | 0.005 |
| $S_9$ | 5.084 | 0.019 | 5.073 | 0.017 | 4.897 | 0.019 | 4.763 | 0.016 | 4.748 | 0.016 |
| $S_{10}$ | 5.129 | 0.044 | 5.114 | 0.066 | 4.951 | 0.039 | 4.814 | 0.036 | 4.799 | 0.027 |
| $S_{11}$ | 5.215 | 0.023 | 5.224 | 0.007 | 5.022 | 0.127 | 4.888 | 0.083 | 4.871 | 0.081 |
| $S_{12}$ | 5.424 | 0.012 | 5.415 | 0.007 | 5.371 | 0.003 | 5.315 | 0.003 | 5.293 | 0.002 |
| $S_{13}$ | 5.573 | 0.002 | 5.557 | 0.002 | 5.381 | 0.001 | 5.323 | 0.001 | 5.314 | 0.003 |
| $S_{14}$ | 5.625 | 0.003 | 5.614 | 0.002 | 5.511 | 0.008 | 5.384 | 0.009 | 5.367 | 0.008 |
| **$S_{15}$** | **5.711** | **0.018** | **5.657** | **0.012** | **5.599** | **0.020** | **5.426** | **0.021** | **5.409** | **0.015** |
| $S_{16}$ | 5.803 | 0.004 | 5.781 | 0.004 | 5.636 | 0.005 | 5.437 | 0.001 | 5.461 | 0.001 |
| $S_{17}$ | 5.936 | 0.003 | 5.894 | 0.045 | 5.798 | 0.008 | 5.593 | 0.008 | 5.599 | 0.008 |
| $S_{18}$ | 6.014 | 0.049 | 5.922 | 0.015 | 5.93 | 0.064 | 5.71 | 0.056 | 5.697 | 0.056 |
| $S_{19}$ | 6.060 | 0.042 | 5.951 | 0.066 | 5.97 | 0.044 | 5.76 | 0.034 | 5.756 | 0.034 |
| $S_{20}$ | 6.1126 | 0.037 | 6.054 | 0.019 | 6.118 | 0.029 | 5.937 | 0.016 | 5.934 | 0.017 |

**Table C3:** Mean position of hole and electron (POS), Excitonic participation ratio (PR), charge transfer ratio ($\omega_{CT}$), coherence length ($\omega_{COH}$), natural transition orbital participation ratio ($PR_{NTO}$), number of entangled states ($Z_{HE}$) and exciton size ($\tilde{d}_{exc}$, Å) for singlet excited states of the BDI-H $v$dW dimer for two representative trajectories (a) TrX and (b) TrY.

**(I) TrX (a) t = 0 fs**

| state | POS | PR | $\omega_{CT}$ | $\omega_{COH}$ | $PR_{NTO}$ | $Z_{HE}$ | $\tilde{d}_{exc}$ |
|---|---|---|---|---|---|---|---|
| $S_1$ | 1.55 | 1.96 | 0.13 | 1.28 | 1.69 | 1.99 | 3.50 |
| $S_2$ | 1.63 | 1.38 | 0.69 | 1.31 | 1.02 | 1.08 | 4.25 |
| $S_3$ | 1.35 | 1.82 | 0.26 | 1.53 | 1.83 | 2.14 | 3.68 |
| $S_4$ | 1.03 | 1.06 | 0.04 | 1.04 | 1.06 | 1.17 | 3.01 |
| $S_5$ | 1.97 | 1.06 | 0.06 | 1.06 | 1.06 | 1.18 | 3.11 |
| $S_6$ | 1.47 | 1.24 | 0.79 | 1.26 | 1.05 | 1.15 | 4.35 |
| $S_7$ | 1.03 | 1.06 | 0.05 | 1.06 | 1.39 | 1.67 | 3.58 |
| $S_8$ | 1.96 | 1.08 | 0.07 | 1.07 | 1.35 | 1.62 | 3.60 |
| $S_9$ | 1.80 | 1.46 | 0.36 | 1.35 | 1.11 | 1.33 | 3.71 |
| $S_{10}$ | 1.09 | 1.20 | 0.17 | 1.20 | 1.29 | 1.70 | 3.51 |
| $S_{11}$ | 1.66 | 1.49 | 0.59 | 1.42 | 1.13 | 1.35 | 3.94 |
| $S_{12}$ | 1.55 | 1.16 | 0.86 | 1.15 | 1.08 | 1.23 | 5.27 |
| $S_{13}$ | 1.38 | 1.53 | 0.57 | 1.50 | 1.69 | 2.46 | 4.18 |
| $S_{14}$ | 1.90 | 1.21 | 0.17 | 1.21 | 1.45 | 1.94 | 3.45 |
| **$S_{15}$** | **1.08** | **1.17** | **0.12** | **1.14** | **2.16** | **2.92** | **3.17** |

**(b) t = 118 fs**

| state | POS | PR | $\omega_{CT}$ | $\omega_{COH}$ | $PR_{NTO}$ | $Z_{HE}$ | $\tilde{d}_{exc}$ |
|---|---|---|---|---|---|---|---|
| $S_1$ | 1.97 | 1.06 | 0.03 | 1.03 | 1.06 | 1.19 | 3.57 |
| **$S_2$** | **1.84** | **1.37** | **0.30** | **1.28** | **1.04** | **1.09** | **3.82** |
| **$S_3$** | **1.66** | **1.40** | **0.67** | **1.30** | **1.03** | **1.09** | **4.28** |
| $S_4$ | 1.95 | 1.11 | 0.06 | 1.07 | 1.17 | 1.39 | 3.68 |
| $S_5$ | 1.05 | 1.11 | 0.09 | 1.09 | 1.09 | 1.23 | 3.02 |
| $S_6$ | 1.44 | 1.26 | 0.78 | 1.25 | 1.37 | 1.62 | 4.17 |
| $S_7$ | 1.21 | 1.49 | 0.35 | 1.46 | 1.24 | 1.52 | 3.72 |
| $S_8$ | 1.39 | 1.38 | 0.72 | 1.32 | 1.07 | 1.19 | 4.32 |
| $S_9$ | 1.94 | 1.13 | 0.07 | 1.08 | 1.13 | 1.39 | 3.65 |
| $S_{10}$ | 1.69 | 1.59 | 0.44 | 1.48 | 1.16 | 1.44 | 4.49 |
| $S_{11}$ | 1.69 | 1.66 | 0.35 | 1.50 | 1.28 | 1.69 | 4.23 |
| $S_{12}$ | 1.15 | 1.35 | 0.26 | 1.27 | 1.65 | 2.05 | 4.01 |
| $S_{13}$ | 1.46 | 1.23 | 0.79 | 1.24 | 1.25 | 1.53 | 4.63 |
| $S_{14}$ | 1.08 | 1.16 | 0.12 | 1.13 | 1.20 | 1.54 | 3.35 |
| $S_{15}$ | 1.98 | 1.04 | 0.03 | 1.03 | 1.20 | 1.52 | 3.44 |

**(II) TrY (a)t = 0 fs**

| state | POS | PR | $\omega_{CT}$ | $\omega_{COH}$ | $PR_{NTO}$ | $Z_{HE}$ | $\tilde{d}_{exc}$ |
|---|---|---|---|---|---|---|---|
| $S_1$ | 1.05 | 1.10 | 0.08 | 1.08 | 1.08 | 1.24 | 3.45 |
| $S_2$ | 1.03 | 1.06 | 0.06 | 1.06 | 1.09 | 1.24 | 3.25 |
| $S_3$ | 1.49 | 1.16 | 0.86 | 1.17 | 1.03 | 1.10 | 4.42 |
| $S_4$ | 1.74 | 1.56 | 0.45 | 1.43 | 1.09 | 1.26 | 3.94 |
| $S_5$ | 1.98 | 1.05 | 0.05 | 1.05 | 1.05 | 1.14 | 2.80 |
| $S_6$ | 1.19 | 1.47 | 0.21 | 1.28 | 1.61 | 2.09 | 3.69 |
| $S_7$ | 1.51 | 1.85 | 0.31 | 1.66 | 1.51 | 2.03 | 3.78 |
| $S_8$ | 1.85 | 1.35 | 0.13 | 1.18 | 1.44 | 1.95 | 3.69 |
| $S_9$ | 1.18 | 1.43 | 0.20 | 1.27 | 1.32 | 1.73 | 3.66 |
| $S_{10}$ | 1.51 | 1.36 | 0.71 | 1.39 | 1.33 | 1.79 | 4.27 |
| $S_{11}$ | 1.11 | 1.25 | 0.05 | 1.07 | 1.61 | 2.15 | 2.96 |
| $S_{12}$ | 1.74 | 1.62 | 0.27 | 1.44 | 1.61 | 2.24 | 3.49 |
| $S_{13}$ | 1.58 | 1.32 | 0.77 | 1.27 | 1.19 | 1.49 | 4.05 |
| $S_{14}$ | 1.51 | 1.10 | 0.91 | 1.09 | 1.13 | 1.34 | 4.74 |
| **$S_{15}$** | **1.12** | **1.27** | **0.14** | **1.19** | **2.09** | **2.68** | **3.87** |

**(a) t = 228.5 fs**

| state | POS | PR | $\omega_{CT}$ | $\omega_{COH}$ | $PR_{NTO}$ | $Z_{HE}$ | $\tilde{d}_{exc}$ |
|---|---|---|---|---|---|---|---|
| $S_1$ | 1.46 | 1.70 | 0.54 | 1.73 | 1.03 | 1.11 | 4.01 |
| **$S_2$** | **1.74** | **1.61** | **0.38** | **1.61** | **1.04** | **1.14** | **3.91** |
| **$S_3$** | **1.82** | **1.41** | **0.07** | **1.10** | **1.28** | **1.51** | **3.27** |
| $S_4$ | 1.24 | 1.56 | 0.13 | 1.19 | 1.29 | 1.55 | 3.25 |
| $S_5$ | 1.18 | 1.43 | 0.33 | 1.33 | 1.07 | 1.21 | 3.72 |
| $S_6$ | 1.62 | 1.37 | 0.71 | 1.31 | 1.08 | 1.20 | 4.27 |
| $S_7$ | 1.83 | 1.39 | 0.18 | 1.25 | 1.24 | 1.56 | 4.02 |
| $S_8$ | 1.12 | 1.28 | 0.13 | 1.16 | 1.36 | 1.72 | 3.93 |
| $S_9$ | 1.58 | 1.52 | 0.62 | 1.52 | 1.22 | 1.45 | 3.86 |
| $S_{10}$ | 1.59 | 1.87 | 0.35 | 1.73 | 1.49 | 1.84 | 3.73 |
| $S_{11}$ | 1.37 | 1.83 | 0.27 | 1.54 | 1.74 | 2.19 | 3.71 |
| $S_{12}$ | 1.96 | 1.08 | 0.06 | 1.06 | 1.34 | 1.65 | 2.88 |
| $S_{13}$ | 1.49 | 1.56 | 0.73 | 1.45 | 1.49 | 1.94 | 4.29 |
| $S_{14}$ | 1.37 | 1.44 | 0.65 | 1.38 | 1.71 | 2.11 | 4.96 |
| $S_{15}$ | 1.15 | 1.35 | 0.25 | 1.34 | 1.41 | 1.87 | 3.53 |

# Appendix D

**Table D1:** Geometrical parameters of optimized $S_0$-min, $S_1$-min, and all the enol (E1, E2, and E3) and keto (K1, K2, and K3) isomers at different levels of theory. Atom numbering is in accordance with Figure 6.3. Bond distances are in angstrom (Å) and dihedral angles in degrees (°). The cc-pVDZ basis set is used. $\Phi_I$ = N5-C4-C3-C2 and $\Phi_P$ = C1-C2-C3-C4.

| Isomers | Methods | C2-C3 | C4-C3 | $\Phi_P$ | $\Phi_I$ | O-H | N-H |
|---|---|---|---|---|---|---|---|
| $S_0$ | **CASSCF (10,9)** | 1.468 | 1.353 | 0.0 | 0.0 | 0.956 | 1.799 |
| | **CASSCF (4,4)** | 1.437 | 1.334 | 0.1 | 0.0 | 0.954 | 1.822 |
| | **MS-CASPT2 (10,9)** | 1.452 | 1.378 | 0.0 | 0.0 | 0.998 | 1.652 |
| | **XMS-CASPT2 (4,4)** | 1.466 | 1.371 | 0.2 | 0.0 | 1.002 | 1.630 |
| $S_1$ | **CASSCF (10,9)** | 1.488 | 1.377 | 1.1 | 0.6 | 1.411 | 1.031 |
| | **CASSCF (4,4)** | 1.483 | 1.372 | 1.6 | -5.5 | 1.235 | 1.014 |
| | **XMS-CASPT2 (10,9)** | 1.462 | 1.401 | -6.5 | 3.4 | 1.408 | 1.112 |
| | **XMS-CASPT2 (4,4)** | 1.452 | 1.393 | -1.6 | -0.3 | 1.577 | 1.059 |
| **K1** | **CASSCF (10,9)** | 1.379 | 1.419 | -176.6 | -174.7 | - | 0.996 |
| | **CASSCF (4,4)** | 1.386 | 1.412 | -176.5 | -175.0 | - | 0.995 |
| | **XMS-CASPT2 (10,9)** | 1.393 | 1.414 | -168.8 | 11.3 | - | 1.015 |
| | **XMS-CASPT2 (4,4)** | 1.395 | 1.411 | -169.6 | 8.9 | - | 1.015 |
| **K2** | **CASSCF (10,9)** | 1.372 | 1.431 | 169.5 | 159.6 | - | 0.996 |
| | **CASSCF (4,4)** | 1.384 | 1.415 | 166.2 | 160.6 | | 0.998 |
| | **XMS-CASPT2 (10,9)** | 1.396 | 1.418 | 166.9 | 162.2 | - | 1.014 |
| | **XMS-CASPT2 (4,4)** | 1.397 | 1.416 | 166.9 | 162.3 | | 1.015 |
| **K3** | **CASSCF (10,9)** | 1.383 | 1.414 | -179.7 | 178.2 | - | 0.998 |
| | **CASSCF (4,4)** | 1.375 | 1.408 | -179.6 | 178.7 | - | 0.999 |
| | **XMS-CASPT2 (10,9)** | 1.387 | 1.419 | -179.9 | -179.7 | - | 1.015 |
| | **XMS-CASPT2 (4,4)** | 1.392 | 1.413 | 179.9 | 179.9 | - | 1.016 |
| **E1** | **CASSCF (10,9)** | 1.466 | 1.355 | 179.8 | -0.0 | 0.942 | - |
| | **CASSCF (4,4)** | 1.440 | 1.333 | 179.9 | -0.0 | 0.941 | - |
| | **XMS-CASPT2 (10,9)** | 1.457 | 1.372 | 179.8 | -0.0 | 0.966 | - |
| | **XMS-CASPT2 (4,4)** | 1.458 | 1.373 | 179.9 | -0.0 | 0.966 | - |
| **E2** | **CASSCF (10,9)** | 1.470 | 1.360 | 37.3 | -179.8 | 0.952 | - |
| | **CASSCF (4,4)** | 1.441 | 1.333 | 26.2 | -178.0 | 0.954 | - |
| | **XMS-CASPT2 (10,9)** | 1.456 | 1.381 | 32.4 | -178.5 | 0.992 | - |
| | **XMS-CASPT2 (4,4)** | 1.466 | 1.375 | 34.4 | 179.7 | 1.001 | - |

| Isomers | Methods | C2-C3 | C4-C3 | $\Phi_P$ | $\Phi_I$ | O-H | N-H |
|---|---|---|---|---|---|---|---|
| **E3** | **CASSCF (10,9)** | 1.470 | 1.359 | -164.1 | 179.3 | 0.945 | - |
| | **CASSCF (4,4)** | 1.454 | 1.334 | -171.1 | 179.3 | 0.945 | - |
| | **MS-CASPT2 (10,9)** | 1.461 | 1.376 | -164.4 | 179.8 | 0.967 | - |
| | **XMS-CASPT2 (4,4)** | 1.459 | 1.377 | -166.7 | 177.1 | 0.972 | - |

**Table D2:** Relative Energies (RE, eV) of all MECIs with respect to $S_0$-min at CASSCF and XMS-CASPT2 levels of theory. The basis set cc-pVDZ was used.

| Methods | K-CI1 | K-CI2 | K-CI3 | K-CI4 | E-CI1 | E-CI2 | E-CI3 | E-CI4 |
|---|---|---|---|---|---|---|---|---|
| **CASSCF(10,9)** | 4.694 | 4.657 | 3.283 | 3.197 | 3.744 | 3.767 | 12.268 | 12.163 |
| **CASSCF(4,4)** | 4.652 | 4.674 | 3.462 | 3.462 | 3.319 | 3.344 | 9.306 | 7.007 |
| **XMS-CASPT2(10,9)** | 3.083 | 3.149 | 2.836 | 2.812 | 2.749 | 2.706 | 8.174 | 8.722 |
| **XMS-CASPT2(4,4)** | 3.250 | 3.231 | 2.895 | 2.895 | 2.814 | 2.781 | 10.839 | 10.734 |

**Table D3:** Geometrical parameters optimized of four keto (K-CI1, K-CI2, K-CI3, and K-CI4) and four enol (E-CI1, E-CI2, E-CI3, and E-CI4) minimum energy conical intersections (MECIs) at CASSCF(10,9) and CASSCF(4,4) levels of theory. Atom numbering is in accordance with Figure 6.3. Bond distances are in angstrom (Å) and dihedral angles in degree (°). The cc-pVDZ basis set is used. $\Phi_I$ = N5-C4-C3-C2 and $\Phi_P$ = C1-C2-C3-C4.

| Isomers | Methods | C2-C3 | C4-C3 | $\Phi_P$ | $\Phi_I$ | O-H | N-H |
|---|---|---|---|---|---|---|---|
| **K-CI1** | **CASSCF (10,9)** | 1.421 | 1.449 | 9.6 | -99.2 | - | 0.999 |
| | **CASSCF (4,4)** | 1.455 | 1.454 | 9.8 | -104.2 | - | 0.998 |
| **K-CI2** | **CASSCF (10,9)** | 1.426 | 1.453 | -10.1 | 96.7 | - | 0.999 |
| | **CASSCF (4,4)** | 1.459 | 1.460 | -9.8 | 100.8 | - | 1.000 |
| **K-CI3** | **CASSCF (10,9)** | 1.479 | 1.357 | -87.2 | 0.8 | - | 0.995 |
| | **CASSCF (4,4)** | 1.478 | 1.421 | -78.6 | -14.4 | - | 0.996 |
| **K-CI4** | **CASSCF (10,9)** | 1.468 | 1.357 | 84.6 | -3.5 | - | 0.994 |
| | **CASSCF (4,4)** | 1.478 | 1.420 | 78.5 | 14.3 | - | 0.985 |
| **E-CI1** | **CASSCF (10,9)** | 1.398 | 1.469 | -1.8 | -105.1 | 1.010 | - |
| | **CASSCF (4,4)** | 1.375 | 1.462 | -1.2 | -104.5 | 0.989 | - |
| **E-CI2** | **CASSCF (10,9)** | 1.398 | 1.469 | 0.2 | 106.4 | 1.006 | - |
| | **CASSCF (4,4)** | 1.378 | 1.462 | 3.1 | 105.5 | 0.988 | - |
| **E-CI3** | **CASSCF (10,9)** | 1.438 | 1.475 | -99.1 | 8.9 | 0.942 | - |
| | **CASSCF (4,4)** | 1.349 | 1.464 | -52.8 | -3.4 | 0.949 | - |
| **E-CI4** | **CASSCF (10,9)** | 1.496 | 1.465 | 60.5 | 18.6 | 0.942 | - |
| | **CASSCF (4,4)** | 1.482 | 1.419 | 57.3 | 45.6 | 0.943 | - |

# List of Publications

## Thesis Work

1. Lama, B.; Sarma, M. Unraveling the mechanistic pathway for the dual fluorescence in green fluorescent protein (GFP) chromophore analogue: a detailed theoretical investigation. *J. Phys. Chem. B* **2022**, *126*, 9930–9944.
2. Lama, B.; Sarma, M. Ultrafast Hot Exciton Nonadiabatic Excited-State Dynamics in Green Fluorescent Protein Chromophore Analogue. *J. Phys. Chem. B* **2024**, *128*, 6786–6796.
3. Lama, B.; Sarma, M. Photodynamics Simulation Insights into Excited-State Relaxation Mechanisms via Z/E Isomerization in Para-Amino Substituted GFP Chromophores. *J. Chem. Phys.* **2025**, *163*, 054305.
4. Lama, B.; Sarma, M. Entangled Light-Matter Interactions to Exploit the Multidimensional Excited-State Dynamics of an Ortho-Derivative GFP Chromophore. *(To be submitted).*

## Outside Thesis Work

1. Keot, N.; Lama, B.; Singh, H. K.; Bhattacharyya, H. P.; Sarma, M. Unveiling the Noncovalent Interaction of Thiazol-2-ylidene and Its Derivatives as N-heterocyclic Carbene with Different Proton Donor Molecules. *ChemPhysChem*, **2023**, *24*, e202300413 (1–11).
2. Rajbongshi, B. K.; Abdullah, S.; Lama, B.; Bhattacharyya, H. P.; Sarma, M. Regioselective and solvent-dependent photoisomerization induced internal conversion in red fluorescent protein chromophore analogues. *RSC Adv.*, **2024**, *14*, 18373–18384.

# List of Conference Attended

1. **B. Lama** and M. Sarma, *"Photoinduced Excited-State Relaxation Mechanism in Para-Amino Derivatives of GFP Chromophore"* in **Molecular Excited States (MolEx)** held at Toruń (Poland), June 09-13, 2025 (Poster).

2. **B. Lama** and M. Sarma, *"Hot Excitonic Behavior in a GFP Chromophore Derivative via Excited-State Nonadiabatic Dynamics"* in **29th PhotoIUPAC Symposium on Photochemistry** held at Valencia (Spain), July 14-19, 2024 (Poster).

3. **B. Lama** and M. Sarma, *"Hot Exciton Behavior in Green Fluorescent Protein (GFP) Chromophore Analogue via Nonadiabatic Dynamics"* in **Theoretical Chemistry Symposium- 2023 (TCS-2023)** held at Indian Institute of Technology Madras, Chennai (India), December 07-10, 2023 (Poster).

4. **B. Lama** and M. Sarma, *"Ultrafast Excited-State Intramolecular and Intermolecular Proton Transfer (ESIPT) Mechanism in Sulfonamide Analogues of GFP: A Theoretical Investigation"* in **Current Trends in Theoretical Chemistry (CTTC-2022)** held at DAE Convention Centre, BARC, Anushaktingar, Mumbai (India), September 22-24, 2022 (Poster).

5. **B. Lama** and M. Sarma, *"Theoretical and Computational Investigation on Dual Fluorescence Mechanism of Green Fluorescent Protein (GFP)-like Chromophore"* in **Theoretical Chemistry Symposium-2021 (TCS-2021)** organized by IISER Kolkata, IACS Kolkata, Kalyani University and S.N. Bose National Centre for Basic Sciences Kolkata, December 11-14, 2021 (Poster).

6. **B. Lama** and M. Sarma, *"Theoretical and Computational Investigation of the Excited State Dynamics of the Green Fluorescent Protein and its variants"* in **57th Annual Convention of Chemists, 2020 & International Conference on Recent Trends in Chemical Sciences (RTCS-2020)** organized by Indian Chemical Society, Kolkata, December 26-29, 2020 (Poster).

7. **B. Lama** attended the conference **Introduction to Gaussian: Theory and Practice Workshop** held at Kolkata (India), January 14-18, 2019 (Participant).

8. **B. Lama** attended the workshop **Introduction to Machine Learning using Python** held at Indian Institute of Technology Guwahati (India), November 16-17, 2019 (Participant).